DOE/ER/40321--11

DE93 013385

MASS AND CHARGE DISTRIBUTIONS IN IRON-INDUCED REACTIONS AND EXCITATION ENERGY DIVISION BETWEEN THE FRAGMENTS OF THE 672-MeV $^{56}Fe + ^{165}Ho$ REACTION

By

Houria Madani

Dissertation submitted to the Faculty of the Graduate School
of the University of Maryland in partial fulfillment
of the requirements for the degree of
Doctor of Philosophy
1993

Advisory Committee:

Professor Alice C. Mignerey, Chair/Advisor
Professor Chia C. Chang
Professor James Griffin
Professor John Moore
Professor William B. Walters

ABSTRACT

Title of Dissertation: Mass And Charge Distributions In Iron-Induced Reactions And Excitation Energy Division Between The Fragments Of The Reaction ^{56}Fe On ^{165}Ho At 672 MeV.

Houria Madani, Doctor Of Philosophy, 1993

Dissertation directed by: Alice C. Mignerey, Professor of Chemistry
Department of Chemistry and Biochemistry

The projectile-like and target-like fragments produced by the 12-MeV/nucleon $^{56}Fe + ^{165}Ho$ reaction were detected in coincidence. The measured parameters were the mass, charge, kinetic energy and, scattering angle of the projectile-like fragments, and the scattering angle of the target-like fragments. The mass and charge distributions of the projectile-like fragments were generated as a function of energy loss, and characterized by their centroids, variances, and correlation coefficients.

The neutron drift of the measured projectile-like products is mostly due to evaporative processes, while the charge drift is a result of a net transfer of protons from the projectile-like fragment to the target-like fragment. The result is a weak drift of the system towards mass asymmetry, opposite to the direction that minimizes the potential energy of the composite system. The increase in the variances with energy loss is consistent with a nucleon exchange mechanism as a mean for energy dissipation.

The predictions of two nucleon exchange models are compared to the experimental results of the 672-MeV ^{56}Fe + ^{165}Ho reaction and other Fe-induced reactions. The fairly good agreement between the experimental and theoretical variances verifies the prevalence of a nucleon exchange mechanism in these reactions. Significant differences between the two models in their prediction of the centroids are a consequence of their different approaches in simulating the deep-inelastic process. A better agreement with the data was observed with Tassan-Got's model than with Randrup's model.

The information from the coincidence measurement and two-body kinematics are used to reconstruct the pre-evaporation masses of the projectile-like and target-like fragments of the reaction. Statistical evaporation calculations are used to translate these masses into excitation energies of the primary fragments. The excitation energy division between the two fragments is then determined as a function of total kinetic energy loss and mass division.

The ratio of excitation energy stored in the projectile-like fragment decreases with increasing energy loss, in qualitative agreement with previous measurements. However, higher ratios are observed for the 672-MeV ^{56}Fe on ^{165}Ho system and are attributed to the increased bombarding energy. Excitation energy partition is correlated to the direction of nucleon transfer for selective energy loss bins. Monte Carlo simulations of the experiment were not conclusive in attributing the correlation to instrumental resolution.

DEDICATION

To my family, and to the memory of my father Abdelaziz Madani

and my brother Abdennour Madani.

ACKNOWLEDGMENTS

I wish to thank my advisor Dr. Alice C. Mignerey for her support and guidance during my years in graduate research. Working in her group has been a rewarding and enjoyable experience.

I am also grateful to Dr. Herbert Breuer for his help in the data analysis process. I thank my colleagues and the personnel of Oak Ridge National Laboratory who participated in running the experiment upon which this thesis is based. I gratefully acknowledge the many fruitful discussions with my fellow students.

Special thanks go to my friend Rachid Dahmani for his moral support and his constantly cheerful mood during our years together in graduate school. His presence made the long studying hours more bearable.

Finally, I thank my family and friends for their love and continual moral support.

This work was supported by the Director, Office of energy Research, Division of Nuclear Physics of the Office of High Energy and Nuclear Physics, of the U.S. Department of Energy under Contract DOE/ER/

TABLE OF CONTENTS

LIST OF TABLES

LIST OF FIGURES

CHAPTER I INTRODUCTION

The advent of heavy-ion ($A \geq 4$) beams in the 1960's provided a new tool for probing the properties of the nucleus and the nuclear force. Descriptions of the new heavy-ion induced nuclear reactions lend themselves to a macroscopic approach, based on principles traditionally used in nuclear chemistry and statistical mechanics. In this new approach, the global properties of the interacting nuclei are studied instead of the microscopic properties of individual nucleons.

A collision between two heavy nuclei leads to different types of reactions depending on the bombarding energy and the distance between the centers of the two colliding nuclei, called the impact parameter. Since the wavelength associated with the relative motion of the two nuclei is smaller than the interaction radius R, a semi-classical approach can be used to study these collisions.

The types of heavy-ion reactions that occur at low bombarding energies, below the Fermi energy domain (~28 MeV/u) are illustrated in Figure I.1. The two nuclei are approximated by two rigid spheres interacting with an impact parameter b, during an interaction time t. However, because of the Coulomb repulsion the projectile does not always 'hit' the target, even if b is smaller than R. The projectile is deflected from its initial trajectory with a deflection angle which depends on the impact parameter, the Coulomb energy, the center-of-mass energy, and the interaction radius. When the interaction radius R is equal to the distance of closest approach D, i.e., when the two ions barely touch, grazing trajectories are obtained. The value of the impact parameter is then defined as b_{gr}. At grazing trajectories, elastic scattering or direct reactions may occur. Direct collisions consist of one step transfer of one or a few nucleons from one nucleus to the other. These interactions are characterized by a discrete change of angular momentum. Because of short

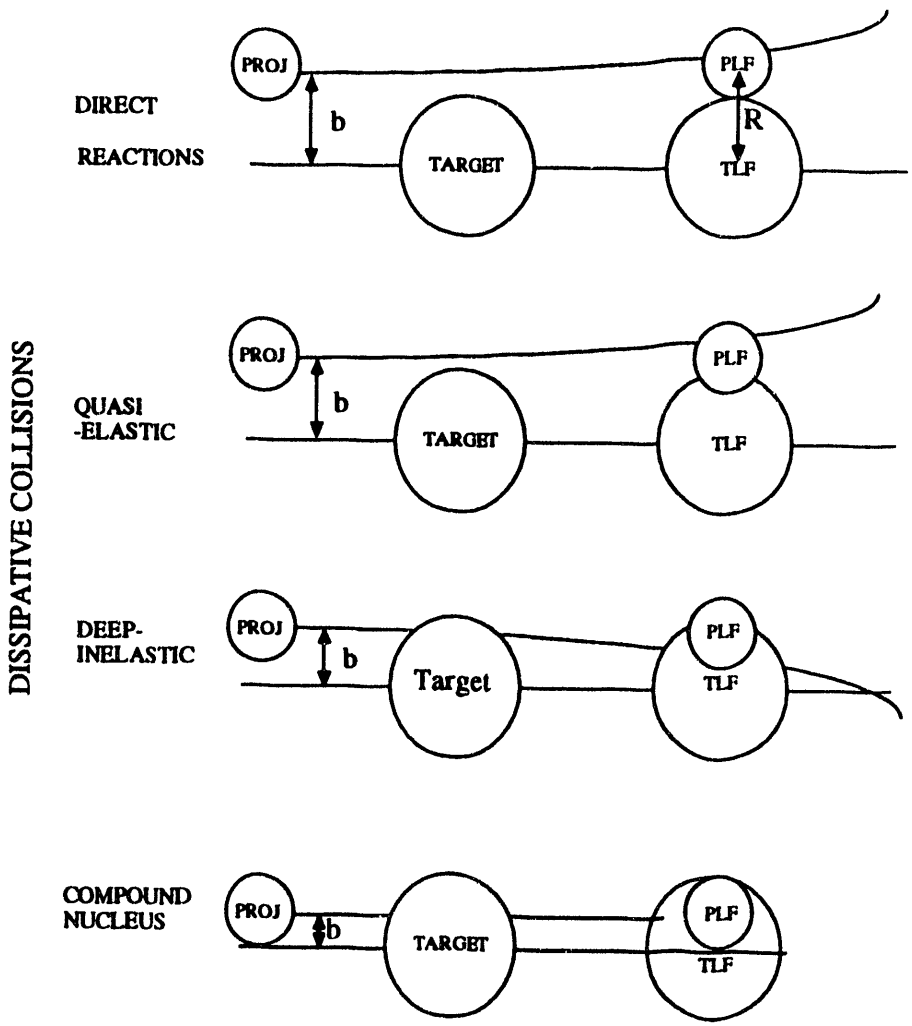

Figure I.1
Pictoral representation of the various reaction mechanisms in heavy-ion collisions at low bombarding energies.

interaction times ($t \approx 10^{-22}$ sec), only a small amount of kinetic energy is lost.

When the impact parameter is much smaller than the grazing value ($b << b_{gr}$) close collisions occur, which are characterized by interaction times (10^{-16} to 10^{-20} sec) longer than those of direct reactions. An increased interpenetration of the two nuclei is expected in this type of collision. This may lead to the formation of an excited compound nucleus (CN) which decays by fission, emission of light particles (p, n, α) or gamma emission.

Until about two decades ago, direct and compound nucleus reactions were the only processes observed in heavy-ion reactions. However, the results of several experiments with various systems showed the existence of a different type of reaction: deep-inelastic reactions (DIR). They form an intermediate process between direct reactions and compound nucleus formation. The impact parameter in these cases has to be larger than a critical value for CN formation.

Deep-inelastic reactions can be seen as a flow of nucleons from one nucleus to the other through a window opened by the collisions. This allows for the dissipation of energy and angular momentum. However, the possibility of energy damping by giant resonances in the quasi-elastic region was also postulated by Broglia *et al.* [BRO76]. Experimental evidence confirmed the existence of this collective mode of excitation [FRA80, MIG81].

In deep-inelastic reactions, large amounts of relative kinetic energy are converted into excitation energy of the dinuclear system, which rotates and separates into a projectile-like fragment (PLF) and a target-like fragment (TLF), whose atomic and mass numbers are close to those of the projectile and target, respectively. After a complete separation of the two fragments and after they are totally accelerated by Coulomb's repulsive potential, they deexcite by evaporation

of light particles and gamma emission. The reactions studied in the present work fall in the deep-inelastic region and thus the focus will be on this type of collision.

I.A. Deep-Inelastic Reactions

The tremendous amount of data from experiments of heavy-ion reactions in the deep-inelastic region resulted in the understanding of some of their general features [LEF78, GOB80, FRE84, SCH84, BOR90]. At low bombarding energies (a few MeV/u above the Coulomb barrier), the two reaction fragments have a close resemblance to the entrance channel nuclei in terms of their masses and charges. This implies that the system retains its binary character during the whole interaction phase. The detection in coincidence of the two fragments produced in a deep-inelastic reaction confirms the binary character of this mechanism [LEF78, SCH84].

The center-of-mass kinetic energy distribution and the angular distributions of the reaction products are best described by contour plots of the double differential cross section $d^2\sigma/d\Omega dE$, as a function of the PLF angle in the center-of-mass (θ_{cm}), and TKE the total kinetic energy in the center-of-mass frame, as a function of the PLF angle in the center-of-mass. This type of plot, shown in Figure I.2, was first constructed by Wilcynski [WIL73, SIW76] for potassium isotopes emitted in the 328-MeV Ar + Th reaction. Its main feature is the existence of two ridges of maximum cross section. The first one is peaked around the grazing angle ($\theta_{gr} \sim 34^o$) and at a center-of-mass kinetic energy close to the initial kinetic energy and is thus attributed to quasi-elastic events. As the kinetic energy decreases, this ridge moves towards more forward angles. A second ridge starts at the most forward angles and moves toward larger angles as the energy decreases slightly.

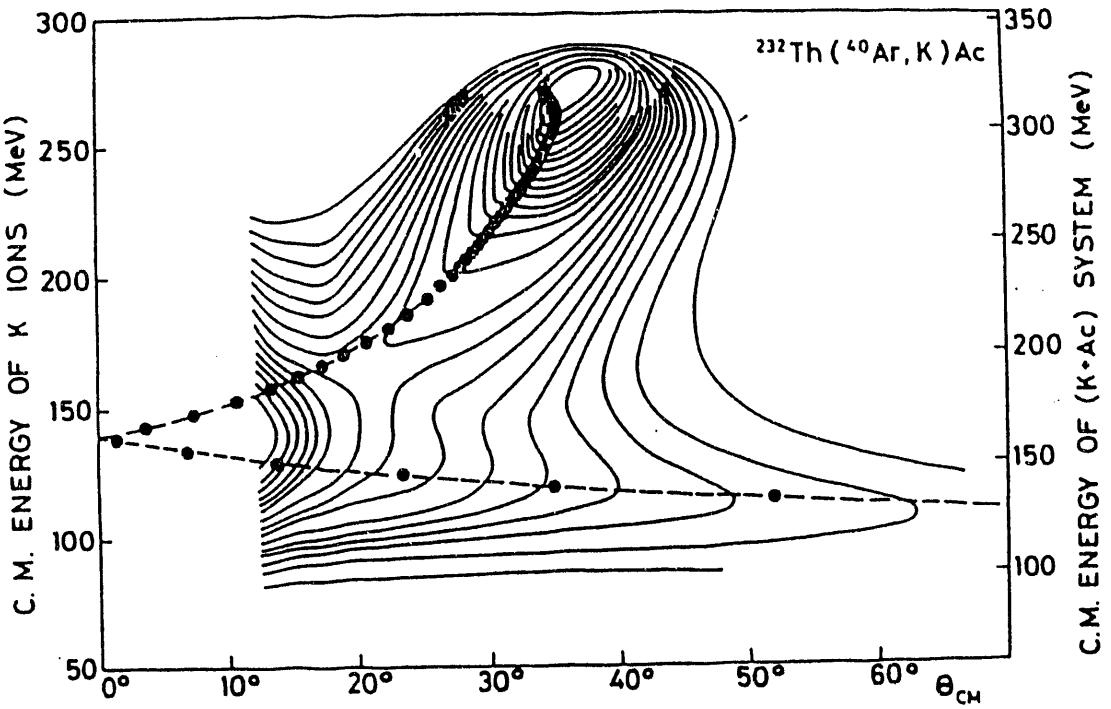

Figure I.2

Contour diagram of the double differential cross section $\frac{d^2\sigma}{d\Omega dE}$ as a function of the scattering angle θ_{cm} and kinetic energy TKE for the ^{232}Th + ^{40}Ar reaction at 388 MeV for potassium isotopes. The circles indicate calculations performed with angular momentum values ranging from $\ell = 180\ \hbar$ to $\ell = 250\ \hbar$ [SIW76].

This pattern in the Wilcynski plot is interpreted as being due to deflections of the reaction products from

grazing trajectories. The deflection angle depends on the value of the angular momentum ℓ (or the impact parameter b).

The ℓ value for deep-inelastic reactions lies between an ℓ_{crit} value for fusion and a maximum angular momentum ℓ_{max} corresponding to grazing trajectories. As ℓ decreases from ℓ_{max} the trajectories are more and more deflected from the grazing values towards more forward values and sometimes the system rotates past 0^o and to negative angles. Experimentally, the detection system does not distinguish between events at positive or negative angles, therefore the patterns seen experimentally are the positive part of the plot shown in the top part of Figure I.3. The bottom part of Figure I.3 shows a schematic view of the evolution of the deflection angle with angular momentum.

The most striking feature of deep-inelastic reactions is the conversion of a large portion of relative kinetic energy into internal excitation of the outgoing fragments. This total kinetic energy loss (TKEL) ranges from 0 MeV for elastic events to (E_{cm} - V_c) MeV for fully damped events, where E_{cm} is the initial center-of-mass kinetic energy and V_c is the Coulomb potential of the two separating nuclei. Since the total kinetic energy loss is related to the time scale of the collision, it can be considered as a "clock" for these reactions. Therefore, the study of the behavior of observables in deep-inelastic reactions with energy loss is analogous to following the evolution of the interacting system with time. The evolution of the post-evaporation mass and charge distributions of the projectile-like fragments produced in a deep-inelastic reaction are two examples of these observables and are further discussed in the next section.

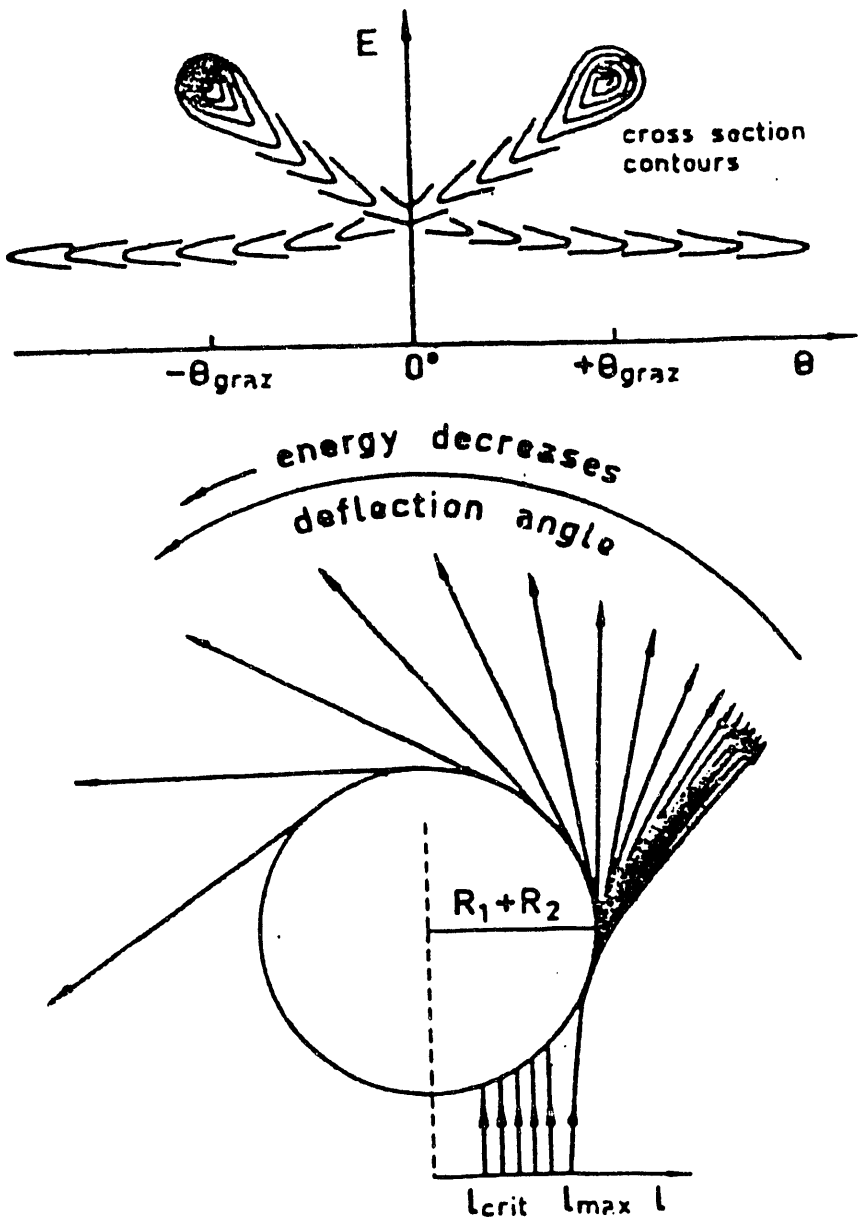

Figure I.3
Schematic representation of the classical trajectories leading to different deflection angles in deep-inelastic reactions.

I. B Mass and Charge Distributions.

One of the characteristic features of deep-inelastic reactions is memory of the entrance channel. This is inferred from the mass and charge distributions of the detected fragments, which show that the masses and charges of the reaction products are close to the masses and charges of the projectile and target. Thus, the use of very asymmetric systems facilitates the distinction between the deep-inelastic mechanism and the compound nucleus or fusion mechanisms. The evolution of the system with interaction time can be studied by looking at the behavior of mass and charge distributions with TKEL. In general, only the mass and charge distributions of the PLF's are determined, the characteristics of the TLF's are deduced kinematically using the binary character of the process.

The nuclide distribution of the PLF's in the N-Z (A-Z) plane is characterized by its centroids <N> (<A>) and <Z>, its variances σ_N^2 (σ_A^2) and σ_Z^2 and the correlation factor ρ_{NZ} (ρ_{AZ}). The broadening of the PLF mass and charge distributions with increasing TKEL is indicative of the presence of nucleon transfer between the fragments [SCH84, BOR90]. However, there is yet no evidence whether nucleon transfer alone can account for all the excitation energy produced in deep-inelastic reactions. Furthermore, the question of how this excitation energy is shared by the projectile-like and target-like fragments is not yet satisfactorily answered.

Another point to be elucidated is the strong drift towards mass asymmetry that is observed in many asymmetric systems. Such a drift is not expected since it is contrary to the direction that minimizes the potential energy surface (PES) of the composite system. Ambiguous conclusions were drawn from results of experiments performed on different systems. The study of the 887-MeV ^{58}Ni on ^{197}Au by Awes *et al.* [AWE84] resulted in an agreement

between the data and the predictions of the PES gradient only if equal excitation energy was assumed. On the other hand, experiments with ^{58}Ni and ^{64}Ni on ^{238}U, ^{74}Ge on ^{165}Ho, and ^{56}Fe on ^{165}Ho at 8.3 MeV/u by Planeta *et al.* [PLA90] showed that the experimental data do not always follow the direction predicted by the PES gradient. This effect is shown in Figure I.4, where the centroids of the nuclide distributions in the N-Z plane of the PLF's produced by the 8.3-MeV/u ^{74}Ge on ^{165}Ho, ^{56}Fe on ^{165}Ho, ^{58}Ni on ^{238}U, and ^{64}Ni on ^{238}U reactions are plotted for successive bins of energy loss from 0 MeV to 150 MeV. In these plots the measured data are represented by the squares. The primary results, which were obtained by neutron evaporation corrections for the two Ni systems and by kinematical reconstruction for the other two systems, are indicated by the circles. The dashed arrow represents the gradient to the potential energy surface (PES) at injection point, i.e., at the entrance channel. In the PES calculations for these cases shell effects were included in the calculation of the PLF and TLF binding energies while pairing effects were suppressed.

The predictions of Randrup's nucleon exchange model [RAN78, 79, 82] are indicated in Figure I.4 by the solid line. Except for the ^{74}Ge on ^{165}Ho case, the predominant feature is the increase in neutron number and decrease in proton number resulting in the production of neutron-rich PLF's. Another feature observed here is the tendency of the system to follow the trajectory indicated by the PES gradient, when it has a large magnitude, as in the ^{58}Ni on ^{238}U system. In the remaining cases, the trajectory followed by the system departs from the direction of the gradient early in the reaction. In all four cases the experimental data drastically differ from the predictions of Randrup's model, which indicates an evolution of the systems towards symmetry.

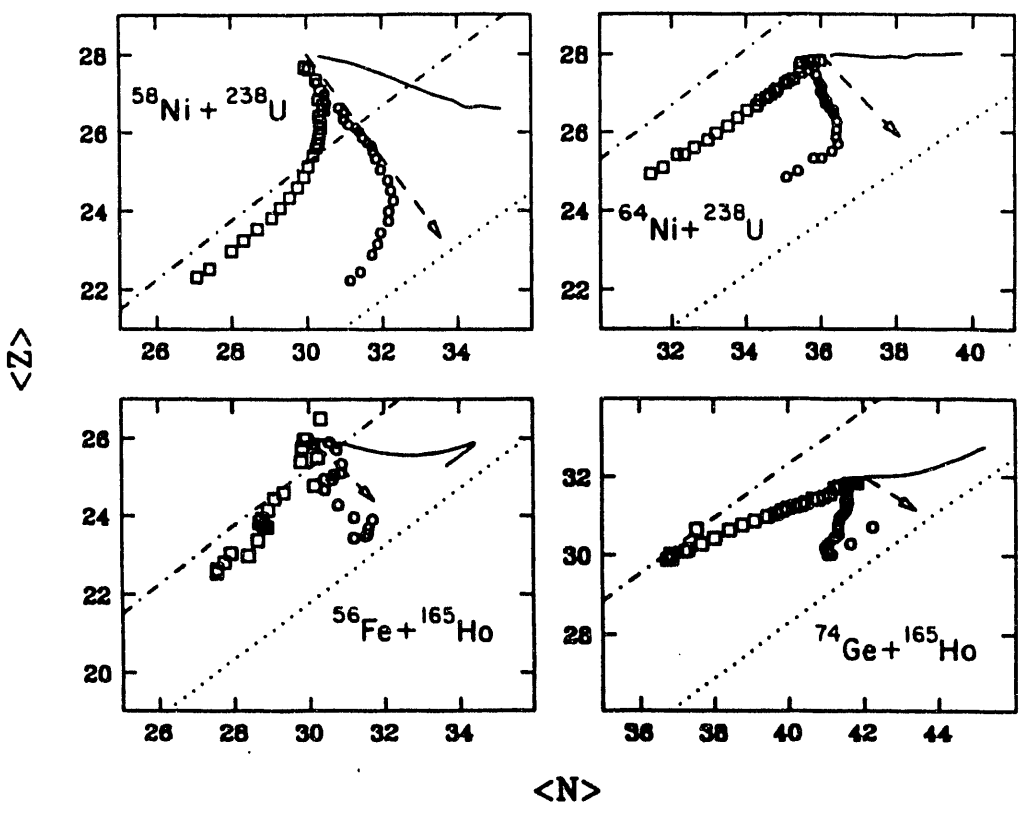

Figure I.4
Evolution of the centroids of the nuclide distributions in the N-Z plane as a function of energy loss for the 8.3-MeV/u ^{74}Ge on ^{165}Ho, ^{56}Fe on ^{165}Ho, ^{58}Ni on ^{238}U, and ^{64}Ni on ^{238}U systems. Measured distributions are indicated by squares, primary distributions by circles, and Randrup's model predictions by the solid line. The arrows show the gradients to the potential energy surface of the systems at the injection points [PLA90].

Several nucleon exchange models have been developed to describe deep-inelastic reactions in terms of mass and charge distributions. It is important to realize that the fragments detected are post-evaporative, while the distributions predicted by the models describe the emitted fragments in their excited state. Therefore, evaporation corrections have to be taken into account before making any comparisons between experimental and theoretical distributions. As an example, Figure I.5 compares the experimental mass and charge distributions of the PLF's produced in the 270-MeV ^{37}Cl on ^{40}Ca reaction [MAR91, 92] to the pre-evaporation (solid lines) and post-evaporation (dashed lines) distributions predicted by Randrup's [RAN78, 79, 82] model in Figure I.5. The values of post-evaporative <Z> and <N> are in good agreement with the experimental data.

I.C Excitation Energy Division

Knowing how the excitation energy of the system is divided between the two heavy fragments of a deep-inelastic reaction is important to the understanding of the underlying mechanisms in this type of reaction. However, since the primary fragments evaporate shortly ($\approx 10^{-16}$ s) after their formation, the excitation energy of the composite system formed after the collision cannot be measured directly; it has to be inferred from other observables.

One extreme for excitation energy division is equal division between the reaction partners, in which case the lighter fragment will have a higher temperature than the heavier one. At the other extreme is a division according to the two partners' mass ratios, in which case the two primary fragments are in thermal equilibrium. Experimental data have shown an equipartition of the excitation energy in some

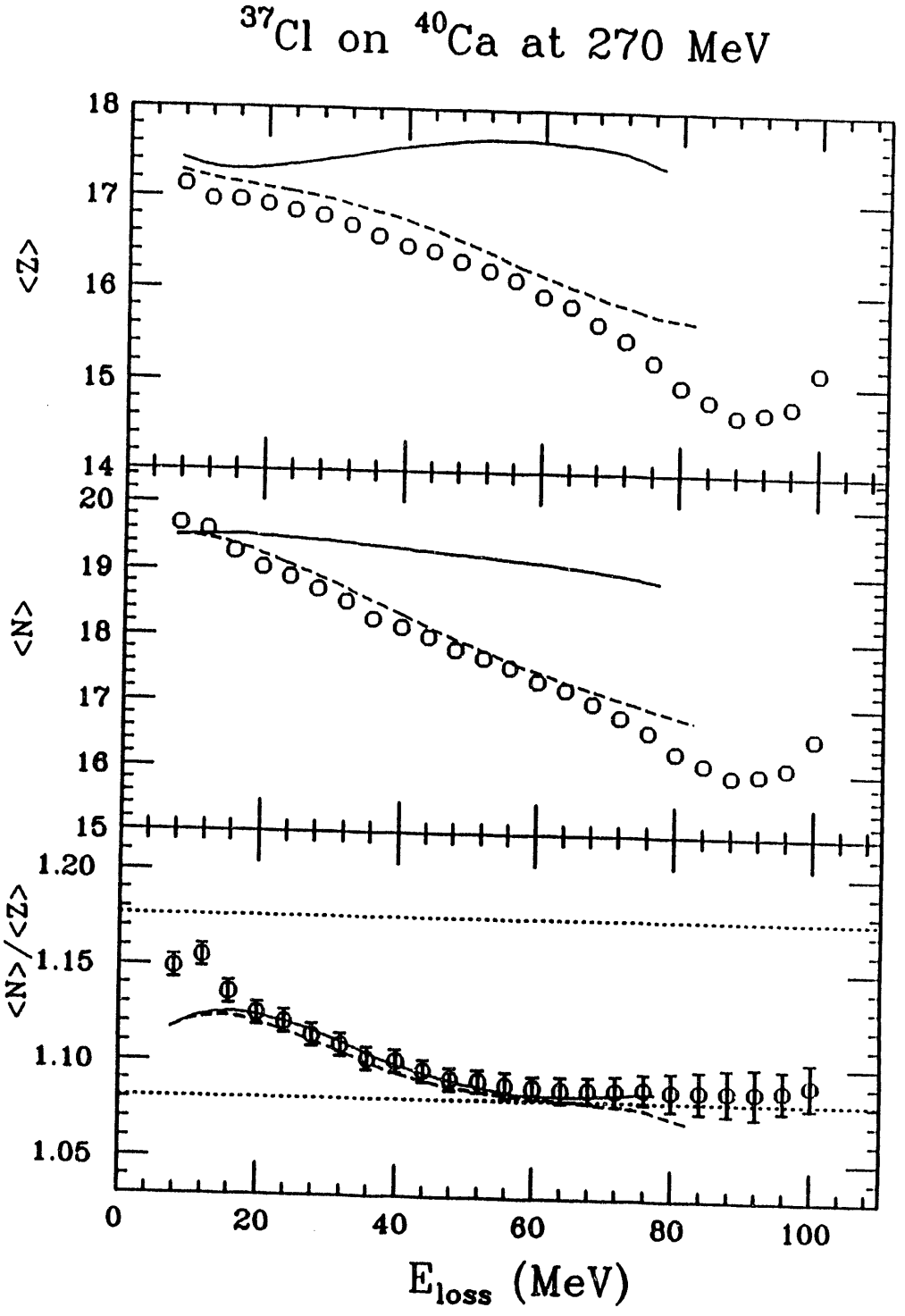

Figure I.5
Experimental results (circles) and theoretical predictions (lines) for <Z>, <N>, and <N>/<Z> for the ^{37}Cl on ^{40}Ca at 270 MeV. The solid lines indicate Randrup's model predictions for the primary distributions, and the dashed lines indicate the model predictions for the secondary distributions after evaporation corrections [MAR91, 92].

cases [AWE84, VAN84, SOH85, 87A, 87B, SOB86, WIL87] and a division according to the fragments' masses in other cases [BAB78, CAU78, EYA78, GOUL78, HIL79, TAM79]. Results from some of the most recent data agree with theoretical predictions of a smooth transition from equal division at low TKEL to thermal equilibrium at higher TKEL [BEN85, 87, 88, KWI90, PEN90]. These contradictory results lead to the conclusion that the methods being used for evaluating the excitation energy of each fragment have to be re-examined.

Various types of experiments have been performed to determine each fragment's excitation energy [BAB78, CAU78, EYA78, PLA78, HIL79, TAM79, VAN84, BEN85, 87, 88, SOH85, KWI90, PEN90]. A kinematical coincidence technique in which the PLF and the TLF are detected simultaneously was one of the first methods tried in the 1970's for excitation energy determination [BAB78]. Based on the fact that deep-inelastic reactions are binary, the PLF primary mass (pre-evaporation) can be evaluated from measured secondary (post-evaporation) quantities. The use of an evaporation code then allows the determination of the excitation energy of the PLF. The results obtained by Babinet *et al.* [BAB78] suggested that thermal equilibrium was attained by the two fragments and therefore, the excitation energy of the system was divided according to the mass ratios of the reaction fragments.

Other experiments based on the detection of neutrons emitted from the PLF and the TLF were performed. The study of the 400 MeV Cu + Au system by Tamain *et al.* [TAM79] confirmed the finding of thermal equilibrium in deep-inelastic reactions. However, studies of the systems $^{58}Ni + ^{58}Ni$ and $^{58}Ni + ^{197}Au$ at 15.3 MeV/u by Awes *et al.* [AWE84] showed an important disagreement with the previous conclusions. In this case only the projectile-like fragments were detected and the excitation energy division was inferred from comparing PLF

charge distributions to theoretical distributions obtained by applying evaporation corrections to primary distributions predicted by Randrup's model [RAN78, 79, 82]. The results in this case seemed to be more consistent with the scenario where the excitation energy is divided equally between the two fragments at small energy losses (less than 100 MeV) and tends to a mass partition for higher values of energy loss. However, the predictions were based on primary distributions which do not have the strong negative charge drift exhibited by the experimental data. Therefore, it is not possible to make any rigorous conclusions.

The study of the 505-MeV ^{56}Fe on ^{165}Ho system with the kinematics coincidence technique by Benton *et al.* [BEN85, 88, 89] showed an evolution of the system from equal excitation energy division at low TKEL towards a division according to the fragment masses at higher TKEL. However, no evidence of reaching thermal equilibrium was observed.

A feature observed in experimental studies of the excitation energy division between the fragments of the reaction ^{56}Fe on ^{165}Ho at 505 MeV [BEN 85, 88] and the reaction ^{74}Ge on ^{165}Ho at 629 MeV [KWI90] is the correlation between excitation energy division and exit channel. However, Tõke *et al.* questioned these results and suggested that the correlation can be attributed to instrumental effects [TOK89, 90, 91]. Monte Carlo simulations were performed to reproduce the parameters and the resolution of the experimental set-up [TOK89, 90, 91]. The results of the simulation for the ^{74}Ge on ^{165}Ho system showed that some of the excitation energy division dependence on the primary mass of the projectile was indeed due to finite resolutions of some of the measured variables. However, these instrumental effects could not account for all the correlation between excitation energy sharing and exit channel.

I. D Research Goals

The primary goal of the present study of the 672-MeV ^{56}Fe on ^{165}Ho system is to address the question of how the excitation energy of the system is partitioned between the two complex fragments that are emitted in deep-inelastic collisions. The use of the coincidence method to detect both reaction fragments, PLF and TLF, allows a less ambiguous characterization of the PLF in terms of its primary mass before evaporation. This in turn makes the determination of the PLF's excitation energy by this type of analysis more rigorous than by analyses based on the study of mass and charge distributions of secondary fragments.

The kinematic coincidence technique is based on the assumption that the detected fragments are close in mass and charge to the primary fragments before deexcitation, and on the premise that the only way the reaction products dispose of their excitation energy is via evaporation, a process which can be simulated by statistical models. Therefore, it is important to choose reaction partners that are the least likely to undergo fission. The ^{56}Fe on ^{165}Ho system is thus an adequate choice, as both Fe and Ho are not heavy enough to have a significant fission cross section. In addition, since this system is asymmetric, it is easy to determine whether the system attains thermal equilibrium by studying the ratio of the PLF excitation energy to the total excitation energy of the system.

The ^{56}Fe on ^{165}Ho system has been extensively studied by other authors at different bombarding energies and with different experimental methods. Therefore, it is useful to correlate the results of the present study to previous results and add to the already existing pool of knowledge about this system. It is particularly worthwhile to compare the present results to those obtained by Benton *et al.* [BEN85, 88] for the same reaction at lower bombarding energy and using the same

kinematic coincidence method. The study of the 672-MeV ^{56}Fe on ^{165}Ho system constitutes, in fact, a continuation of the study of the same system at 505 MeV bombarding energy, and allows for exploration of a wider range of total kinetic energy loss.

A study of the mass and charge distributions of the detected PLF was also performed on the present data, to explore the negative drift of the asymmetric system towards mass asymmetry. The comparison of the data from the present experiment to two different nucleon exchange models, Randrup's model and Tassan-Got's model, was performed. The similarities and differences between the two models, along with their success or failure in reproducing the experimental data, are examined to gain a better understanding of the types of mechanisms that occur in deep-inelastic reactions. It is particularly interesting to see how Tassan-Got's stochastic nucleon exchange model, which was designed for higher bombarding energies, reproduces the experimental data.

The experimental technique, along with the various methods utilized to extract information from the experimental data in the present work, are described in Chapter II. The results obtained for the nuclide distributions of the projectile-like fragments, and their excitation energy are presented in Chapter III. Chapter IV contains a description of Randrup's [RAN78, 79, 82] and Tassan-Got's [TAS88, 89, 91] nucleon exchange models and presents the results of comparing their predictions to experimental data of various Fe-induced reactions. A discussion of the experimental results in comparison with previous findings, and their physical meaning is presented in Chapter V. To conclude, Chapter VI summarizes the results of this study.

CHAPTER II EXPERIMENTAL SET-UP AND DATA REDUCTION

The experiment was performed at the Holifield Heavy Ion Research Facility (HHIRF) of the Oak Ridge National Laboratory. The projectile-like fragments (PLF's) and the target-like fragments (TLF's) of the reaction ^{56}Fe + ^{165}Ho at 12 MeV/u were detected in coincidence. This allowed for a kinematic reconstruction of the reaction and, thus, the extraction of primary quantities that could not be directly measured, such as the mass of the projectile-like fragment before it de-excites by evaporation. The reaction parameters (grazing angle, grazing angular momentum, critical angular momentum for fusion, interaction radius, and Coulomb barrier) were obtained from the Atomic Data and Nuclear Data Tables of W. W. Wilcke *et al.* [WIL80]. They are summarized in Table II.1 along with the experimental parameters (bombarding energy, detection angle, and center-of-mass energy). A description of the experiment and the data reduction procedure follows.

II.A. Experimental Set-Up

The reaction took place in a 30-cm diameter scattering chamber, under vacuum. A 672-MeV ^{56}Fe beam was used to bombard a 195-$\mu g/cm^2$ ^{165}Ho target with 50 μg of carbon backing. The experimental set-up is depicted in Figure II.1. To minimize the energy loss of the heavy target-like products and ensure that they reach the recoil detector, the target was tilted at an angle of -35° with respect to the beam. The multiple scattering effects by the reaction products before they enter the detectors are also minimized by this orientation of the target. The beam current

Table II.1 Reaction Parameters for the Reaction ^{56}Fe on ^{165}Ho at 12 MeV/u

Parameters	Values
Lab grazing angle $\theta_{1/4}$	20.2°
Center-of-mass $\theta_{1/4}$	27.0°
$L_{grazing}$	330 Ó
Lcrit	111 Ó
Interaction Radius	13.22 fm
Coulomb Barrier V_c	190 MeV
Laboratory Bombarding Energy	672 MeV
Center-of mass energy E_{cm}	502 MeV
Laboratory detection angle θ_{exp}	16°

EXPERIMENTAL SET-UP

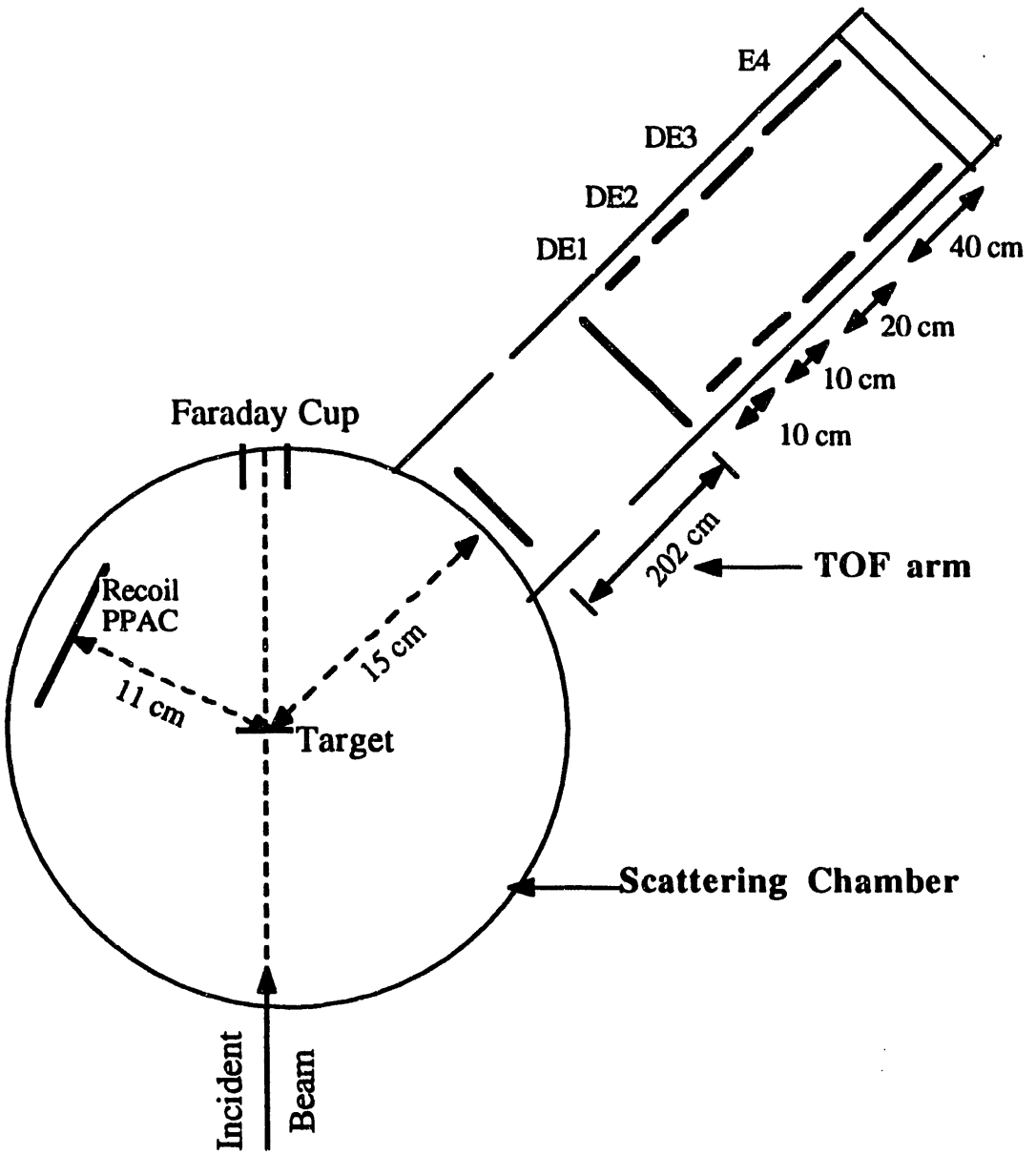

Figure II.1 Diagram of the experimental set-up used at the time-of-flight facility at HHIRF. Dimensions of the various elements are not to scale.

was between 20 and 40 nA throughout the experiment.

A time-of-flight (TOF) arm connected to the scattering chamber, was used to detect the projectile-like fragments, and determine their velocity by measuring their time-of-flight between two timing detectors. It was positioned at a laboratory angle of 16° with respect to the beam throughout most of the experiment. A few runs were performed at 14° and 10° laboratory angles for calibration purposes. The projectile-like fragments entered the time-of-flight arm through an oval aperture of 0.32 cm and 0.64 cm minor and major axes, respectively. They were then detected by a parallel plate avalanche counter (PPAC) mounted in the time-of-flight arm 23 cm behind the TOF aperture. A second PPAC was positioned at 225 cm behind the TOF aperture, resulting in a flight path of 202 cm between the two PPAC's, for the projectile-like fragments. The PPAC closest to the time-of-flight arm aperture had an active area of 2 cm by 2 cm, and was used as a start detector The second PPAC had an active area of 8 cm by 8.5 cm and was used as a stop detector. Each of the two PPAC's consisted of four 50 $\mu g/cm^2$ polypropylene windows. The two external widows were aluminized with 40 $\mu g/cm^2$ of the metal, and served as gas containment windows. The two internal windows were used as cathodes. The anode plane of each PPAC was mounted between the two cathodes and was used for the time measurement. The anode voltages were set to + 455 volts and + 420 volts for the start and the stop detector, respectively, and the cathode was grounded.

The stop PPAC was also used to provide position in addition to timing information. Each cathode of the stop PPAC was aluminized with parallel strips of the metal spaced 2 mm apart. The metal strips were connected in series via delay chips to outputs at two ends of the cathode plane. The two cathodes were mounted in a configuration where the aluminum strips of one were perpendicular

to the strips of the other. Both horizontal (x-left and x-right) and vertical (y-up and y-down) positions could thus be obtained. Both PPAC's were filled with isobutane gas at a pressure of 2.7 torr.

The energy of the projectile-like fragments was measured using a gas ionization chamber located behind the time-of-flight arm, as shown in Figure II.1. The entrance to the gas ionization chamber was a 200-$\mu g/cm^2$ mylar window placed at a distance of 10.5 cm behind the stop PPAC. It had dimensions of 9.5 cm by 9.5 cm. Two horizontal support bars were placed on the window dividing it into three equal sections of 9.5 cm by 3.6 cm each. The gas ionization chamber had four anodes of lengths 10 cm, 10 cm, 20 cm, and 40 cm, starting by the one closest to the target, separated by 0.8 cm gaps. Since they were used to measure the kinetic energy deposited in the gas, these four elements will generally be referred to as the DE1, DE2, DE3, and E4 detectors, respectively. The ionization chamber was filled with tetrafluoromethane (CF_4) at a pressure of 500 torr.

The target-like fragments (TLF's) were detected using another PPAC positioned inside the scattering chamber, and referred to as the recoil PPAC. The recoil PPAC provided the TLF's horizontal (x-) and vertical (y-) positions, which were translated into in-plane and out-of-plane TLF scattering angles, respectively. The recoil PPAC was mounted 375 mm from the target. It subtended an in-plane angle of 75° and was positioned to cover angles ranging from a minimum of 15° to a maximum of 90°. It was filled with isobutane at a pressure of 4.02 torr. The anode voltage for this PPAC was + 440 volts and the cathode was grounded. The x- and y-position of the target-like fragments were measured with the recoil PPAC in the same way as the position of the projectile-like fragments was measured with the stop PPAC.

A calibration mask, placed in front of the recoil detector during a calibration run, was used for the calibration of the target-like fragment scattering angle. The mask consisted of a square aluminum plate of 10 cm by 10 cm with equally spaced holes, arranged in the pattern shown in Figure II.2. To determine the angular position of the holes, the calibration mask was placed in front of the beam line, at 0^{o} with respect to the beam, as shown in Figure II.3. Each of the ten in-plane holes was then viewed through a transit line and its relative angular position recorded. The absolute angular differences between consecutive holes could then be determined and used in the angular calibration.

A two dimensional plot of the in-plane angle versus the out-of-plane angle, for data taken during the calibration run, is displayed in Figure II.4. The pattern obtained was used for the identification of the holes of the mask. A gold target was used during the TLF angle calibration run to maximize the elastic cross section. Since Au is heavier than Ho, a larger grazing angle results for the reaction Fe + Au at 12 MeV/u. Hence, more elastic events could be detected.

Most of the data analysis was performed with the LISA program [BRE89]. This program, which was originally developed in Germany, allows for interactive manipulation and display of the raw data. The data can be read from a magnetic tape or a hard disk and sorted into spectra. Various operations, such as channel number determination and Gaussian fits can then be performed on the displayed spectra. A flow chart of the LISA code is shown in Figure II.5. The necessary calibrations, corrections, and calculations on the data were performed on an event-by-event basis with the user subroutine INSERT. To avoid an event-by-event reading of relevant parameters that are calculated only once, such as the energy losses in the detector windows and gas, the INSONE subroutine was used. It allows a one-time reading of a given parameter whose value can be subsequently

CALIBRATION MASK

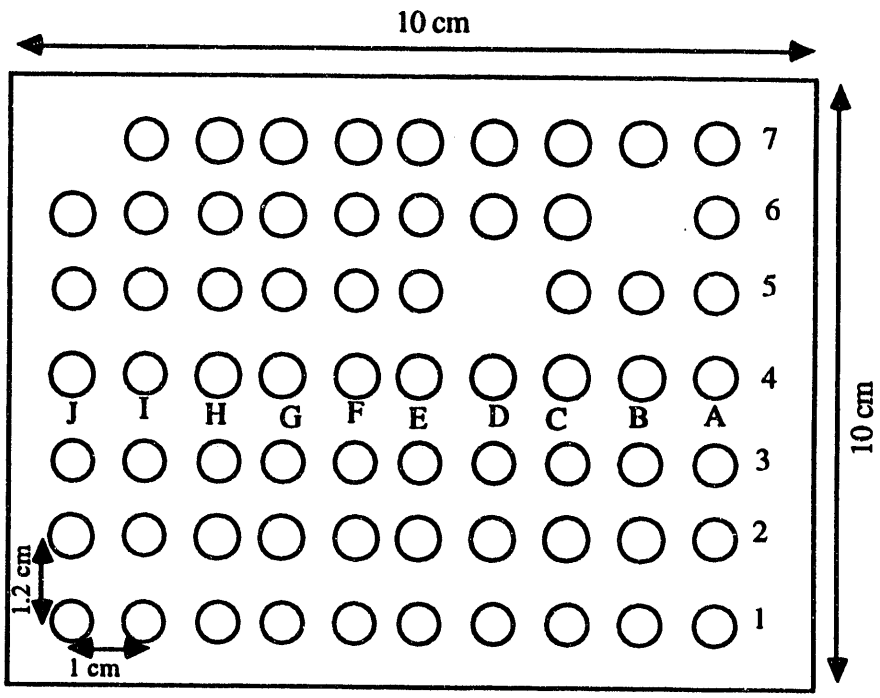

Figure II.2 Recoil detector calibration mask.

RECOIL DETECTOR POSITION

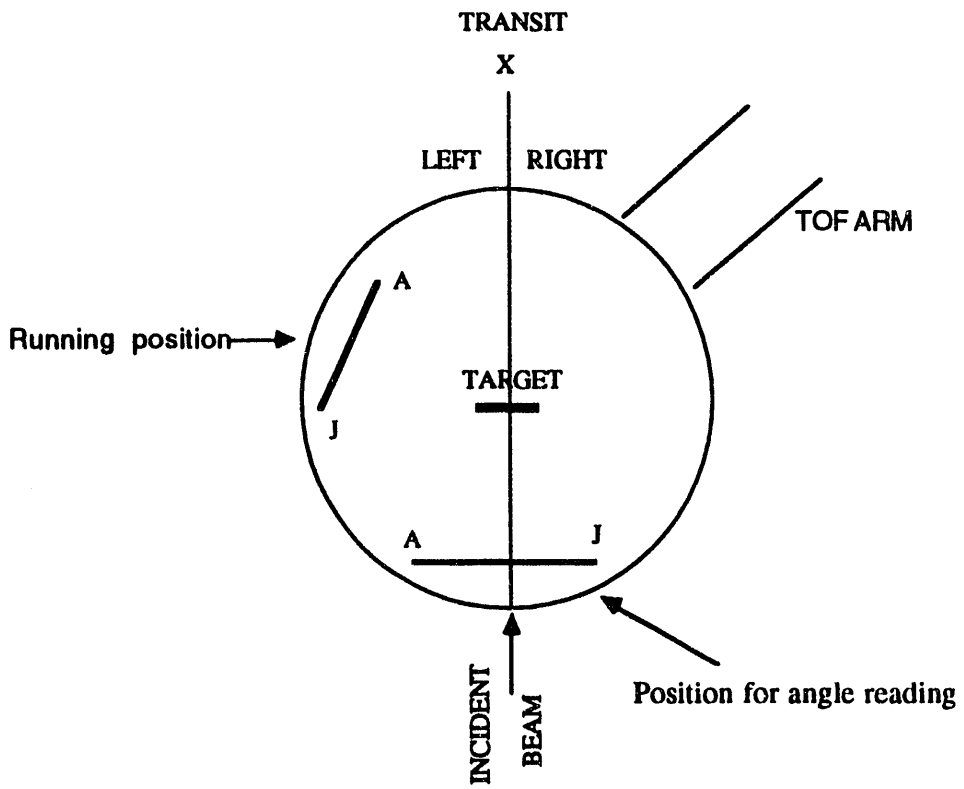

Figure II.3 Position of the recoil PPAC (with the calibration mask on) in the scattering chamber during the calibration of the TLF angle. The running position (calibration mask off) is also indicated.

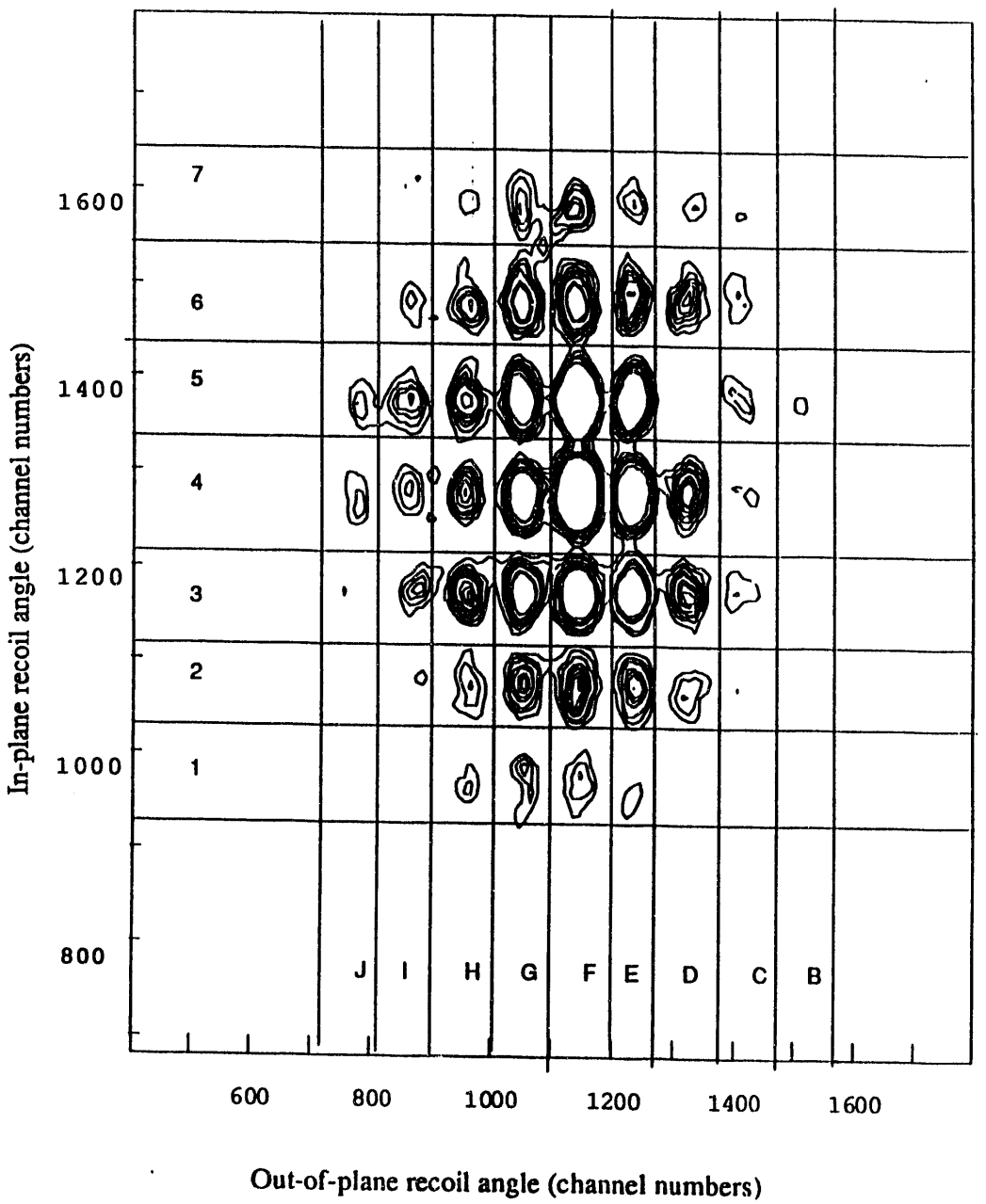

Figure II.4 In-plane recoil angle versus out-of-plane recoil angle in the reaction $^{56}Fe + ^{197}Au$ at 672 MeV.

LISA ANALYSIS ROUTINE FLOWCHART

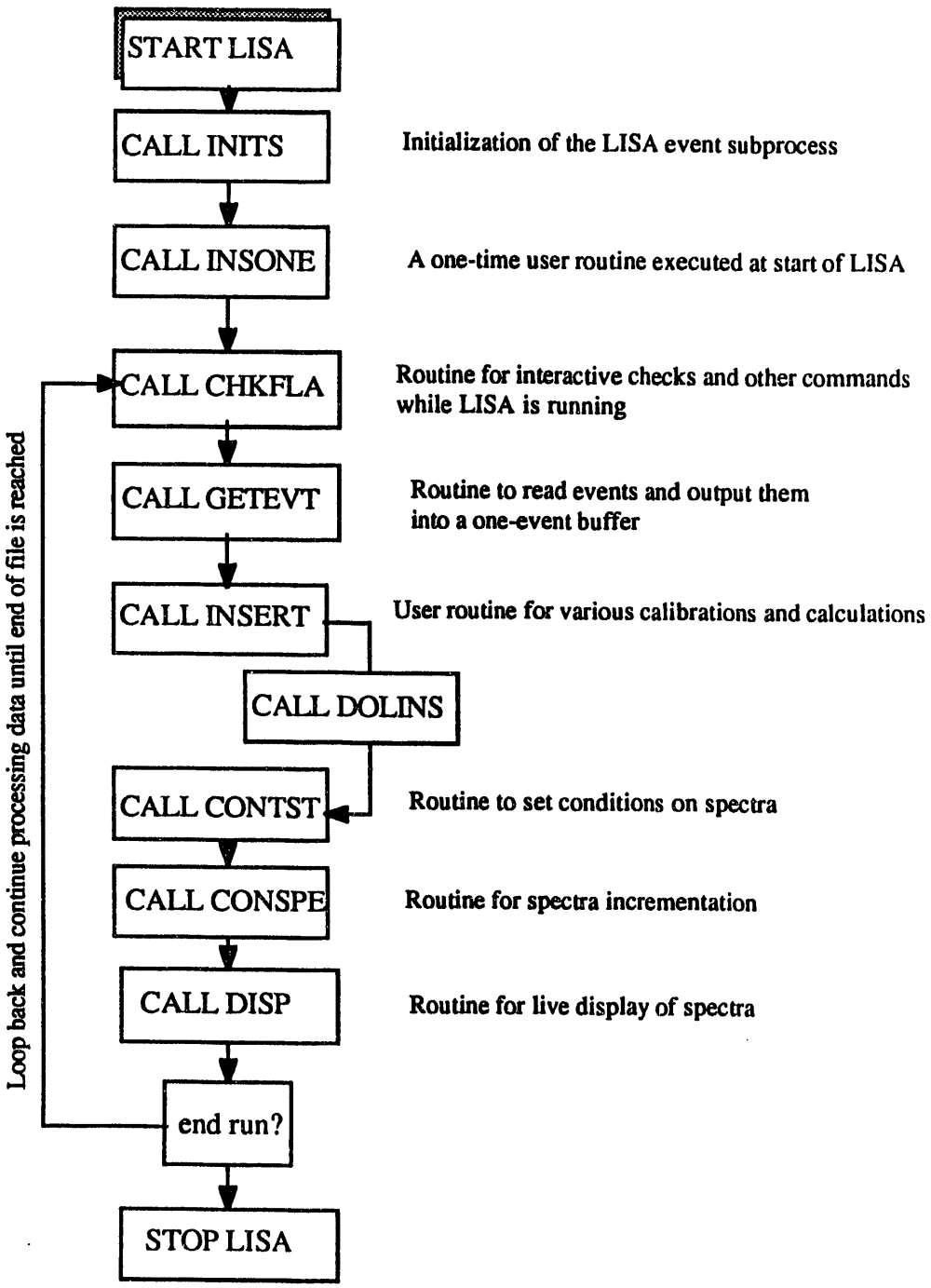

Figure II.5 Flowchart of the LISA analysis routine.

used in the event-by-event replay of the data.

II.B Electronics

A simplified schematic representation of the electronic set-up is shown in Figure II.6. The electronic devices displayed in the diagram are described in Table II.2. The data were collected using the CAMAC data acquisition system. It was possible to do on-line data processing while the data was being stored on tape by use of a programmable processor (Event Handler) developed by D.C. Hensley [HEN79].

The event handler is mainly used to read the parameters of an event from the CAMAC modules and store them in a buffer that can be accessed by the host computer. The event handler is triggered by the occurrence of an event. In the present experiment, the event trigger was a coincidence between a time-of-flight event and an energy signal from the DE2 element of the gas ionization chamber. After being triggered, the event handler reads a gated latch to determine which detectors have fired. If a valid event has occurred, the data are read from the CAMAC addresses and stored in a buffer in the host computer. The data are then written on magnetic tape event-by-event by the host computer. At the same time, these data are accessed through a histogramming program to generate spectra that are displayed during the data acquisition to monitor the experiment.

II.C CALIBRATION OF THE MEASURED OBSERVABLES

II.C.1 Kinetic Energy Calibration

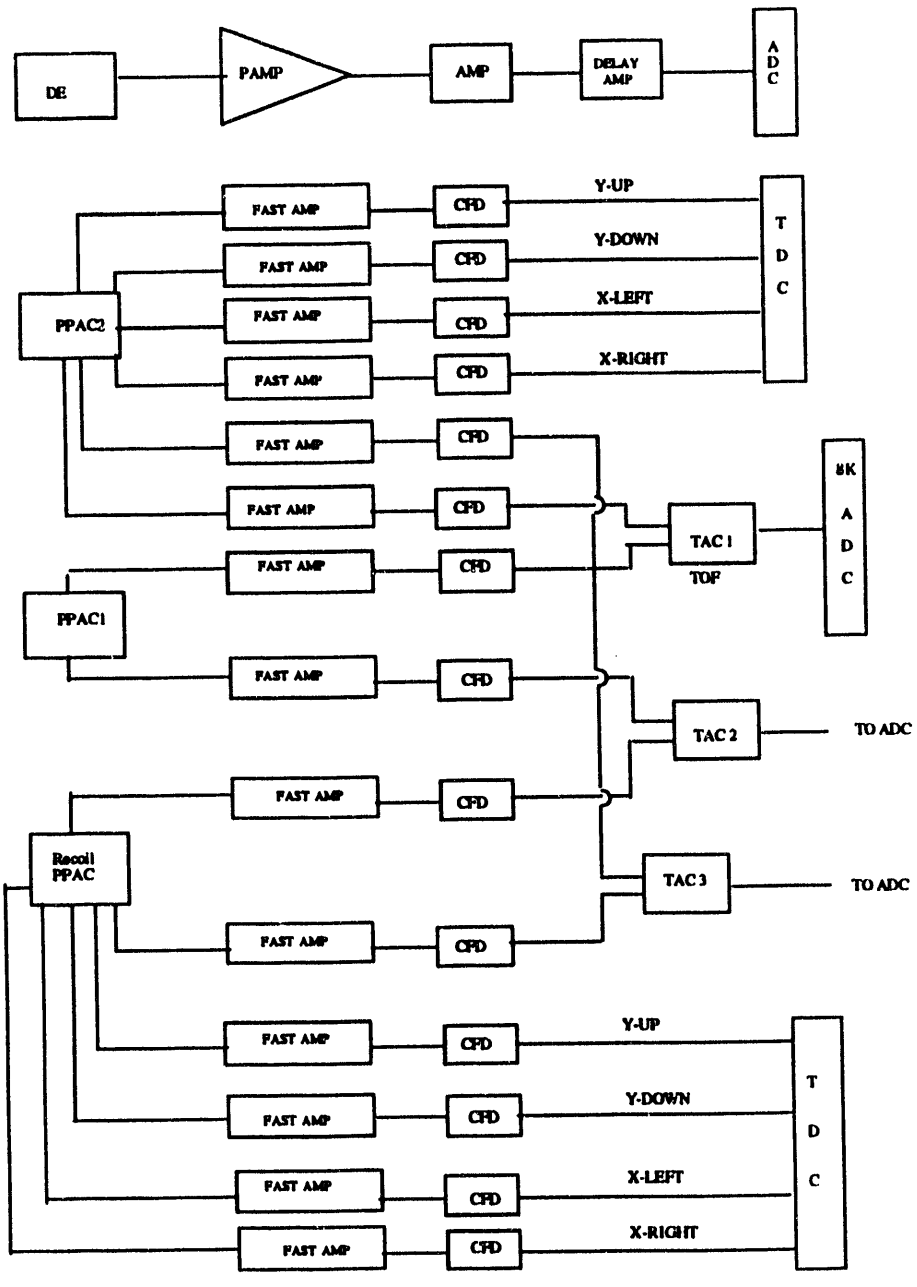

Figure II.6 Schematic outline of the electronics associated with the detection system.

Table II.2 Electronic Devices

Abbreviation	Electronic Module
PAMP	Pre-Amplifier
AMP	Amplifier
CFD	Constant Fraction Discriminator
ADC	Analog-to-Digital Convertor
TAC	Time-to-Analog Convertor
TDC	Time-to-Digital Convertor

The kinetic energy of the projectile-like fragments was calibrated using precision pulser signals sent through the electronics associated with each of the four energy detectors. In addition, the gain of the pre-amplifiers and the rest of the energy detectors' electronics was monitored throughout the experiment, by pulser signals. The precision pulsers used for calibration were incremented by accurate voltage steps to cover the entire range of ADC channel numbers. This resulted in a series of peaks with periodic separations. The voltaic gain of each energy detector with all its associated electronics was determined using the separations between the pulser peaks. The gains of the DE1, DE2, and E4 detectors were then normalized to that of the DE3 detector. The four energy spectra could thus be added to result in a total energy signal that described the laboratory kinetic energy of the projectile-like fragments.

The absolute energy calibration was performed using elastic events. These are represented by the highest yield peak in the kinetic energy spectrum shown in Figure II.7. The laboratory kinetic energy of elastic events was determined with the kinematical formulas of elastic scattering. Energy losses in half of the target (the projectile is assumed to interact in the middle of the target), and in the various windows and gas media that the projectile-like fragments traverse before entering the gas ionization chamber, are taken into account. The STOPX [OAK87] program from Oak Ridge was used to calculate these energy losses, which were subtracted from the calculated kinetic energy before performing the final absolute calibration. The energy resolution was then determined by fitting a Gaussian curve to the elastic energy peak. It was found to be on the order of 2.5 % full width at half maximum (FWHM). An acceptable energy resolution for good particle identification should be on the order of 1 %. It was therefore necessary to improve the energy resolution by investigating the reasons for the spread in the

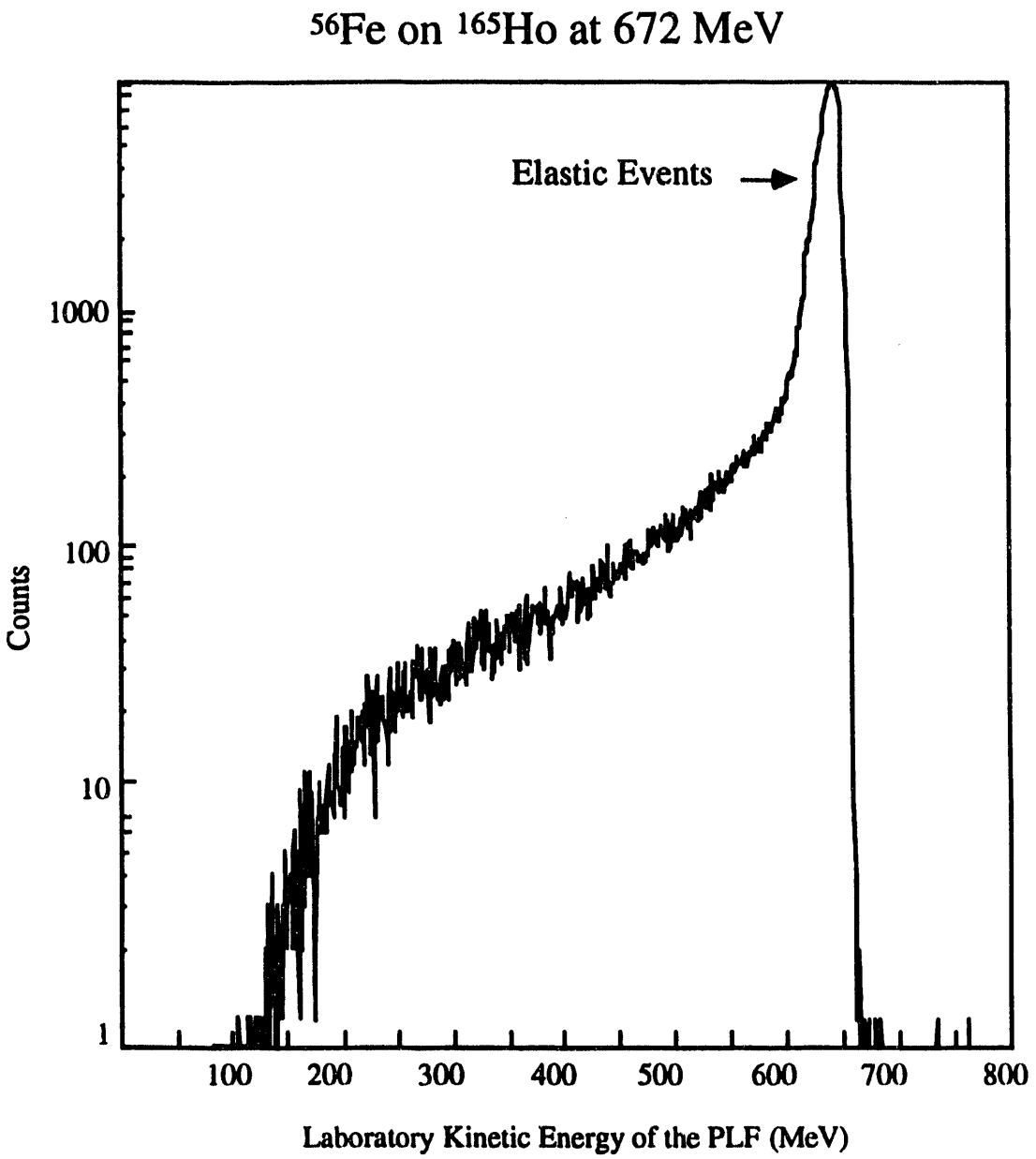

Figure II.7 Laboratory kinetic energy of the post-evaporation PLFs.

kinetic energy distribution.

Contour maps of the PLF laboratory energy versus the x- and y-positions, displayed in Figure II.8, show a dependence of the energy upon the horizontal position but almost none on the vertical position. Corrections were necessary to eliminate this dependence. However, before proceeding with any corrections, it was necessary to check each energy signal individually to determine if they all had the same type of position dependence. The DE1 energy signal was found to be independent of both horizontal and vertical positions, while the elastic peak in the other three elements showed the same slope when plotted against the x-position and no slope when plotted against the y-position. Thus, After adding the DE2, DE3, and E4 energy spectra, the resulting energy was corrected for position dependence with a third degree polynomial and added to DE1. The new energy resolution obtained was 1.2 % FWHM.

II.C.2 Charge Calibration

The projectile-like fragment charge was determined with the DE-E method. The energy loss $\frac{dE}{dx}$ of a nonrelativistic charged particle in matter is proportional to the square of its charge Z according to Bethe's formula

$$\frac{dE}{dx} \alpha \frac{m Z^2}{E}, \qquad \text{(II.1)}$$

where m, Z, and E are the mass, charge and energy of the particle, respectively.

The sum of the calibrated energies from the first and second elements of the gas ionization chamber served as DE, and was plotted versus the total kinetic energy E (i.e., sum of all four elements of the ionization chamber). The Z = 26 line that corresponds to the elastic scattering of ^{56}Fe on ^{165}Ho was identified as

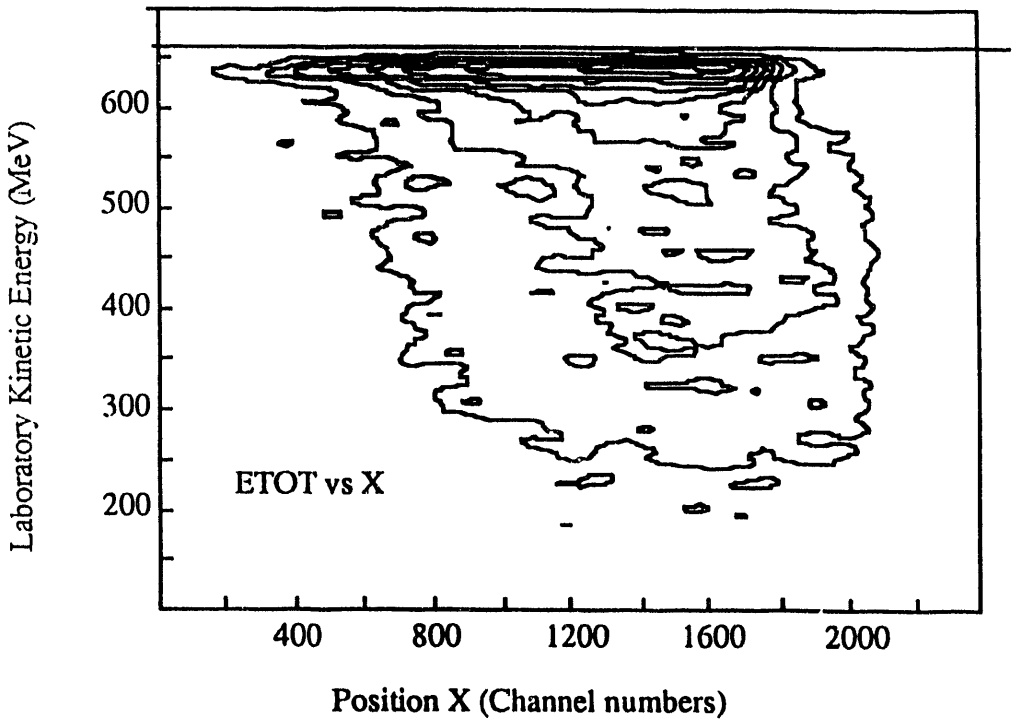

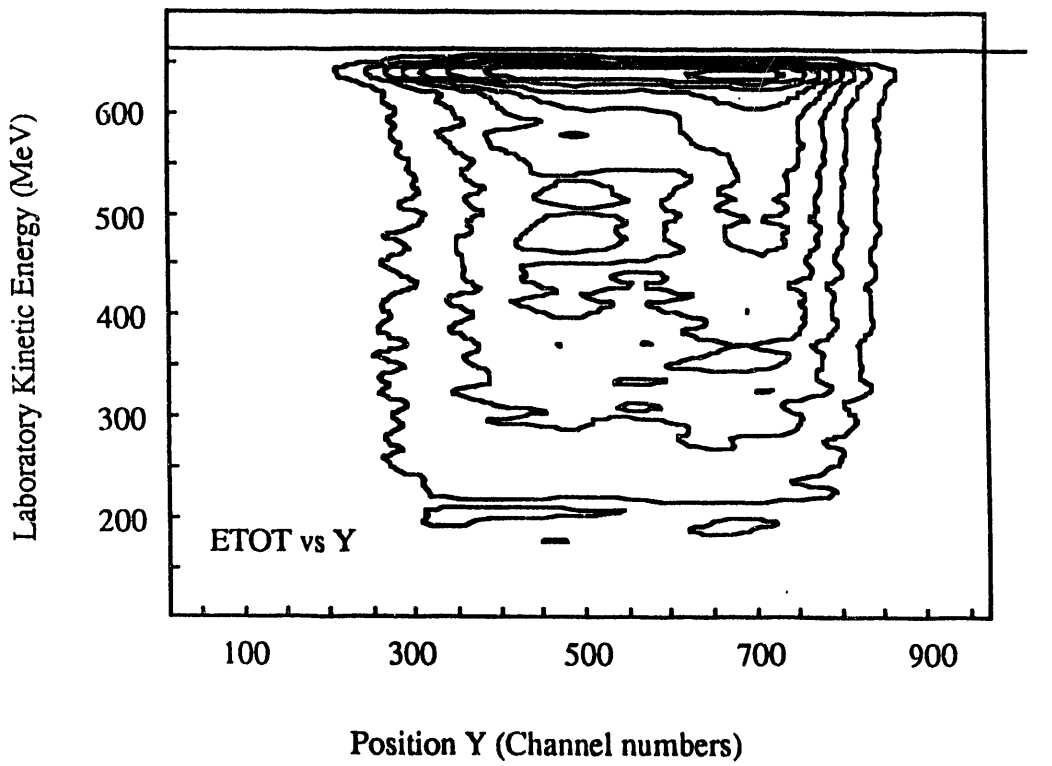

Figure II.8 Dependence of the PLF kinetic energy upon X- and Y-positions as determined by the stop PPAC. The horizontal line in each plot is used as a reference.

the darkest line in the DE-E plot shown in Figure II.9. The other Z assignments were made relative to Z = 26. From Figure II.9, it is evident that DE values vary strongly with the projectile-like fragment kinetic energy. In the types of analyses used in the present study, the mass and charge of the detected fragments have to be independent of the fragment energy. The Z lines were therefore straightened empirically by the use of polynomials.

The discontinuities in the Z lines were observed at energy values corresponding to the regions of the gaps between the DE3 and E4 anodes of the gas ionization chamber. They are attributed to different efficiencies of charge collection by the anodes in the regions of these gaps. This effect is expected at all regions of the DE-E plane corresponding to the gaps between anodes, but at a considerably lesser degree. However, since a large fraction of the PLF's lose most of their energy in the DE3 and E4 detectors, the effect of the gap between DE3 and F4 is magnified. Hence, different polynomials were used for different regions of the DE-E plane.

The empirical corrections resulted in straight lines corresponding to discrete atomic numbers separated by one unit of charge. Further corrections via polynomial fits were applied to obtain the final absolute calibration of the atomic numbers. A contour plot of the straight and calibrated Z lines is displayed in Figure II.10 as a function of the laboratory kinetic energy. The accepted range of variation of the Z centroids with energy was 0.1 units of charge. Histograms of calibrated Z were generated for energy gates spanning the entire energy range to monitor the variation of the charge centroids with energy. Spectra displaying the charge for the 100-300 MeV bin and the 500-600 MeV are shown in Figure II.11. Gaussian fits to the Z peaks showed that the charge variation is within the accepted

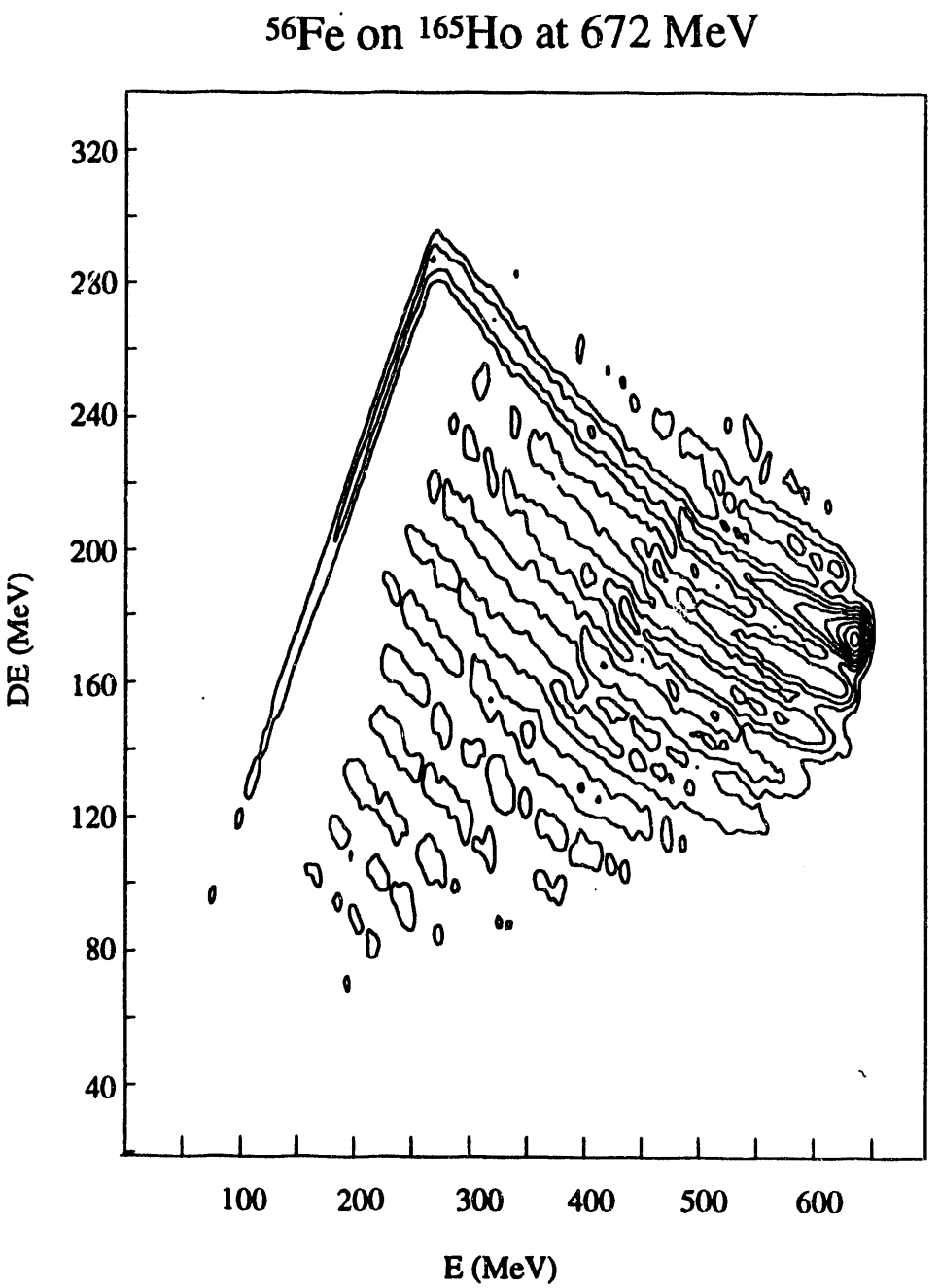

Figure II.9 Contour plot of DE versus E, where DE = DE1 + DE2, and E is the total laboratory kinetic energy.

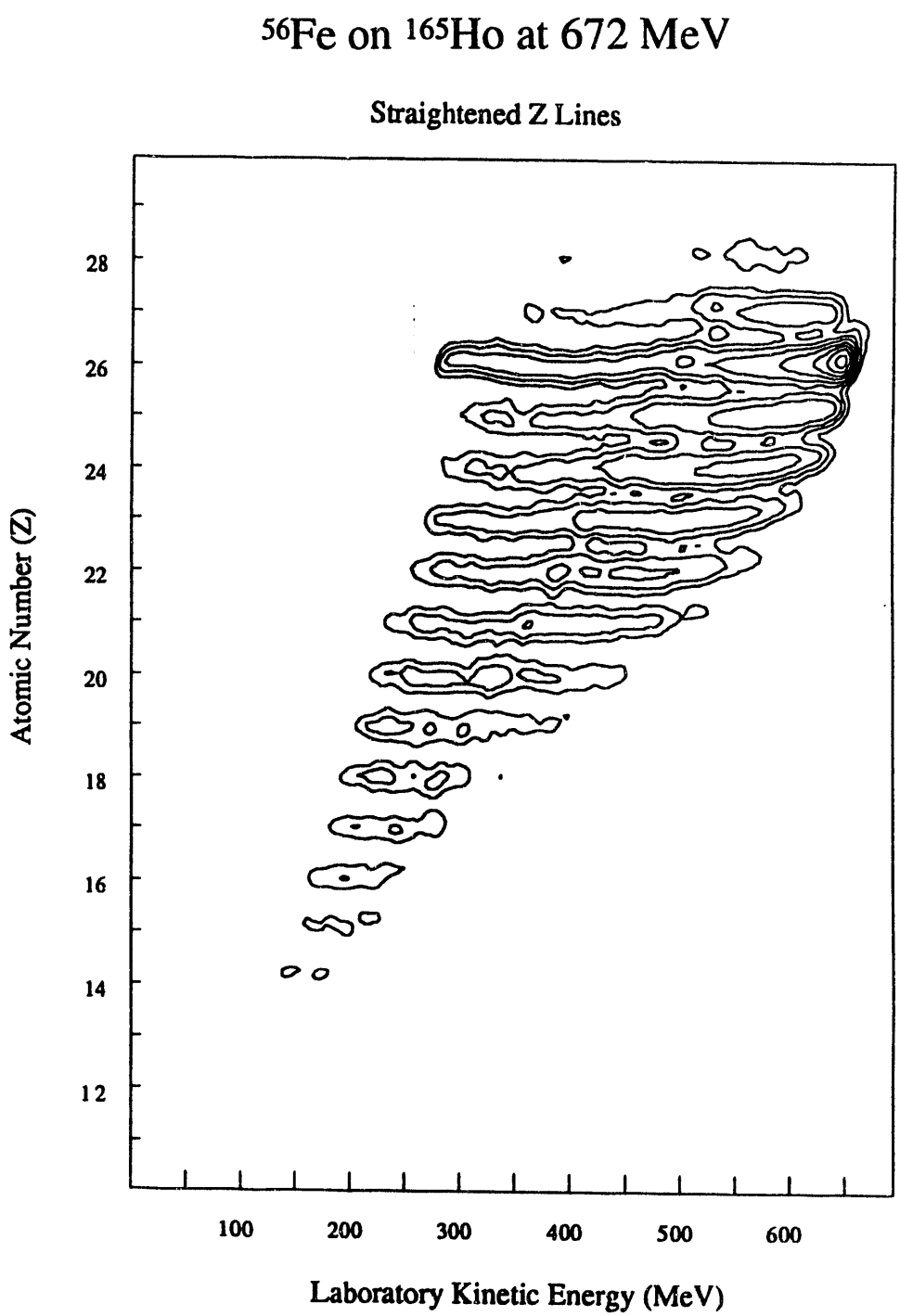

Figure II.10 Contour plot of the calibrated PLF atomic number (Z) as a function of the PLF laboratory energy.

range of 0.1 charge units. The charge resolution obtained was on the order of 0.36 units of charge at FWHM.

II.C.3 Mass Determination

The time-of-flight of the projectile-like fragments is used for their mass determination. The mass of a given PLF is proportional to its kinetic energy and the square of its time-of-flight according to the formula:

$$M = \frac{2}{X^2} ET^2 \qquad \text{(II.2)}$$

where M and E are the mass and kinetic energy of the particle, respectively, and X is the distance traveled by the particle during the time T.

The time measurement was made using a Time-to-Analog converter (TAC). The time-of-flight was recorded on an 8K channel Analog-to-Digital converter (ADC). A time calibrator was used to insert pulses of 10 ns period into the TAC. Delay lines were also used to get pulses delayed by 2 ns. The functional dependence of time on channel number was obtained from the 2 ns delays and the corresponding separations in channel numbers. The raw time-of-flight includes an offset T_0 due to delay between the start and stop signals. This was included in the calibration by defining a new time-of-flight as

$$TOF = TOF_{measured} - T_0 \qquad \text{(II.3)}$$

The value of T_0 is determined by trial and error using the criterion that there should be is no dependence of mass on energy. A two-dimensional spectrum of

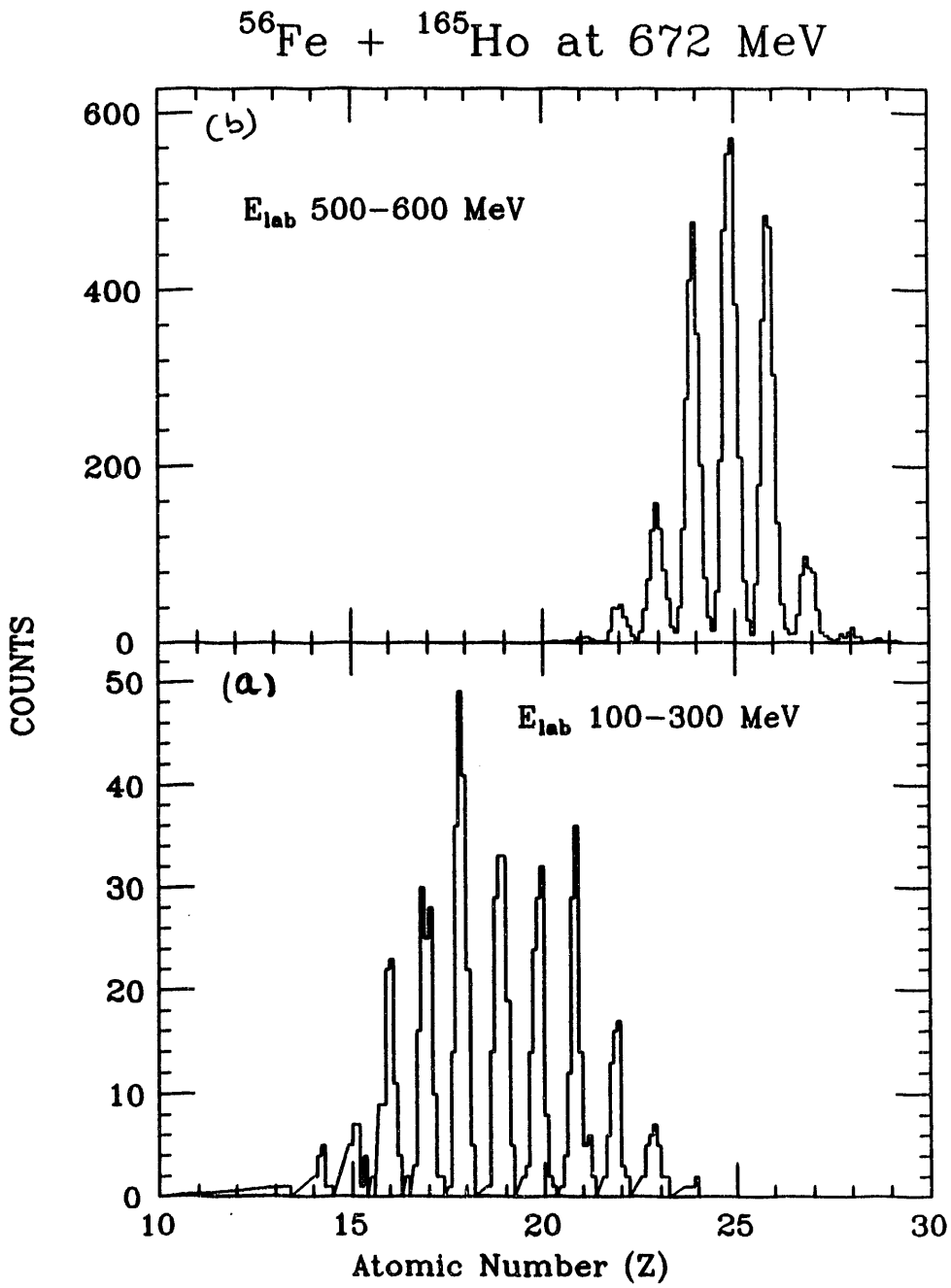

Figure II.11 Spectra of the calibrated Z for:
(a)Laboratory energy in the 100-300 MeV range
(b)Laboratory energy in the 500-600 MeV range.

mass versus energy was generated for different values of T_0, until the mass-energy slope was the closest possible to zero. Good mass separation depends on both energy and time-of-flight resolutions. The resolution of the time-of-flight obtained after calibration was 450 ps. A correction similar to the one used to eliminate the dependency of energy on position was also needed for the time-of-flight. The resolution obtained for the time-of-flight was about 380 ps after application of the position correction.

From equation II.1, and considering, that the uncertainty in the distance X is negligible with respect to the uncertainties in E and T, the mass resolution can be written as

$$\frac{\delta M}{M} = \frac{\delta E}{E} + 2\frac{\delta T}{T}, \qquad \text{(II.4)}$$

where $\frac{\delta M}{M}$, $\frac{\delta E}{E}$, and $\frac{\delta T}{T}$ are the ratios of FWHM to centroid value of the mass, energy, and time-of-flight, respectively. Identification of the different isotopes is possible when δM is less than ~ 0.9 mass units. The mass resolution obtained with our detection system ranged between 0.9 and 1.35 mass units for different elements, and different kinetic energy ranges. An example of mass resolution for iron (Z = 26) isotopes is displayed in Figure II.12 for events with kinetic energies between 500 and 580 MeV. A two-dimensional display of the PLF mass versus kinetic energy is shown in Figure II.13 for inclusive Z values. Events corresponding to elastic scattering and to slit scattering are excluded. The same type of spectrum was generated for events corresponding to iron (Z=26) only and is displayed in Figure II.14. The predominant feature in these figures is the abrupt shift in mass lines at certain values of PLF kinetic energy. Similar spectra were generated with gates on different Z values and the

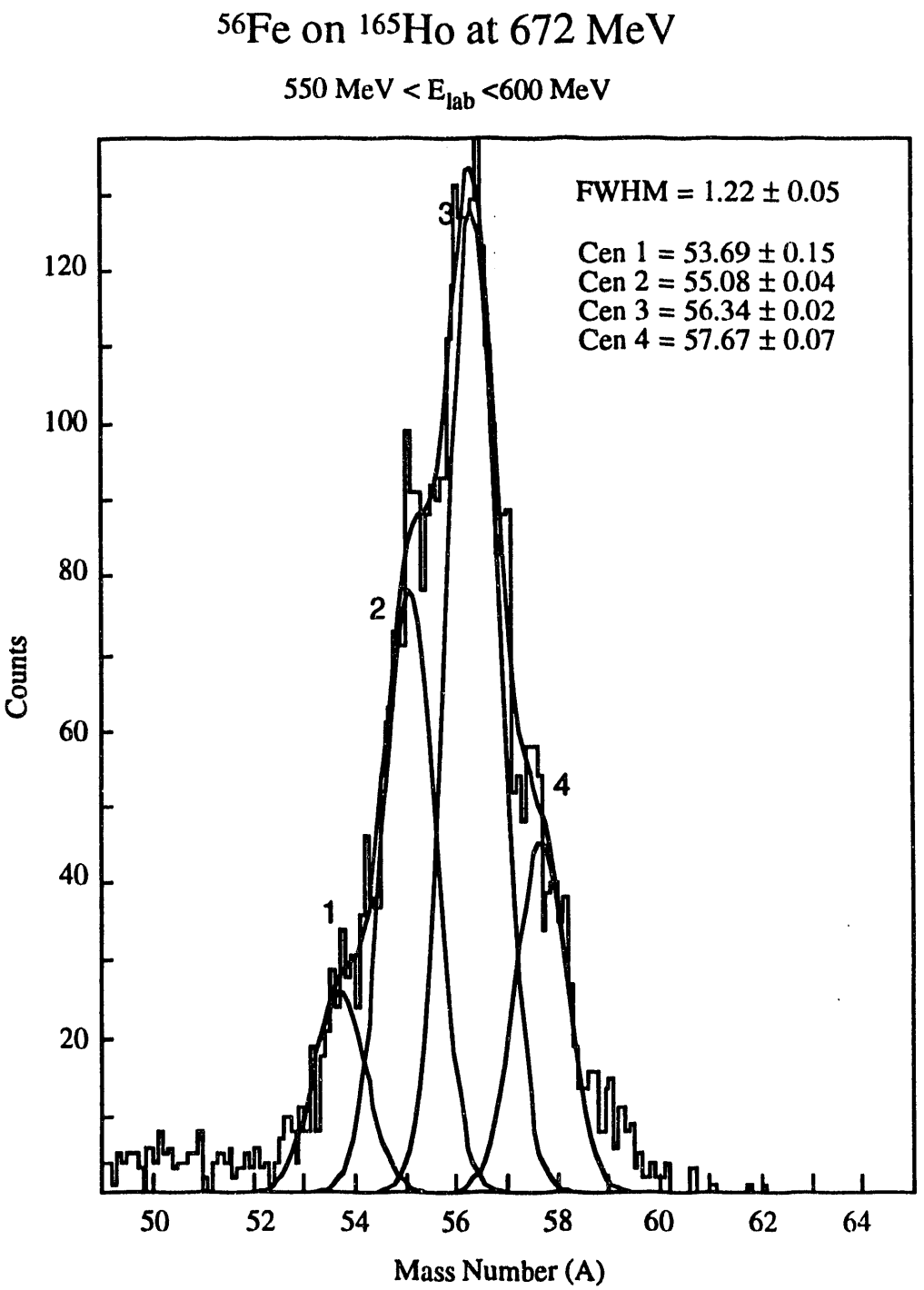

Figure II.12 Isotopic distribution for Fe (Z=26). The mass resolution at FWHM is about 1.22 mass units, as obtained by Gaussian fit.

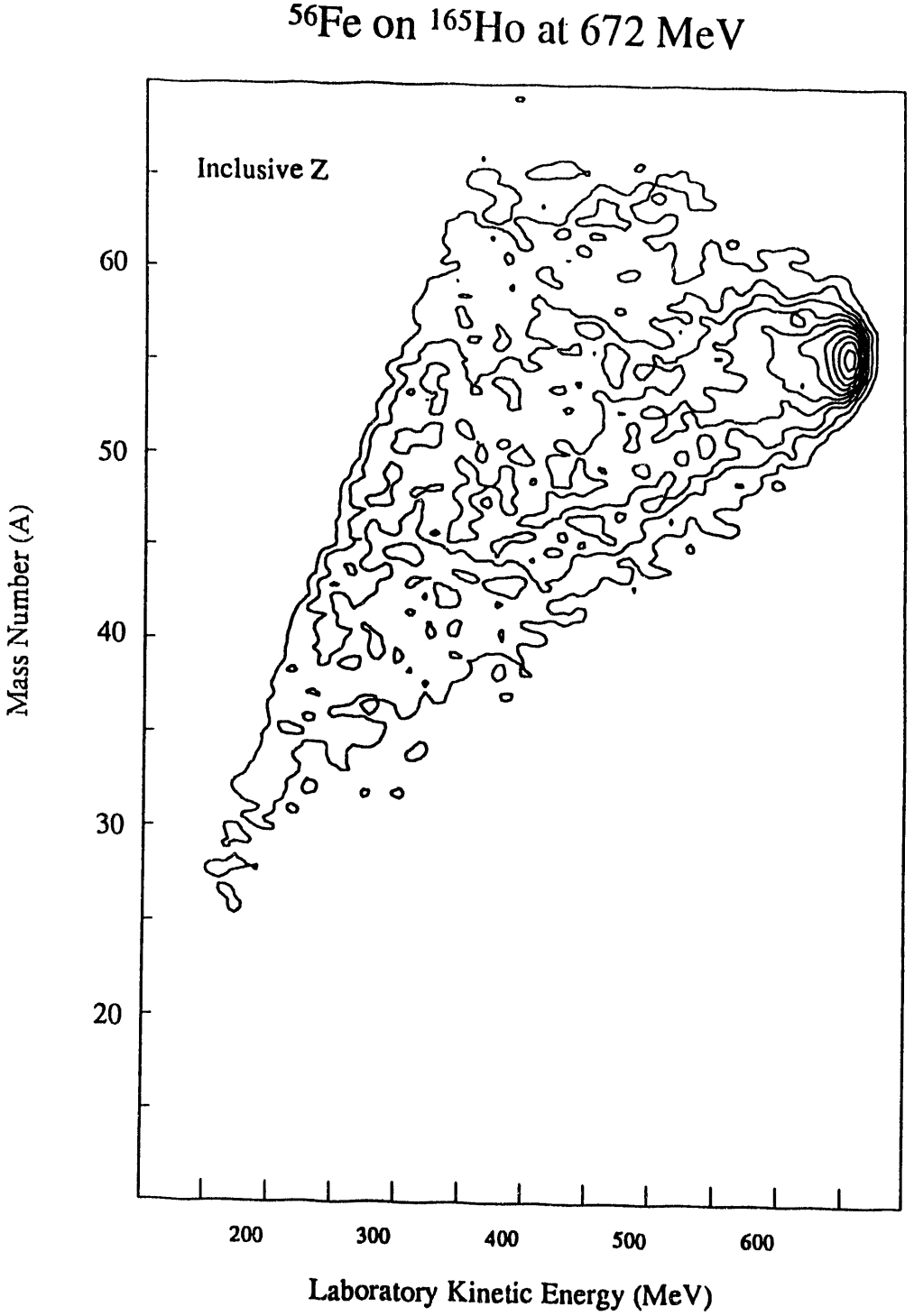

Figure II.13 Contour plot of the PLF mass number (A) versus the PLF laboratory energy for inclusive Z.

same feature was observed for all the cases considered. The energy at which the discontinuity occurs varies from one element to the other. This is visible in the contour plots of mass versus kinetic energy for vanadium, chromium, manganese and cobalt displayed in Figure II.15.

A replay of the data was performed with the requirements that only those events where the PLF's reached the E4 detector were selected; the events obtained in this replay are referred to as the "right region" of the mass-kinetic energy plane. In another replay, only events for which the PLF's stopped in the DE3 detector were retained; these events are referred to as the "left region" of the mass-kinetic energy plane. Contour plots of mass versus PLF kinetic energy obtained with the two replays are displayed in Figure II.16. They show that the discontinuity in mass lines occurs at energies corresponding to the gap between the DE3 and E4 detectors. It is therefore thought to be a magnification of the same effect observed in the Z spectra and discussed in Section II.C.2. Empirical corrections using polynomials were made to match the masses of the two regions of the mass-kinetic energy plane and to make the correct mass assignments. The resulting mass versus kinetic energy after this first correction is shown in Figure II.17 for vanadium (Z = 23), chromium (Z = 24), manganese (Z = 25), and cobalt (Z = 27). The isotopic distributions of each element were then generated individually and the mass dependence on energy was corrected with polynomials. For mass spectra with worst-case resolution, isotopic identification was ambiguous. Therefore, a deconvolution method was utilized for mass-separation enhancement. This procedure, which is generally used in optical spectroscopy to improve peak

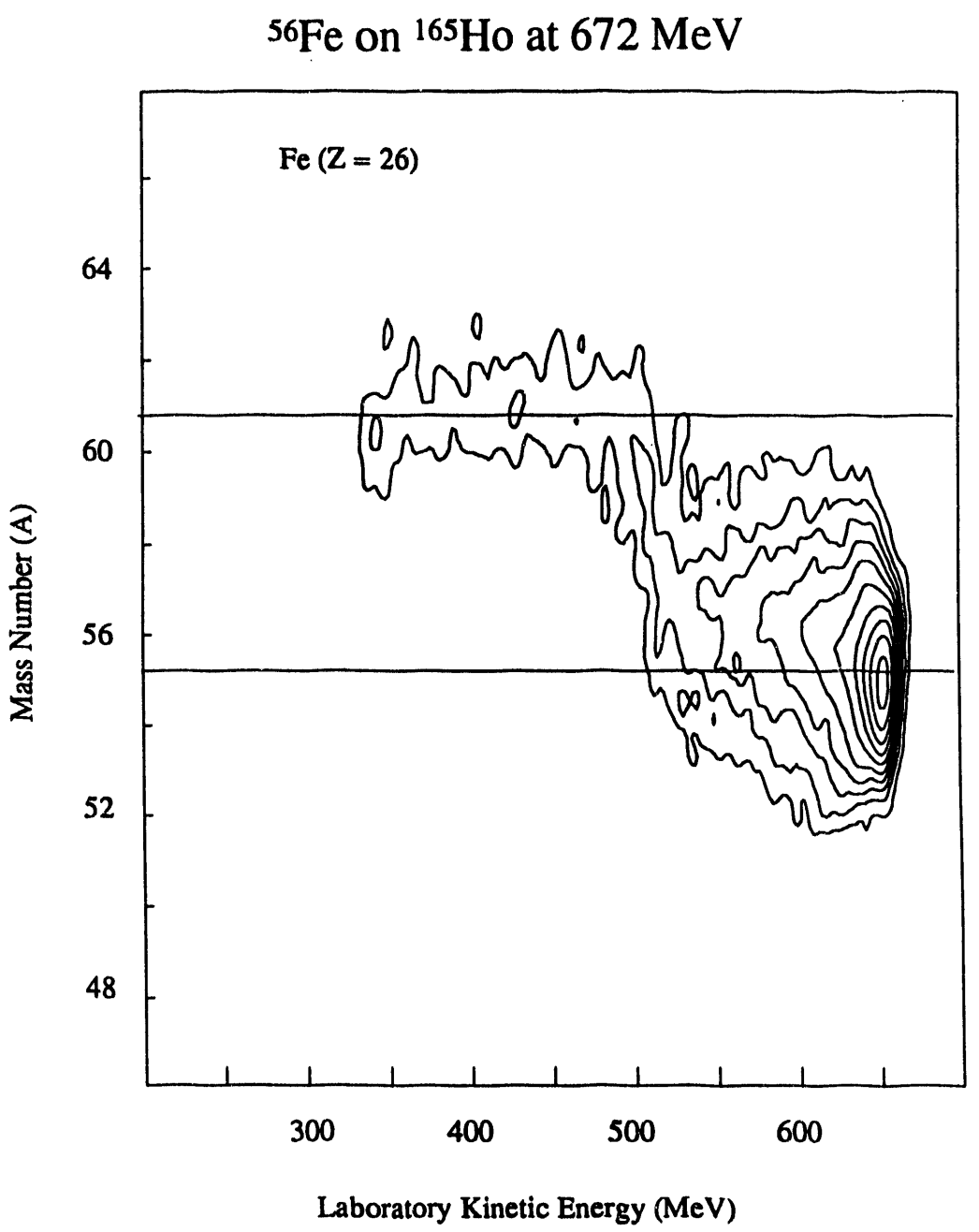

Figure II.14 Contour plot of the PLF's mass number versus the PLF laboratory energy for Fe (Z= 26). The horizontal solid lines indicate the position of the ^{56}Fe mass line.

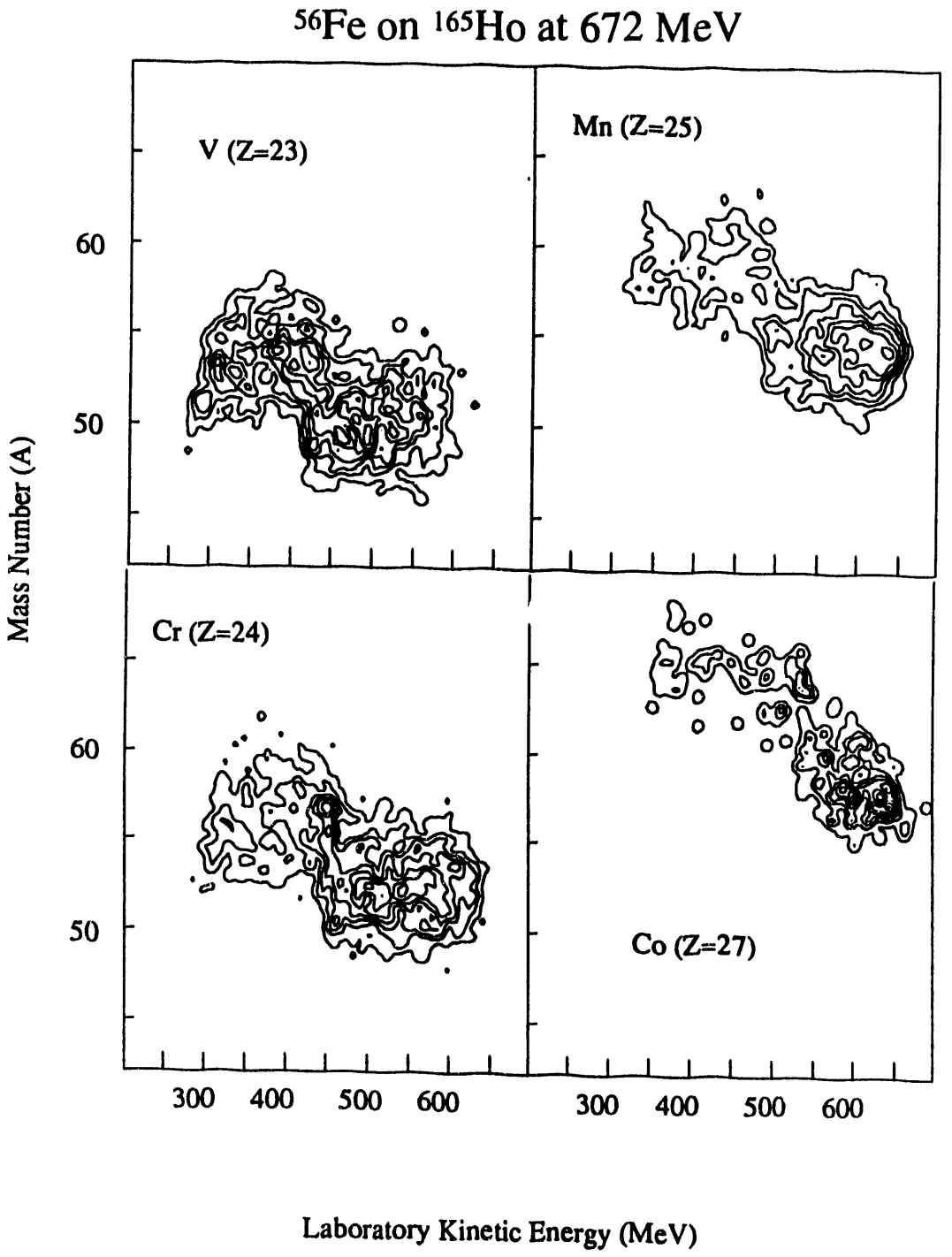

Figure II.15 Contour plots of the PLF mass number versus the PLF laboratory energy for V (Z = 23), Cr (Z=24), Mn (Z=25), and Co (Z=27).

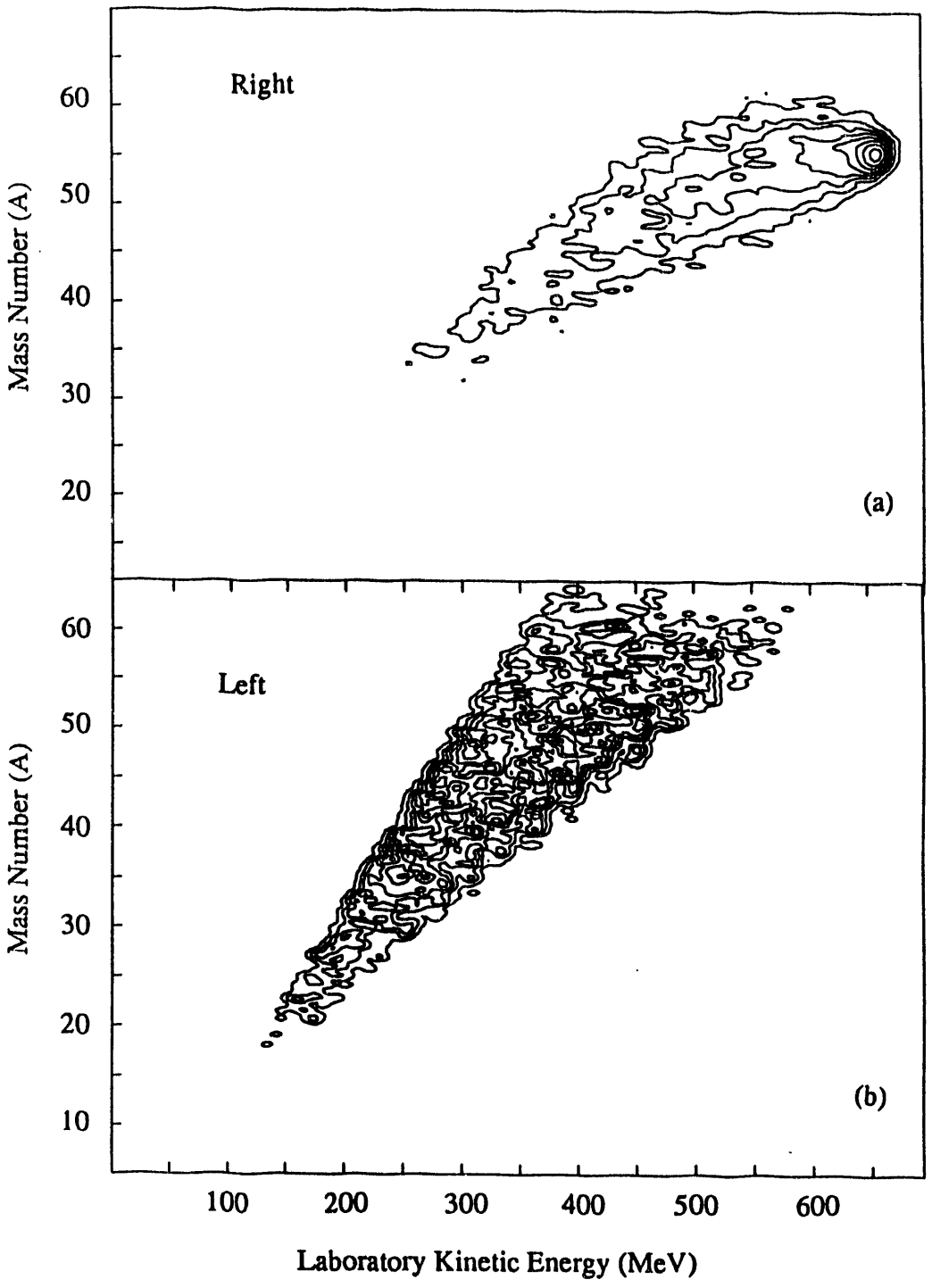

Figure II.16 Contour plots of PLF mass versus PLF laboratory energy showing the "left" and the "right" regions of the mass-energy plane.
(a) Events where the PLF's reach the E4 element of the gas ionization chamber.
(b)Events where the PLF's stop at the ΔE3 element of the gas ionization chamber.

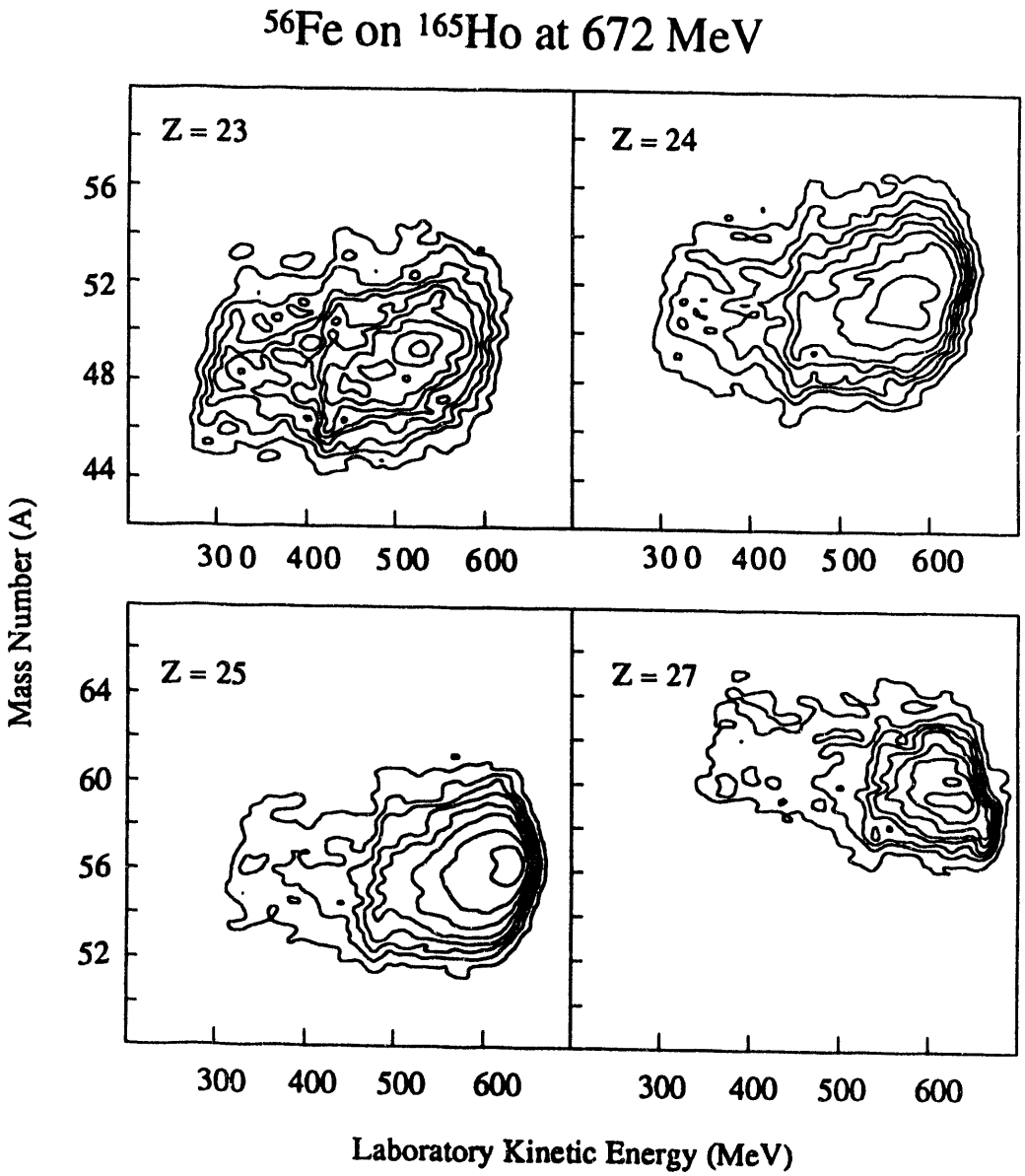

Figure II.17 Contour plots of the PLF mass as a function of the PLF kinetic energy for V, Cr, Mn and Co, after matching the "left" and "right" regions.

separation, was previously investigated by our group and proved successful in the determination of the mass distributions of ^{35}Cl on ^{209}Bi at 15 MeV/u [MAR91]. Detailed information about the deconvolution technique can be found in [MAR91, 93] and references therein. A brief description of the procedure and its results for the present data follows in Section II.C.4.

II.C.4 Deconvolution

The deconvolution procedure mainly consisted of smoothing the data to improve the signal to noise ratio, and deconvolving the smoothed spectra by application of the equation

$$\mathbf{O} = \mathbf{S}^{-1}\,\mathbf{I}, \qquad \text{(II.5)}$$

where **O** is the observed object, $\mathbf{S}^{-1}$ is the spread function and **I** is the image of the object.

A set of mass spectra with good mass resolution ($\approx$ 0.5 mass units), obtained from another experiment, was used as a test set for verification of the applicability of this method [MAR91, 93]. Randomized Gaussian functions were utilized to blur the well resolved mass spectra. The blurred spectra were then smoothed by a quartic point function and deconvolved. The original, distorted and deconvolved spectra for the test case are displayed in Figure II.18. It is evident that the deconvolved data reproduce the original data very well, indicating that the use of this deconvolution method for better peak separation is justified, at least in the type of data analyzed here. A comparison between the original and the deconvolved mass spectra of sulfur isotopes obtained in the 15 MeV/u ^{35}Cl on

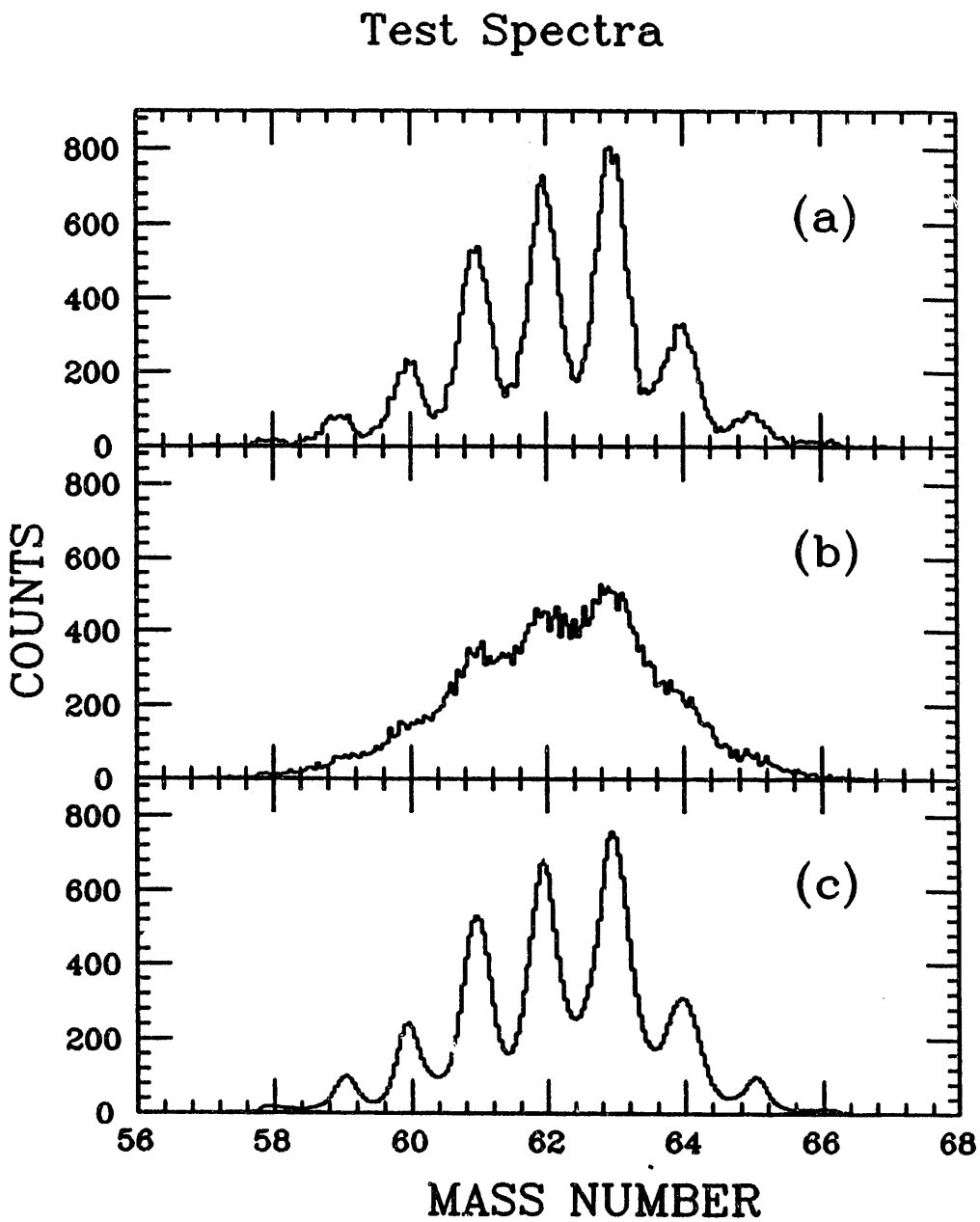

Figure II.18 Test spectra for the deconvolution method:
(a) original, (b) distorted (or blurred), and (c) deconvolved mass spectra [MAR91].

^{209}Bi data, for which the mass resolution was larger than 0.9 mass units, is shown in Figure II.19 [MAR91, 93]. The S isotopes are easily identified in the deconvolved mass spectrum, which is in good agreement with the experimental spectrum. The original and the deconvolved mass spectra of Fe (Z = 26), and Mn (Z = 25) isotopes obtained with the present data are displayed in Figures II.20 and II.21, respectively. The deconvolved and original mass centroids in both plots are in reasonable agreement. It should be emphasized that the deconvolved spectra (when they are necessary) were used only in the determination of the various polynomials that describe the energy dependence of the mass parameter and for absolute mass calibration. All the data analysis was otherwise performed on an event-by-event basis.

II.C.5 Final Mass Calibration

Once the functional dependence of mass on energy was determined, a new (corrected) mass was defined as

$$\text{corrected mass} = \text{energy-dependent mass} - f(E_{lab}) + \text{constant}, \qquad \text{(II.6)}$$

where $f(E_{lab})$ is a polynomial function describing the mass in terms of kinetic energy, and the constant is used to make the correct mass assignment. Examples of the mass distributions obtained are shown in Figures II.22 through II.24 for chromium (Z = 24), manganese (Z = 25), and cobalt (Z = 27), respectively, for values of kinetic energy excluding elastic events. The centroids and widths of individual masses were determined by fitting Gaussian curves (indicated here by the solid lines superimposed on the histogram) to the mass peaks. The parameters of the Gaussian fit (centroid, FWHM) are also indicated.

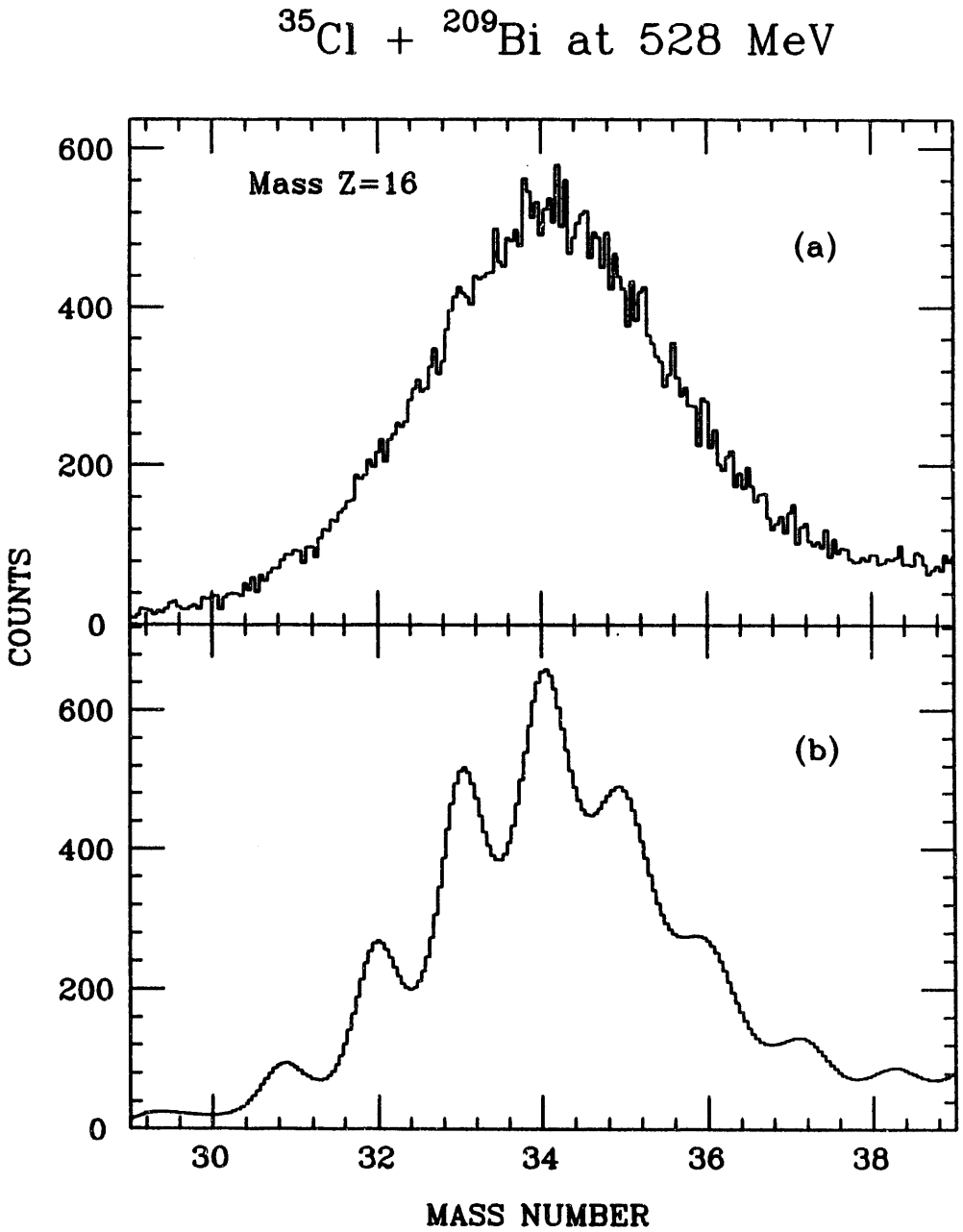

Figure II.19 Comparison between (a) the original mass spectrum and (b) the deconvolved mass spectrum obtained for S (Z = 16) isotopes in the 15 MeV/u ^{35}Cl on ^{209}Bi reaction [MAR91].

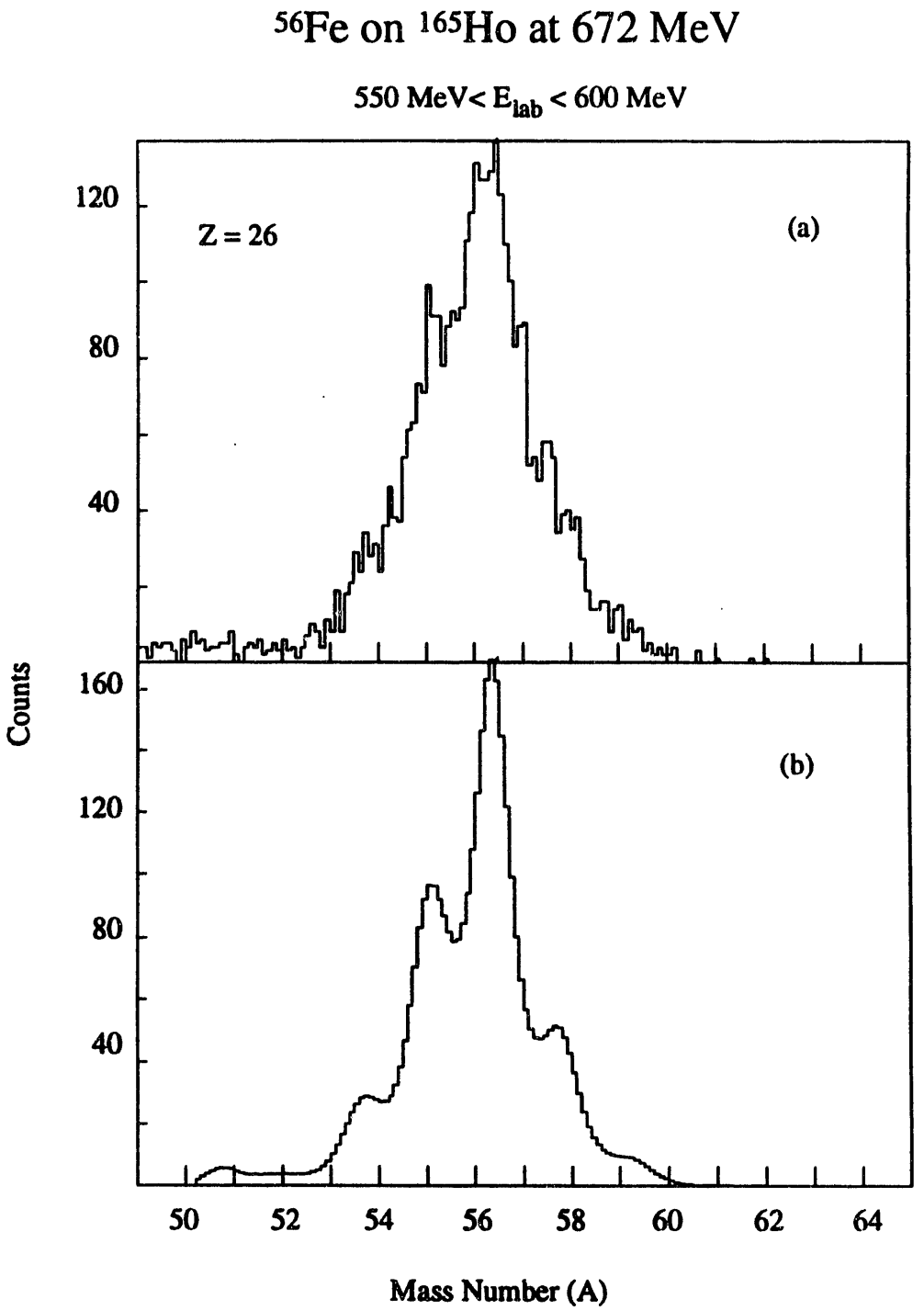

Figure II.20 Comparison between (a) the original mass spectrum and (b) deconvolved mass spectrum obtained for Fe (Z = 26) isotopes in the 672-MeV/u ^{56}Fe on ^{165}Ho reaction.

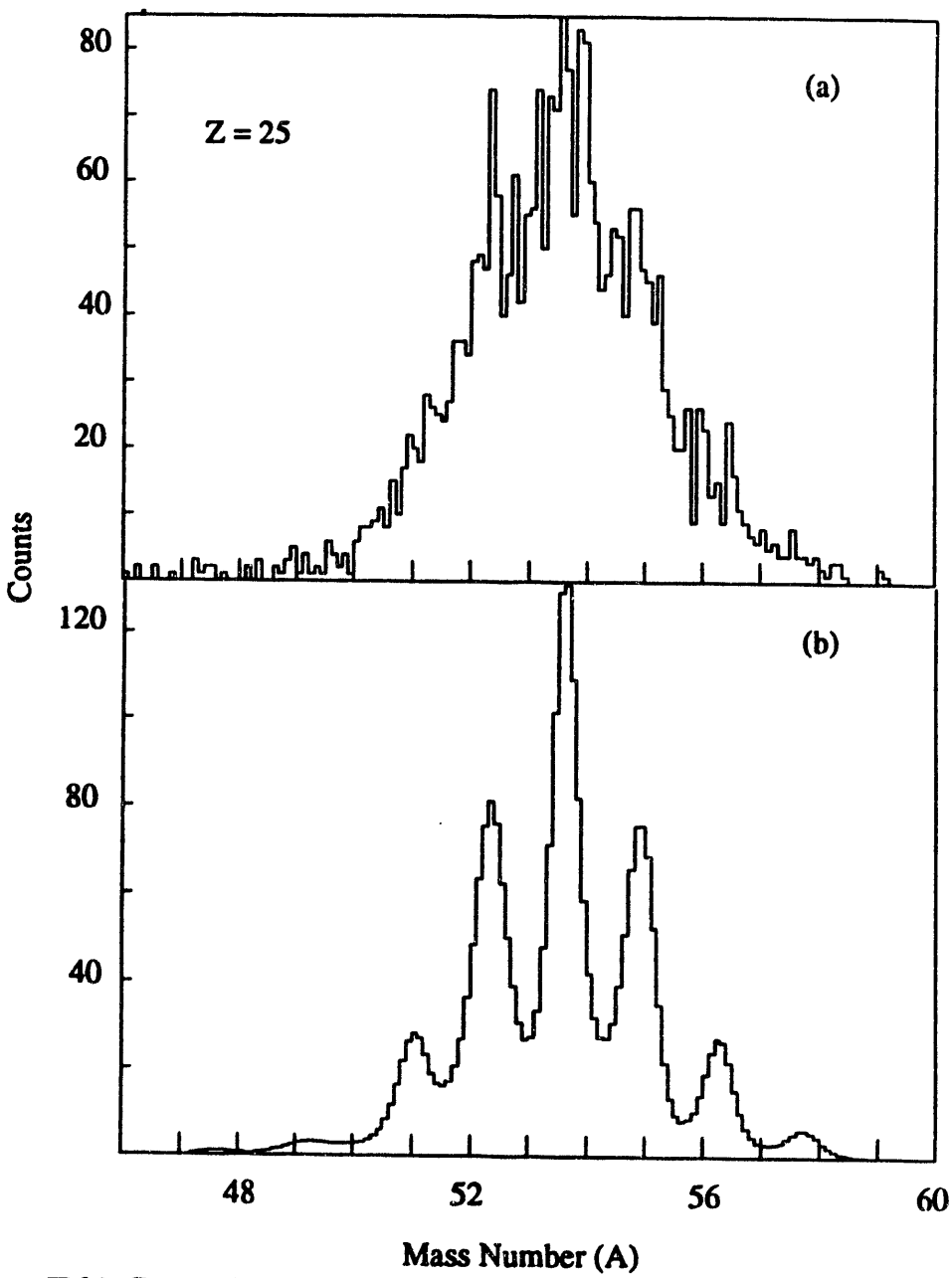

Figure II.21 Comparison between (a) the original mass spectrum and (b) deconvolved mass spectrum obtained for Mn (Z = 25) isotopes in the 672-MeV/u ^{56}Fe on ^{165}Ho reaction.

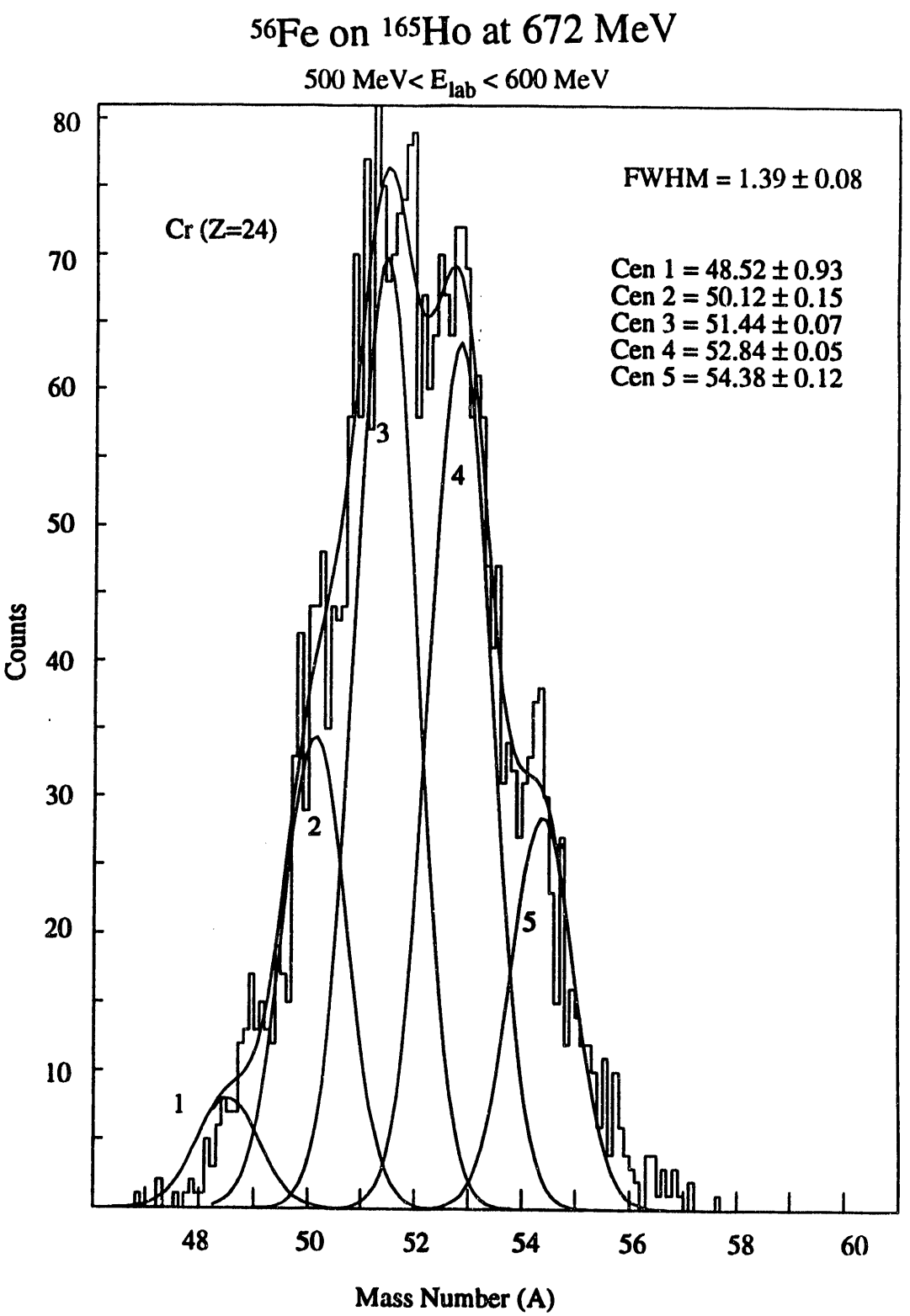

Figure II.22 PLF mass for Z= 24 and E_{lab} in the 500-600 MeV range.

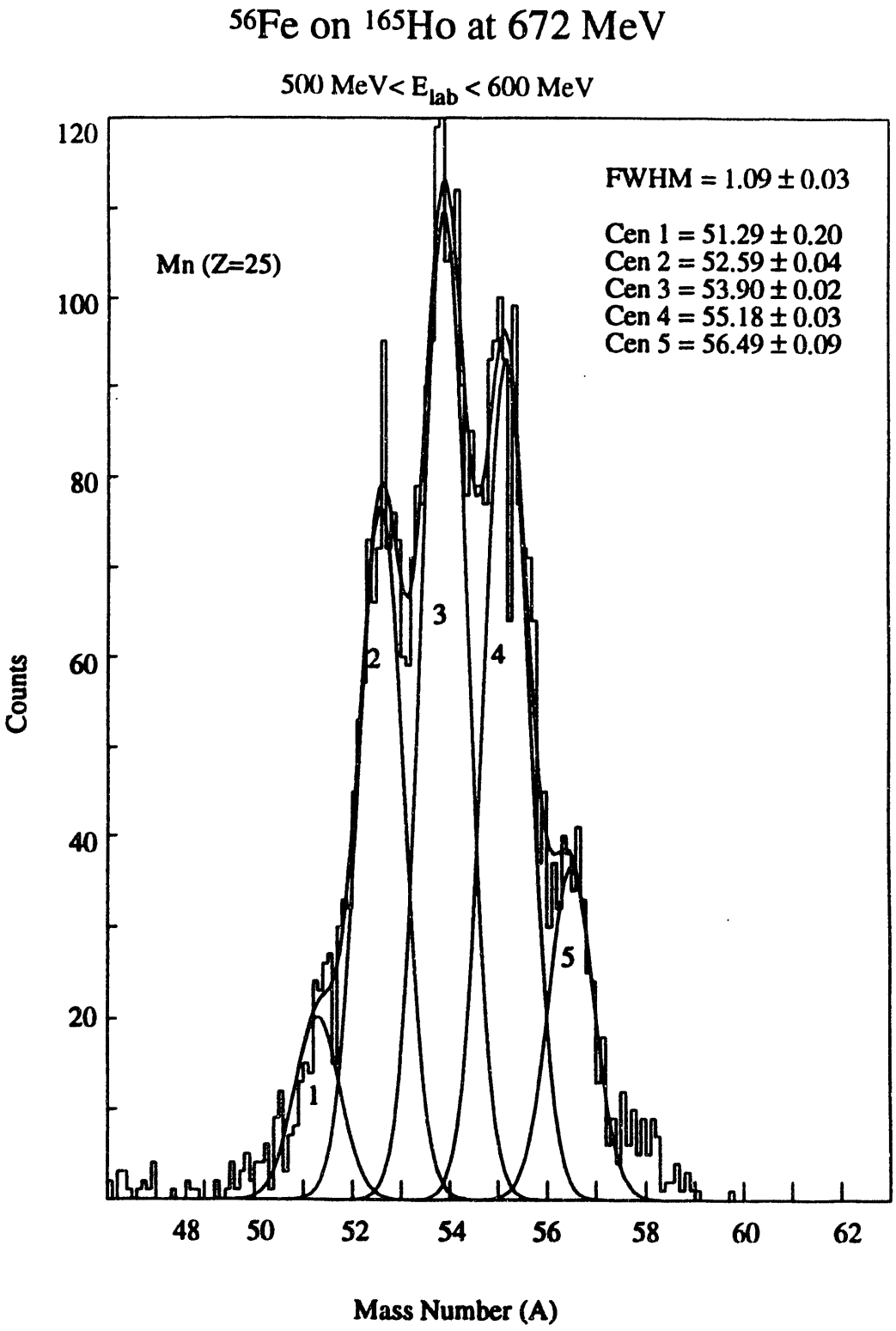

Figure II.23 PLF mass for Z = 25 and E_{lab} in the 500-600 MeV range.

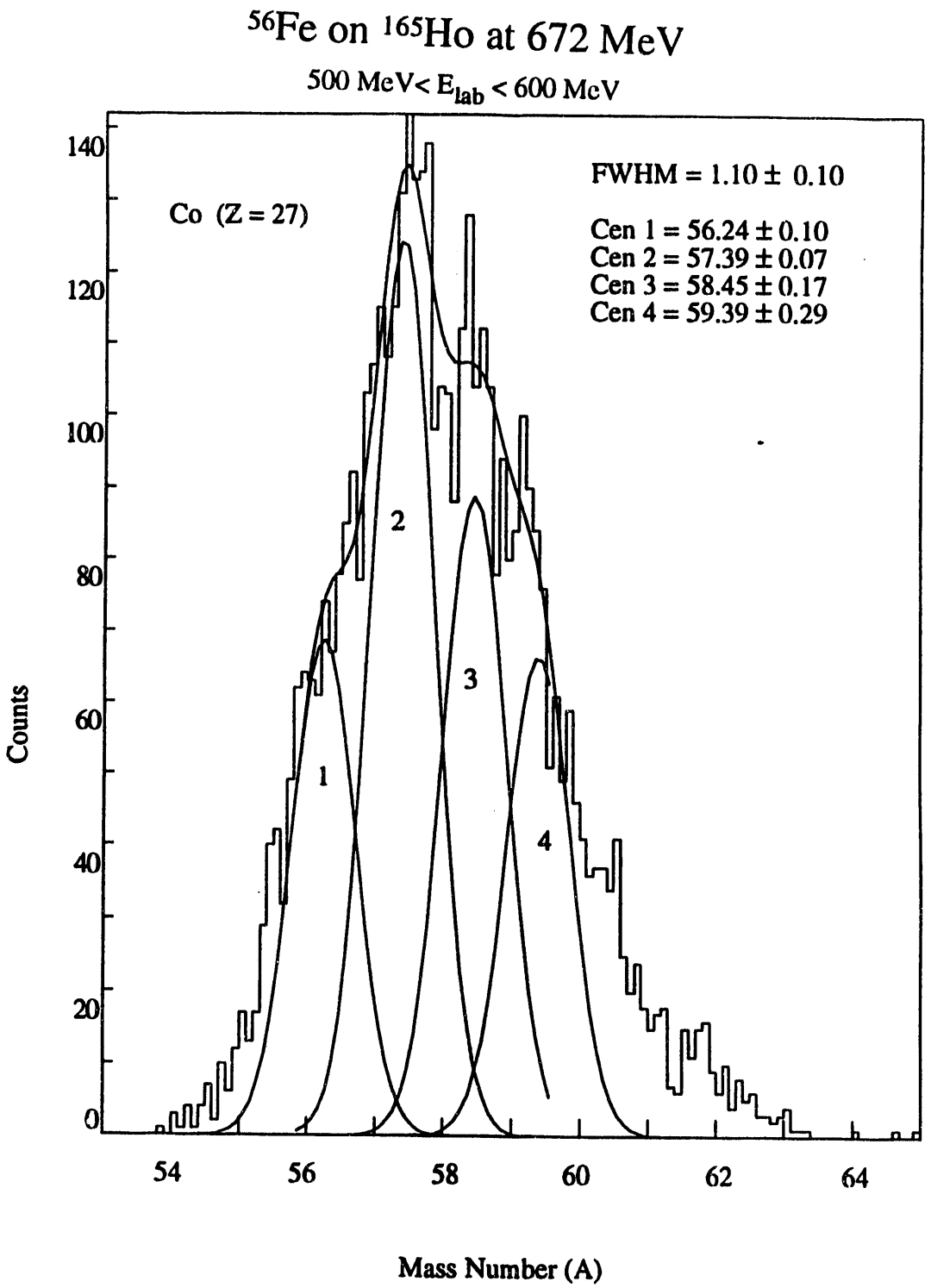

Figure II.24 PLF mass for Z = 27 and E_{lab} in the 500-600 MeV range.

Some of the features of the isotopic distributions are an unequal spacing between adjacent masses, and a slight shift in mass centroids from one element to the other. The correct mass calibrations were performed individually using equation II.6 for events where elements with atomic numbers between 23 and 27 were detected. Because of lower statistics, an extrapolation was performed for the remaining events. The polynomial function obtained with the isotopic distribution of vanadium (Z = 23) was used for elements with Z < 23 and that obtained with the cobalt (Z = 27) isotopic distribution was used for elements with Z>27. The calibrated mass for inclusive Z is displayed in Figure II.25.

Finally, the corrected mass was plotted against the corrected charge as displayed in Figure II.26. Elastic events and slit scattering are excluded from this plot. Ideally, there should not be any shift in the mass and charge centroids, contrary to what is seen in this figure. Therefore, further corrections were made to obtain individual charge centroids independent of mass and vice versa, as shown in Figure II.27. The neutron number was determined event-by-event by subtracting the atomic number Z from the mass number A and was used in all the subsequent analysis of mass and charge distributions.

II.D DATA REDUCTION

Two questions, often addressed regarding deep-inelastic collisions, were investigated in the present study. First, the mass and charge drifts of the reaction products were studied by following the evolution of the nuclide distribution of the detected fragments with total kinetic energy loss (TKEL). The determination of TKEL is described in Section II.D.1. The TLF events were not used in this case. The mass and charge distributions of the PLF's were determined in terms of their

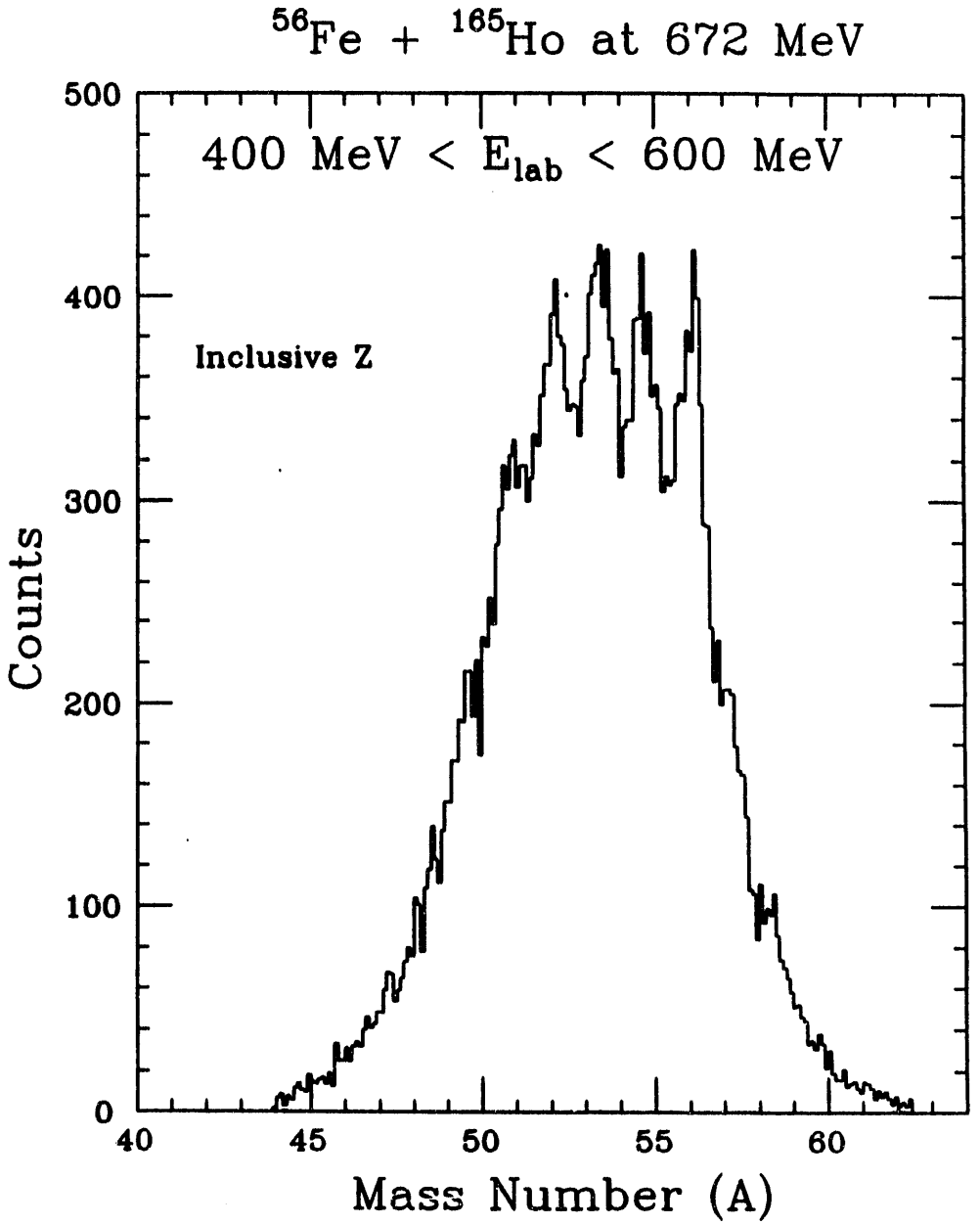

Figure II.25 PLF mass for inclusive Z. Elastic events are excluded by gating out the elastic energy peak.

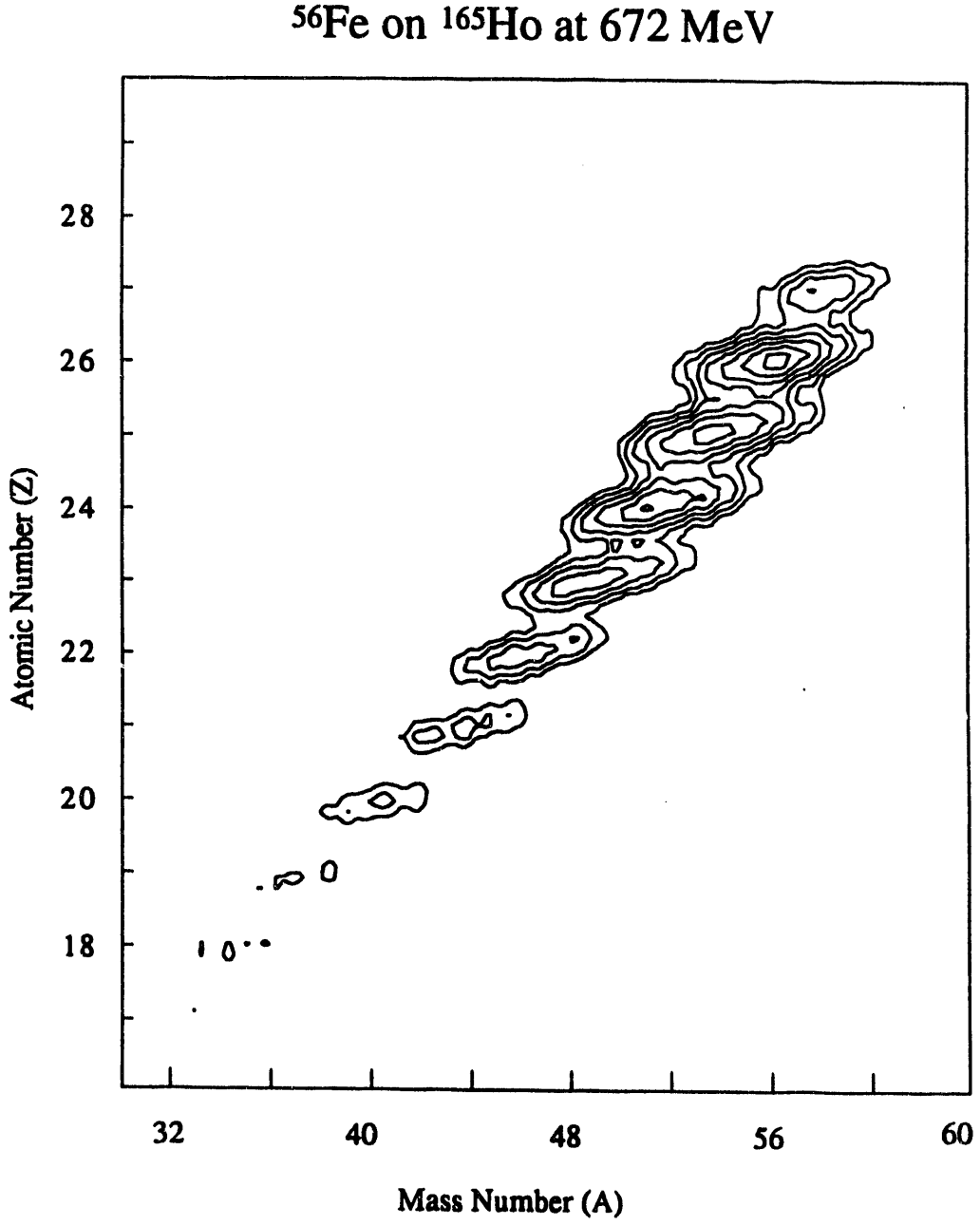

Figure II.26 Atomic number (Z) as a function of mass number (A) for 672-MeV/u ^{56}Fe on ^{165}Ho reaction. Elastic events (E_{lab} >630 MeV) gated out.

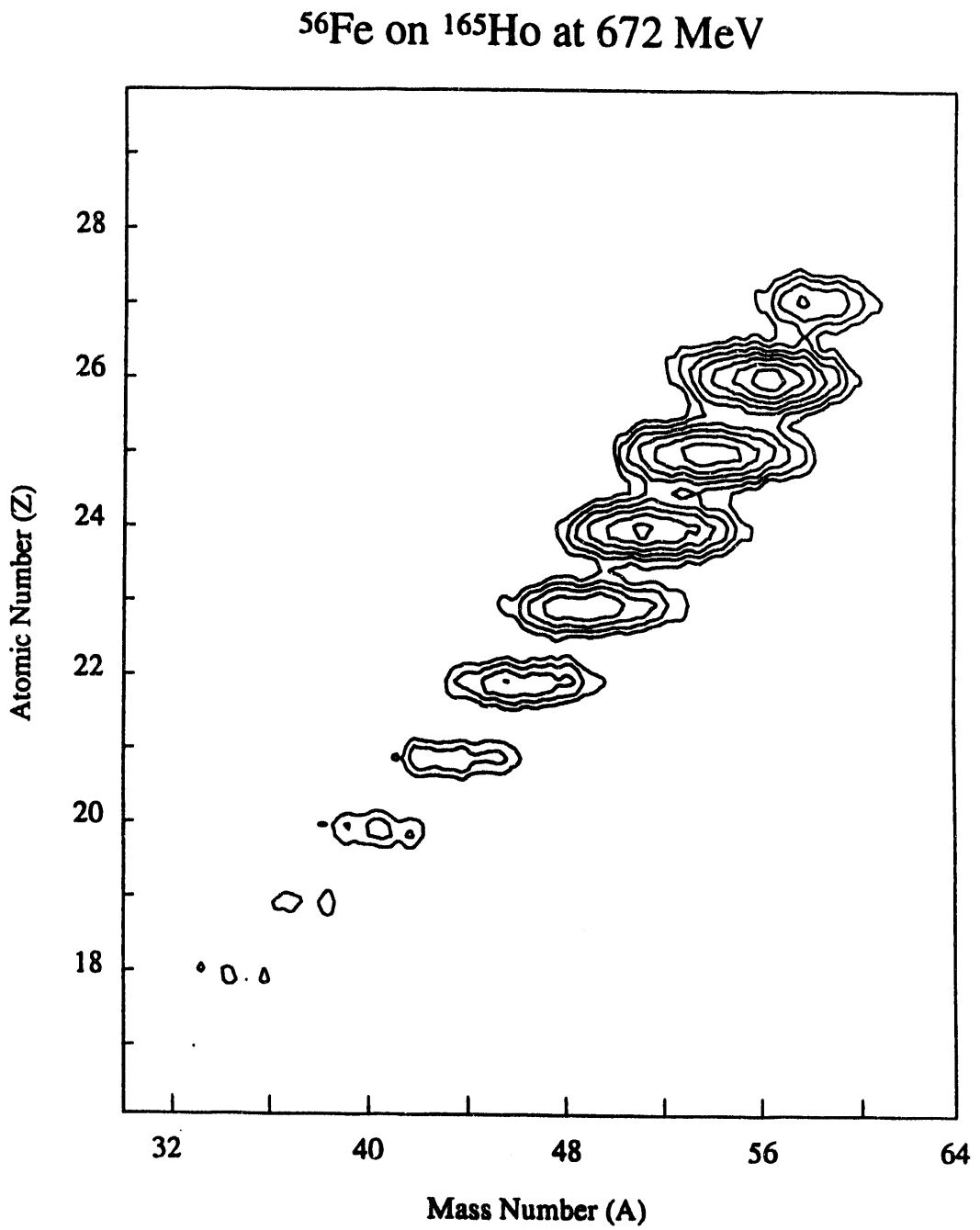

Figure II.27 Atomic number (Z) as a function of mass number (A) for 672-MeV/u ^{56}Fe on ^{165}Ho reaction after correcting for the interdependence between A and Z. Elastic events (E_{lab} > 630 MeV)are gated out.

centroids, their widths and a correlation factor between the two distributions, as described in Section II.D.2. These experimental distributions were to be compared to model predictions to determine the history of the system from the beginning of the collision at low relative kinetic energy damping to full kinetic energy damping. As the measured parameters describe the system after evaporation, corrections accounting for this process were necessary. The Projection Angular-Momentum Coupled Evaporation code, PACE II by Gavron [GAV80] was the evaporation code of choice in this study.

Second, the TLF events detected in coincidence with the PLF were used to determine the primary mass of the PLF by two-body kinematics reconstruction. The excitation energy of the PLF was then determined using results from the PACE II evaporation code. The division of the total excitation energy between the two primary reaction fragments could thus be determined as described in section II.D.3.

II.D.1 Excitation Energy and Evaporation Corrections

The amount of kinetic energy converted into forming the reaction products in their ground states (Q_{gg}), in addition to their excitation energy, is referred to as the total kinetic energy loss (TKEL) and is equivalent to the Q of the reaction. It is defined as the difference between the center-of-mass energy before the reaction takes place and the total kinetic energy (TKE) available in the center-of-mass after the collision. The total kinetic energy is given by

$$TKE = \left(1 + \frac{M_3}{M_4}\right) E_{PLF} \sqrt{M_1 M_3 E_{PLF} E_{PROJ}} \times 2M_4 \cos\theta - \left(1 - \frac{M_1}{M_4}\right) E_{PROJ}, \qquad \text{(II.7)}$$

where E_{PROJ} is the laboratory kinetic energy of the primary projectile-like fragment, and M_1, M_3 and M_4 are the projectile mass, and the primary projectile- and target-like fragments masses, respectively, and θ is the scattering angle of the PLF. The TKEL can then be determined as

$$TKEL = TKE - E_{CM} = \left(1+\frac{M_3}{M_4}\right)E_{PLF} - \left(1-\frac{M_1}{M_4}\right)E_{PROJ} - 2\cos\theta\sqrt{\frac{E_{PROJ}\,E_{PLF}\,M_1\,M_3}{M_4^2}} \qquad (II.8)$$

The total excitation energy of the system E^* is

$$E^* = TKEL + Q_{gg} \quad , \qquad (II.9)$$

where Q_{gg} is the energy required to form the primary fragments in their ground states. A table of Q_{gg} values was generated for a range of isotopes that included all the nuclides that can be produced in the reaction studied here.

Equation II.8 is true only for primary quantities while the measured quantities describe secondary fragments. Therefore, the value of TKEL had to be corrected for the binding energy and the kinetic energy of the evaporated particles with an iterative procedure that used results from the evaporation code PACE II. This code simulates the statistical emission of neutrons, protons, alpha particles and gamma rays by a Monte Carlo technique. It had been shown in earlier studies [LOC85, AWE84] of heavy-ion collisions that there is a satisfactory agreement between experimental data and PACE II predictions for the energy regime of the present experiment.

Among the inputs to the program are general parameters that are not exclusively characteristic of the system being studied. Two examples are the level

density parameter, and the type of yrast band. The default values of the program which were taken from Gilbert and Cameron were used since good agreement with experimental data has been obtained with these values in earlier studies [LOC85] . Other inputs to the program are directly provided by the user. They include the number of cascades (1000), the PLF mass number (56 amu) and atomic number (26), the PLF's angular momentum, and excitation energy.

The angular momentum or spin of the PLF was determined using the assumption of the sticking limit, where the two reaction products form a single entity. However, evaporation calculations with different values for the nuclear spin showed that the amounts of mass and charged evaporated are not strongly dependent on spin, provided that the spin considered lies within a reasonable range of values, as shown in Figure II.28 [BEN85]. The spin values *l*, of the PLF's produced by the 672-MeV ^{56}Fe on ^{165}Ho reaction were between 2 and 15 ħ. Therefore, only the initial spin of the primary PLF was calculated assuming the sticking limit, using the method described by Benton *et al.* [BEN85, 87, 88], and this was used for the whole excitation energy range.

Two possibilities were considered for the excitation energy parameter when running the evaporation calculations. An equal sharing of the total available excitation energy E^*_{TOT} by the PLF and the TLF is expressed by the equation

$$E^*_{PLF} = E^*_{TLF}. \qquad \text{(II.10)}$$

In this case, the lighter fragment (the PLF for the present work) has a higher nuclear temperature than the heavier fragment. The nuclear temperature τ of a nucleus is related to its excitation energy through the equation

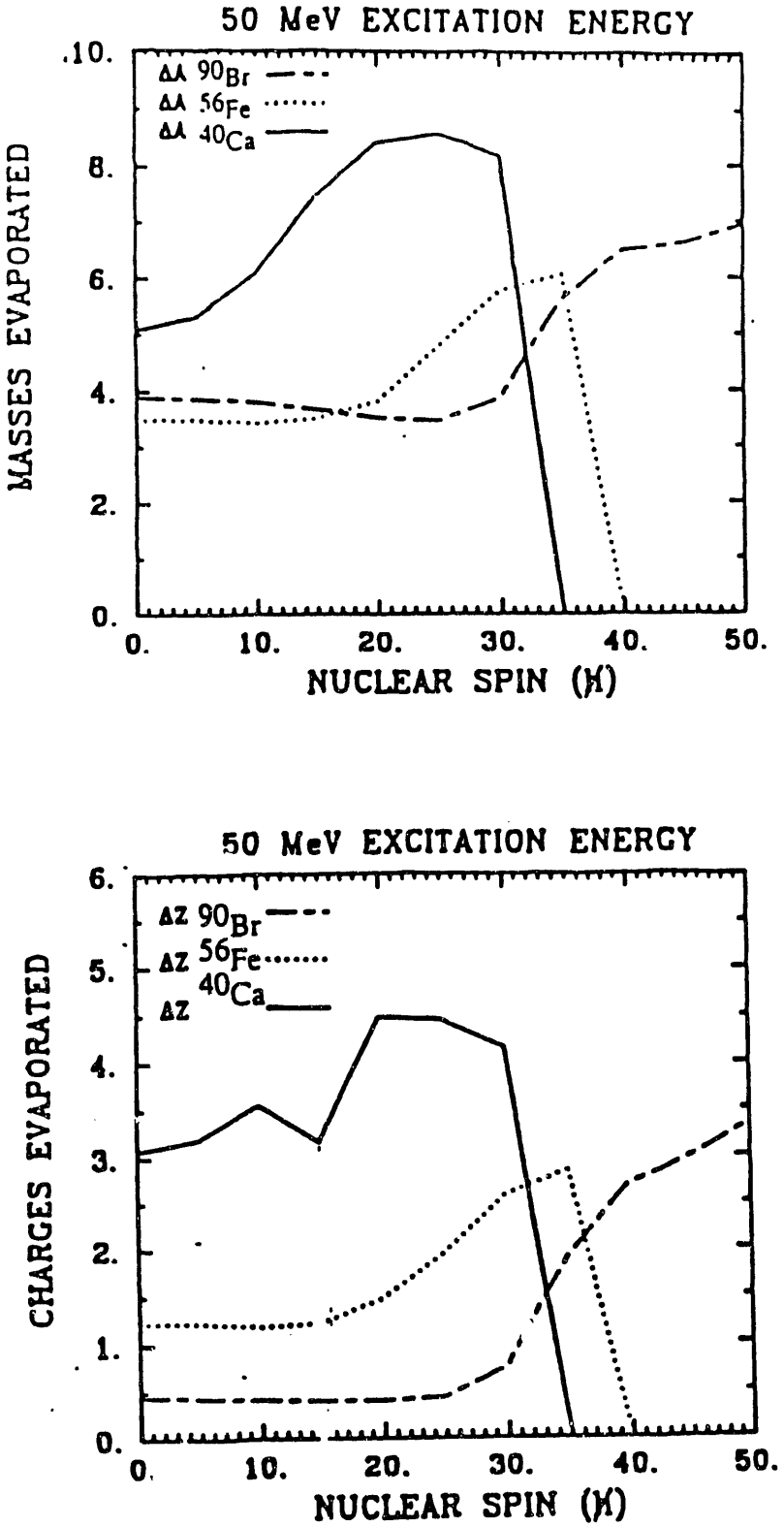

Figure II.28 Calculations of evaporated charges and masses from the PACE II evaporation code, for three different nuclides as a function of initial spin for an initial excitation energy of 50 MeV [BEN85].

$$E^* = a\tau^2, \qquad \text{(II.11)}$$

where a is the level density parameter and is assumed to be proportional to the nucleus mass.

In the second case considered, the two fragments are assumed to be in statistical equilibrium and thus have equal nuclear temperatures. Therefore, E^*_{TOT} is divided between the reaction fragments in proportion to their mass ratios, as given by the equation

$$\frac{E^*_{PLF}}{E^*_{TLF}} = \frac{M_{PLF}}{M_{TLF}} \qquad \text{(II.12)}$$

Both alternatives for the excitation energy division were considered in the correction of the energy loss scale (TKEL) for evaporation effects.

To obtain the amount of evaporated mass as a function of excitation energy, a range of excitation energies extending from 0.25 to 2 MeV/u was used in steps of 0.25 MeV/u. For each step, a range of nuclei with mass and atomic numbers chosen to yield the experimental values after evaporation, were evaporated. The functional forms of the evaporated mass, in terms of available excitation energy, were determined by linear fits, as shown in Figure II.29, where the evaporated mass is plotted versus the excitation energy. The polynomial that best fits the evaporated mass is

$$\Delta A = -.2032 + 9.5277 \times 10^{-2} (E^*) - 1.4971 \times 10^{-4} (E^{*2}). \qquad \text{(II.13)}$$

An iteration procedure was then employed to compute a new corrected value for TKEL. The convergence of the iteration was tested by requiring that the

difference between the values of TKEL obtained in two consecutive iterations be less than 0.1 MeV. The steps of the iteration are outlined below.

1- Determine E^*_{PLF} with one of the two assumptions of excitation energy division.

2- Determine ΔM, the mass difference between primary and secondary masses in terms of E^*_{PLF} using equation II.D.11.

3- Add ΔM to the projectile-like fragment mass M_3.

4- Calculate the TLF mass M_4 as $M_1+M_2-M_3$, where M_3 is now the corrected PLF mass obtained in step 3.

5- Calculate the kinetic energy of the projectile-like fragment, E3, with the equation

$$E_3 = \frac{E_{3(EXP)}(M_3 + \Delta M)}{M_3}. \qquad \text{(II.14)}$$

6- Reestimate TKEL with the new values of E3, M3, and M4.

7- Repeat steps 1 through 6 until the difference between two consecutive values of TKEL is smaller than 0.1 MeV or the number of iterations is 100. Events that did not satisfy the convergence criterion were aborted. In this study, there was no need to discard any events as convergence was reached after a few iterations.

II.D.2 Mass and Charge Distributions

The mass and charge distributions of the projectile-like fragments were determined by moment analysis. Contour plots of Z versus N were generated for

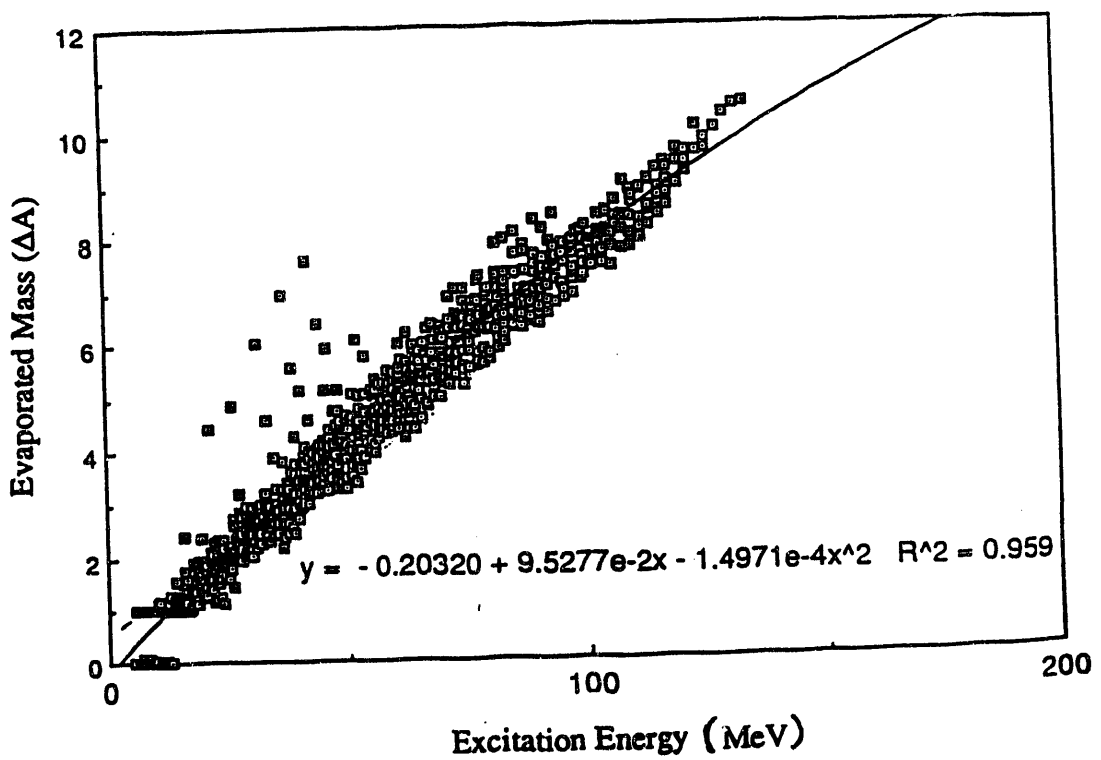

Figure II.29 Calculations of evaporated mass versus excitation energy from PACE II for a range of possible PLF's for the reaction $^{56}Fe + ^{165}Ho$ at 672 MeV. A quadratic polynomial shown as the line was used to determine ΔA for a given excitation energy.

different gates of TKEL. Examples of these plots are displayed in Figure II.30. The widths of the gates were 20 MeV for TKEL values between 0 and 200 MeV, and 40 MeV for TKEL between 240 and 380 MeV. The first and second moments of the distributions were determined in terms of N and Z. If the distributions were pure Gaussians these would be equivalent to the distribution centroids and variances, respectively, in a Gaussian formulation described by the equation

$$P=h\exp-\frac{1}{2(1-\rho^2)}\left(\frac{(N-\langle N\rangle)^2}{\sigma^2_N}+\frac{(Z-\langle Z\rangle)^2}{\sigma^2_Z}-\frac{2\rho(N-\langle N\rangle)(Z-\langle Z\rangle)}{\sigma_Z\,\sigma_N}\right), \quad \text{(II.15)}$$

where P is the probability, h is a normalization factor, $\langle N\rangle$ and $\langle Z\rangle$ are the neutron and proton centroids, respectively, σ_N and σ_Z are their respective variances, and ρ_{NZ} is the correlation factor.

In a moment analysis, the charge centroids and variances are expressed by the equations

$$\langle Z\rangle=\frac{1}{n}\sum_{i=1}^{n}Z_i, \quad \text{(II.16)}$$

and

$$\sigma_Z^2=\frac{1}{n-1}\sum_{i=1}^{n}(Z_i-\langle Z\rangle)^2. \quad \text{(II.17)}$$

Analogous equations are used for the neutron centroid and variance. The correlation factor is given by

$$\rho_{NZ}=\frac{\sigma_{NZ}}{\sigma_N\,\sigma_Z}, \quad \text{(II.18)}$$

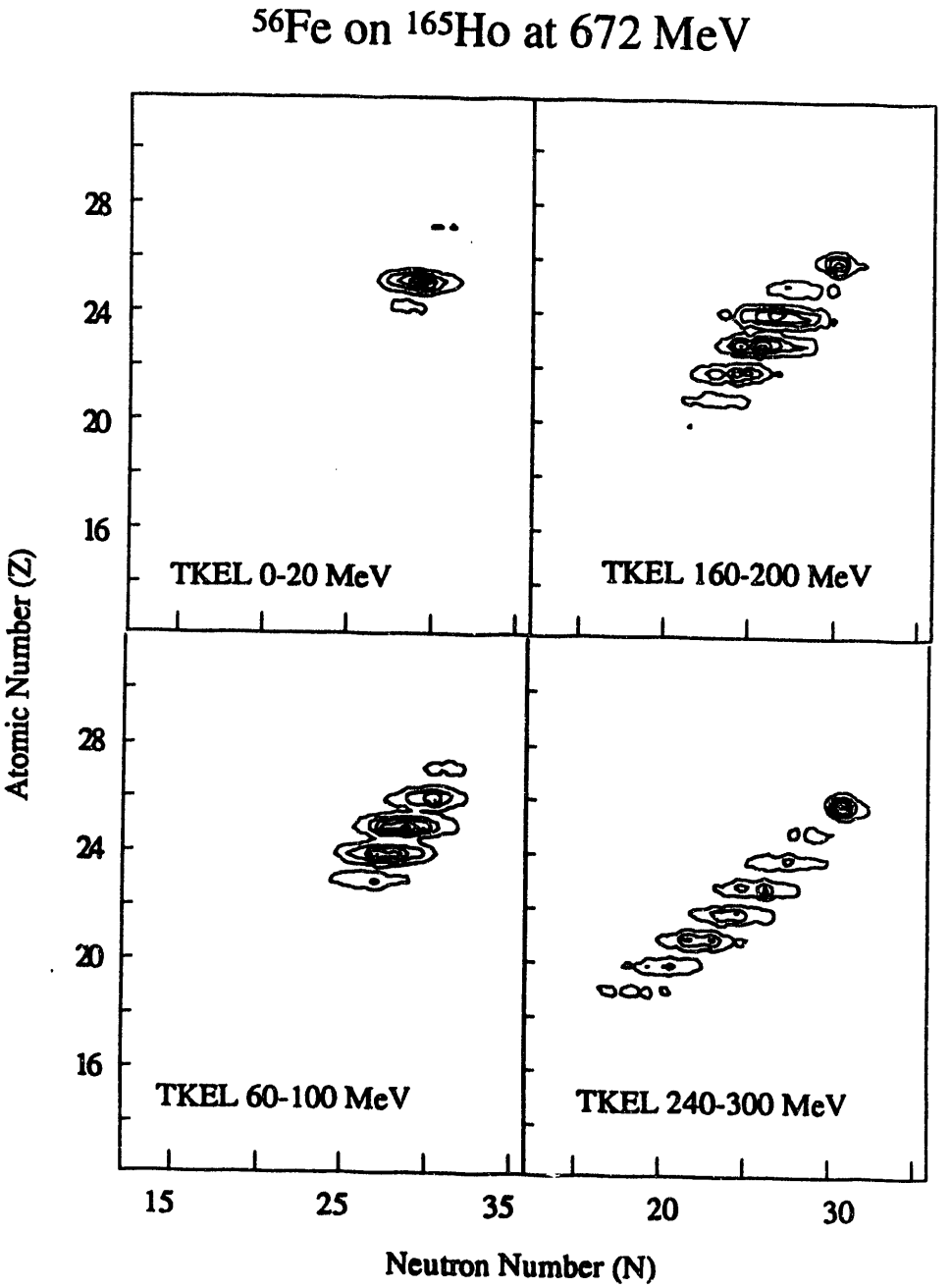

Figure II.30 Contour plots of the PLF atomic number (Z) as a function of its neutron number (N) for four TKEL bins: 0-20 MeV, 60-100 MeV, 160-200 MeV, and 240-300 MeV.

where σ_{NZ} is the covariance and is written as

$$\sigma_{NZ} = \frac{1}{n-1} \sum_{i=1}^{n} (Z_i - \langle Z \rangle)\,(N_i - \langle N \rangle). \qquad \text{(II.19)}$$

When the distributions deviate from pure Gaussian shapes, the centroids obtained by performing two-dimensional Gaussian fits on the distributions or by using the methods of moments, do not differ much because the centroids are not very sensitive to the choice of limits imposed by the presence of long tails in the distributions. However, it was found that the variances determined by moment analysis tend to be greater than those obtained by Gaussian fits [MAR91, 92]. It was shown that in general when the distributions do not depart considerably from Gaussian shapes, the two approaches yield similar values for the centroids and variances [MAR91, 92]. The errors on the centroids and variances obtained with the moment analysis approach are larger than the equivalent Gaussian error bars commonly used because in addition to statistical errors, they include the uncertainty due to the method employed in the moments determination. The errors quoted when using Gaussian fits usually measure only the goodness of the fit. Therefore, the moment analysis method was opted for in this study.

II.D.3 Primary Mass and Excitation Energy of the PLF

The kinematic coincidence technique, where the projectile-like and the target-like fragments are detected in coincidence, was used to extract information about the primary reaction fragments before evaporation takes place. One basic assumption in this technique is the invariance of the average velocity and scattering angle of the emitted fragment by particle evaporation. Assuming the validity of

this assumption, which is based on the statistical properties of evaporation, the PLF's primary mass can be obtained by the application of two-body kinematics.

For non-relativistic cases, momentum conservation is expressed by the two equations

$$P_{PROJ} = P_{PLF}\cos(\theta_{PLF}) + P_{TLF}\cos(\theta_{TLF}), \qquad \text{(II.20)}$$

and

$$P_{PLF}\sin(\theta_{PLF}) = P_{TLF}\sin(\theta_{TLF}), \qquad \text{(II.21)}$$

where P_{PROJ} is the projectile momentum, P_{PLF} and P_{TLF} are the momenta of the PLF and the TLF, respectively, and θ_{PLF} and θ_{TLF} are their respective scattering angles. Classically, the linear momentum P of a particle of mass M traveling with a velocity V is

$$P=MV. \qquad \text{(II.22)}$$

The mass of the PLF can thus be written as

$$M_{PLF} = M_{PROJ}\frac{V_{PROJ}}{V_{PLF}\left[\cos(\theta_{PLF})+\sin(\theta_{PLF})\cot(\theta_{TLF})\right]} \qquad \text{(II.23)}$$

where M_{PROJ} and V_{PROJ} are the projectile mass and velocity, and V_{PLF} is the PLF's velocity.

All the parameters in equation II.23 are either known exactly, or unchanged, on the average, by particle evaporation; therefore, the primary mass of

the PLF is determined with a fairly good approximation. The primary kinetic energy is obtained by scaling the measured kinetic energy with the ratio of the primary mass to the measured mass as

$$E_{PLF} = \frac{M_{PLF} E_{SEC}}{M_{SEC}}, \qquad \text{(II.24)}$$

where E_{SEC} and M_{SEC} are the measured PLF's kinetic energy and mass, respectively. Finally, the mass evaporated from the PLF, ΔA, can be determined using the result of equation II.23 and the measured PLF mass as follows

$$\Delta A = M_{PLF} - M_{SEC} \qquad \text{(II.25)}$$

A contour plot of evaporated mass as a function of TKEL is shown in Figure II.31.

The amount of evaporated charge ΔZ and evaporated mass ΔA from a primary PLF with atomic number Z'_{PLF}, mass number A'_{PLF}, and excitation energy E^*_{PLF} can be expressed as a function of Z'_{PLF}, A'_{PLF}, and E^*_{PLF} and the secondary PLF mass A''_{PLF} and charge Z''_{PLF} by the two equations

$$\Delta A_{PLF} = A'_{PLF} - A''_{PLF} = f_{DA}(Z'_{PLF}, A'_{PLF}, E^*_{PLF}), \qquad \text{(II.26)}$$

and

$$\Delta Z_{PLF} = Z'_{PLF} - Z = f_{DZ}(Z'_{PLF}, A'_{PLF}, E^*_{PLF}). \qquad \text{(II.27)}$$

The quantities ΔA_{PLF} and ΔZ_{PLF} are generated by running PACE II. The results were tabulated and stored as computer files, which will be referred to as the

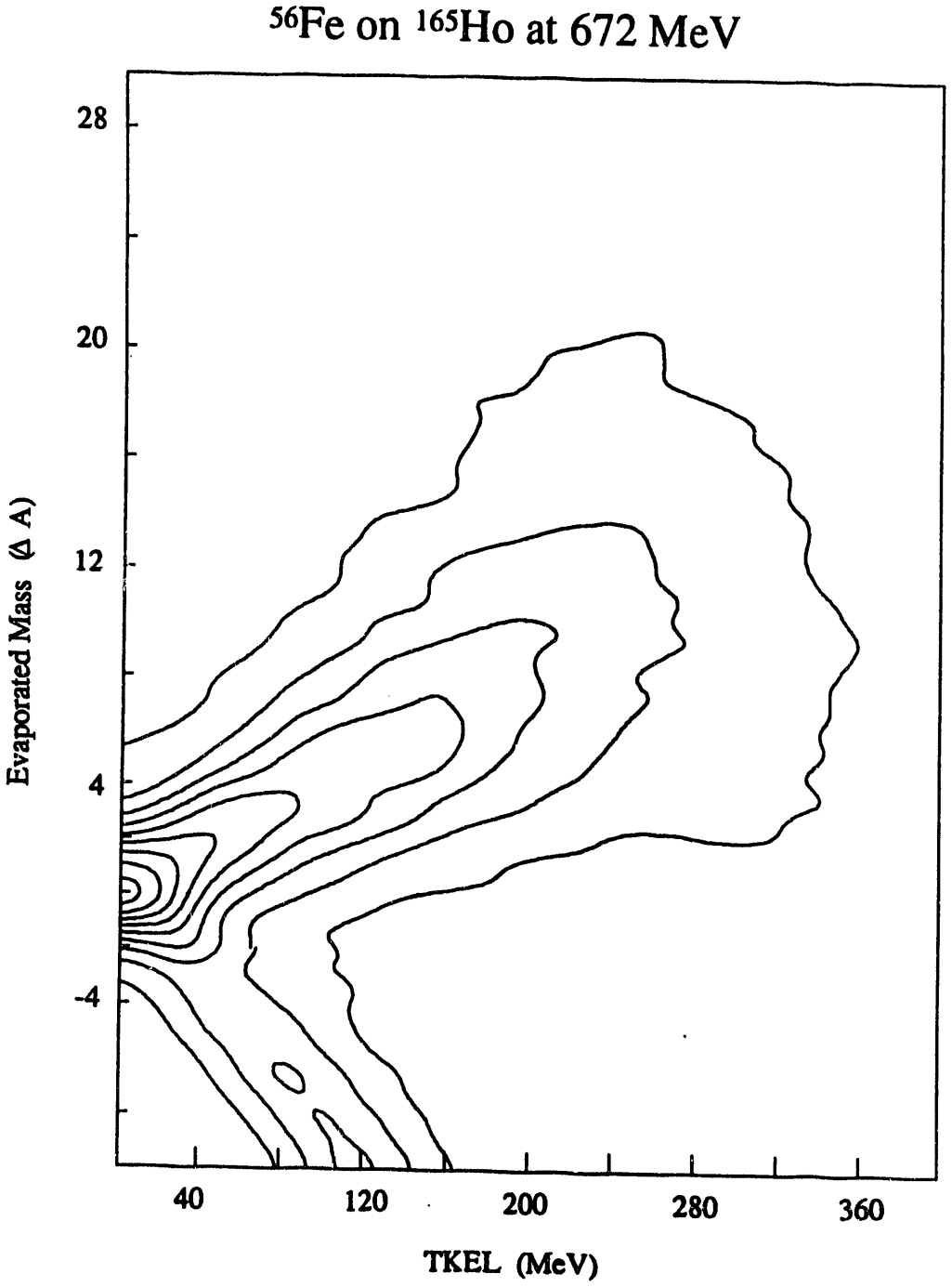

Figure II.31 Contour plot of ΔA, the amount of mass evaporated from the PLF as a function of TKEL in the reactio ^{56}Fe on ^{165}Ho at 672 MeV.

ΔA and ΔZ tables. To generate these tables, the evaporation code was run for 25 isotopes of each element with atomic numbers between 10 and 36 and for excitation energies between 0 and 300 MeV. Ten MeV steps were used for excitation energies lower than 100 MeV, and 50 MeV steps were used for higher excitation energies. The functions f_{DA} and f_{DZ} were then determined by interpolation of the values calculated for the chosen set of Z, A, and E* values that were obtained using PACE II [KWI90]. Therefore, the excitation energy and the primary charge of the PLF can be evaluated using results from the evaporation code PACE II.

In equations II.26 and II.27, the three unknowns are Z'_{PLF}, ΔZ_{PLF} and E^*_{PLF}. They were determined by employing a self consistent iteration procedure in which equations II.26 and II.27 were solved event-by-event at each iteration. The detailed steps are outlined in references [KWI90] and [BEN85]. Starting at an assumed value for Z'_{PLF}, the value of $E^*_{PLF}(i)$ at each iteration (i) was determined by solving equation II.26. It is then possible to solve equation II.27 for ΔZ_{PLF}. The convergence of the iteration was reached when

$$\varepsilon(i)=|\Delta Z_{PLF}(i)-\Delta Z_{PLF}(i-1)| < 0.1 \qquad \text{(II.28)}$$

For events that did not satisfy inequality II.28, the convergence was accelerated by defining a new value for $Z'_{PLF}(i)$ as

$$Z'_{PLF}(i)=Z'_{PLF}(i-1)+.9\varepsilon(i). \qquad \text{(II.29)}$$

Only events with positive values of ΔA_{PLF} were selected, and the maximum number of iterations allowed was 20.

The excitation energy of the PLF obtained for the 672-MeV ^{56}Fe on ^{165}Ho system is displayed in Figure II.32 for all events, excluding those with negative values of ΔA. Another parameter of interest, which describes the excitation energy division more directly, is the ratio of the PLF excitation energy to the total excitation energy, E^*_{PLF}/E^*_{TOT}. The E^*_{PLF}/E^*_{TOT} is defined as a percentage in this study, and is therefore expected to have values between 0 % and 100 %. Any values outside this range are not physically possible. A histogram representing the E^*_{PLF}/E^*_{TOT} ratio for the present data is shown in Figure II.33, for events excluding those with negative values of ΔA.

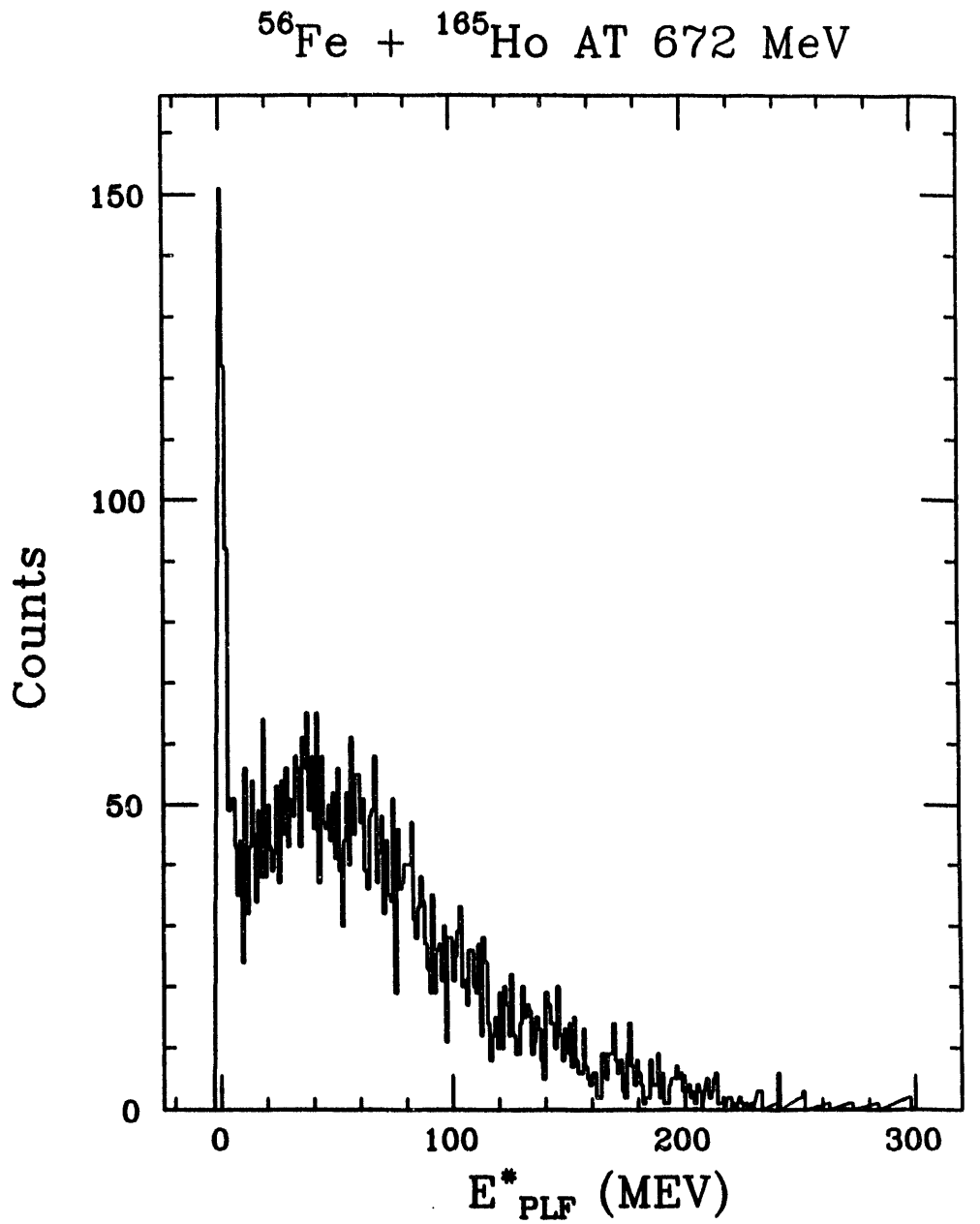

Figure II.32 The PLF's excitation energy for inclusive data in the reaction ^{56}Fe on ^{165}Ho at 672 MeV.

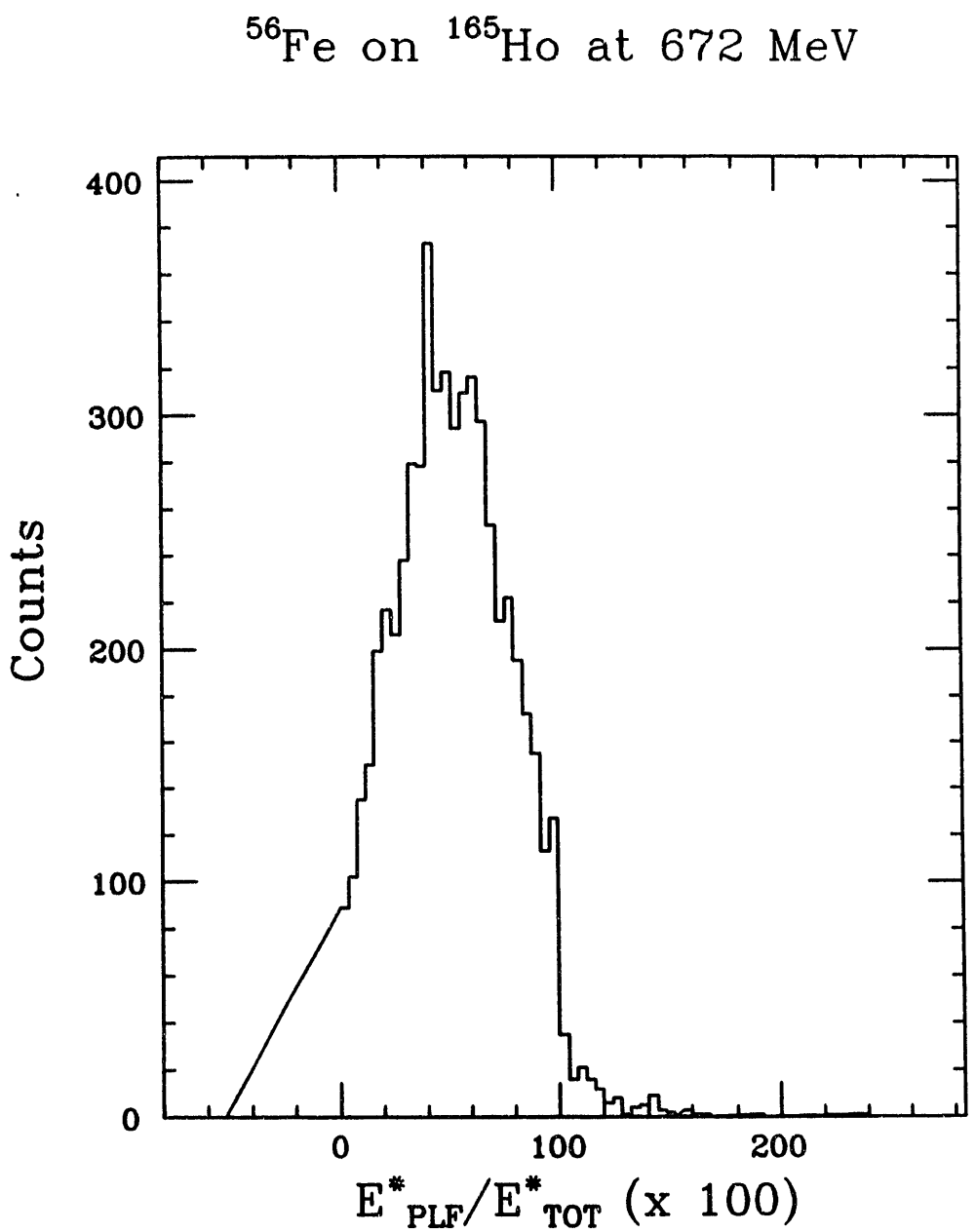

Figure II.33 The percentage of excitation energy stored in the PLF in the reaction ^{56}Fe on ^{165}Ho at 672 MeV. Most of the events are between the 0% and 100% limits.

CHAPTER III RESULTS

This Chapter presents the results of analysis of the data taken for the 672-MeV ^{56}Fe on ^{165}Ho system. The data have been sorted to exclude unwanted events, such as slit scattering. In Section III.A the secondary proton and neutron distributions of the projectile-like fragments (PLF's) are presented in terms of their centroids and variances, obtained by the moment analysis procedure described in Section II.D.1 The evolution of these distributions with the total kinetic energy loss (TKEL) is examined. The primary distributions obtained by applying evaporation corrections to the measured distributions, are also presented in Section III.A.

The results obtained for the excitation energy of the PLF, as determined with the two-body kinematical reconstruction method described in Section II.D.3, are presented in Section III.B. The behavior of the excitation energy division with energy damping is examined by following the evolution of the PLF excitation energy ratio E^*_{PLF}/E^*_{TOT} with TKEL. The E^*_{PLF}/E^*_{TOT} ratio is also plotted as a function of A'_{PLF}, the mass of the primary fragments, and as a function of A''_{PLF}, the mass of the secondary fragments, to investigate a possible correlation between the excitation energy division and the exit channel.

III.A N and Z Distributions

Contour plots of the measured nuclide distributions in the N-Z plane are displayed in Figure III.1 for four different bins of TKEL. For low energy damping these distributions tend to be circular and centered around the neutron number and charge of the projectile. As TKEL increases, the distributions exhibit the tendency to elongate towards more elliptical shapes whose axes are tilted. An increase in the

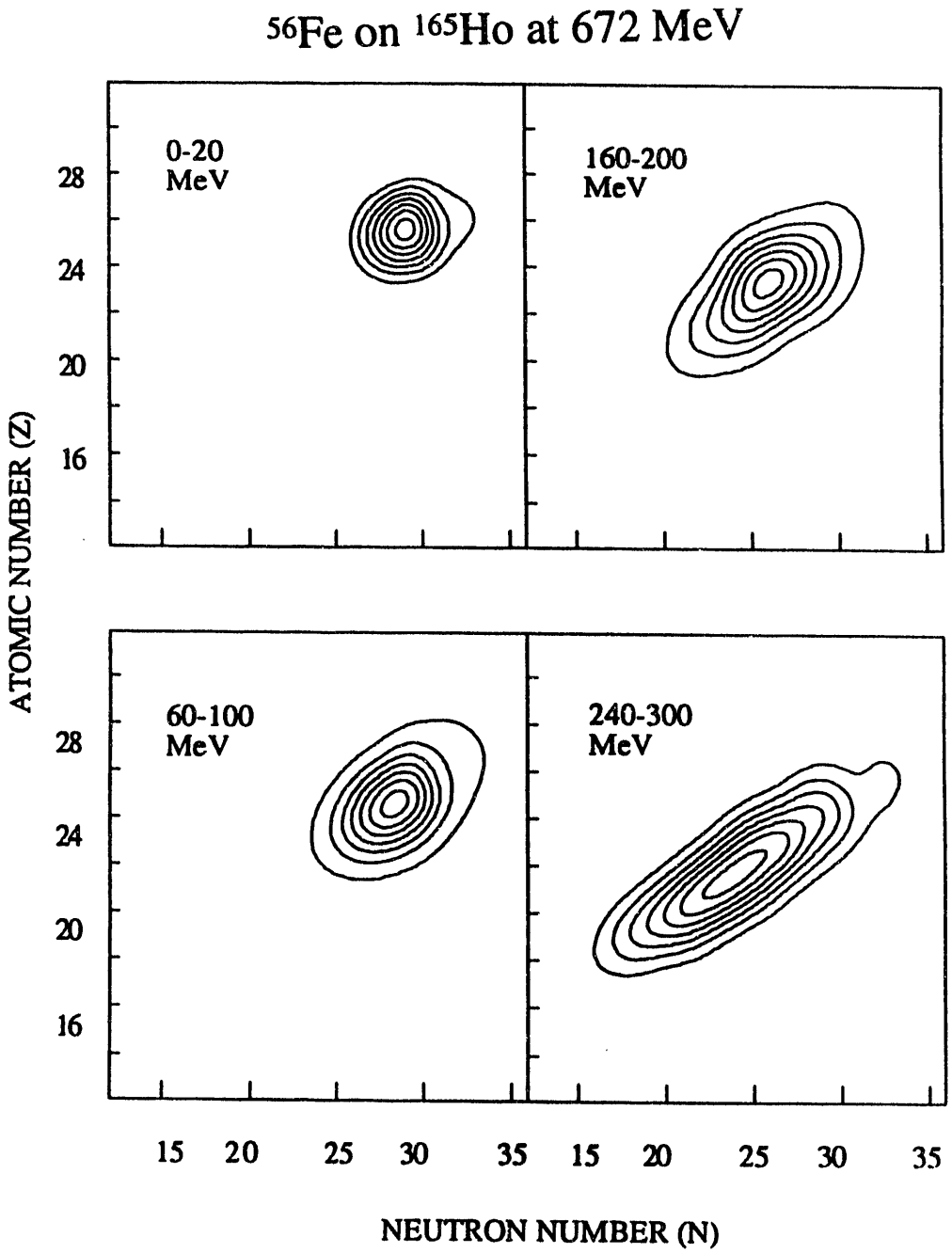

Figure III.1 Contour plots of the measured charge versus the measured neutron number for four representative bins of total kinetic energy loss (TKEL), for the 672-MeV ^{56}Fe on ^{165}Ho reaction.

magnitude of the tilt with increasing TKEL is indicative of the increase in the correlation factor ρ_{NZ} with increasing TKEL. The shapes of the N-Z distributions show a close resemblance to two-dimensional Gaussian shapes. They can, therefore be characterized by their centroids <N> and <Z> and their variances σ_N^2 and σ_Z^2, along with the correlation factor ρ_{NZ} which measures the mutual dependence between N and Z. These parameters can be determined by different methods [FRE84]. Two examples are: the fitting of two-dimensional Gaussians to the distributions, and the use the moment analysis method to determine the distributions' first and second moments, equivalent to the means and variances, respectively, for Gaussian distributions. Both methods yield similar results for distributions that are characterized by Gaussian shapes [MAR91].

As mentioned in Section II.D.1 the moment analysis technique described in that section was used to determine the N and Z centroids, the N/Z ratio, the variances, σ_Z^2 and σ_N^2, and the correlation factor ρ_{NZ} for the PLF neutron and charge distributions, for consecutive bins of total kinetic energy loss (TKEL). Bins of 10 MeV were used for TKEL values smaller than 100 MeV. For TKEL values between 100 MeV and 240 MeV, 20 MeV energy loss bins were used. Above a TKEL value of 240 MeV, where the number of events is too low, bins of 40 MeV of energy loss were applied. The error bars on the experimental data shown in these plots were calculated by the method of statistical error propagation in the formulas of the first and second moments of the distributions. They are larger than the equivalent Gaussian error bars commonly used because in addition to statistical errors, they include the uncertainty due to the method employed in the moments determination. The errors quoted when using Gaussian fits usually measure only the goodness of the fit. The results obtained for the centroids and variances are summarized in Tables A.1 and A.2, and in Figures III.2 and III.3.

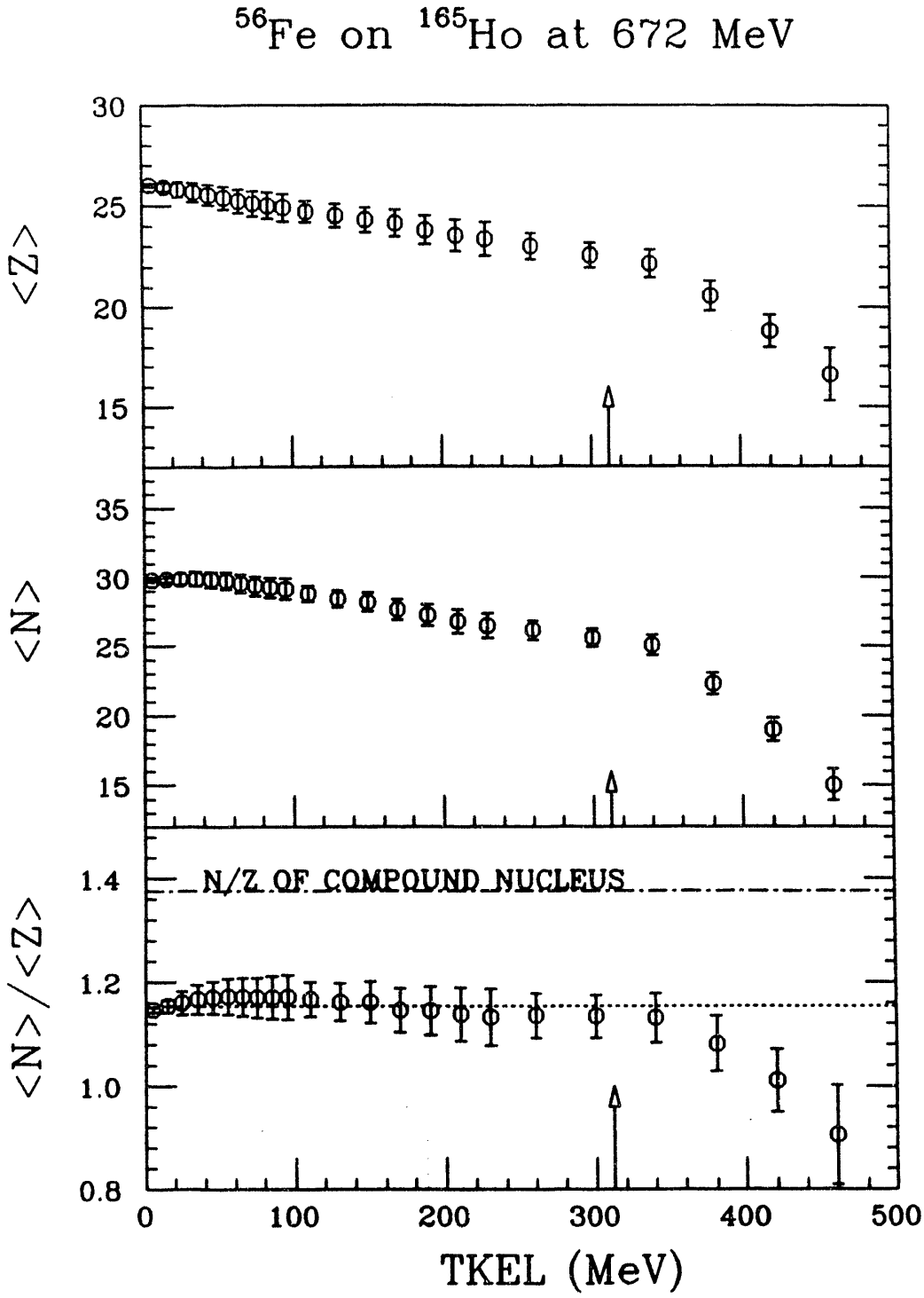

Figure III.2 The N and Z centroids and the N/Z ratio as a function of TKEL for the 672-MeV ^{56}Fe on ^{165}Ho reaction. The TKEL scale is corrected for evaporation effects assuming an equipartition of the excitation energy between the reaction fragments. The dotted line indicates the N/Z ratio of the projectile. The arrow indicates the limit imposed by the entrance channel Coulomb barrier.

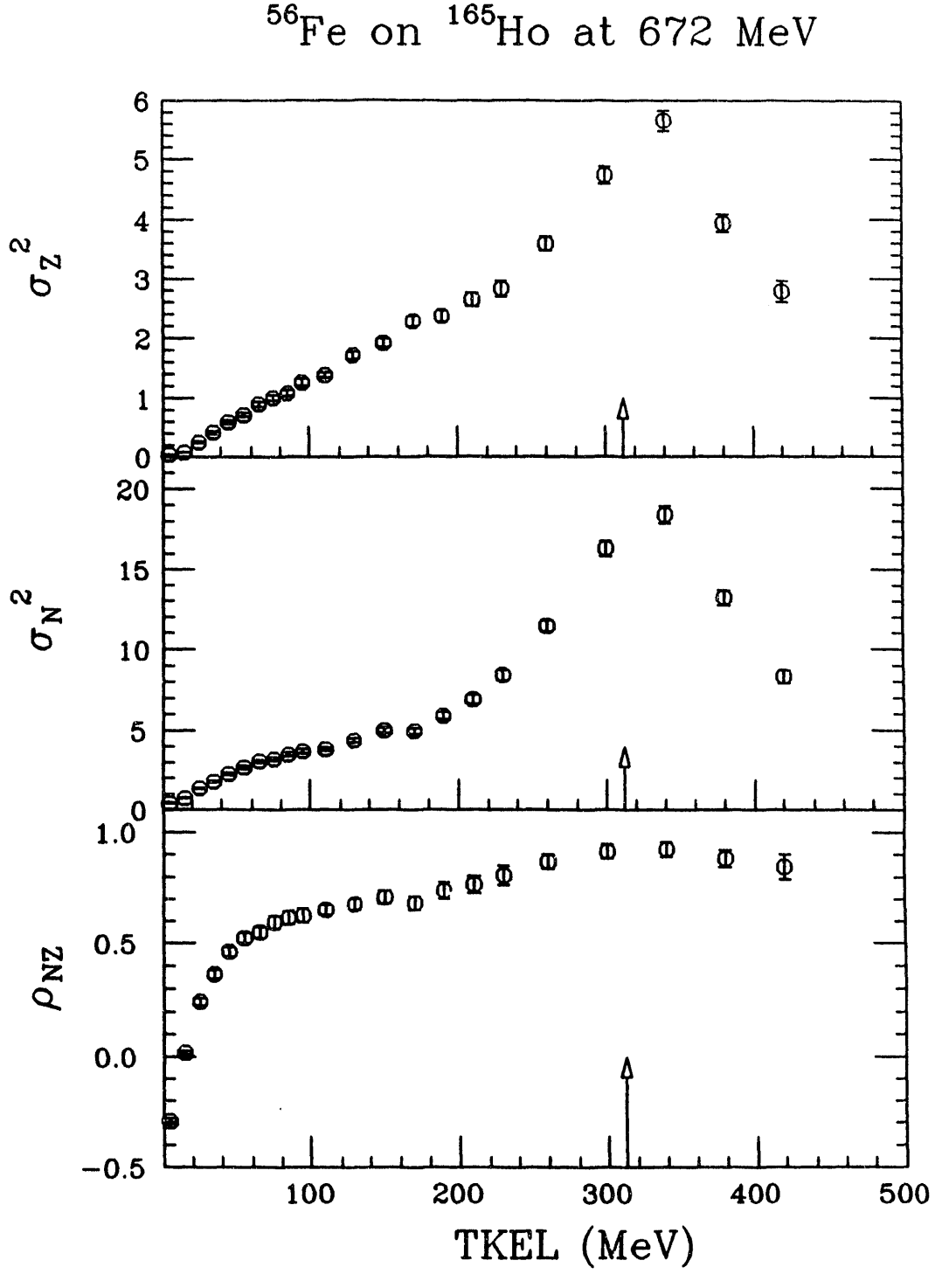

Figure III.3 The charge and neutron variances and the correlation factor as a function of TKEL for the 672-MeV ^{56}Fe on ^{165}Ho reaction. The TKEL scale is corrected for evaporation effects assuming an equipartition of the excitation energy between the reaction fragments. The arrows indicates the entrance channel Coulomb barrier.

As shown in Figure III.2, the Z centroids decrease steadily with increasing energy loss. The N centroids remain nearly constant for the first 100 MeV of energy damping, then decrease gradually with increasing TKEL. A steeper slope is observed for TKEL values above 300 MeV for both <N> and <Z>. The N/Z ratio remains constant, within the error bar, and equal to the N/Z ratio of the projectile for most of the TKEL range. A decrease in N/Z is observed above 300 MeV of TKEL.

The variances σ_Z^2 and σ_N^2 and the correlation factor ρ_{NZ} are plotted as a function of TKEL in Figure III.3. Both variances increase with increasing TKEL. They reach a maximum value at about 300 MeV of energy loss, which is the same region where the slope of the centroids and the <N>/<Z> ratio changes, then start decreasing. The neutron variance values are higher than those of the proton variance for the whole range of energy loss. The correlation factor ρ_{NZ} raises rapidly from -0.3 at 5 MeV of TKEL to about 0.65 at 100 MeV of TKEL. Above 100 MeV, ρ_{NZ} increases less rapidly with increasing TKEL and reaches values close to 1, which indicates total correlation between N and Z. In Figures III.2 and III.3, the total kinetic energy loss scale has been corrected for evaporation using the assumption of equal partition of the excitation energy between the two primary fragments, as outlined in Section II.B.1.

The results obtained for the centroids and variances when the total kinetic energy loss scale is corrected for evaporation with the assumption that the two primary fragments are in thermal equilibrium are summarized in Tables A.3 and A.4, respectively. Comparisons between the results obtained with the two assumptions for the division of the excitation energy are shown in Figures III.4 and III.5. The centroids <N> and <Z>, the N/Z ratio, the variances σ_Z^2 and σ_N^2, and the correlation factor ρ_{NZ} are plotted versus TKEL. The circles and squares refer to the equal division and thermal equilibrium assumptions, respectively. Only a slight difference

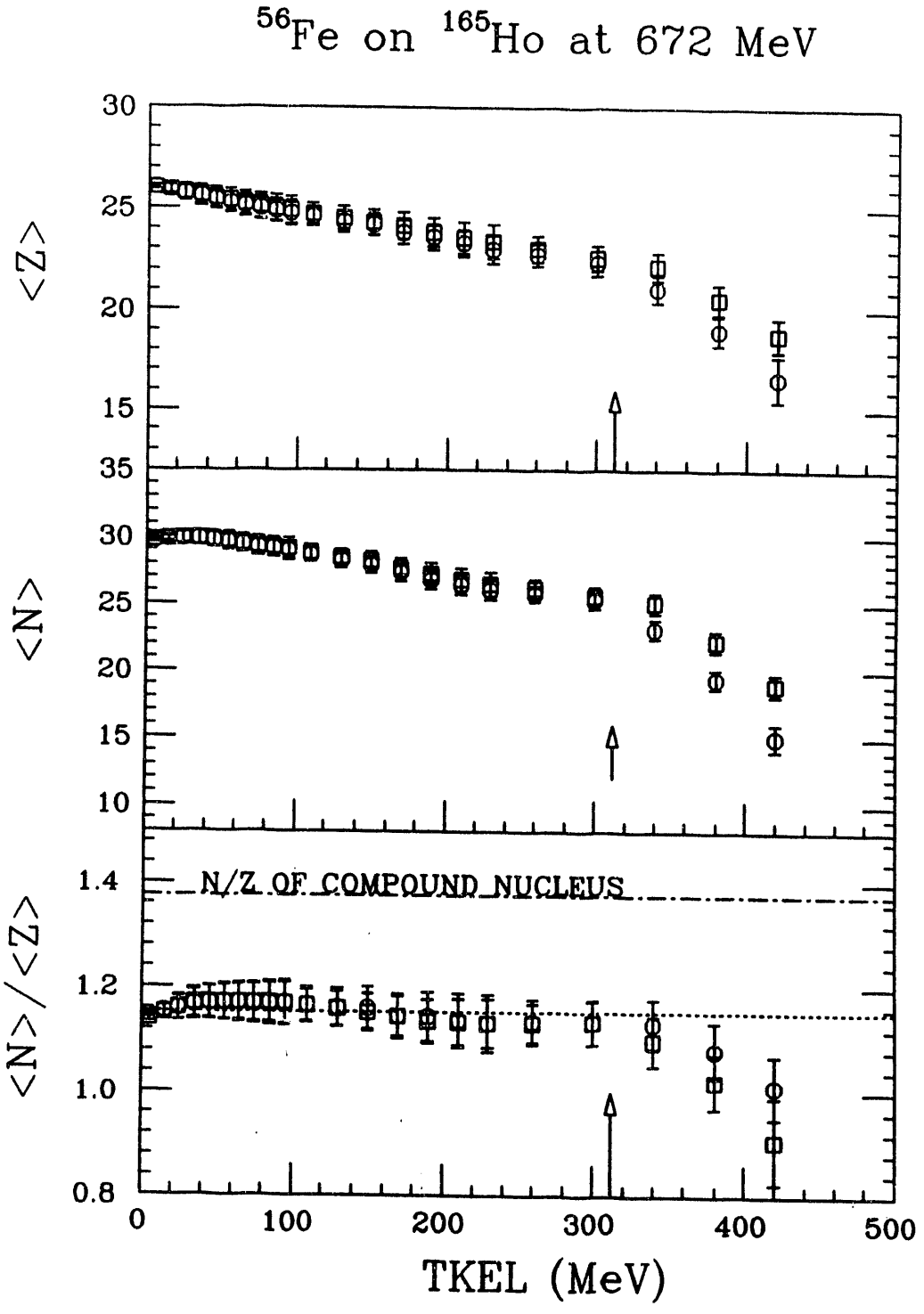

Figure III.4 Comparison between the N and Z centroids and the N/Z ratios obtained for the 672-MeV ^{56}Fe on ^{165}Ho reaction, with the two different corrections to the TKEL scale. The circles refer to the equipartition of the excitation energy, and the squares refer to the thermal equilibrium limit. The arrows indicates the entrance channel Coulomb barrier.

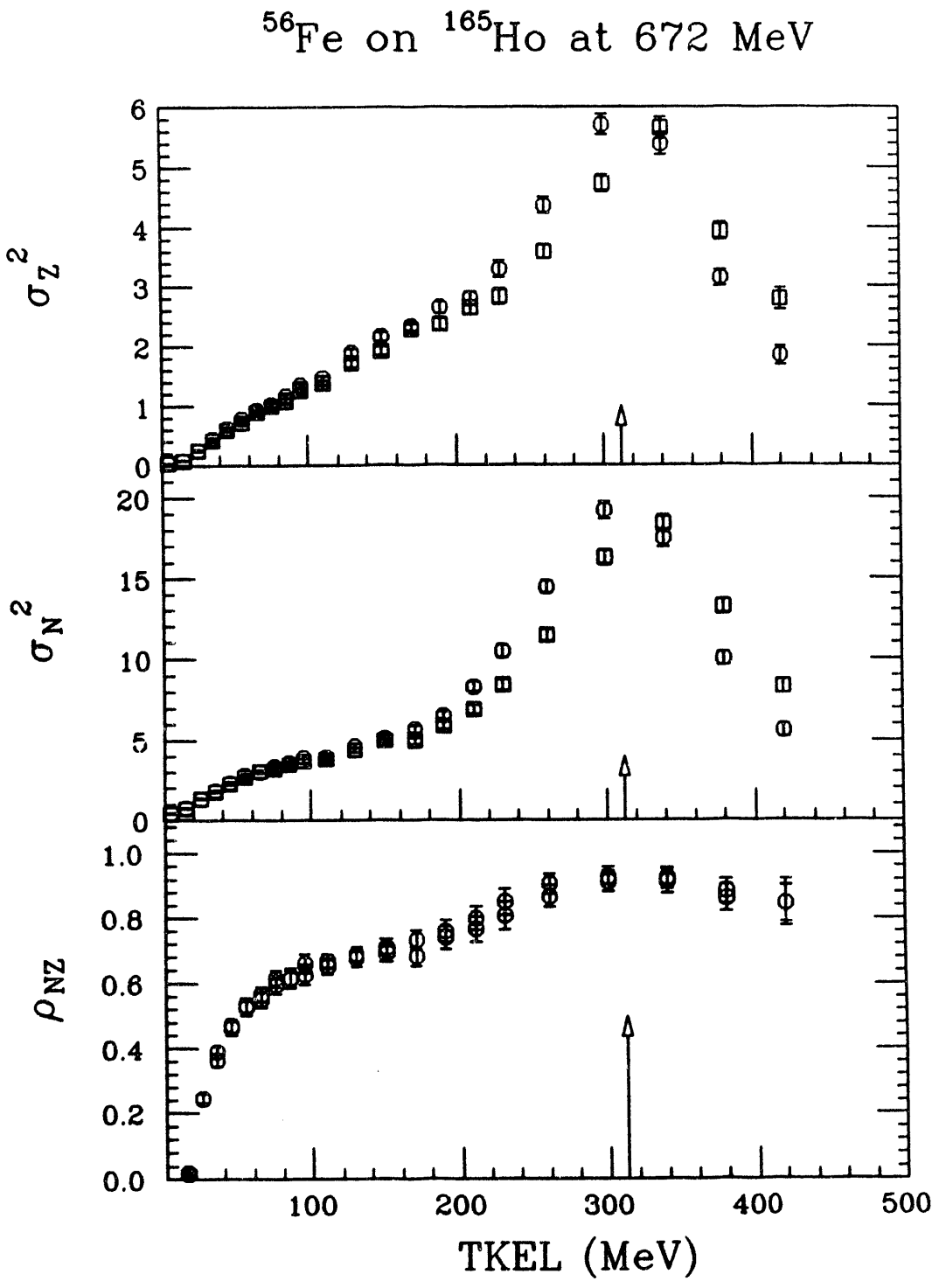

Figure III.5 Comparison between the neutron and proton variances and the correlation factor obtained for the 672-MeV ^{56}Fe on ^{165}Ho reaction with the two different corrections to the TKEL scale. The circles refer to the equipartition of the excitation energy, and the squares refer to the thermal equilibrium limit. The arrows indicates the entrance channel Coulomb barrier.

between the two cases is observed for the centroids and the variances at TKEL values higher than 360 MeV, where the centroids and widths obtained with the thermal equilibrium assumption are slightly higher. Evaporation corrections of the energy loss scale do not seem to cause a noticeable effect on the behavior of the distributions with TKEL, especially in the range of energy damping below the entrance channel Coulomb barrier (312 MeV).

The mass of the primary PLF, A'_{PLF}, was evaluated by adding the amount of evaporated mass computed with PACE II to the measured post-evaporation PLF mass. Charge evaporation was assumed to be negligible, based on studies which showed that most of the contribution to the evaporated mass is from neutrons [BRE83a, BRE83b, HIL79]. This assumption is confirmed in the present study by the determination of primary charge and neutron number distributions with a kinematic reconstruction method combined with evaporation calculations using the PACE II code as will be shown in Chapter V. The two extremes of equal excitation energy division and thermal equilibrium were again considered. A primary PLF neutron number N'_{PLF} was determined by subtracting the measured PLF charge from the calculated primary mass. The primary N centroids and variances obtained with both assumptions are summarized in Table A.5 and the N'_{PLF} centroids are displayed in Figure III.6. The $\langle N'_{PLF} \rangle$ values of the equal excitation energy division case increase from N of the projectile (30) at 0 TKEL to about 36 at the highest TKEL, while in the thermal equilibrium case $\langle N'_{PLF} \rangle$ remains nearly constant and equal to the N of the projectile.

III.B Excitation Energy Division

The excitation energy stored in the PLF was determined using the kinematic

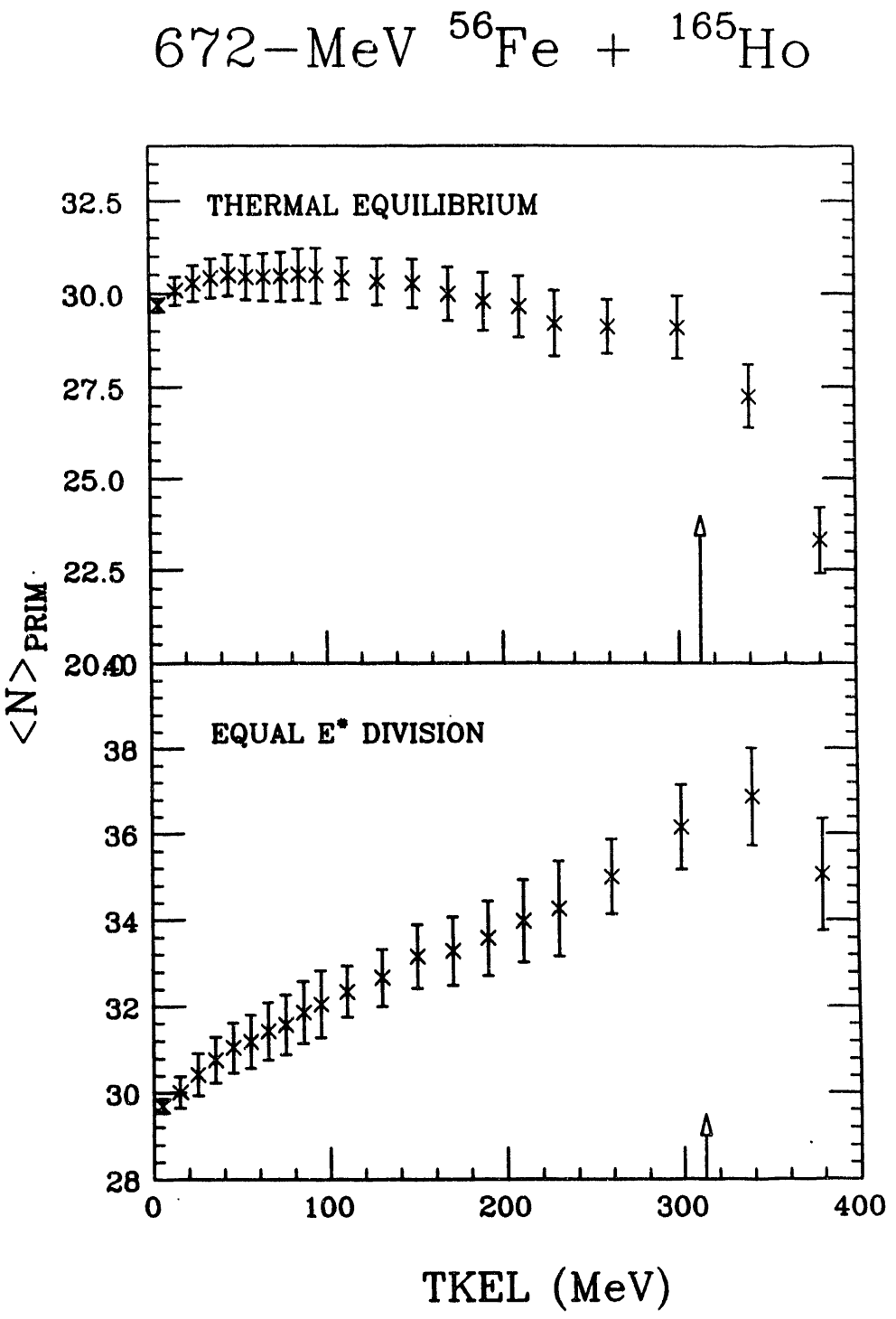

Figure III.6 The neutron number of the primary PLF's obtained for the 672-MeV ^{56}Fe on ^{165}Ho reaction by applying neutron evaporation corrections to the measured distributions, with the assumptions of equipartition of the excitation energy and thermal equilibrium. The arrows indicate the limit imposed by the entrance channel Coulomb barrier.

reconstruction technique, along with results from PACE II evaporation code, as described in Section II.D.3. A contour plot of the excitation energy of the PLF versus total kinetic energy loss is displayed in Figure III.7. The limits of zero TLF excitation energy, equal sharing of the excitation energy by the PLF and the TLF, and thermal equilibrium, are indicated by the dotted, dashed and solid lines, respectively. Most of the events are in the region comprised by the 0 TLF excitation energy limit and the thermal equilibrium limit. The PLF excitation energy ratio E^*_{PLF}/E^*_{TOT} is plotted against TKEL in Figure III.8. The values of the E^*_{PLF}/E^*_{TOT} ratio are between 0% and 100% for most of the events. Slit scattering and events with negative evaporated mass have been eliminated. The limits where all the excitation energy is in the PLF, the equal sharing of the excitation energy and the thermal equilibrium limits are again indicated by the dotted, dashed, and solid lines, respectively. The high yield shown at TKEL values around 0 MeV is due to contributions from elastic scattering that were not completely eliminated by excluding events with negative values of evaporated mass.

The spectra obtained have approximately Gaussian shapes, as shown in the samples displayed in Figures III.9 and III.10 for E^*_{PLF} and E^*_{PLF}/E^*_{TOT}, respectively. Gaussian fits were performed on the E^*_{PLF} and the E^*_{PLF}/E^*_{TOT} distributions to extract their centroids and widths as a function of energy loss. The energy loss scale was divided into bins of 20 MeV. Histograms of counts versus E^*_{PLF}, and counts versus E^*_{PLF}/E^*_{TOT} were generated for each TKEL bin. Bins of 40 MeV were used in some cases for TKEL values above 250 MeV when the number of events was too low for a reliable centroid determination by Gaussian fit.
It is also possible to use a one- dimensional moment analysis approach. In this case it is important to make sure to exclude any long tails from the calculation. Both methods gave similar results for well defined peaks, while it was better to use

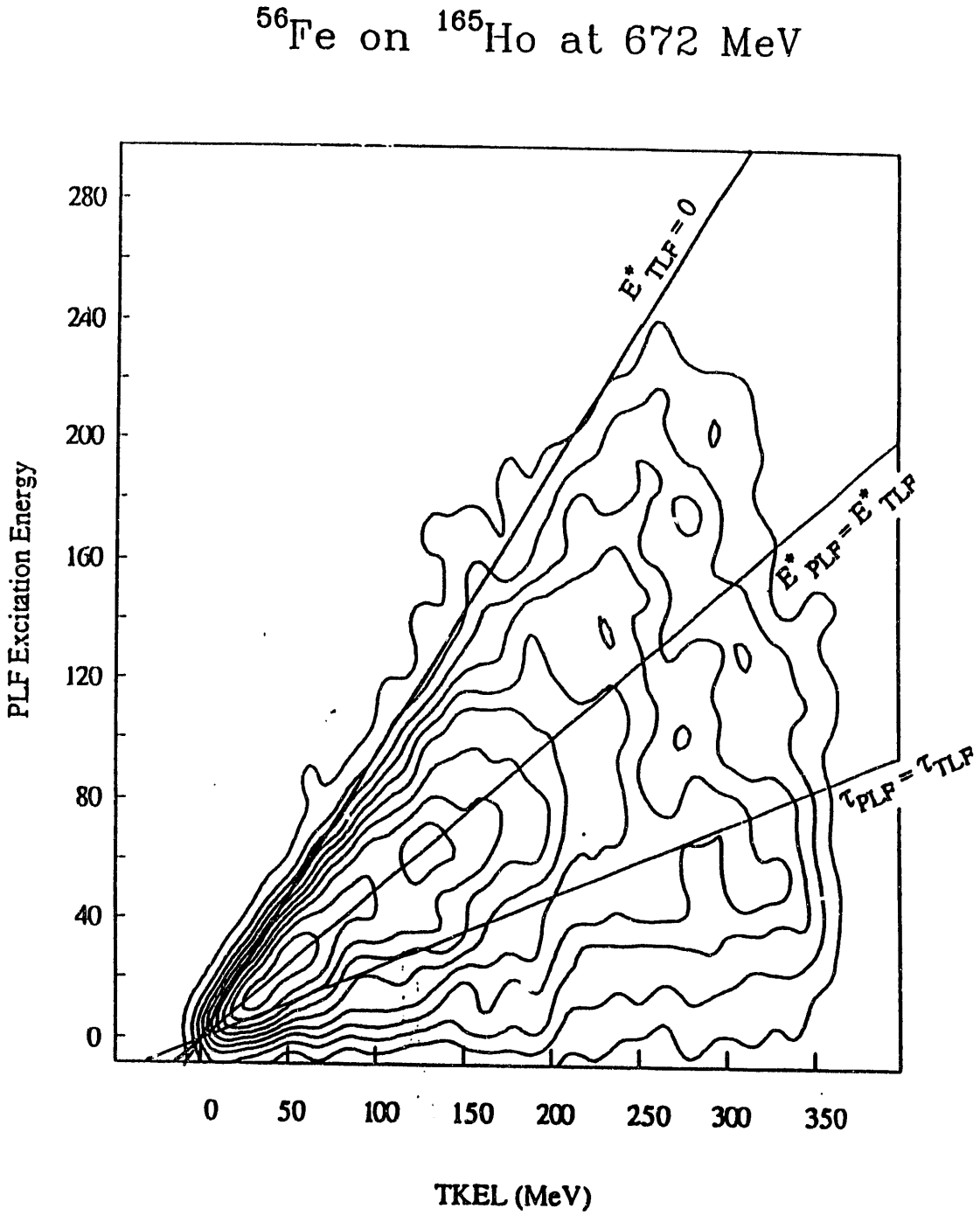

Figure III.7 Contour plot of the PLF excitation energy as a function of TKEL for the 672-MeV ^{56}Fe on ^{165}Ho reaction. The limits of non-excited TLF, equipartition of the excitation energy, and thermal equilibrium are indicated by the straight lines.

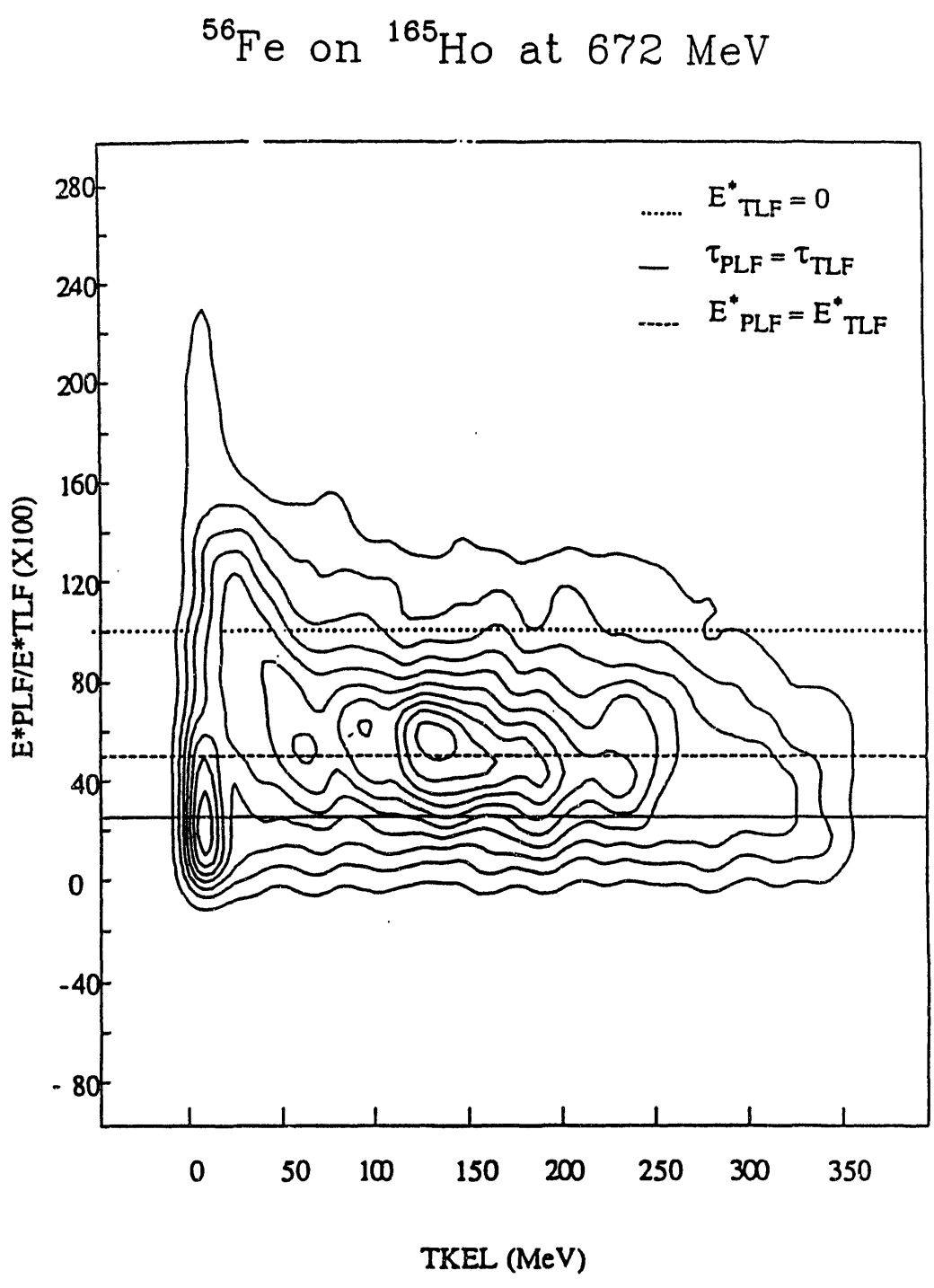

Figure III.8 Contour plot of the E^*_{PLF}/E^*_{TOT} ratio as a function of TKEL for the 672-MeV ^{56}Fe on ^{165}Ho reaction. The limits of non-excited TLF, equipartition of the excitation energy, and thermal equilibrium are indicated by the dotted, dashed, and solid lines, respectiveley.

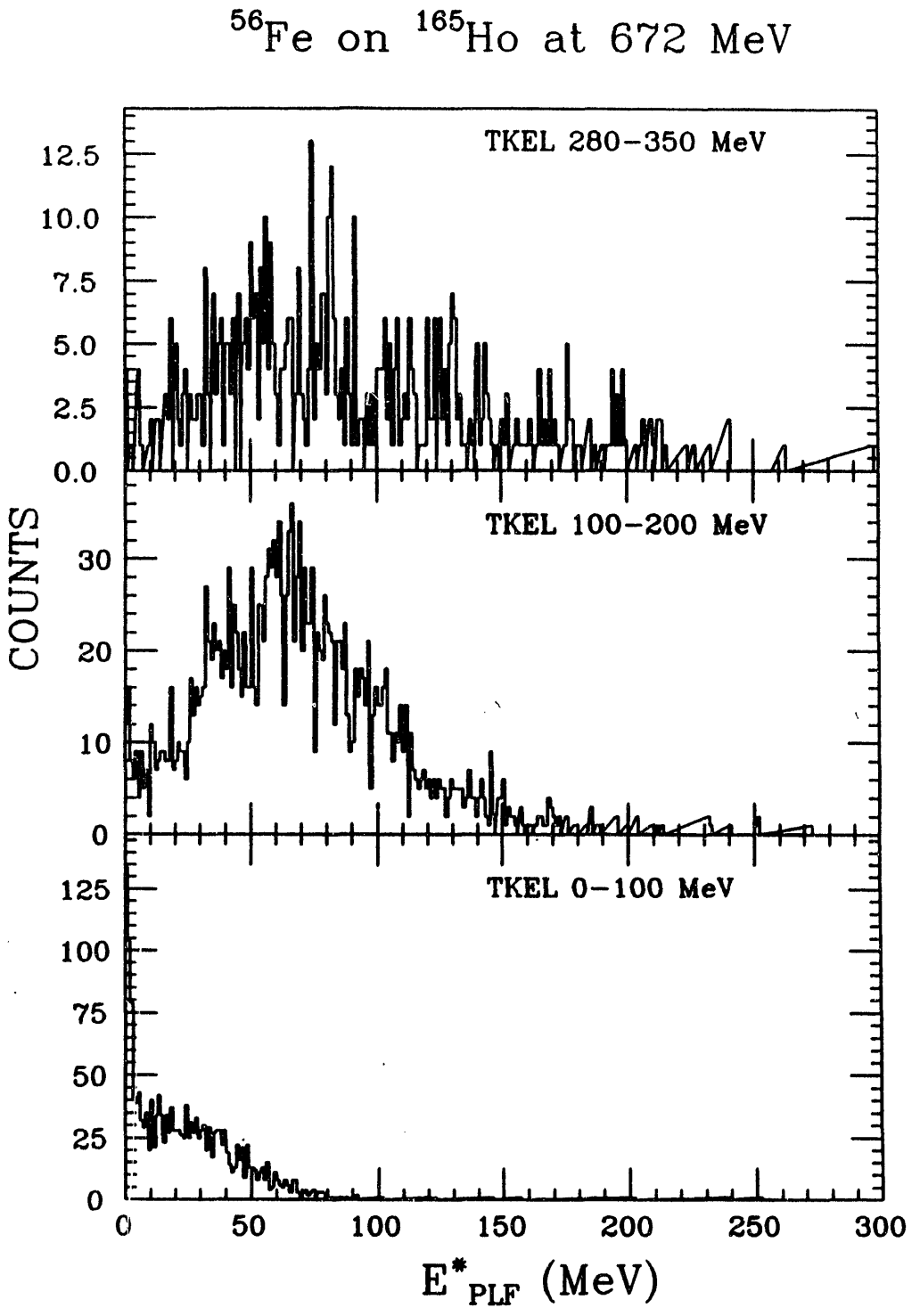

Figure III.9 Histograms of the PLF excitation energy for three representative gates of energy loss, for the 672-MeV ^{56}Fe on ^{165}Ho reaction.

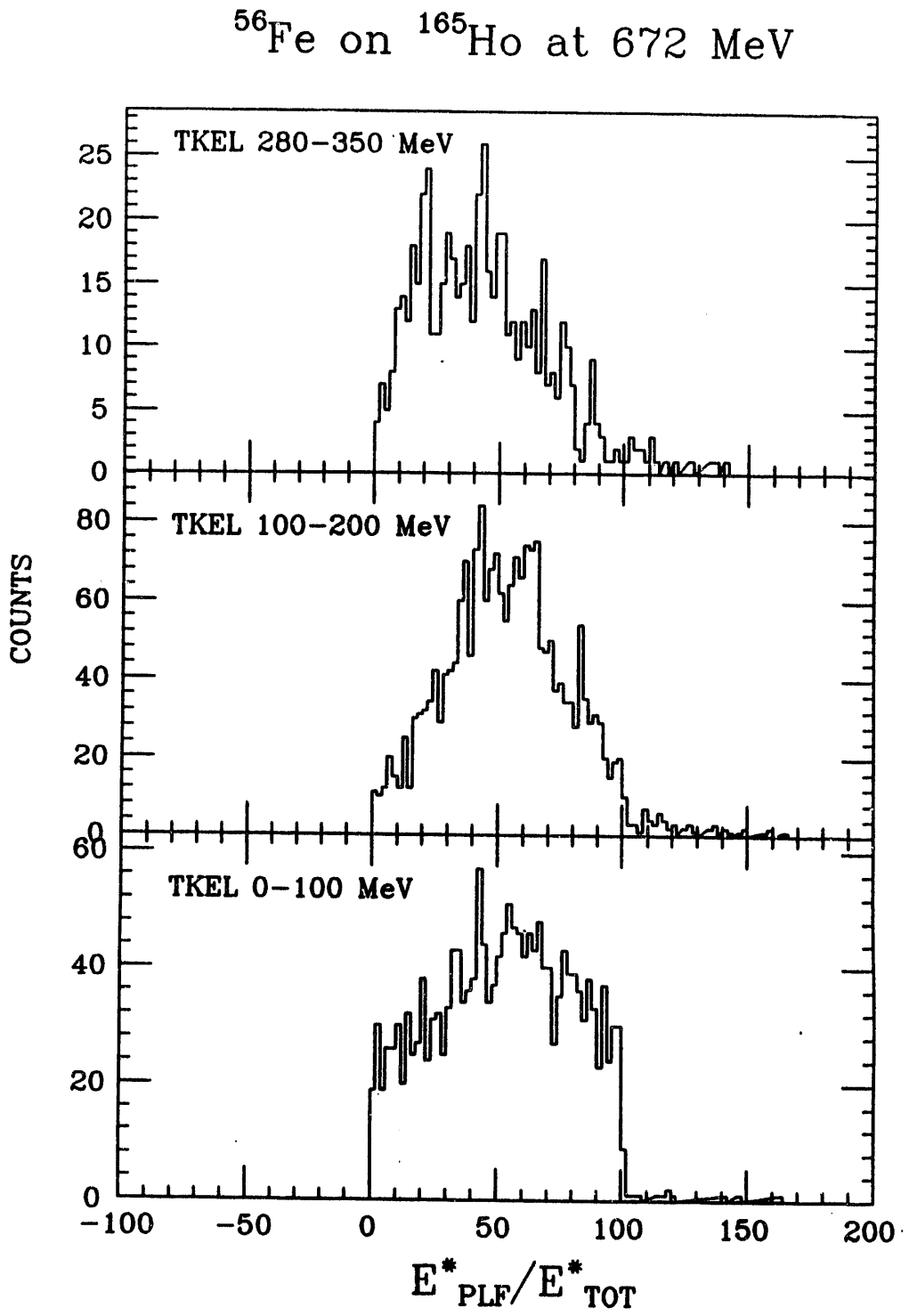

Figure III.10 Histograms of the PLF excitation energy ratio (E^*_{PLF}/E^*_{TOT}) for three representative gates of energy loss, for the 672-MeV ^{56}Fe on ^{165}Ho reaction.

Gaussian fits for cases of low counts. Therefore, the Gaussian fit method was opted for in the present analysis. The E^*_{PLF} and the E^*_{PLF}/E^*_{TOT} centroids for inclusive values of primary PLF mass, as a function of energy loss, are summarized in Tables A.6 and A.7, respectively. Because of the low statistics, it was not possible to obtain reliable values for the E^*_{PLF} and the E^*_{PLF}/E^*_{TOT} widths, therefore these are not studied in the present data analysis. The PLF excitation energy E^*_{PLF} increases almost linearly with increasing energy loss, as shown in Figure III.11. It reaches a maximum value of about 93 MeV at 260 MeV of TKEL, then starts decreasing. However,this apparent lowering of E^*_{PLF} could be attributed to a less accurate determination of the E^*_{PLF} centroids at the high values of TKEL, where only very few events occur as reflected by the increased error bars.

The average mass evaporated from the PLF, $<\Delta A>$, was also determined with one-dimensional Gaussian fits, as a function of energy loss. The values of the ΔA centroids as a function of TKEL are summarized in Table A.8, and displayed in Figure III.12. The behavior of ΔA with energy damping is similar to that of the PLF excitation energy. The average evaporated mass reaches a maximum value close to 12 mass units at 250 MeV of TKEL. It then starts decreasing slightly, perhaps for the same reasons mentioned for the case of E^*_{PLF}.

The evolution of the E^*_{PLF}/E^*_{TOT} centroids with TKEL is shown in Figure III.13. The ratios corresponding to the equal excitation energy division and the thermal equilibrium limits are indicated by the solid and dashed lines, respectively. The E^*_{PLF}/E^*_{TOT} ratios exceed the equal energy division limit for TKEL values below about 120 MeV and remain nearly constant and equal to 50% for TKEL values between approximately 120 MeV and 260 MeV. A sharp decrease of E^*_{PLF}/E^*_{TOT} is observed above 260 MeV of TKEL. However, thermal equilibrium is never reached.

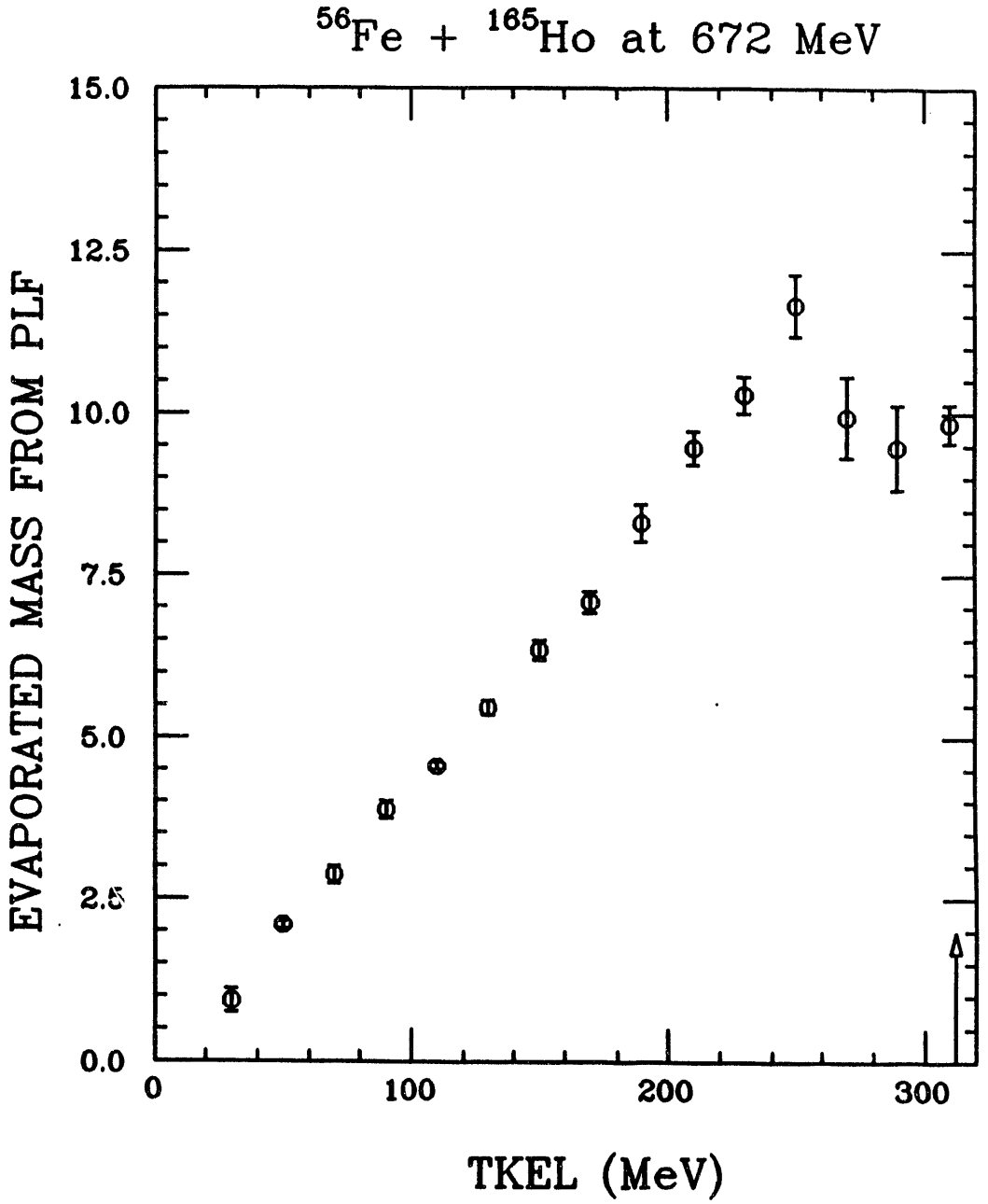

Figure III.11 Centroids of the average mass evaporated from the PLF as a function of TKEL, for the 672-MeV ^{56}Fe on ^{165}Ho reaction.

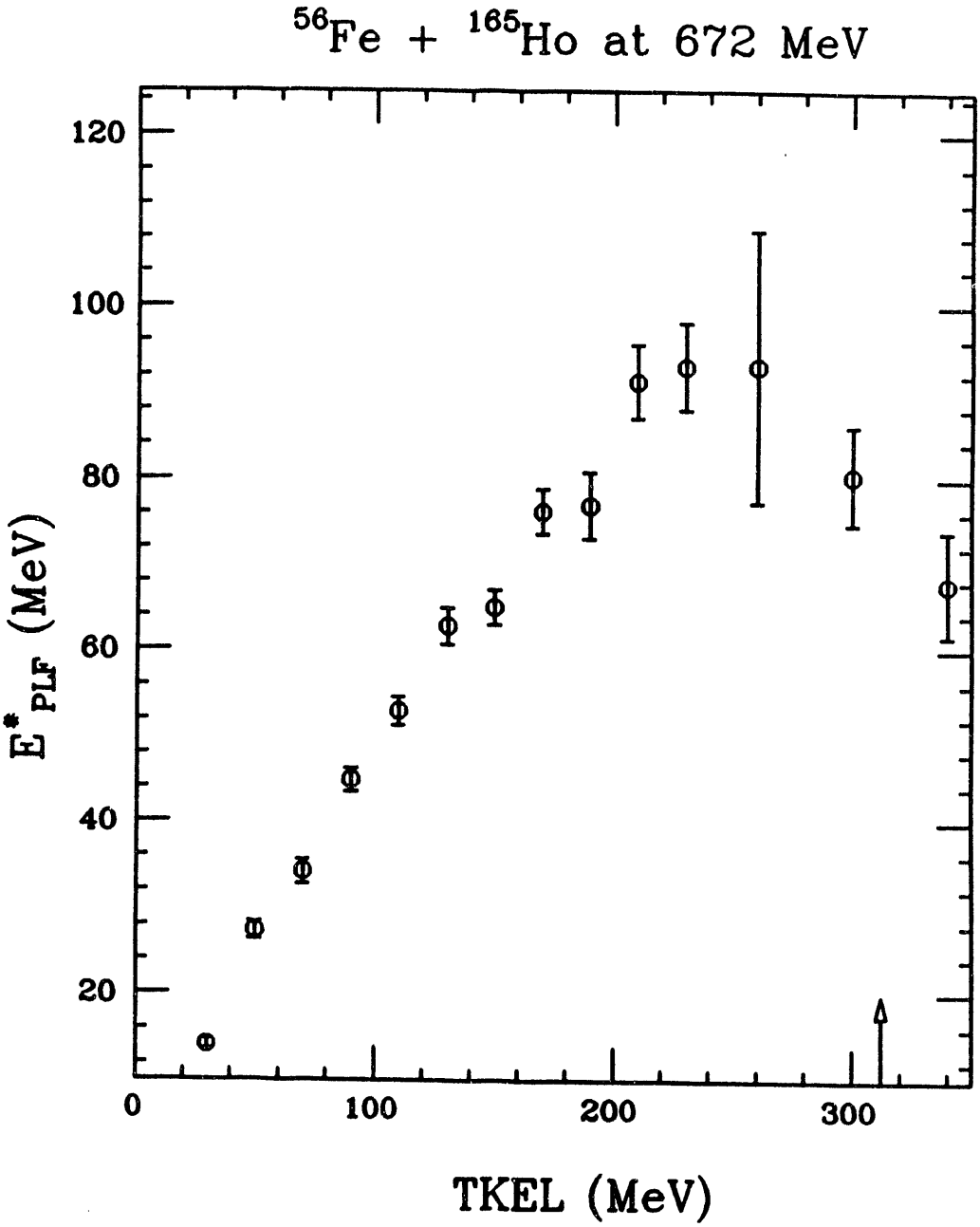

Figure III.12 Centroids of the excitation energy of the PLF as a function of TKEL, for the 672-MeV ^{56}Fe on ^{165}Ho reaction.

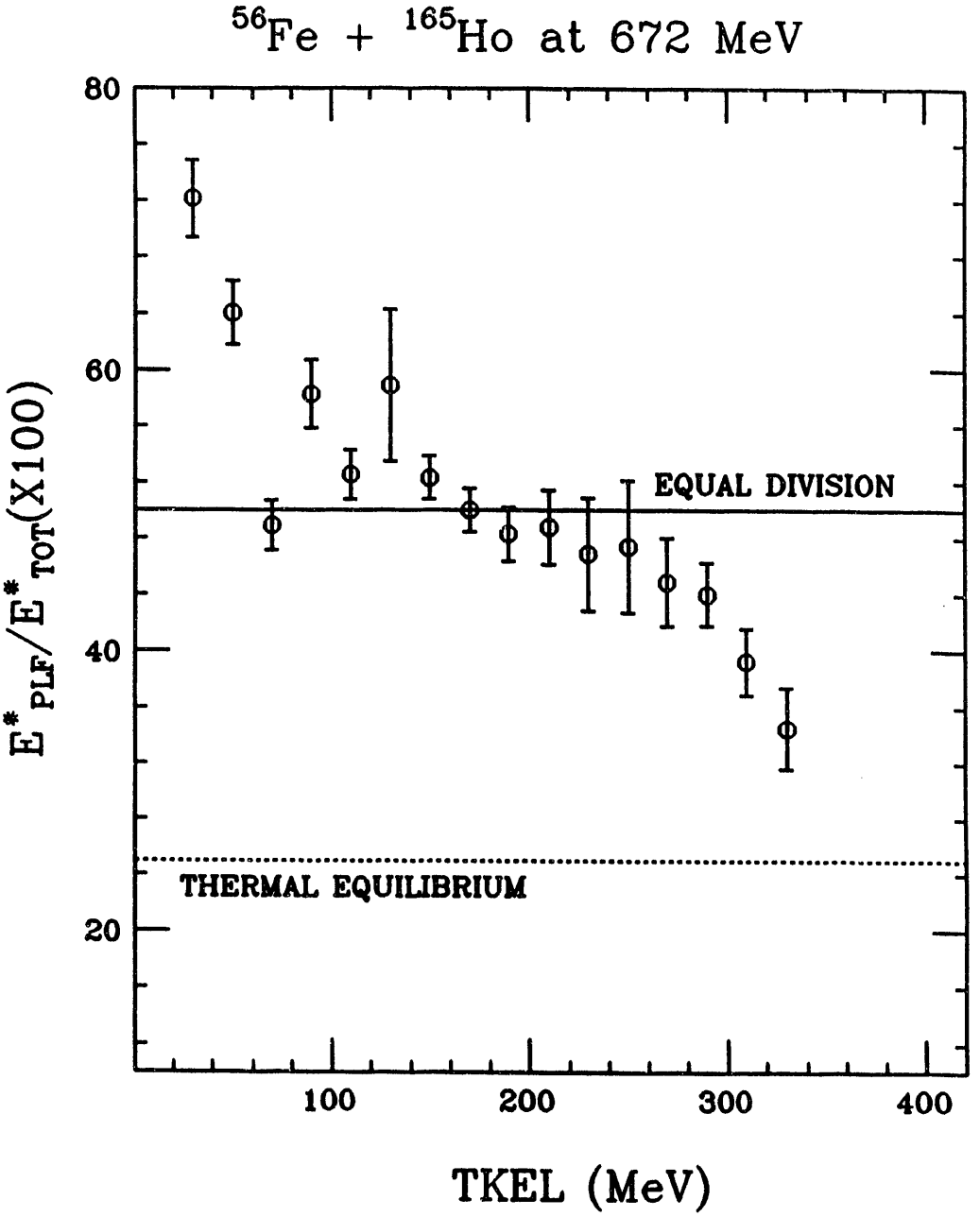

Figure III.13 Centroids of the PLF excitation energy ratio (E^*_{PLF}/E^*_{TOT}) as a function of TKEL for inclusive events for the 672-MeV ^{56}Fe on ^{165}Ho reaction. Elastic and slit-scattering events are gated out.

A closer examination of the excitation energy division is shown in Figure III.14, where the E^*_{PLF}/E^*_{TOT} centroids are plotted versus TKEL for selective bins of primary (pre-evaporation) PLF mass, A'_{PLF}. The data of Figure III.14 are summarized in Table A.9. Figure III.14 shows that the contribution to the low E^*_{PLF}/E^*_{TOT} ratios at low TKEL is mostly due to events with primary masses lower than the mass of the projectile (56). For primary masses higher than 56, the values of the PLF excitation energy ratio are in the 50 % to 70 % range at all values of TKEL. This result suggests a correlation between the excitation energy sharing and the reaction exit channel. Therefore, to investigate this correlation, the E^*_{PLF}/E^*_{TOT} ratio is determined as a function of the mass of the primary PLF, A'_{PLF}.

Since the mass of the secondary PLF, A''_{PLF}, is evaluated more accurately than A'_{PLF}, the E^*_{PLF}/E^*_{TOT} ratio is also plotted versus A''_{PLF}. To obtain the E^*_{PLF}/E^*_{TOT} ratio as a function of A'_{PLF} and A''_{PLF}, the spectra of E^*_{PLF}/E^*_{TOT} ratio were generated for consecutive bins of A'_{PLF} and A''_{PLF}, and their centroids determined by Gaussian fits. The results are summarized in Table A.10 and Figure III.15 for E^*_{PLF}/E^*_{TOT} versus A'_{PLF}, and in Table A.11 and Figure III.16 for E^*_{PLF}/E^*_{TOT} versus A''_{PLF}. Since inclusive values of TKEL are considered in the results of Tables A.10 and 11, the E^*_{PLF}/E^*_{TOT} centroids contain a dependence on TKEL. The noticeably different behavior of E^*_{PLF}/E^*_{TOT} versus A'_{PLF} and A''_{PLF} will be discussed further in Chapter V.

The dotted line in Figures III.15 and III.16 describes how the excitation energy would be divided if the fragments were in thermal equilibrium. It is determined as a function of the fragment mass (A'_{PLF} or A''_{PLF}). The excitation energy of a projectile-like fragment (or any excited nucleus) can be written in terms of its mass and nuclear temperature τ as

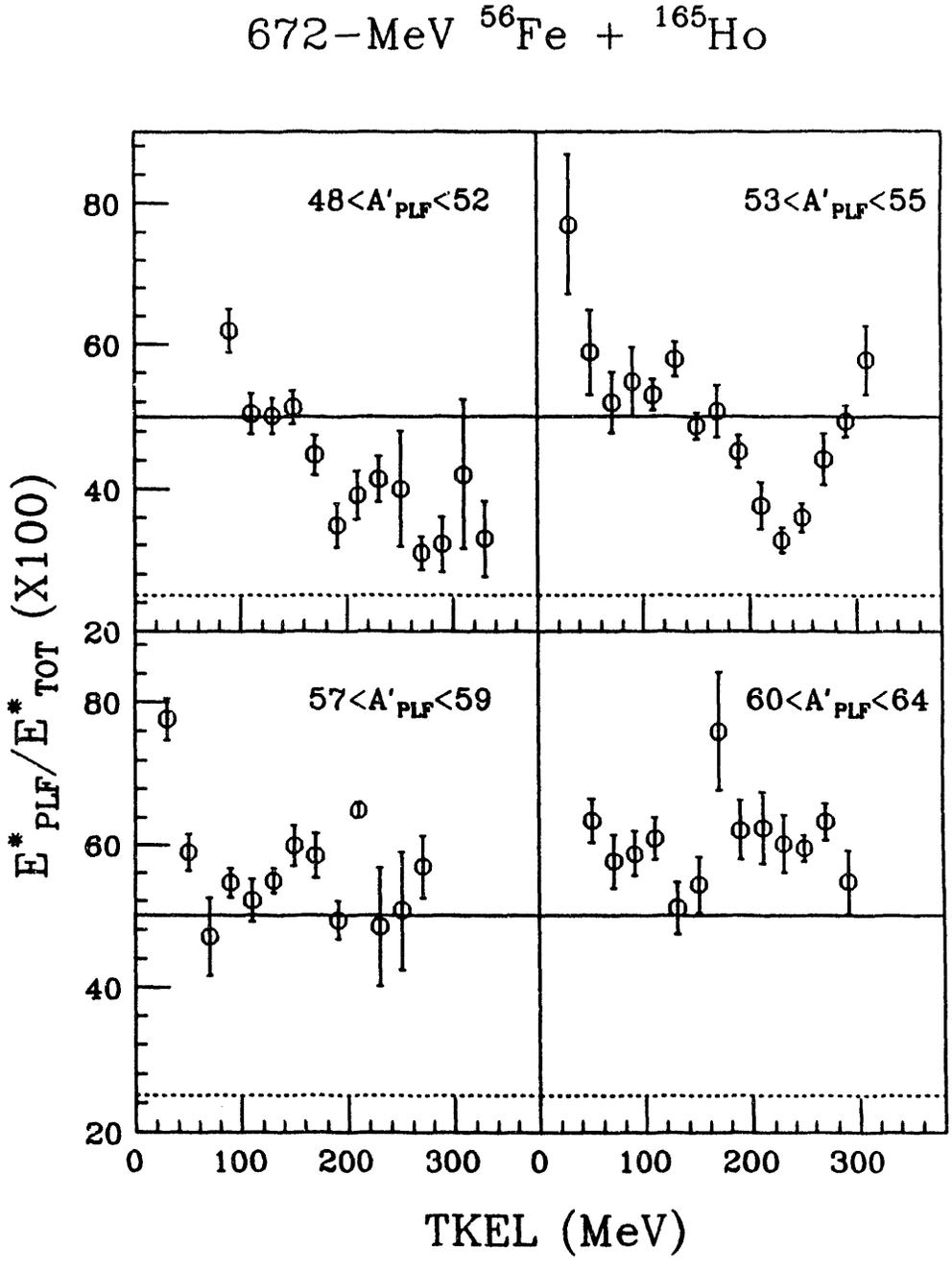

Figure III.14 Centroids of the PLF excitation energy ratio (E^*_{PLF}/E^*_{TOT}) as a function of TKEL for four gates on the mass of the primary PLF, for the 672-MeV ^{56}Fe on ^{165}Ho reaction. The limits of equipartition of the excitation energy and thermal equilibrium are indicated by the solid and dotted lines, respectiveley.

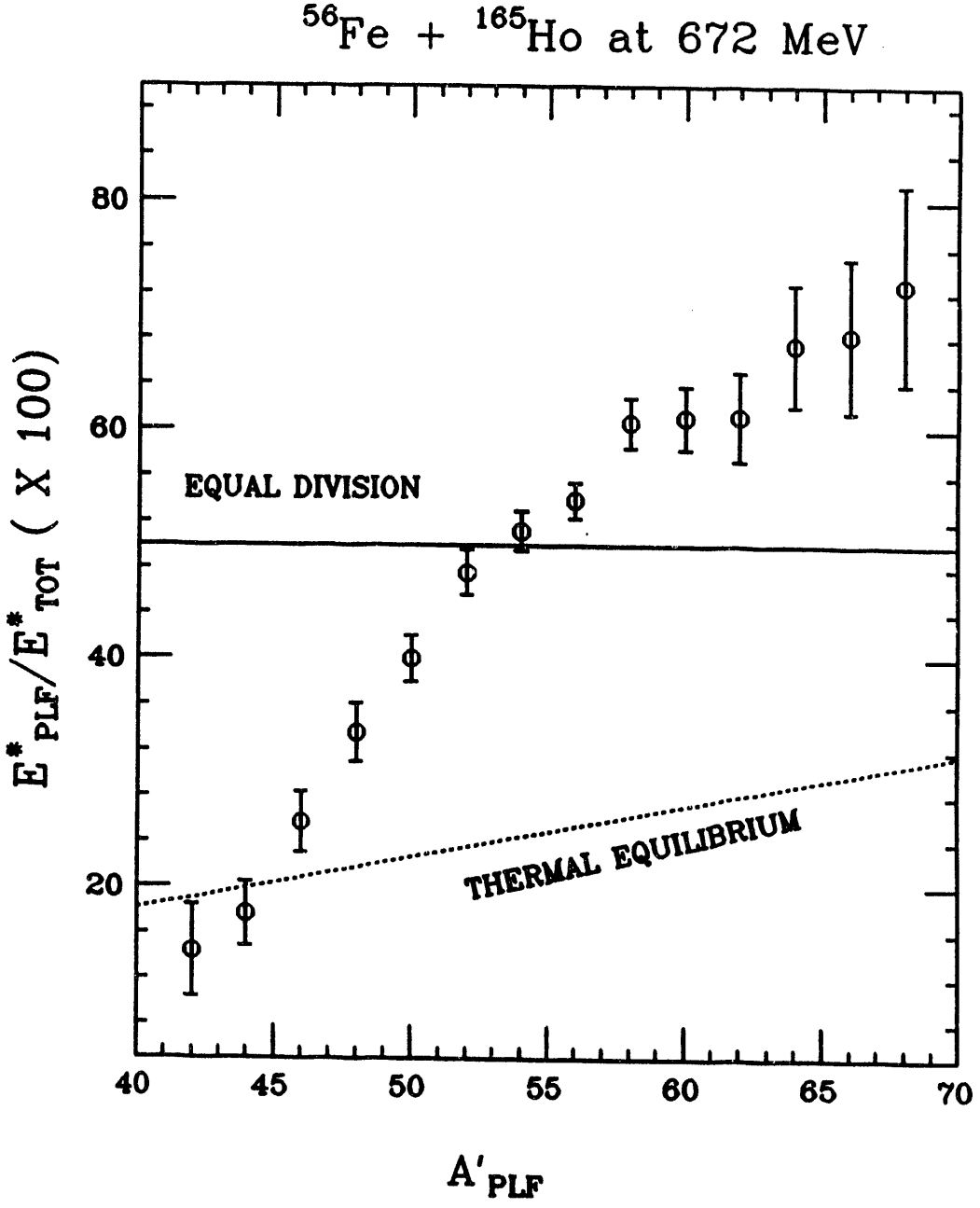

Figure III.15 Centroids of the PLF excitation energy ratio (E^*_{PLF}/E^*_{TOT}) as a function of the mass of the primary PLF (A'_{PLF}) for inclusive events, for the 672-MeV ^{56}Fe on ^{165}Ho reaction Elastic and slit-scattering events are gated out. The limits of equipartition of the excitation energy and thermal equilibrium are indicated by the solid and dotted lines, respectiveley.

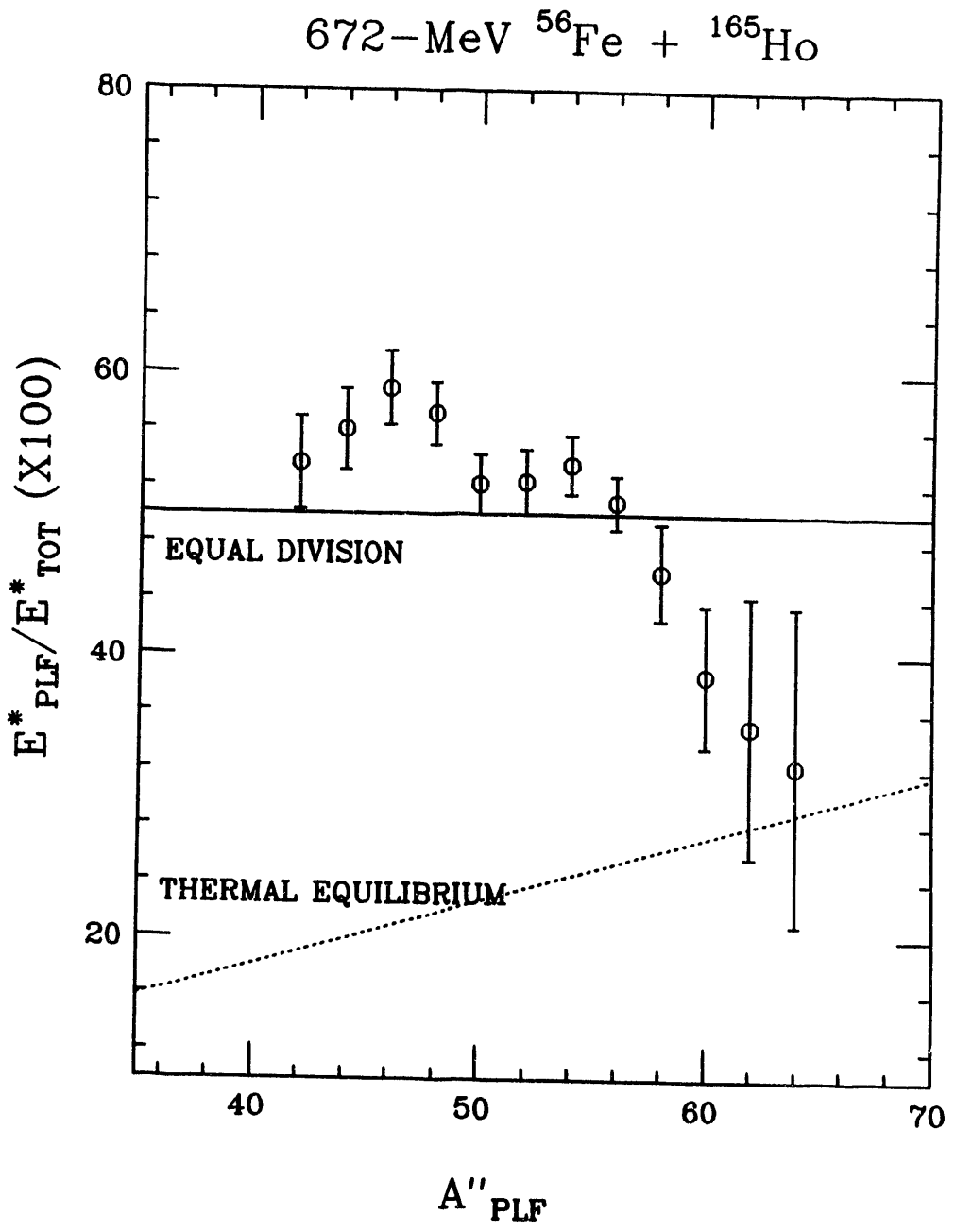

Figure III.16 Centroids of the PLF excitation energy ratio (E^*_{PLF}/E^*_{TOT}) as a function of the mass of the secondary PLF (A''_{PLF})for inclusive events, for the 672-MeV ^{56}Fe on ^{165}Ho reaction Elastic and slit-scattering events are gated out. The limits of equipartition of the excitation energy and thermal equilibrium are indicated by the solid and dotted lines, respectiveley.

$$E^*_{PLF} = a_{PLF}\,\tau^2_{PLF} \qquad \text{(III.1)}$$

where a_{PLF} is the level density parameter, assumed to be proportional to the PLF mass. Equation III.1 is also valid for the target-like fragment. Therefore, when the two fragments have equal temperatures, the total excitation energy of the system is expressed as

$$E^*_{TOT} = E^*_{PLF} + E^*_{TLF} = (a_{PLF} + a_{TLF})\tau^2. \qquad \text{(III.2)}$$

The ratio of the PLF excitation energy to the total excitation energy as a function of the PLF mass can thus be derived from equation III.2, and expressed as

$$E^*_{PLF}/E^*_{TOT} = A'_{PLF}/A_{TOT}. \qquad \text{(III.3)}$$

For the ^{56}Fe on ^{165}Ho system,

$$E^*_{PLF}/E^*_{TOT}\ X\ 100 = 0.452\ A'_{PLF}. \qquad \text{(III.4)}$$

The thermal equilibrium limit determined in this fashion is more accurate than the constant value of 25 % used in Figures III.13 and III.14. In those cases it was necessary to assume a constant value for A'_{PLF}. As a default the mass of the projectile was used.

An evolution of the system from thermal equilibrium at low values of A'_{PLF} towards E^*_{PLF}/E^*_{TOT} values even higher than the equipartition of the excitation energy limit with increasing A'_{PLF} is observed in Figure III.15. In contrast, when plotted against the secondary PLF mass (A''_{PLF}), the E^*_{PLF}/E^*_{TOT} ratio indicates

that the excitation energy is shared nearly equally by the two fragments for A''_{PLF} values lower than 56. Above A''_{PLF} of 56, the E^*_{PLF}/E^*_{TOT} ratio decreases towards values approaching thermal equilibrium. However, it is important to remember that the secondary mass gives a picture of the system after deexcitation. The PLF excitation energy ratios versus A'_{PLF} and A''_{PLF} for different bins of energy loss are shown in Figures III.17 and 18, respectively. These results are also summarized in Tables A.12 and A.13 respectively. A slight dependence of the E^*_{PLF}/E^*_{TOT} ratio on A'_{PLF} is observed in Figure III.17 for the three selected bins of TKEL. A different scenario is observed when the PLF excitation energy ratio is plotted as a function of A''_{PLF}, as shown in Figure III.18. For the low and the intermediate TKEL bins, the E^*_{PLF}/E^*_{TOT} ratio shows a parabolic dependence on A''_{PLF}. At the highest TKEL bin, the excitation energy seems to be divided nearly equally between the two reaction fragments at all values of A''_{PLF}. The results presented in this chapter will be discussed further in Chapters IV and V.

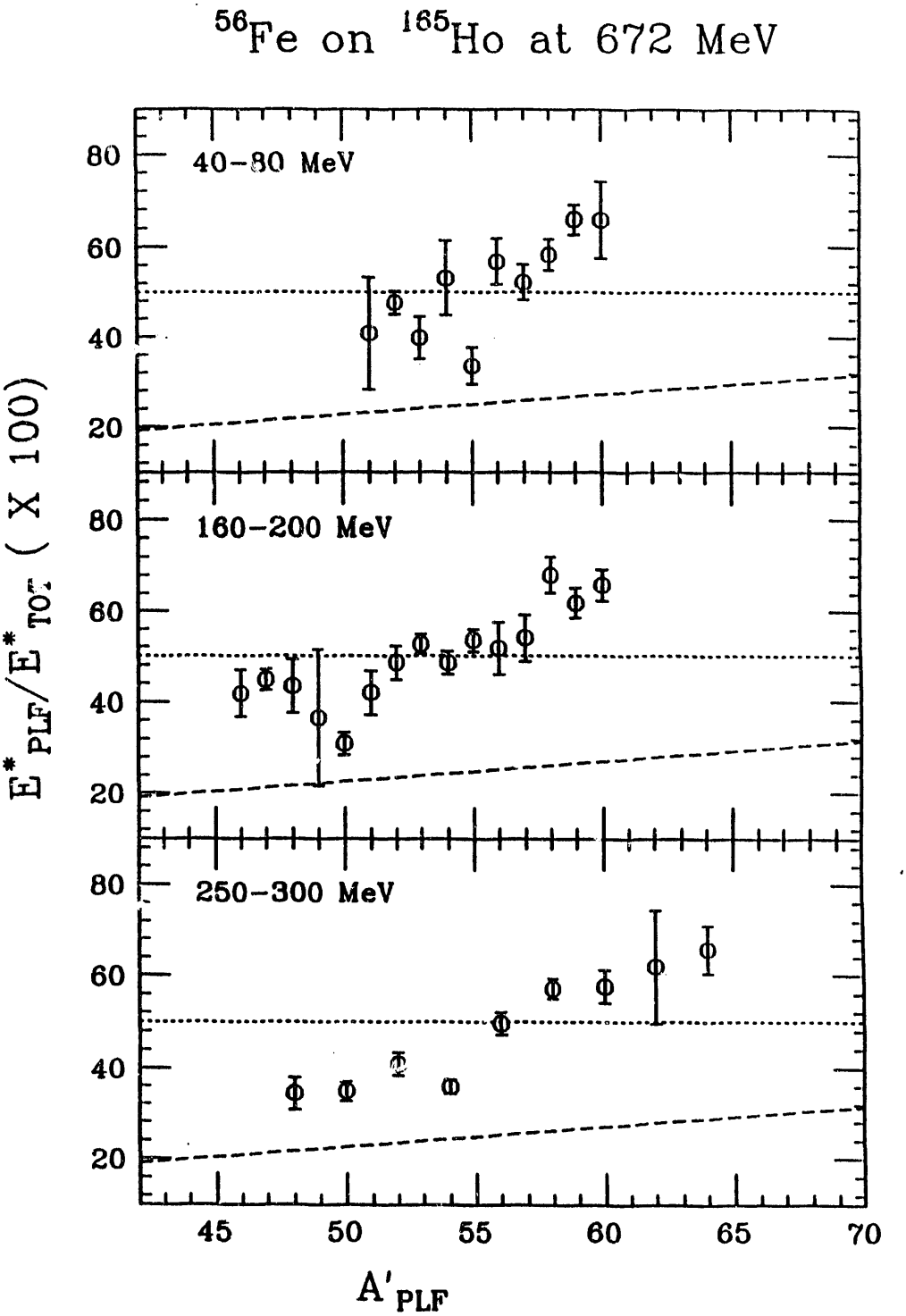

Figure III.17 Centroids of the PLF excitation energy ratio (E^*_{PLF}/E^*_{TOT}) as a function of the primary PLF mass (A'_{PLF}) for three gates on TKEL, for the 672-MeV ^{56}Fe on ^{165}Ho reaction. The limits of equipartition of the excitation energy and thermal equilibrium are indicated by the dotted and dashed lines, respectiveley.

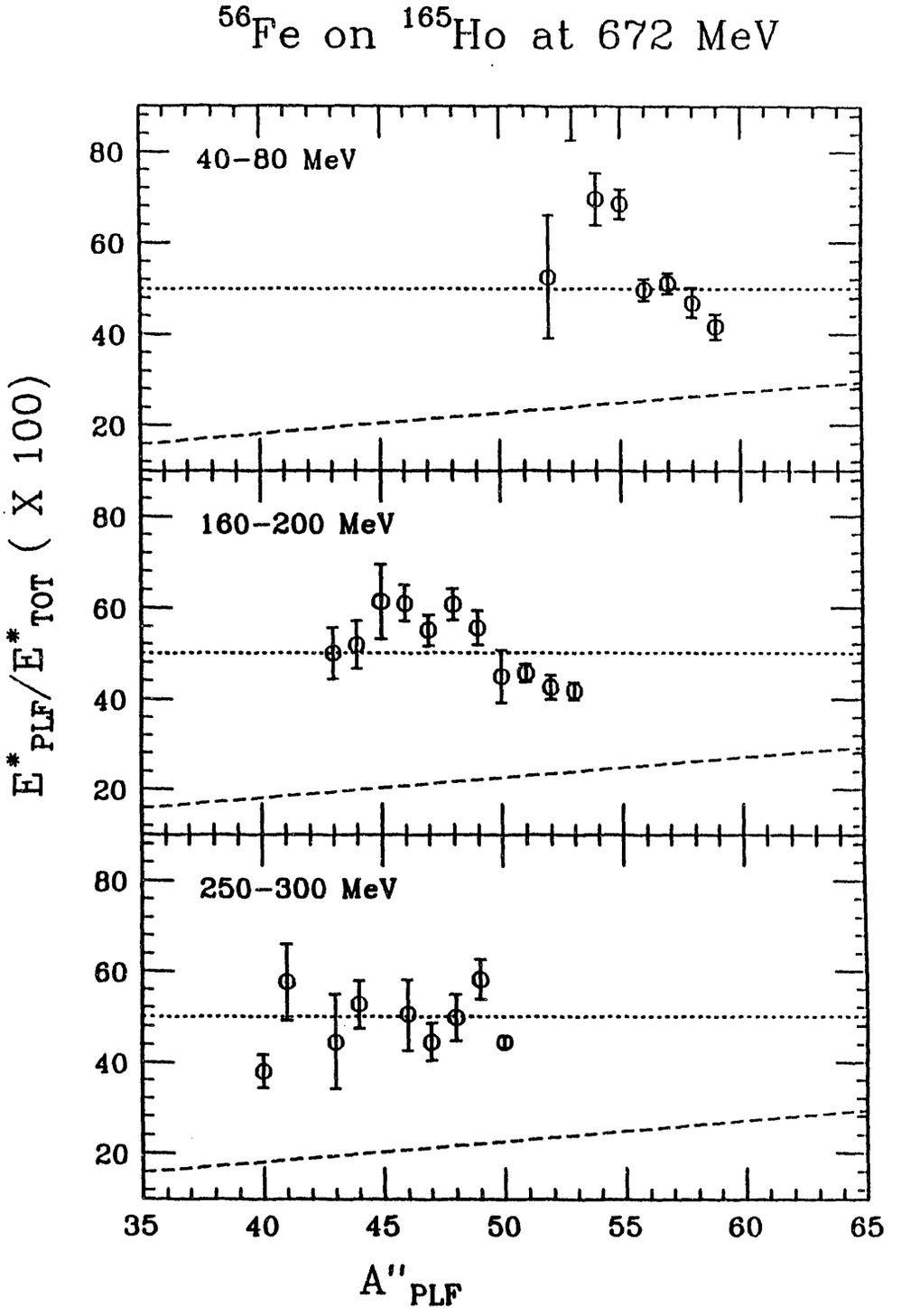

Figure III.18 Centroids of the PLF excitation energy ratio (E^*_{PLF}/E^*_{TOT}) as a function of the secondary PLF mass (A''_{PLF})for three gates on TKEL, for the 672-MeV ^{56}Fe on ^{165}Ho reaction. The limits of equipartition of the excitation energy and thermal equilibrium are indicated by the dotted and dashed lines, respectivelcy.

CHAPTER IV MODEL CALCULATIONS

Several models based on different concepts have been developed to describe the mechanisms involved in the system evolution towards equilibrium in deep-inelastic reactions. Some of these models are based on the concept of energy dissipation by collective nuclear modes [BRO74, BRO76, BRO78a, BRO78b, BRO80] while, in another category of models, the effects of collective modes are neglected and the energy damping is attributed solely to the stochastic exchange of nucleons between the colliding ions [BEC73, GRO74, GRO75, HOF76, GRO77, RAN78a,78b,BLO78, NOR74, NOR75, FEL84, CAR 83, GRI81, 82, DE82, SAM85]. Detailed discussions of the various nucleon exchange models which describe deep-inelastic reactions can be found in review articles by Freiesleben and Kratz [FRE84], and by Schröeder and Huizenga [SCH84].

The focus in the present study is on two models based on the stochastic exchange of nucleons between the reaction partners: Randrup's model [RAN78, 79, 82] and Tassan-Got's model [TAS88, 89,91]. The fundamental concepts on which the two models are based are briefly described, and their main differences are outlined. More details can be sought in references [RAN78, 79, 82], and [TAS 88, 89, 91], and in a review article by Weidenmüller [WEI80], where the theoretical derivations of the equations used in the various transport models are extensively discussed. The success of Randrup's model and Tassan-Got's model in describing the deep-inelastic mechanism is examined by comparing their predictions to the experimental data of the 672-MeV ^{56}Fe on ^{165}Ho reaction, and to other sets of data [MER86, BEN85,88] for systems produced by Fe-induced reactions.

IV.A Basic Theory

Experimental evidence, such as the broadening of the charge and mass distributions of the detected fragments with increasing total kinetic energy loss, supports the idea of energy damping by means of nucleon transfer between the primary fragments of a heavy-ion reaction in the deep-inelastic region. This same feature enables the description of the process occurring in deep-inelastic collisions in terms of transport phenomena. In early work by Nörenberg [NOR74, 75], a master equation describing peripheral deep-inelastic processes was derived from the following Liouville-von Neumann equation

$$i\hbar\frac{d}{dt}\rho_{ji}(t) = [H,\rho(t)]_{ji} = \sum_{lk} L_{(ji,lk)}(t)\rho_{ik}(t), \qquad \text{(IV.1)}$$

where $\rho_{ji}(t)$ is the density operator, H is the Hamiltonian, and $L_{ji,lk}$ is the Liouville operator.

The main steps used by Nörenberg to derive the master equation are as follows. A more extensive description of the procedure can be found in references [NOR75] and [LEF78].

1- The internal motion is separated from the relative motion of the di-nucleus system.

2- Macroscopic variables are introduced through the "coarse graining" of the total channel space using a coarse graining operator. This is equivalent to dividing the total channel space $\mathcal{H}$ into subsets $\mathcal{H}_\mu$. The following pre-master equation is obtained

$$\frac{d}{dt} P_\nu(t) = \sum_\mu \left(\int_0^{t-t_0} d\tau\, K_{\nu\mu}(t,\tau)\right) \left[d_\nu P_\mu(t-\tau) - d_\mu P_\nu(t-\tau)\right], \qquad \text{(IV.2)}$$

where $P_\nu(t)$ is the macroscopic occupation probability and $K_{\nu\mu}(t,\tau)$ is a memory kernel which connects the past time $(t-\tau)$ to the present time t.

3- The Markoff approximation is used. A Markovian process is a stochastic process in which the probabilities of occurrence of future states do not depend on the path followed to arrive to those states. In this approximation, the macroscopic variables are much slower than the microscopic variables. They can be assumed to remain almost constant during a time on the order of the memory time.

The following master equation is obtained

$$\frac{d}{dt} P_\nu(t) = \sum_\mu w_{\nu\mu}(t) \left[d_\nu P_\mu(t) - d_\mu P_\nu(t)\right], \qquad \text{(IV.3)}$$

where $w_{\nu\mu}(t)$ is the transition probability between the subsets ν and μ.

The master equation (IV.3) can be applied to several types of dissipative phenomena, depending on the type of macroscopic variables chosen. It is the basis of most of the models that were developed to study dissipative phenomena in heavy-ion deep-inelastic reactions. The general procedure is to derive a Fokker-Planck type transport equation from the master equation and to evaluate the transport coefficients. The different approaches used for determining these transport coefficients and the various assumptions made about the system (such as considering it as a double nuclear system in Nörenberg's theory) define the differences among models.

In both Randrup's model [RAN78, 79, 82] and Tassan-Got's model [TAS88, 89, 91] the physical picture of the reaction is the same. The two ions are approximated by two spheres that approach each other along Coulomb trajectories until they are within the range of the nuclear field. Then a communication window opens and exchange of nucleons between the two ions occurs. This nucleon transfer is assumed to be the only source of energy dissipation in both models. However, two different approaches and some different basic assumptions are used by the two authors in their determination of the variables of the system. Among the macroscopic variables that are treated are the nuclides' Z and N and fluctuations around their mean values, the excitation energy and the spin of the nucleus. For the purpose of comparing the predictions of these theories to experimental data, only the distributions of the projectile-like fragments (PLF's) are studied. The distributions of the target-like fragments are either not available from the experimental technique used or detected with less precision and accuracy than the PLF's. A brief description of the two theories follows. More details about the two models can be found in References [RAN78, 79, 82] and [TAS88, 89, 91].

IV.A.1 Randrup's Model

In Randrup's model, the two interacting nuclei are represented by two completely degenerate Fermi-Dirac gases. This assumption is based on the low temperatures ($kT \approx 0.5$-2 MeV) that are reached in these reactions. Nucleon-nucleon collisions are mostly prohibited by the Pauli exclusion principle and the two gases interact via one-body dissipation, where relative angular momentum is generated by the interaction of nucleons with the mean field.

The dynamical evolution of the macroscopic variables is described by a Fokker-Planck equation, which is derived from the master equation IV.A.9 by considering the system to be Markovian, and assuming that the macroscopic variables are continuous. In this case the probability of finding one of the two reaction partners (the projectile-like fragment for instance) in state A at time t is given as

$$\frac{\partial P(A,t)}{\partial t} = -\sum_{\alpha}\left(\frac{\partial}{\partial C_\alpha}\right) V_{C_\alpha} P(A,t) + \sum_{(\alpha,\beta)}\left(\frac{\partial^2}{\partial C_\alpha \partial C_\beta} D C_\alpha C_\beta P(A,t)\right) \qquad \text{(IV.4)}$$

where C_α and C_β are observables that describe the system. This would mean that the nucleus in question (the projectile-like fragment for instance) has acquired mass C in the case where the variable C refers to the mass observable. The drift coefficient V_{C_α} governs the evolution of the mean values of the macroscopic variables C, and the diffusion coefficient D_{C_α} governs the evolution of their variances. They are evaluated as

$$V_C = \int d\varepsilon\, N'(\varepsilon) < (f^B - f^A) C >_{flux} \qquad \text{(IV.5)}$$

and

$$2D_{C_1C_2} = \int d\varepsilon N'(\varepsilon) < ((1-f^A)f^B + (1-f^B)f^A) C_1 C_2 >_{flux}, \qquad \text{(IV.6)}$$

where $< >_{flux}$ indicates an averaging over all the angular orientations of the transfer, f^A and f^B are the Fermi functions that indicate the level populations of the partners A and B, and $N'(\varepsilon)$ is the flux of nucleons for an energy interval $d\varepsilon$. For a nearly

degenerate gas representation of the interacting system, as is the case in Randrup's model, the Fermi functions are simplified to the following expressions:

$$f^B - f^A \simeq \omega\, \delta\, (\varepsilon - \varepsilon_F), \tag{IV.7}$$

where δ denotes the Dirac delta function, and

$$(1-f^A)f^B + (1-f^B)f^A \simeq (f^B - f^A)\coth(\frac{\omega}{2\tau}). \tag{IV.7}$$

where τ is the temperature of the system. The quantity ω is the gain in excitation energy when a transfer occurs and is defined as

$$\omega = FA - Up, \tag{IV.8}$$

where

$$FA = \varepsilon_{FB} - \varepsilon_{FA}, \tag{IV.9}$$

which is the difference between the Fermi levels of the two partners, U is the relative velocity vector of nucleus A with respect to B, and p is the momentum vector of the transferred nucleon.

The solution to equation IV.4 can be obtained by the determination of the two transport coefficients. However, solving this equation is a tremendous task and some simplifications are in order.

A mean trajectory approach [RAN82], where an average path is followed by the macroscopic dynamical variables, was the method of choice in Randrup's model.

In this method, a number of dynamical variables, including the proton and neutron numbers of the projectile-like fragments, the radius of the small cylindrical neck that joins the two interacting ions, and the mean spin projection for the target-like fragment, were used. The conservative forces that act on these dynamical variables are derived from the following macroscopic Lagrangian:

$$L = \frac{1}{2}\mu R^2 + \frac{1}{2}I_R\omega R^2 + \frac{1}{2}I_A\omega_A{}^2 + \frac{1}{2}I_B\omega_B{}^2 - V_A - V_B - V_C - V_{AB} \qquad \text{(IV.10)}$$

where μ is the effective mass, I_R is the moment of inertia of the orbital motion, I_A and I_B are the individual moments of inertia of the nuclei A and B, V_A and V_B are the potential energies of the two nuclei, V_C the Coulomb energy, and V_{AB} represents an additional nuclear interaction between A and B.

The Fermi levels that govern the evolution of the system are extracted from this Lagrangian. It was claimed by Tassan-Got [TAS88, 89,91] that this causes the system to drift towards symmetry, and that this effect is due to the presence of a kinetic term in the Lagrangian. The dissipative forces are obtained from a Rayleigh dissipation function and the dynamical equations for the mean trajectory are derived from the Lagrange-Rayleigh equation of motion.

IV.A.2 Tassan-Got's Model

In Tassan-Got's model the stochastic transfer of nucleons between the two fragments is simulated by a Monte Carlo method. In this approach, the possibility and type of transfer are decided by random drawing. The transition probabilities of a proton or a neutron out of or into a fragment are calculated and used for the determination of the characteristics of each transfer.

A phase-space formula accounting for Pauli blocking was used by Tassan-Got to evaluate these transfer probabilities. The probability P of transfer of a nucleon from nucleus 1 to nucleus 2 per unit time is evaluated as

$$P = \int \Phi T n_1 (1-n_2) d^5\sigma, \qquad \text{(IV.11)}$$

where Φ is the phase-space flux per unit area and time, T is the factor of penetrability of the barrier and has values between 0 and 1, and n_1 and n_2 are the rates of occupation of the states considered in nucleus 1 and 2, respectively [TAS88]. The variable σ includes the five parameters that describe the transfer. They are the three components of the velocity vector of the transferred nucleon, and the two parameters that characterize the surface separating the two heavy ions.

A nucleon transfer results in the modification of the initial conditions of the relative motion, which have to be readjusted before the next transfer. This procedure is repeated until the two ions are too far to feel the nuclear interaction. They then move away from each other along Coulomb trajectories. The values of the macroscopic variables of interest are determined event-by-event and stored. Calculations are performed for a wide range of impact parameters to include all the possible incident waves. The advantage of this approach is that it allows the description of the system at each step of the collision instead of following an average path.

IV.B Comparison Between the Two Models and Their Predictions

There are some basic differences between Randrup's model and Tassan-Got's model. The ones that are thought to be more or less crucial are the way the

Fermi levels are calculated in both approaches and the restriction on the direction of transfer in Tassan-Got's formulation. In Randrup's model the Fermi levels are extracted from the Lagrangian, while in Tassan-Got's model the Fermi levels are determined for each nucleus independently as separation energies calculated from mass tables. This is thought to be one of the crucial factors that causes the differences between the predictions of the two models for asymmetric systems. It seems that the presence of a kinetic term in the Lagrangian used in Randrup's model leads the system to drift towards mass symmetry. In Tassan-Got's model the mass and charge drifts are insensitive to relative kinetic energy. Finally, nucleon transfers in Tassan-Got's model are restricted to those where nucleons move towards the window. There are no restrictions on the direction of transfer in Randrup's model.

To test how these differences are translated in terms of charge and neutron distributions, the evolution, with total kinetic energy loss (TKEL), of the mass and charge distributions predicted by the two models for the primary (pre-evaporation) PLF's emitted in various reactions are compared to each other. The results are presented in Figures IV.1 through IV.8, where the centroids $\langle Z \rangle$ and $\langle N \rangle$, the $\langle N \rangle / \langle Z \rangle$ ratio, the variances σ_Z^2 and σ_N^2, and the correlation factor ρ_{NZ} are plotted as a function of TKEL. In all these figures, the prediction of Randrup's model is indicated by the solid line and that of Tassan-Got's model is indicated by the dashed line.

IV.B.1 Symmetric Systems

Before proceeding to a comparison of distributions for asymmetric systems, whose behavior with energy loss prompted the development of many of the various transport models mentioned earlier, it is worthwhile to examine how well Randrup's

model and Tassan-Got's model reproduce the data obtained for symmetric systems, where there should be no net change in <N>, <Z>, and <N>/<Z> of the primary fragments. The centroids <N> and <Z>, and the <N>/<Z> ratio obtained from the two models for the PLF's produced in the 840-MeV ^{56}Fe on ^{56}Fe reaction are shown in Figure IV.1. Both models predict the same behavior for this system and confirm the absence of charge and mass drift, as expected for such symmetric systems. The variances σ_Z^2 and σ_N^2 and the correlation factor ρ_{NZ} are plotted versus TKEL in Figure IV.2. The values predicted by Tassan-Got's model for the variances tend to be slightly smaller than those obtained from Randrup's model. At about 220 MeV of energy loss, σ_N^2 from Randrup's model shows a steeper increase than the more monotonic increase featured in Tassan-Got's model predictions. The correlation factor given by both models increases, with an approximately constant slope from a value of 0 at 0 MeV of TKEL to a value close to 0.8 at a TKEL of 240 MeV. A slight difference is observed in the ρ_{NZ} values from the two models. However, this small difference could be attributed to statistical errors associated with the determinations of the characteristics of the nuclide distributions. Therefore, it seems that the two models give a similar description of the symmetric system 840-MeV ^{56}Fe on ^{56}Fe.

IV.B.2 The 672-MeV ^{56}Fe on ^{165}Ho System

The discrepancy between the two models for asymmetric systems is illustrated in Figures IV.3 through IV.8. The Z and N centroids and the <N>/<Z> ratio of the primary distributions are displayed as a function of TKEL in Figure IV.3 for the 672-MeV ^{56}Fe on ^{165}Ho system. The two models predict nearly the same quantitaive behavior for the <N>/<Z> ratio, which increases from the projectile's

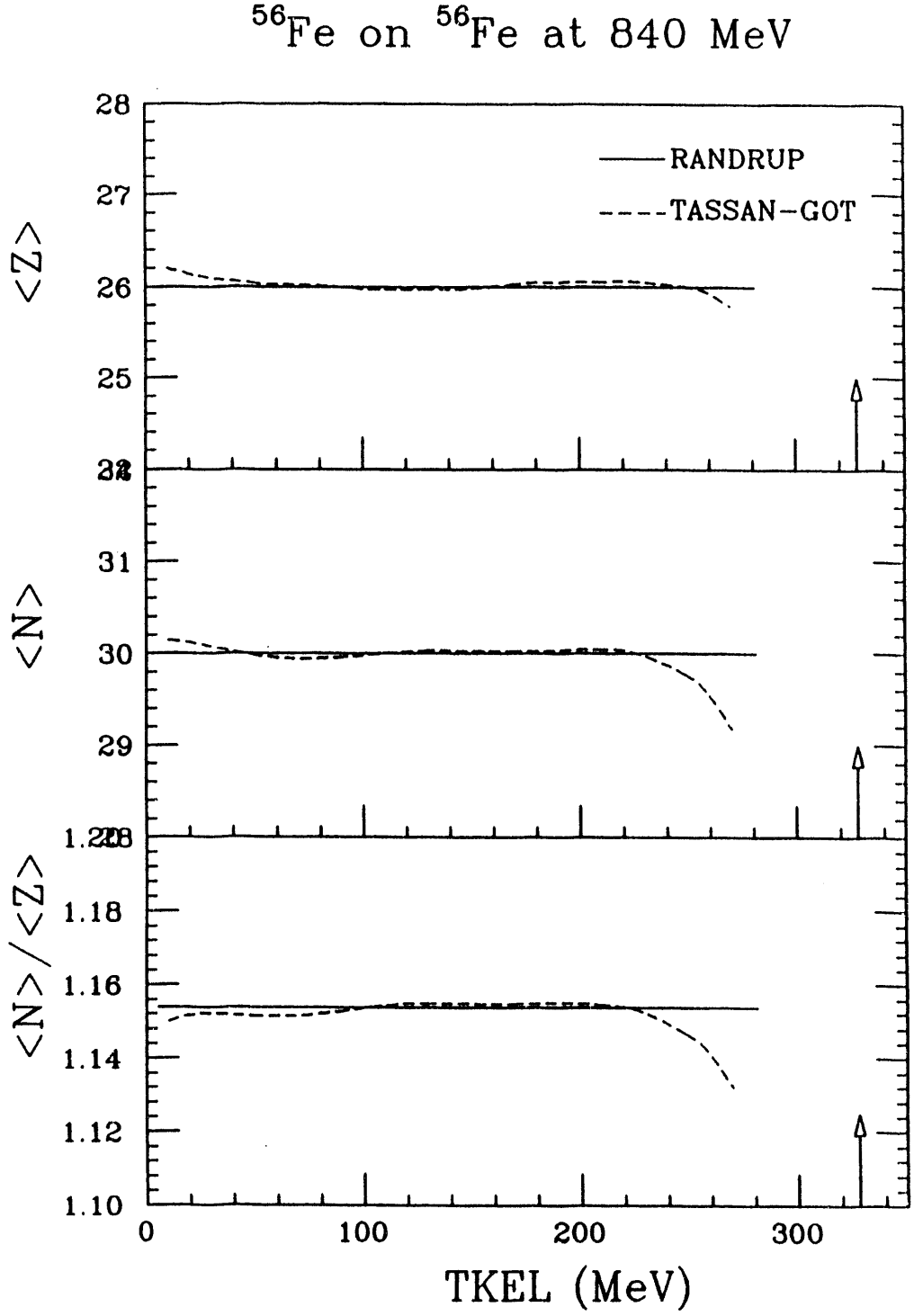

Figure IV.1 Model predictions for <N>, <Z>, and <N>/<Z> for the primary distributions of the 840-MeV ^{56}Fe on ^{56}Fe reaction as a function of energy loss (TKEL). The solid line refers to Randrup's model predictions, and the dashed line refers to Tassan-Got's model predictions. The arrow indicates the value of TKEL corresponding to the spherical Coulomb barrier.

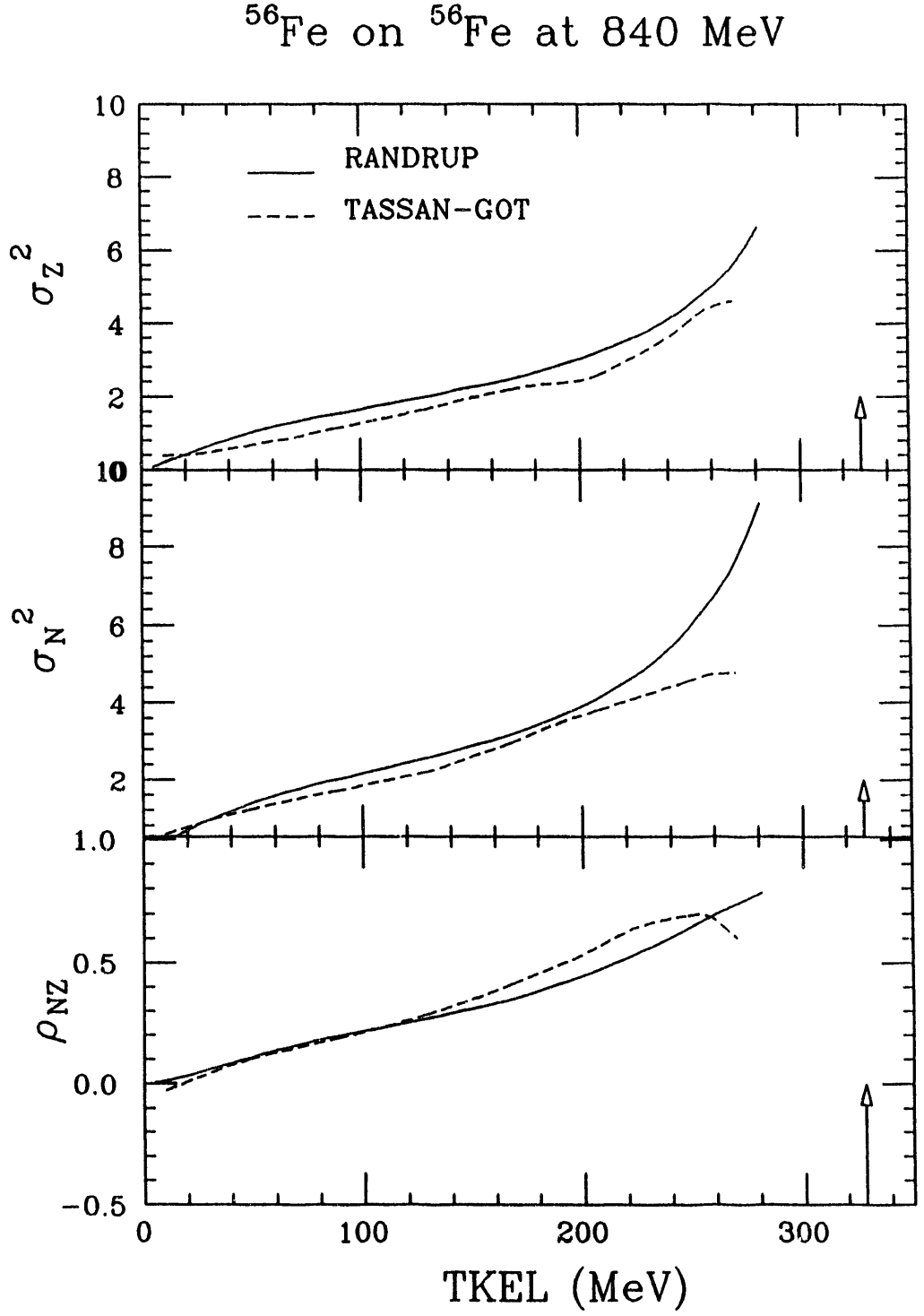

Figure IV.2 Model predictions for σ_Z^2, σ_N^2, and ρ_{NZ} for the primary distributions obtained in the 840-MeV ^{56}Fe on ^{56}Fe reaction as a function of energy loss (TKEL). The solid line refers to Randrup's model predictions, and the dashed line refers to Tassan-Got's model predictions. The arrow indicates the value of TKEL corresponding to the spherical Coulomb barrier.

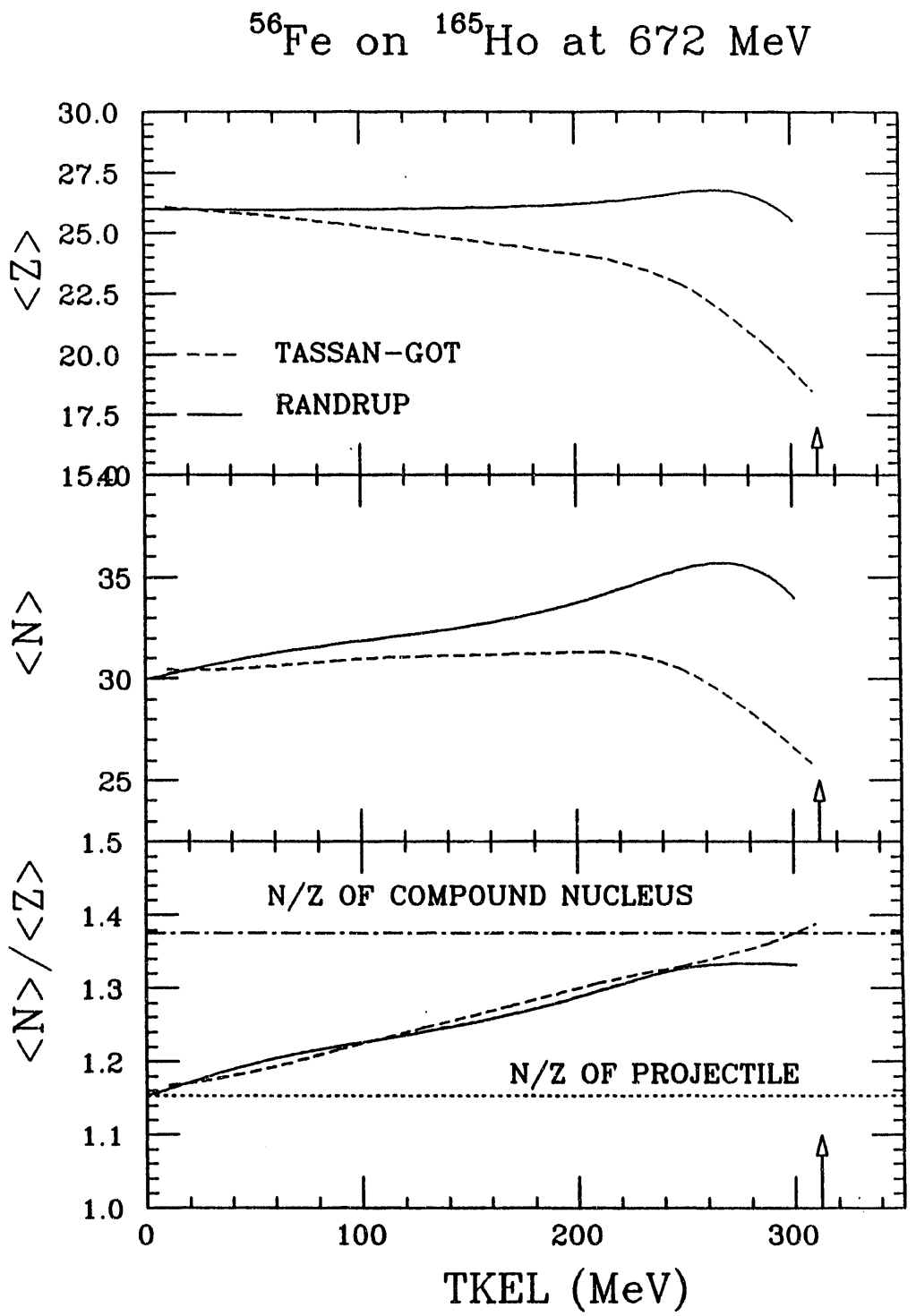

Figure IV.3 Model predictions for <N>, <Z>, and <N>/<Z> for the primary distributions of the 672-MeV ^{56}Fe on ^{165}Ho reaction as a function of energy loss (TKEL). The solid line refers to Randrup's model predictions and the dashed line refers to Tassan-Got's model predictions. The arrow indicates the value of TKEL corresponding to the spherical entrance channel Coulomb barrier. The dot-dashed and dotted lines in the bottom figure indicate the N/Z ratio of the compound nucleus and the projectile, respectiveley.

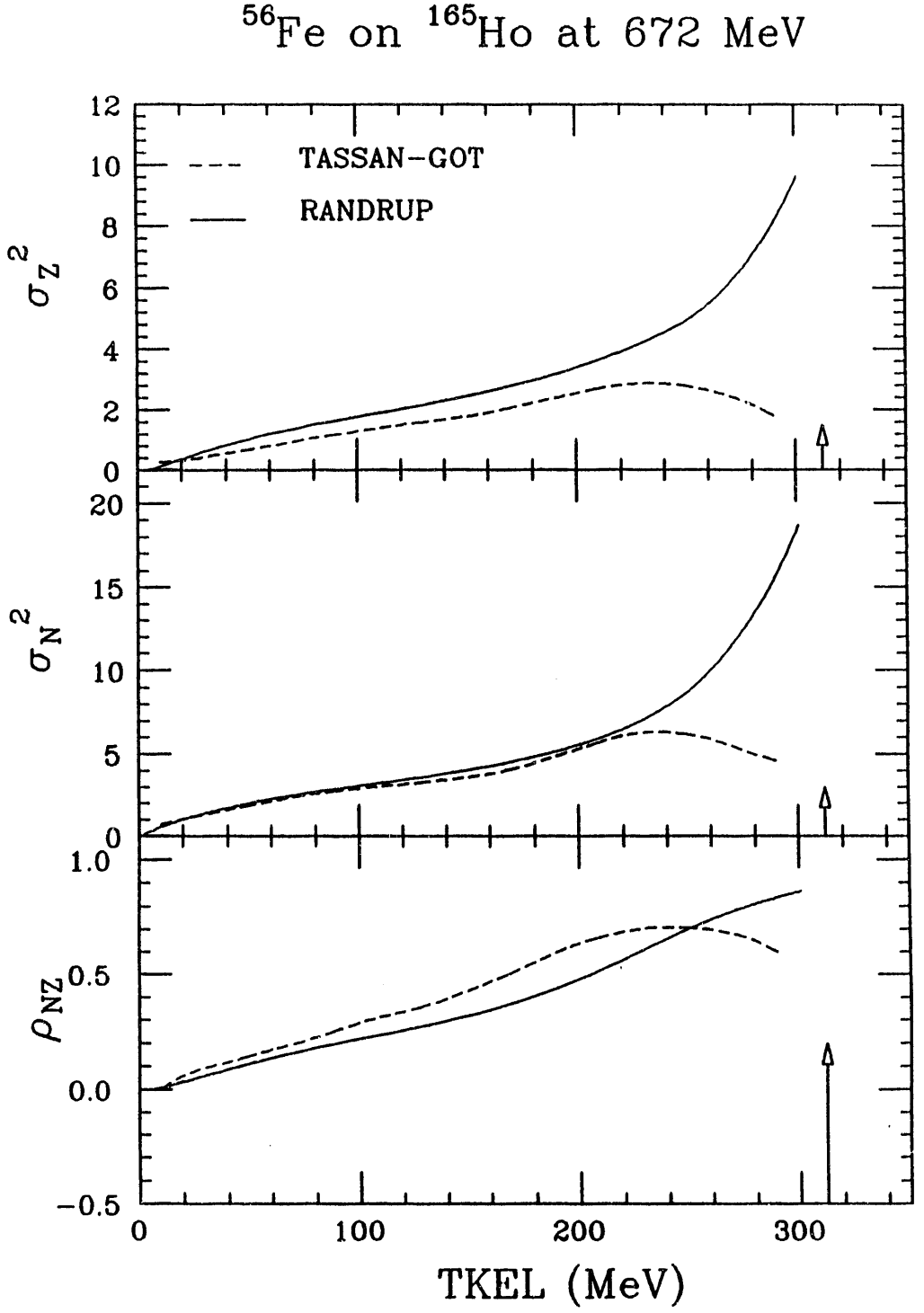

Figure IV.4 Model predictions for σ_Z^2, σ_N^2, and ρ_{NZ} for the primary distributions of the 672-MeV ^{56}Fe on ^{165}Ho reaction as a function of energy loss (TKEL). The solid line refers to Randrup's model predictions and the dashed line refers to Tassan-Got's model predictions. The arrow indicates the value of TKEL corresponding to the spherical entrance channel Coulomb barrier.

N/Z ratio at low TKEL towards a value close to the N/Z of the composite system at the highest TKEL values. This N/Z equilibration is expected for deep-inelastic reactions. However, it is attained by two different means in the two models. In Randrup's model, the N/Z ratio is adjusted by transfer of neutrons (up to 5 neutrons) from the TLF to the PLF and almost no transfer of protons for energy loss values lower than 280 MeV. Above 280 MeV of TKEL both <N> and <Z> start decreasing. In Tassan-Got's model the neutron number remains nearly constant throughout the range of energy loss extending from 0 to 240 MeV, while protons (up to 3 protons) are transferred from the PLF to the TLF. Above 240 MeV the <Z> and

<N> decrease with a relatively steep slope.

This behavior of the centroids <Z> and <N> indicates that in Randrup's model the system evolves towards mass symmetry, while in Tassan-Got's model the system tends to become more asymmetric with increasing energy loss. The reason for this effect is thought to reside in the two different approaches used to compute the Fermi levels in the two models. It seems that the presence of the kinetic term in the Lagrangian is responsible for making the evolution of the N and Z of the system sensitive to relative kinetic energy [TAS89, 90, 91].

The variances σ_N^2 and σ_Z^2, and the correlation factor ρ_{NZ} obtained from the two models are compared in Figure IV.4. The variances from both models are in good agreement for TKEL values lower than about 240 MeV. At this point, the values from Tassan-Got's model start decreasing while those from Randrup's model increase with a steeper slope. This effect was also observed in the study of the ^{35}Cl on ^{209}Bi reaction at 270 MeV and the ^{37}Cl on ^{209}Bi reaction at 529 MeV by Marchetti *et al.* [MAR91, 92]. A possible explanation for this difference in the

behavior is the restriction in Tassan-Got's model of nucleon transfers to only the nucleons moving towards the communication window.

IV.B.3 The 505-MeV ^{56}Fe on ^{165}Ho System

The predictions for the 505-MeV ^{56}Fe on ^{165}Ho system are presented in Figures IV.5 and IV.6. The same general trend is observed for the centroids and the <N>/<Z> ratio. In Randrup's model, a transfer of a maximum of 4.4 units of neutral mass from the TLF to the PLF is predicted for this system, and the charge remains constant within 0.5 units. In Tassan-Got's model, up to 2 protons are transferred from the PLF to the TLF. The neutron number is constant at a value of 31 within 0.5 units. There is an apparent transfer of about 1 unit of neutral mass from the TLF to the PLF at all values of TKEL. There is no evidence that it is an actual transfer or a unusually large uncertainty in the determination of the N centroids for this system. The agreement between the values of the <N>/<Z> ratio obtained from the models is not as good as in the higher bombarding energy case. The same behavior as for the 672-MeV ^{56}Fe on ^{165}Ho system is observed for the variances and the correlation factor, as shown in Figure IV.4.

IV.B.4 The 840-MeV ^{56}Fe on ^{238}U System

The characteristics of the primary charge and neutron distributions are shown in Figures IV.7 and IV.8 for the 840-MeV ^{56}Fe on ^{238}U system. The <N> and <Z> centroids and <N>/<Z> ratio exhibit the same trend as for the two previous systems. However, the difference between the centroids from the two models, the N centroids in particular, seems to be larger for this more asymmetric system. Up to 9 neutrons

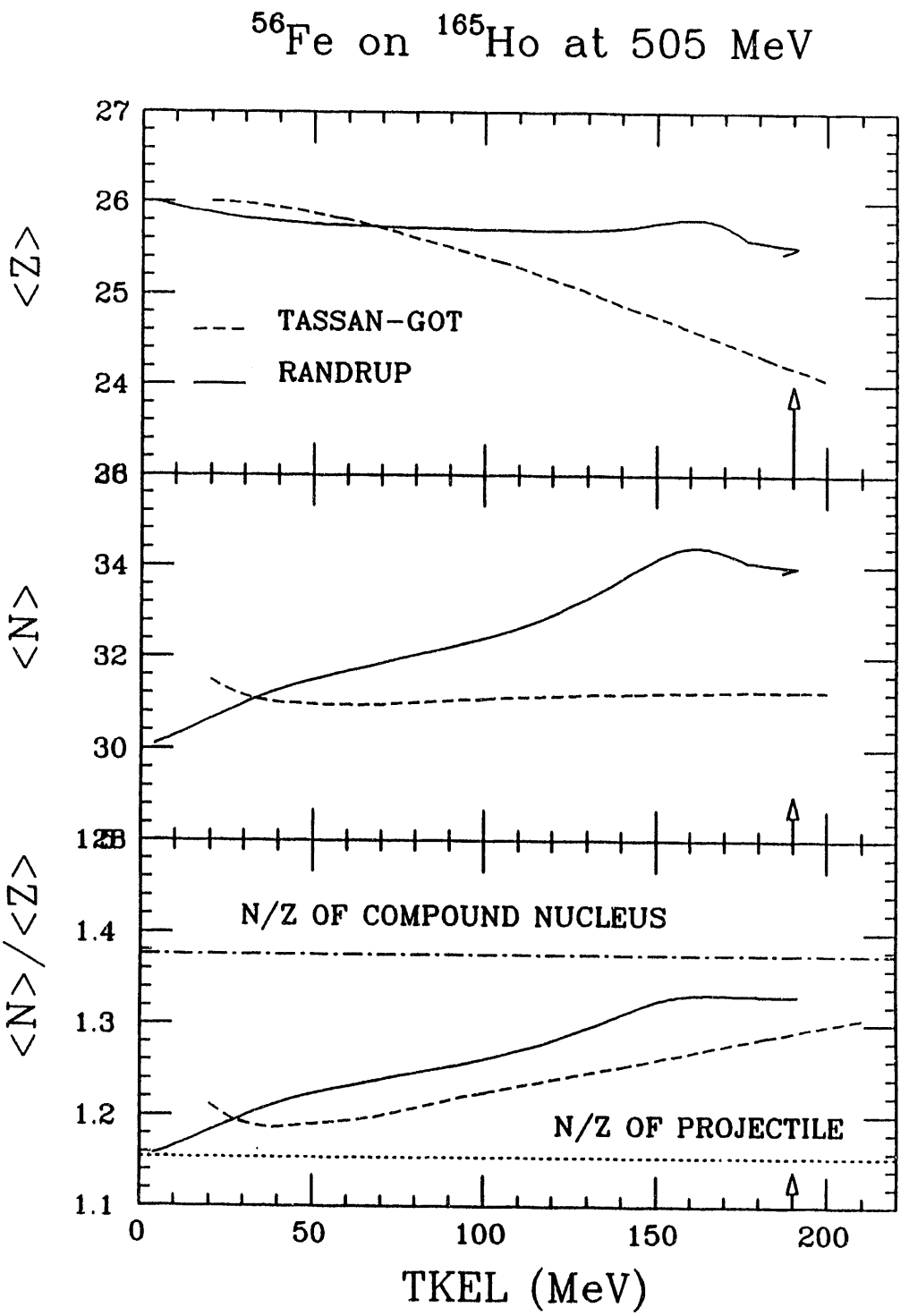

Figure IV.5 Model predictions for <N>, <Z>, and <N>/<Z> for the primary distributions of the 505-MeV ^{56}Fe on ^{165}Ho reaction as a function of energy loss (TKEL). The solid line refers to Randrup's model predictions and theashed line refers to Tassan-Got's model predictions. The arrow indicates the value of TKEL corresponding to the spherical entrance channel Coulomb barrier. The dot-dashed and dotted lines in the bottom figure indicate the N/Z ratio of the compound nucleus and the projectile, respectiveley.

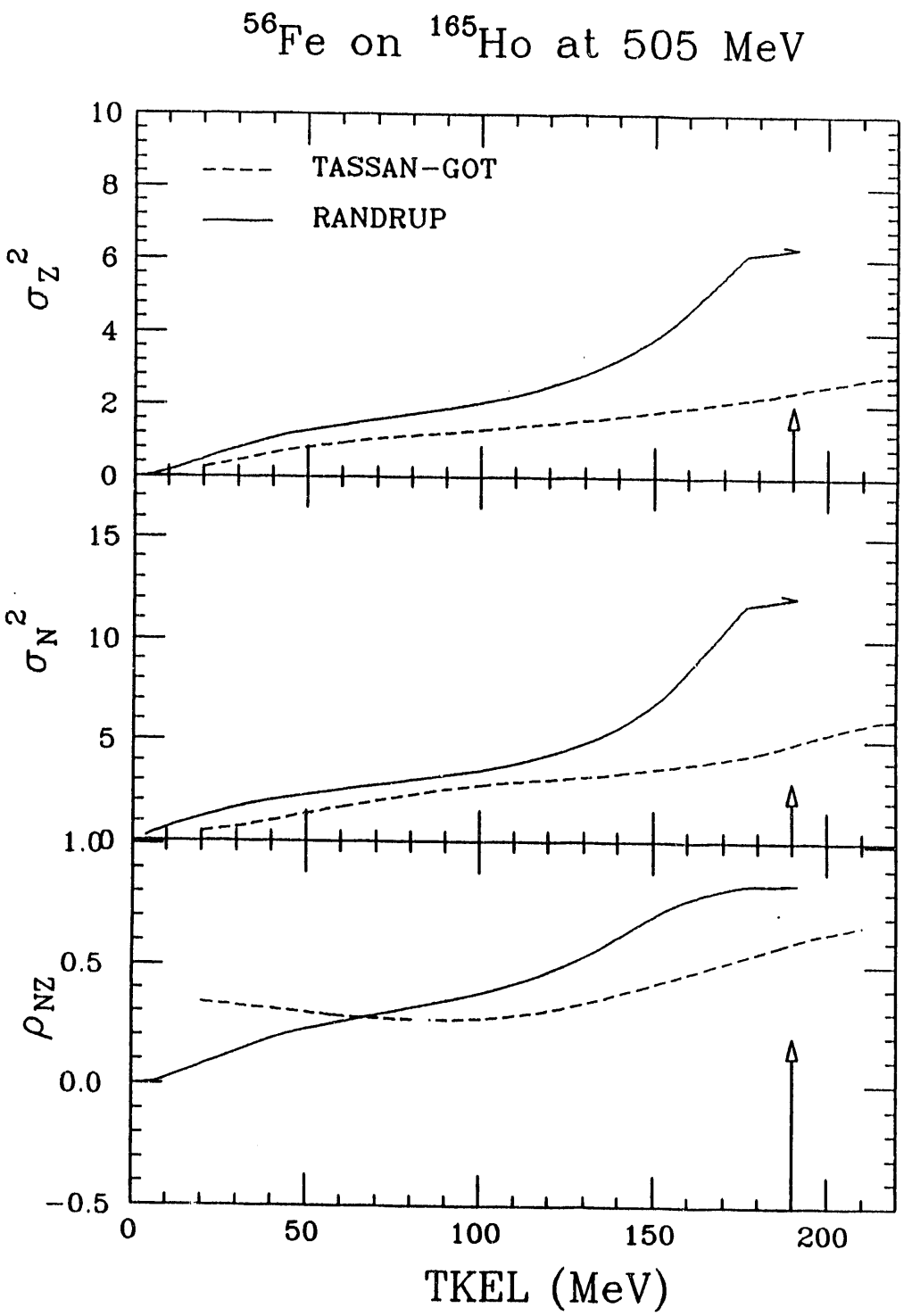

Figure IV.6 Model predictions for σ_Z^2, σ_N^2, and ρ_{NZ} for the primary distributions of the 505-MeV ^{56}Fe on ^{165}Ho reaction as a function of energy loss (TKEL). The solid line refers to Randrup's model predictions, and the dashed line refers to Tassan-Got's model predictions. The arrow indicates the value of TKEl corresponding to the spherical Coulomb barrier.

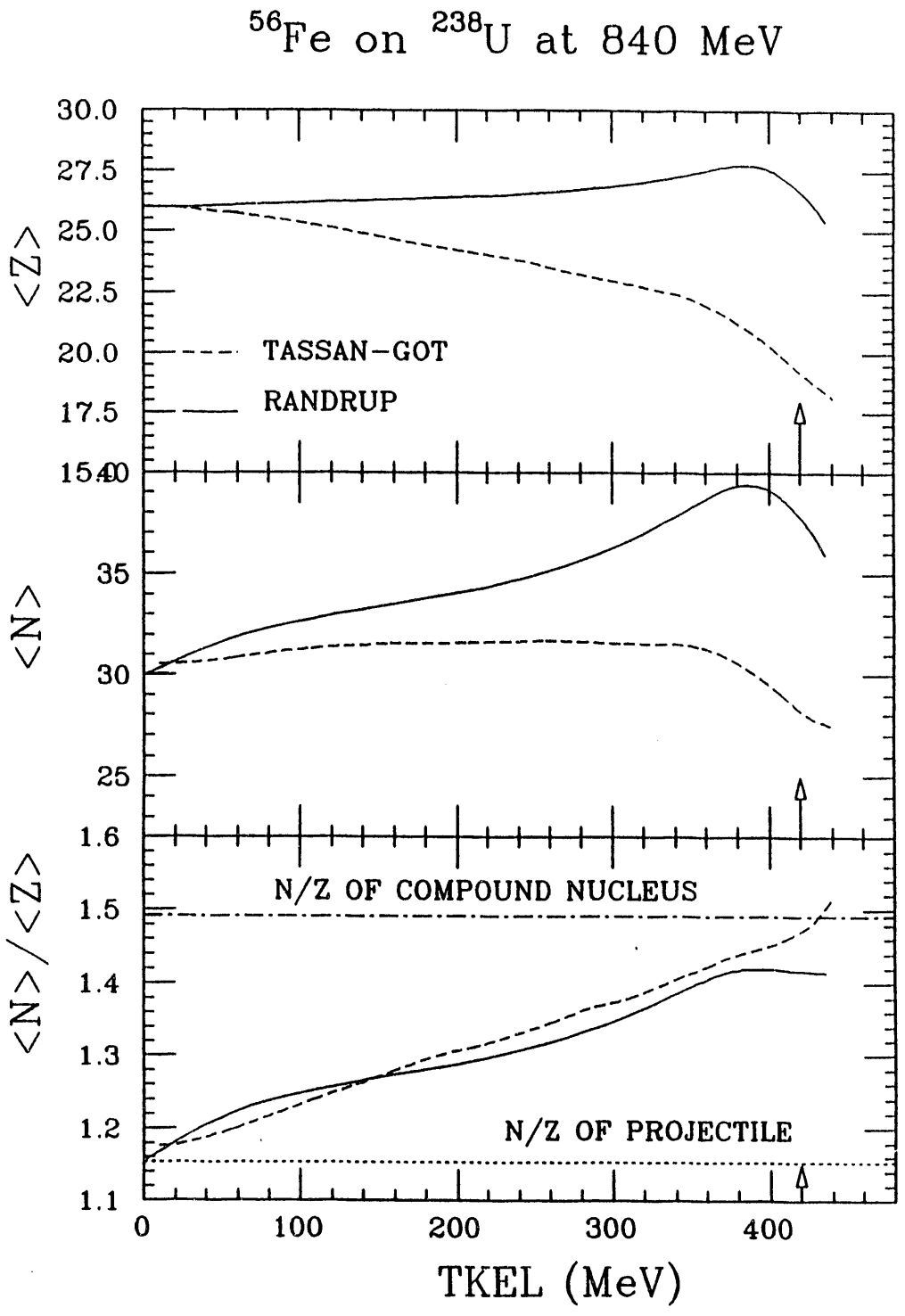

Figure IV.7 Model predictions for <N>, <Z>, and <N>/<Z> for the primary distributions of the 840-MeV ^{56}Fe on ^{238}U reaction as a function of energy loss (TKEL). The solid line refers to Randrup's model predictions and the dashed line refers to Tassan-Got's model predictions. The arrow indicates the value of TKEL corresponding to the spherical entrance channel Coulomb barrier. The dot-dashed and dotted lines in the bottom figure indicate the N/Z ratio of the compound nucleus and the projectile, respectiveley.

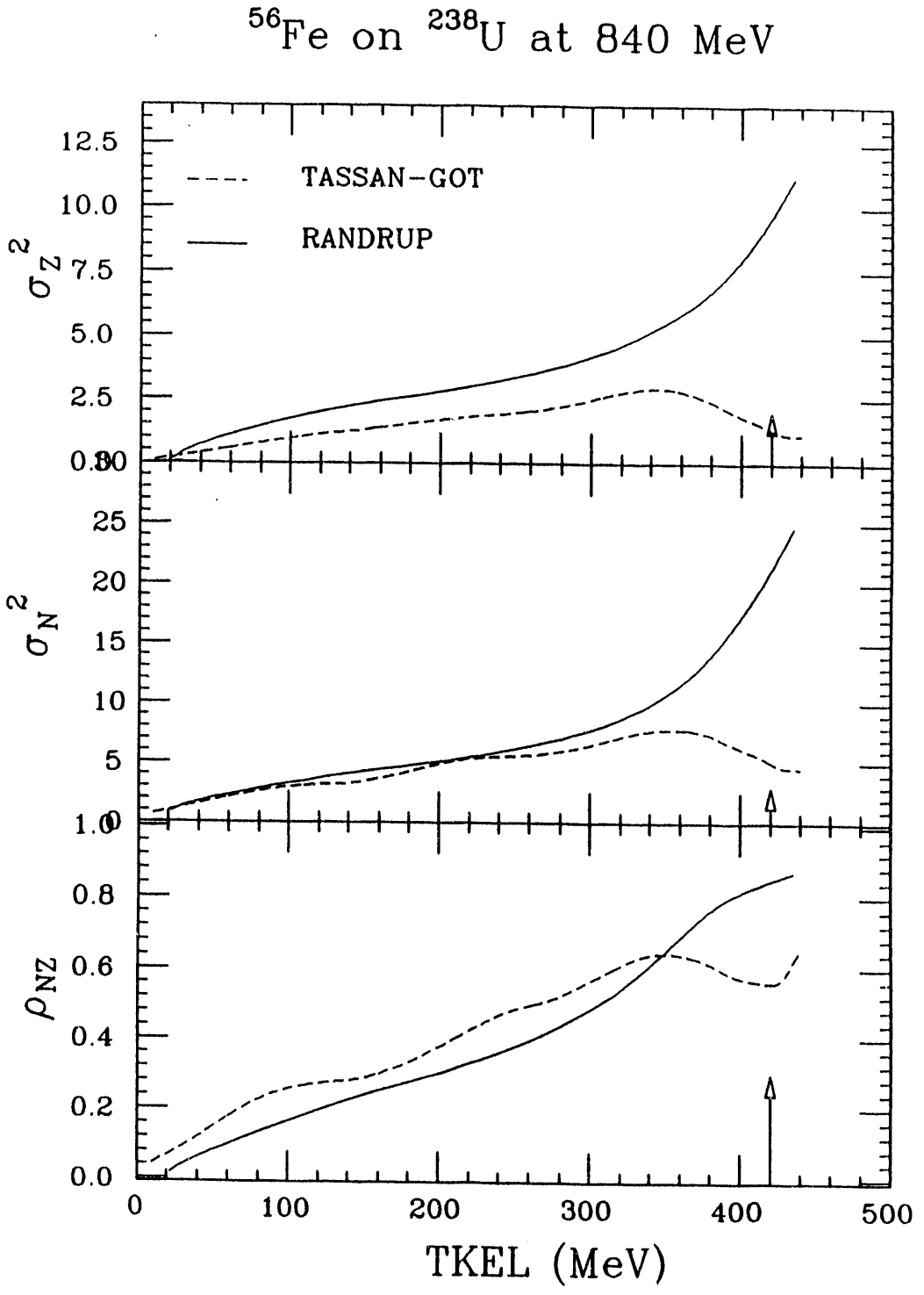

Figure IV.8 Model predictions for σ_Z^2, σ_N^2, and ρ_{NZ} for the primary distributions of the 840-MeV ^{56}Fe on ^{238}U reaction as a function of energy loss (TKEL). The solid line refers to Randrup's model predictions and the dashed line refers to Tassan-Got's model predictions. The arrow indicates the value of TKEL corresponding to the spherical entrance channel Coulomb barrier.

are transferred from the TLF to the PLF in Randrup's model and there is a gain of about 2 charge units by the PLF. According to the predictions of Tassan-Got's model, a maximum of 7.4 charge units are lost by the PLF to the TLF. The variation in the neutron number is only about 1.5 units of neutral mass gained by the PLF, for TKEL lower than 400 MeV. Above 400 MeV of TKEL the PLF loses up to 3 neutrons. The possible explanation for this behavior could be the different ways in which the Fermi levels are calculated in the two models. In Randrup's model a drift towards symmetry is favored and the opposite is true for Tassan-Got's model, where the mass asymmetry of a system is more accentuated [TAS89, 89, 91]. A small difference between the predictions of the two models is observed for the variances, as shown in Figure IV.8. Tassan-Got's model predicts a smaller σ_Z^2 at all values of energy loss. The correlation factor evolves from no correlation ($\rho_{NZ} = 0$) at the first stages of the collision (low TKEL) towards almost full correlation ($\rho_{NZ} \sim 1$) at the later stages (higher TKEL) for both calculations.

IV.C Comparison of Model Predictions to Experimental Data

The observables measured during experiments are secondary quantities which describe the system in its stable state after it has lost all its excitation energy by evaporation of light particles and gamma ray emission. It is therefore essential to account for the loss in proton and neutron numbers by evaporation before attempting any comparisons of experimental data with model predictions. Two possibilities exist for making such corrections. One is to evaluate the amounts of mass and charge evaporated from primary fragments and add them to the measured secondary values. The reconstruction of primary distributions from measured secondary ones is less reliable. Because it is not easy to determine how much evaporated mass is due

to evaporation of protons or neutrons,reliable results are obtained only in cases where neutron evaporation is more significant than proton evaporation. The other method is to perform evaporation calculations on the primary distributions predicted by the models and compare these secondary theoretical distributions to the experimental ones. This procedure was employed in the present analysis.For the sake of consistency, the evaporation code Pace II was used to account for evaporation of the primary distributions obtained from both models.

In the case of Tassan-Got's code, the observables of the system were determined event-by-event and the calculated variables were stored in files that were subsequently used as inputs to Pace II. In Randrup's model, the average values of the observables considered (charge and neutron number for instance) are calculated. It was therefore necessary to generate two dimensional Gaussian distributions to be used with PACE II by employing the averages <Z> and <N>, the variances σ_Z^2 and σ_N^2 and the covariance σ_{NZ} computed by the code.

Another input to the evaporation code is the excitation energy of the primary fragment. In the case of Randrup's model it can be computed using the average rotational energy and the temperatures of the PLF and the TLF that are computed by the code. The total excitation energy ($E^*_{PLF} + E^*_{TLF}$) of a given exit channel is

$$E^* = TKEL + Q_{gg} - E_{rot\text{-}total}, \qquad \text{(IV.12)}$$

where $E_{rot\text{-}total}$ is the total rotational energy of the PLF-TLF system. The rotational energy of each fragment is obtained by scaling the average rotational energy which is given by the code. The general expression of the rotational energy of a spherical nucleus with a moment of inertia I and total angular momentum ℓ is written as

$$E_{rot} = \hbar^2 \frac{\ell(\ell+1)}{2I} . \qquad \text{(IV.13)}$$

The moment of inertia is equal to MR^2, where M is the mass of the nucleus and R is its radius. Assuming the same angular momentum for each nucleus, the rotational energy of each fragment in a given exit channel is then computed as

$$E_{rot} = \langle E_{rot} \rangle \left(\frac{\langle M \rangle}{M}\right)^{5/2}, \qquad \text{(IV.14)}$$

where <> refers to the average quantities calculated by the code.

The excitation energy of each fragment can be evaluated by assuming that their temperatures are equal to the average temperatures that are given by the code. The ratio of excitation energies of the two fragments is given by

$$\frac{E^*_{PLF}}{E^*_{TLF}} = \frac{a_{PLF}\,\tau^2_{PLF}}{a_{TLF}\,\tau^2_{TLF}} \sim \frac{A_{PLF}\tau^2_{PLF}}{A_{TLF}\,\tau^2_{TLF}} \qquad \text{(IV.15)}$$

where A_{PLF} and A_{TLF} are the PLF and TLF masses, a_{PLF} and a_{TLF} are their level density parameters (A/8 was used as the value of a) and τ_{PLF} and τ_{PLF} are their corresponding temperatures. The fraction of excitation energy stored in the PLF can thus be obtained and multiplied by the total excitation energy of the system as given in equation (IV.12). The resulting value is the absolute excitation energy of the PLF and is used in PACE II.

The PLF excitation energy ratios E^*_{PLF}/E^*_{TOT}, obtained from the two models, are compared in Figure IV.9 for the 672-MeV ^{56}Fe on ^{165}Ho system. In both cases the excitation energy of the system is equally shared between the two fragments during the first 120 MeV of TKEL. After that the system tends towards a

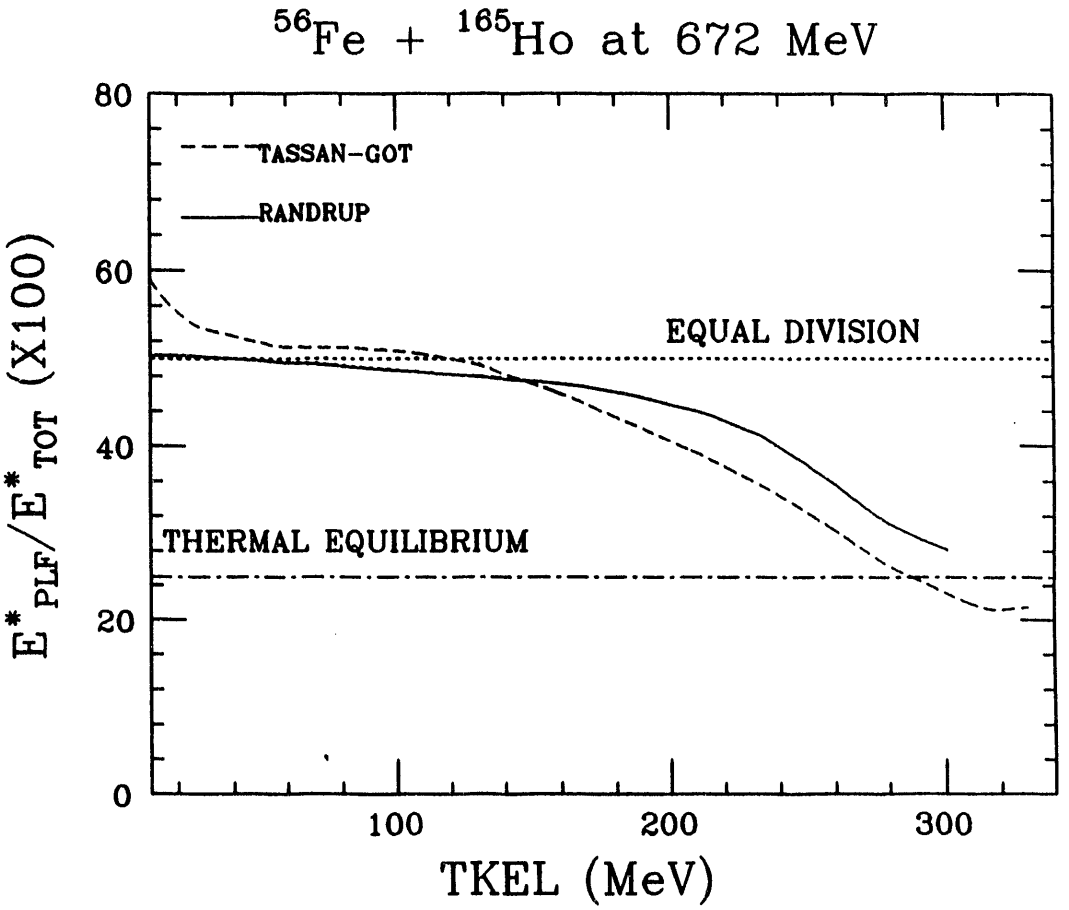

Figure IV.9 The ratio of excitation energy stored in the projectile-like fragments produced by the 672-MeV ^{56}Fe on ^{165}Ho reaction. The solid line refers to Randrup's model calculations, and the dashed line refers to Tassan-Got's model calculations. The limits of equipartition of the excitation energy and thermal equilibrium between the two reaction partners are indicated by the dotted and the dot-dashed lines, respectively.

more thermalized state with increasing energy loss. Since the excitation energies predicted by the two models are nearly similar, as shown in Figure IV.9 for the 672-MeV ^{56}Fe on ^{165}Ho system, and since the same evaporation code was used to obtain the secondary events from the primary events from both models, any discrepancies between the two models' secondary distributions are attributed only to the inherent differences between the models.

The results obtained for the two models after evaporation are compared to experimental data in Figures IV.10 through IV.16. Randrup's model and Tassan-Got's model predictions are again indicated by the solid and dashed lines, respectively. The experimental data is represented by the circles. Large errors are observed for the 672-MeV ^{56}Fe on ^{165}Ho system, where a moment analysis procedure was used for the determination of the means and widths of the distributions, are discussed in Section III.A. Two-dimensional Gaussian fits [BRE82, 83b] were employed to determine the centroids and variances of the distributions for the 505-MeV ^{56}Fe + ^{165}Ho [BEN85, 87, 88] system and the 840-MeV ^{56}Fe on ^{56}Fe and ^{56}Fe on ^{238}U systems [MER86]. Smaller errors are obtained for these two latter systems. When Gaussian fits are used, it seems that the error bars reflect mostly the uncertainties due to the method.

IV.C.1 The 840-MeV ^{56}Fe on ^{56}Fe

The centroids and variances, and the correlation factor predicted by the two models for the PLF secondary distributions of the 840-MeV ^{56}Fe on ^{56}Fe system are compared in Figures IV.10 and IV.11. The experimental <Z>, <N>, and <N>/<Z> are reproduced by both models. However, the two models under predict the

variances, the neutron variance in particular, and fail to reproduce the rapid increase of the correlation factor to full correlation between neutron and proton transfer

IV.C.2 The 672-MeV ^{56}Fe on ^{165}Ho System

The mean values and the variances for the PLF's distributions obtained for the 672-MeV ^{56}Fe on ^{165}Ho system are displayed in Figures IV.12 and IV.13, respectively. The <N>/<Z> ratio is equally well reproduced by the two models. The values predicted for the <N> and <Z> centroids show a good agreement with the experimental data for most of the TKEL range. The predictions from both models depart from the experimental data at high values of energy loss, 230 MeV for Randrup's model and 280 MeV for Tassan-Got's model. As evident from the figures, the theoretical calculations are available only for the range of energy loss allowed by the spherical Coulomb barrier (TKEL ~ 312 MeV) as indicated by the arrows.

The correlation factor is well reproduced by both models. The theoretical charge variances agree with the data for TKEL values lower than 160 MeV. For larger TKEL values, σ_Z^2 is overestimated by both models. At TKEL values close to the maximum energy loss allowed, the two theoretical variances diverge from each other. The σ_Z^2 values obtained from Randrup's model continue to increase with increasing TKEL and reproduce the qualitative behavior of the experimental data. The σ_Z^2 values predicted by Tassan-Got's model decrease sharply, in contrast with the experimental data. The neutron variances are underestimated by the two models, even at the very early stages of the reaction. The theoretical neutron variances exhibit the same behavior as the proton variances at TKEL values larger than 260 MeV. The correlation factor ρ_{NZ} is well reproduced by both models for this asymmetric system,

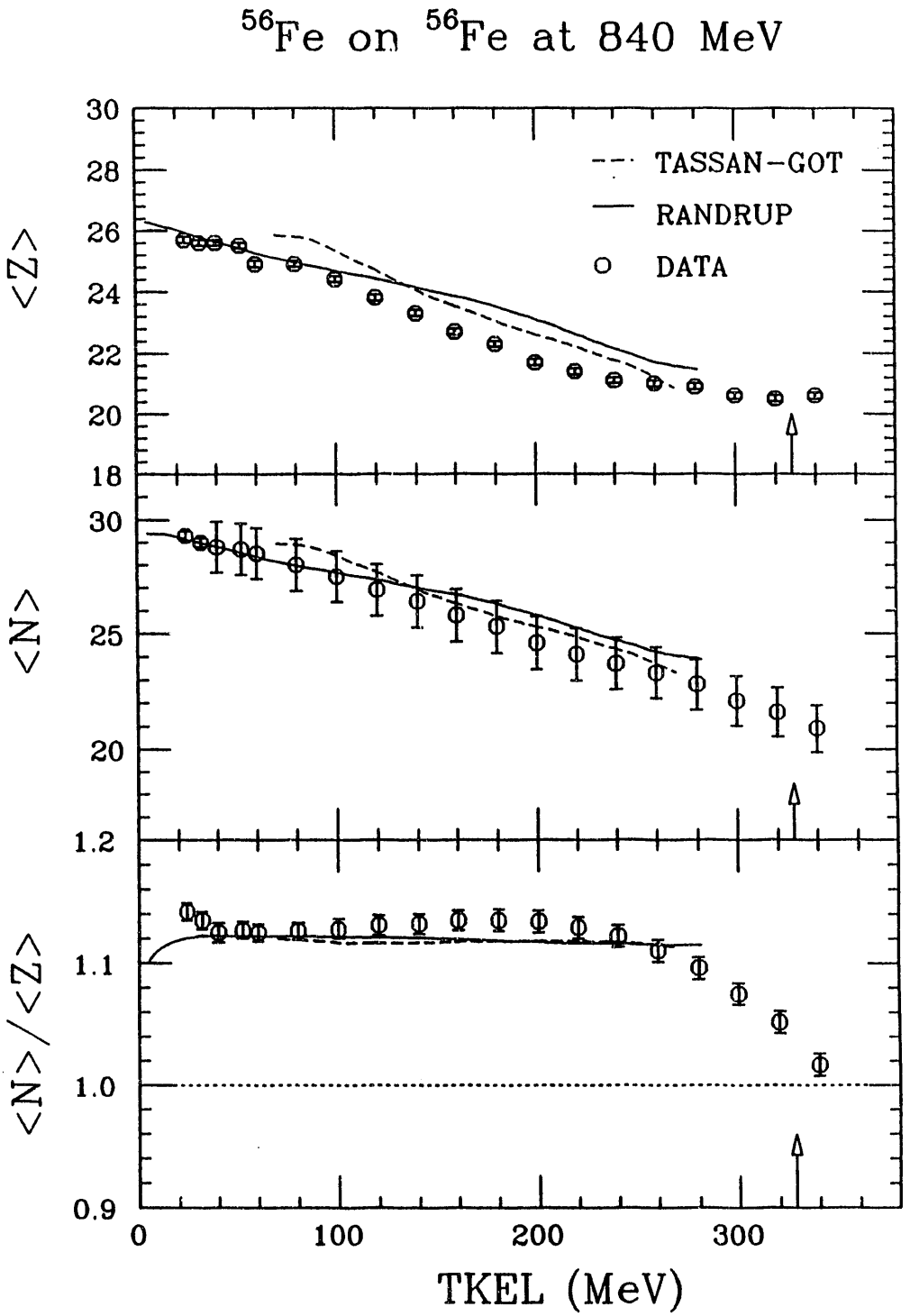

Figure IV.10 Experimental results (circles) and model predictions for <N>, <Z>, and <N>/<Z> for the secondary distributions of the 840-MeV ^{56}Fe on ^{56}Fe reaction [MER86] as a function of energy loss (TKEL). The solid line refers to Randrup's model predictions and the dashed line refers to Tassan-Got's model predictions. The arrow indicates the value of TKEL corresponding to the spherical entrance channel Coulomb barrier. the dotted line indicates the N/Z of the projectile.

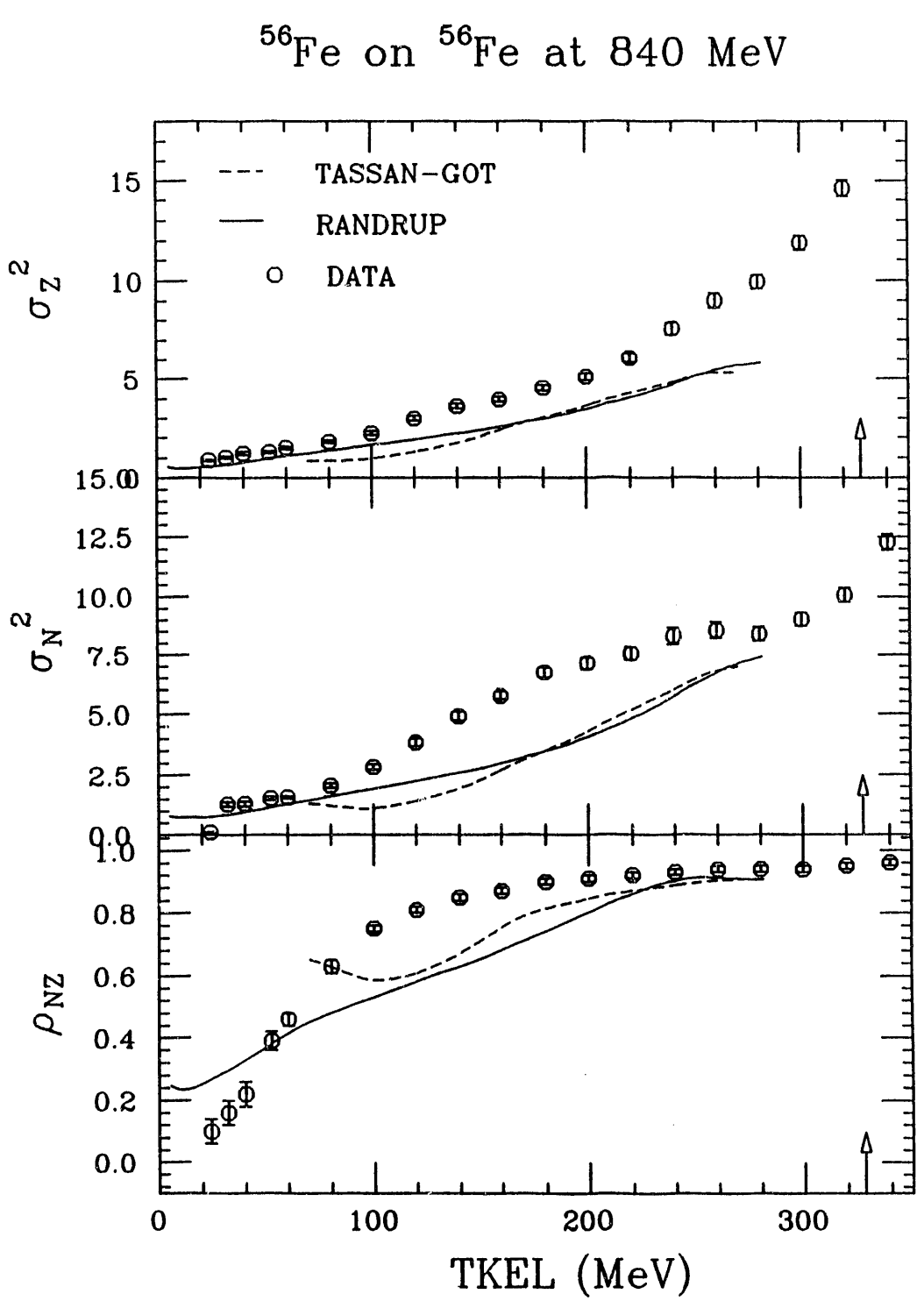

Figure IV.11 Experimental results (circles) and model predictions for σ_Z^2, σ_N^2, and ρ_{NZ} for the secondary distributions of the 840-MeV ^{56}Fe on ^{56}Fe reaction as a function of energy loss (TKEL). The solid line refers to Randrup's model predictions and the dashed line refers to Tassan-Got's model predictions. The arrows indicate the value of TKEL corresponding to the spherical entrance channel Coulomb barrier. The dot-dashed and dotted lines in the bottom figure indicate the N/Z ratio of the compound nucleus and the projectile, respectiveley.

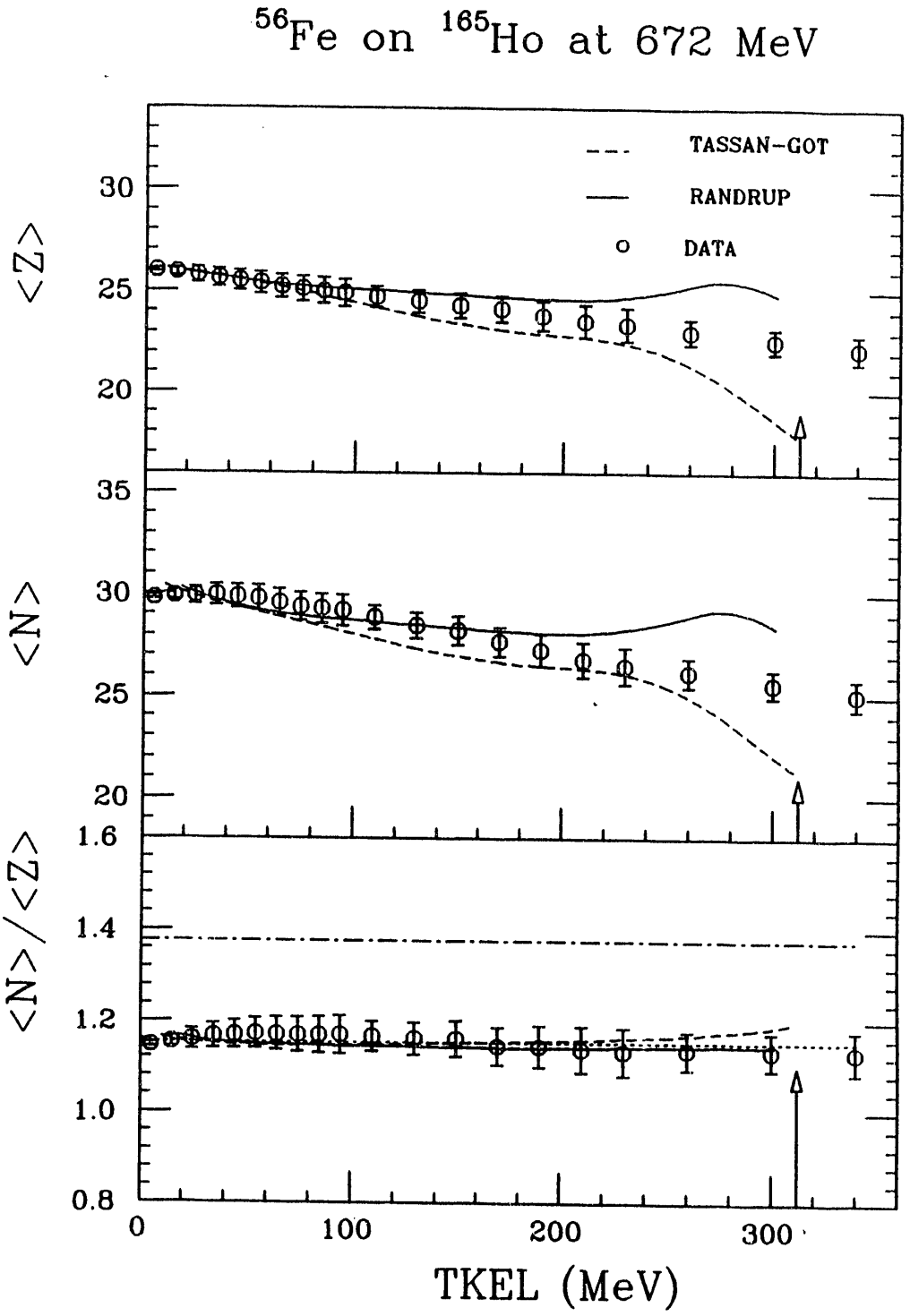

Figure IV.12 Experimental results (circles) and model predictions for <N>, <Z>, and <N>/<Z> for the secondary distributions of the 672-MeV ^{56}Fe on ^{165}Ho reaction as a function of energy loss (TKEL). The solid line refers to Randrup's model predictions and the dashed line refers to Tassan-Got's model predictions. The arrows indicate the value of TKEL corresponding to the spherical entrance channel Coulomb barrier.

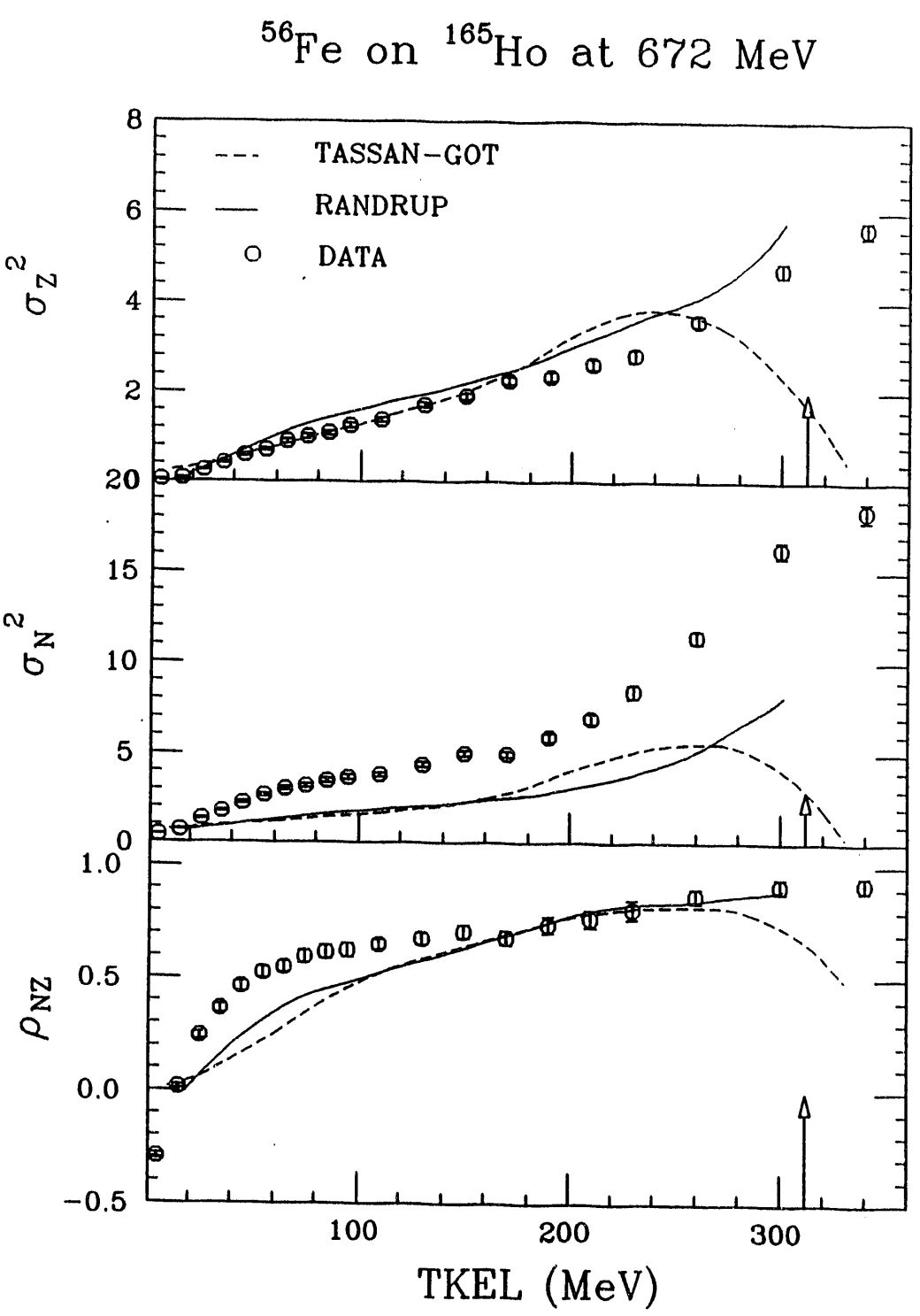

Figure IV.13 Experimental results (circles) and model predictions for σ_Z^2, σ_N^2, and ρ_{NZ} for the secondary distributions of the 672-MeV ^{56}Fe on ^{165}Ho reaction as a function of energy loss (TKEL). The solid line refers to Randrup's model predictions, and the dashed line refers to Tassan-Got's model predictions. The arrow indicates the value of TKEL corresponding to the spherical Coulomb barrier.

unlike the case of symmetric systems.

IV.C.3 The 505-MeV ^{56}Fe on ^{165}Ho System

The experimental <N> and <Z> centroids and the <N>/<Z> ratio obtained for the 505-MeV ^{56}Fe on ^{165}Ho system [BEN85, 88] are compared to theoretical predictions of Randrup's model and Tassan-Got's model in Figure IV.14 . The <N>/<Z> ratio is equally well reproduced by the two models for TKEL values above 50 MeV. The prediction from Randrup's model slightly overestimates the <N>/<Z> ratio above 50 MeV of TKEL. There is a sizable difference in the prediction of the <N> and <Z> centroids, however. Tassan-Got's model reproduces both proton and neutron number centroids for the entire range of allowed energy loss. Randrup's model overestimates <Z> and <N>, and the discrepancy between experimental and theoretical values increases gradually with increasing TKEL. At a TKEL value of about 150 MeV, which is close to the maximum energy loss allowed by the spherical Coulomb barrier (TKEL ~ 190 MeV), the experimental <Z> and <N> show a sharp increase, which may indicate the onset of the fusion-fission mechanism . This effect is not calculated in the models. The variances are not available for this system.

IV.C.4 The 840-MeV ^{56}Fe on ^{238}U System

The results for the 840-MeV ^{56}Fe on ^{238}U system [MER86] are displayed in Figures IV.15 and IV.16. Again the <N>/<Z> ratio is well reproduced by both models for most of the TKEL range; a departure from the experimental data is observed for TKEL values close to the Coulomb barrier (TKEL~ 420 MeV). A large

discrepancy is observed between the experimental <N> and <Z> centroids and the predictions of Randrup's model. Tassan-Got's model reproduces these centroids fairly well. A very good agreement is observed between the data and the predictions of the two theories for the variances and the correlation factor.

The comparisons of model predictions to experimental data show that the experimental charge and neutron centroids are generally better reproduced by Tassan-Got's model than by Randrup's model. The variances and correlation factor are generally well reproduced for the more asymmetric systems by both models.

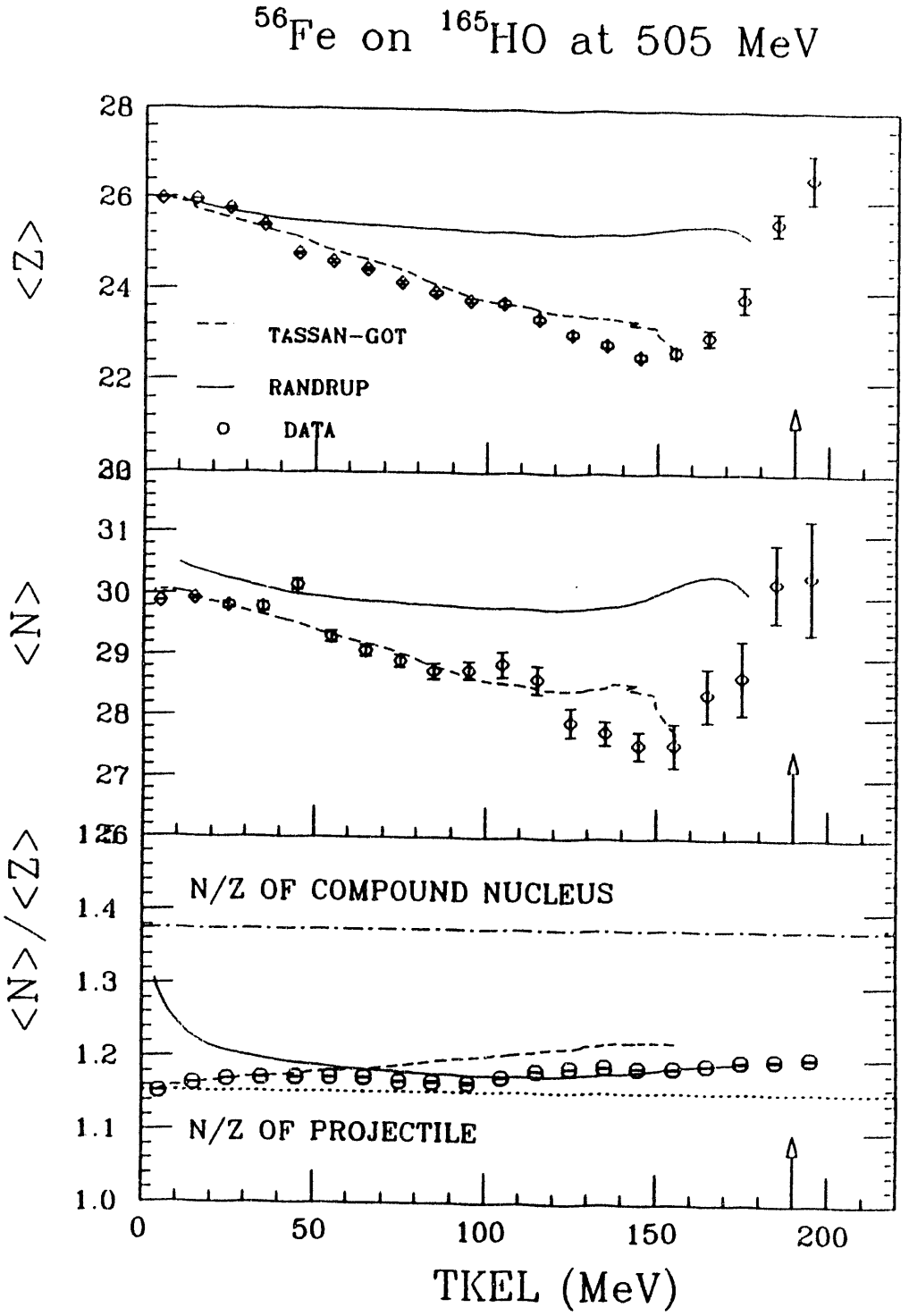

Figure IV.14 Experimental results (circles) and model predictions for <N>, <Z>, and <N>/<Z> for the secondary distributions of the 505-MeV ^{56}Fe on ^{165}Ho reaction [BEN85, 87, 88] as a function of energy loss (TKEL). The solid line refers to Randrup's model predictions, and the dashed line refers to Tassan-Got's model predictions. The arrows indicate the value of TKEL corresponding to the spherical entrance channel Coulomb barrier. The dot-dashed and dotted lines in the bottom figure indicate the N/Z ratio of the compound nucleus and the projectile, respectiveley.

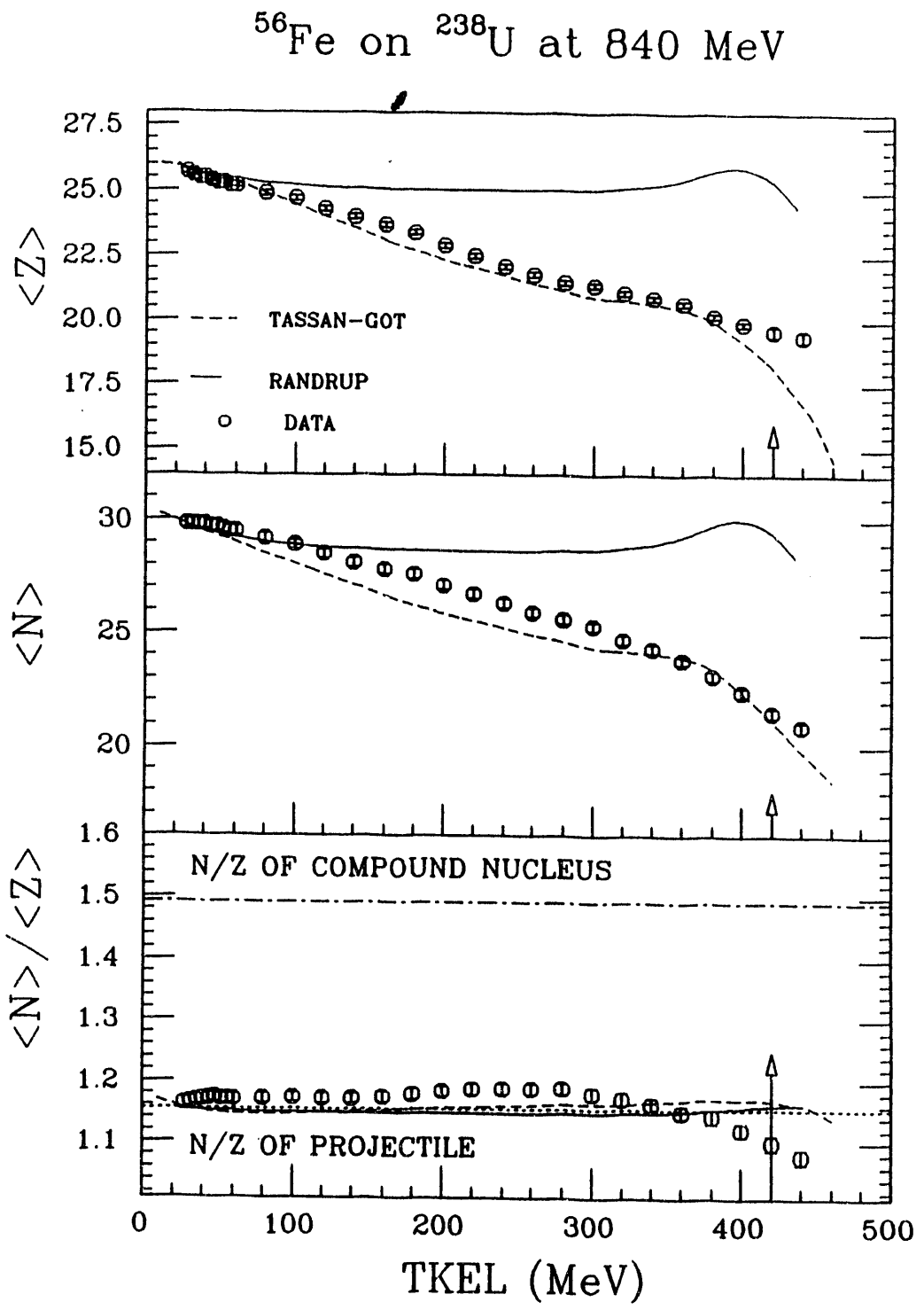

Figure IV.15 Experimental results (circles) and model predictions for <N>, <Z>, and <N>/<Z> for the secondary distributions of the 840-MeV ^{56}Fe on ^{238}U reaction [MER86] as a function of energy loss (TKEL). The solid line refers to Randrup's model predictions and the dashed line refers to Tassan-Got's model predictions. The arrows indicate the value of TKEL corresponding to the spherical entrance channel Coulomb barrier. The dot-dashed and dotted lines in the bottom figure indicate the N/Z ratio of the compound nucleus and the projectile, respectiveley.

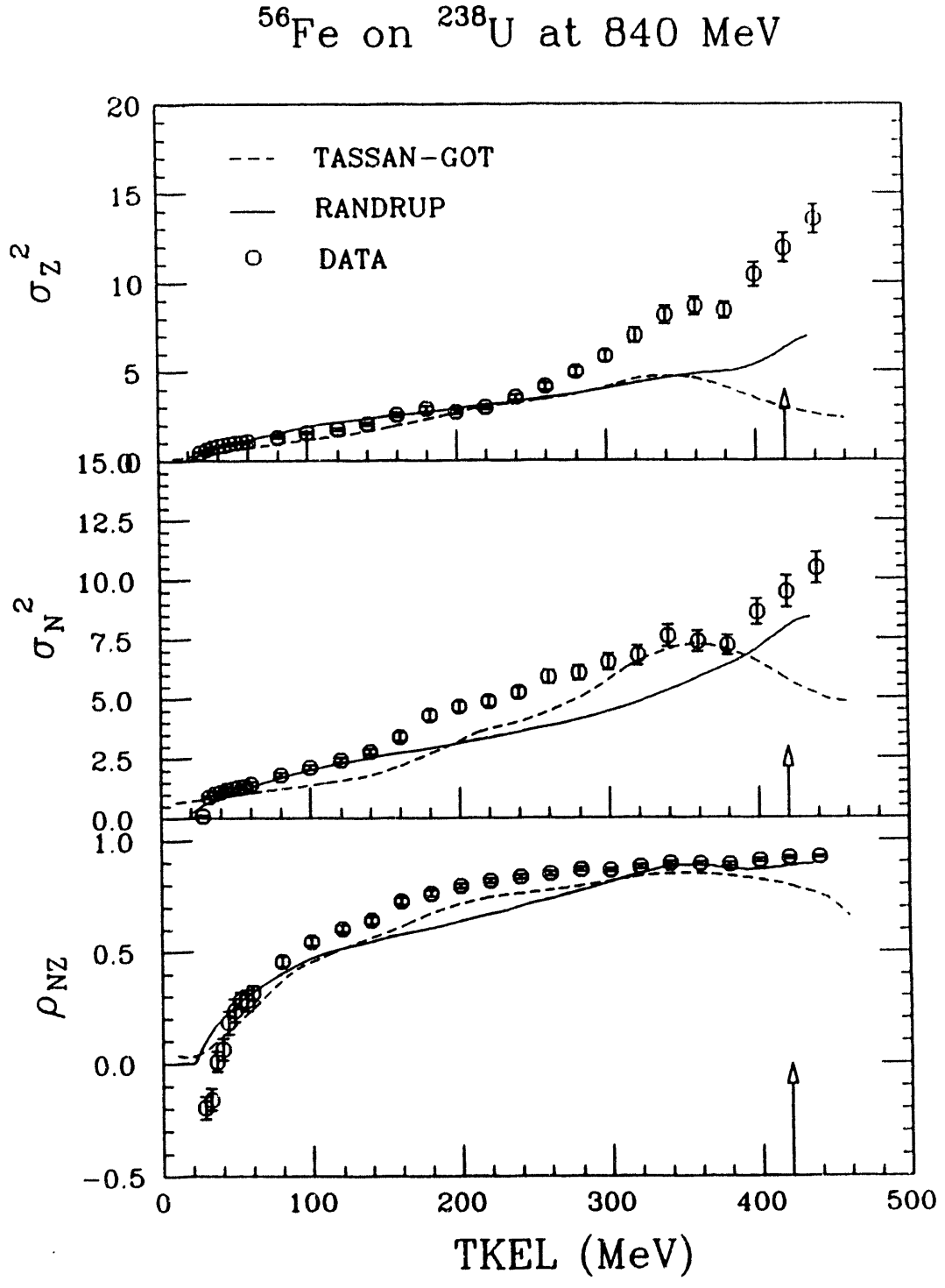

Figure IV.16 Experimental results (circles) and model predictions for σ_Z^2, σ_N^2, and ρ_{NZ} for the secondary distributions of the 840-MeV ^{56}Fe on ^{238}U reaction [MER86] as a function of energy loss (TKEL). The solid line refers to Randrup's model predictions and the dashed line refers to Tassan-Got's model predictions. The arrows indicate the value of TKEL corresponding to the spherical entrance Coulomb barrier.

CHAPTER V DISCUSSION

The experimental and theoretical studies of heavy-ion reactions in the deep-inelastic region resulted in the understanding of their general features, as discussed in Chapter I. However, some aspects of these reactions still remain obscure. It is not yet clearly understood if nucleon transfer alone can account for all the energy dissipation, and how the produced excitation energy is divided between the two reaction fragments. Another point to be elucidated is the role of the potential energy of the composite system in the evolution of the nuclide distribution of the reaction fragments.

The drift of asymmetric systems towards greater mass asymmetry is explored in terms of the mass and charge distributions of the projectile-like fragment and its neutron-to-proton ratio N/Z. Since the primary fragments (pre-evaporation) produced by the collision are short lived, only the secondary (post-evaporation) fragments are detected. Hence, it is necessary to account for the deexcitation through light particle evaporation using evaporation codes. The amount of mass and charge evaporated from a nucleus is related to its excitation energy which has to be used as an input in evaporation codes. In studies where the excitation energy of the fragments cannot be determined, assumptions have to be made for the excitation energy sharing between the two fragments.

The use of the kinematics coincidence technique described in Section II.D.3 provides information about the primary fragments before their deexcitation by evaporation. The parameter of particular interest that is determined with this method is the excitation energy of the primary fragments. The results of the present study of the 672-MeV ^{56}Fe on ^{165}Ho reaction with the kinematics coincidence technique are compared to those obtained, with the same experimental

method, for the 505-MeV ^{56}Fe on ^{165}Ho [BEN85, 87, 88], and the 629-MeV ^{74}Ge on ^{165}Ho [KWI 90] systems.

A strong correlation between the excitation energy division and the mass of the primary projectile-like fragment was observed in the study of the 505-MeV ^{56}Fe on ^{165}Ho reaction by Benton *et al.* [BEN85, 87, 88], and the 629-MeV ^{74}Ge on ^{165}Ho reaction by Kwiatkowski *et al.* [KWI90]. However, it has been claimed by Tõke *et al.* [TOK89], after re-analysis of the 505-MeV ^{56}Fe + ^{165}Ho data, that this exit channel dependence of the excitation energy division is caused by the finite resolution of the measured quantities. A Monte Carlo simulation of the coincidence experiment for the 672-MeV ^{56}Fe on ^{165}Ho reaction is performed to examine the extent of instrumental effects on the determination of the excitation energies of the reaction products. The results of the Monte Carlo simulation for the 629-MeV ^{74}Ge on ^{165}Ho [KWI90] system are also discussed and compared to the results of the present study.

It is important to verify the consistency of the results obtained by the two types of analyses conducted on the present data, the study of the secondary mass and charge distributions of the PLF's, and the kinematic reconstruction method. For this purpose, the primary mass and charge distributions obtained with the kinematics coincidence technique are compared to those obtained by applying neutron evaporation corrections to the measured secondary distributions.

V.A. Drift Towards Mass Asymmetry

Studies of various asymmetric systems revealed a tendency for most of these systems to drift towards greater mass asymmetry with increasing TKEL. This trend is, in general, contradictory to the direction indicated by the gradient to the

potential energy surface (PES) of the composite system. The potential of the system formed by the projectile-like and target-like fragments is usually calculated using the relation

$$V = V_{PLF_{(LD)}} + V_{TLF_{(LD)}} + V_N + V_L - V_C \qquad (V.1)$$

where $V_{PLF_{(LD)}}$ and $V_{TLF_{(LD)}}$ are the liquid drop (LD) model binding energies of the PLF and TLF, respectively, and V_N, V_L and V_C are the nuclear, centrifugal and Coulomb potentials, respectively [PLA90]. As an example, the potential energy surface (PES) for the ^{56}Fe on ^{165}Ho system [BRE83a] is displayed in Figure V.1. The predictions from Randrup's model, indicated by the dashed arrow, for the 465-MeV ^{56}Fe on ^{165}Ho reaction are in accordance with the PES gradient. In contrast, the direction followed by the experimental centroids corrected for neutron evaporation diverges from the PES gradient, as shown by the solid arrow. This same behavior is exhibited in a more drastic fashion by the 465-MeV $^{56}Fe + ^{238}U$ [BRE83a] system, where the direction of the trajectory followed by the experimental centroids is opposite to that of the PES gradient, as shown in Figure V.2.

It was shown in Chapter IV that Tassan-Got's model gives a better general reproduction of the N and Z centroids for asymmetric systems than does Randrup's model. Tassan-Got's model predicts the strong negative drift of such systems. This is illustrated in Figure V.3, where the PES of the $^{40}Ar + ^{197}Au$ system is displayed [TAS88]. The centroids predicted by Tassan-Got's model for the primary distributions of this system (solid line and points), are superimposed on the PES. The direction followed by the centroids diverges from the direction of the PES gradient (dot-dashed line).

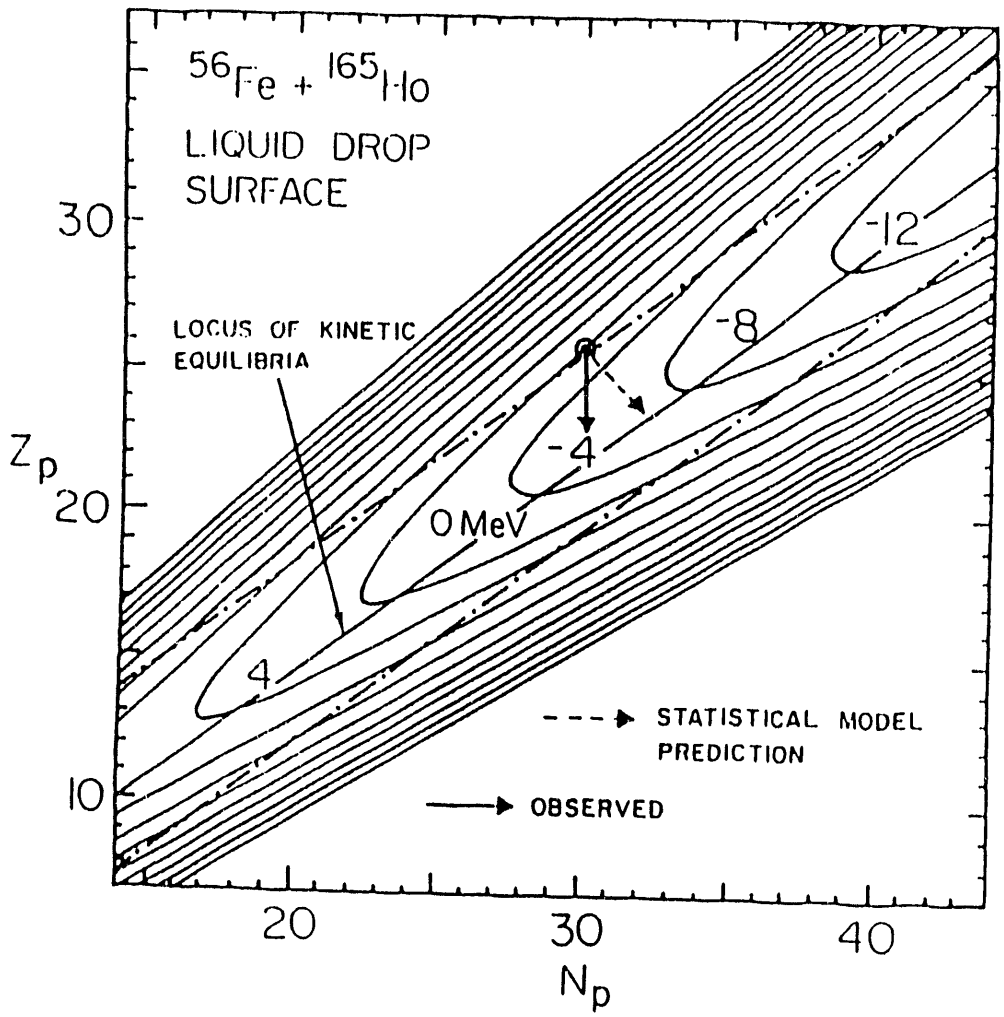

Figure V.1 The potential energy surface plotted in the projectile-like fragment N-Z plane for the ^{56}Fe + ^{165}Ho system. Randrup's model predictions (dashed arrow) follow the direction of the gradient, contrary to the experimental data (solid arrow) [GRIF87, TAS89].

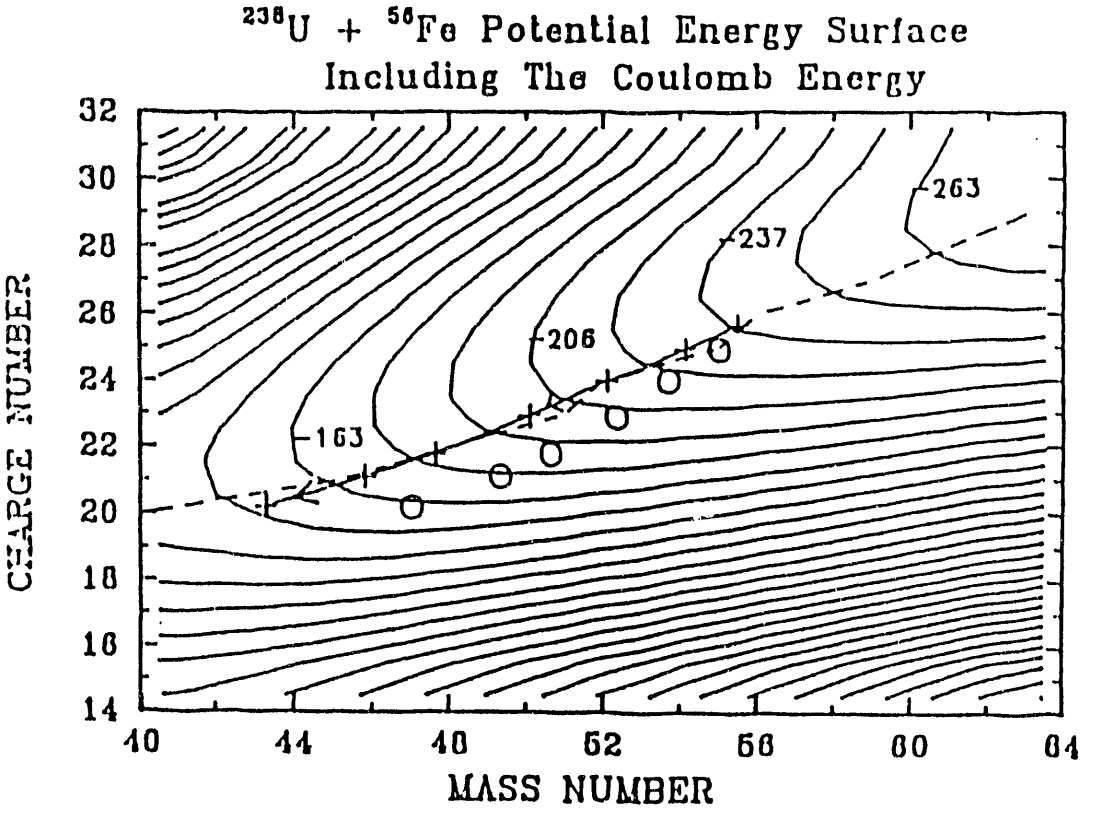

Figure V.2 The potential energy surface defined as ($-Q_{gg} + V_{Coulomb}$) plotted in the projectile-like fragment A-Z plane for the ^{56}Fe + ^{238}U system. The data points (circles) follow a direction opposite to that of the gradient. The β stability line is indicated by the dashes[MER86].

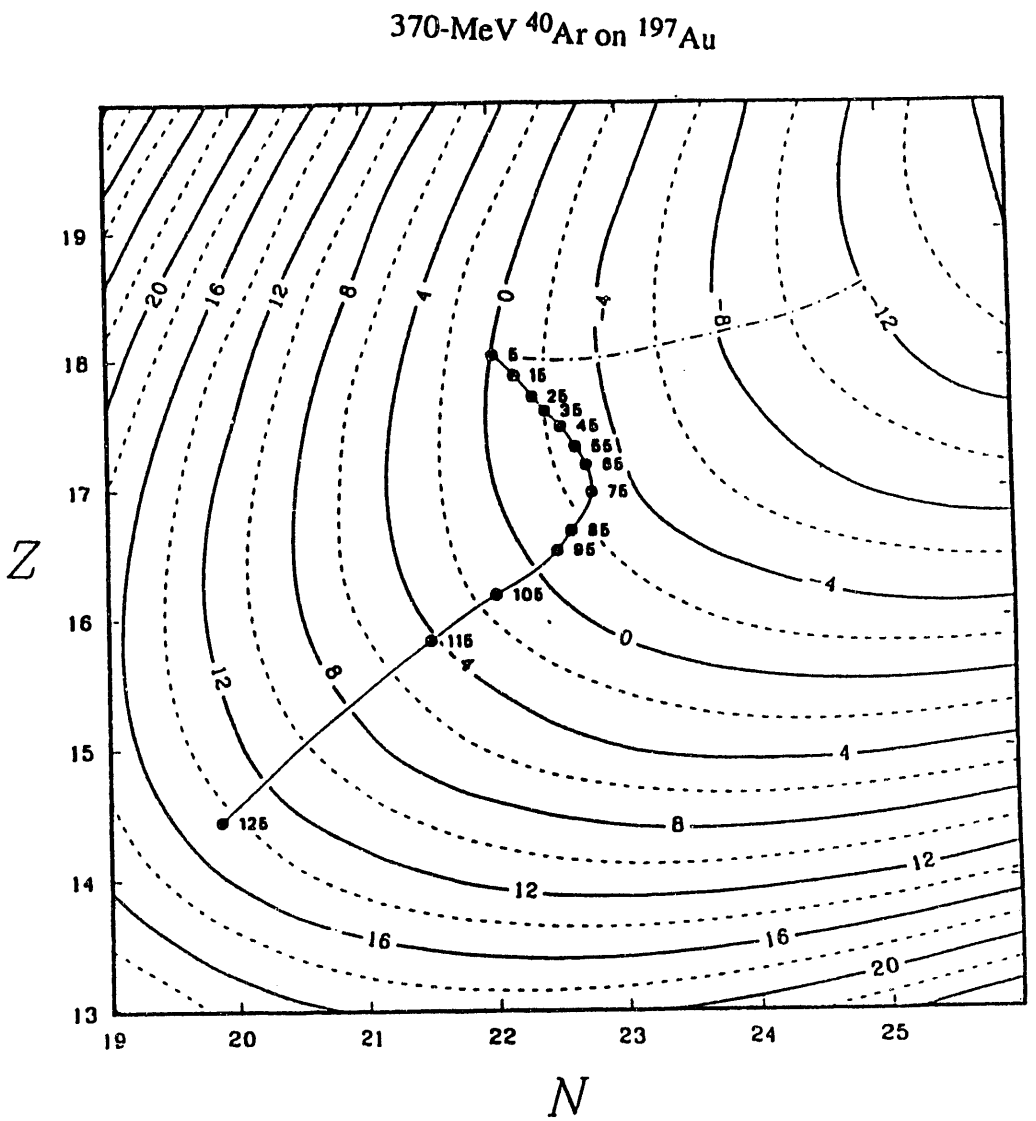

Figure V.3 The potential energy surface plotted on the projectile-like fragment N-Z plane for the ^{40}Ar + ^{197}Au system at 370 MeV. The PES calculations include the Coulomb potential and the centrifugal potential at ℓ = 150 $\hbar$. The trajectory followed by the centroids of the primary distributions (predicted by Tassan-Got's model), as a function of the excitation energy, is shown by circles joined by a solid line. The numbers on the trajectory indicate the excitation energy of the corresponding nuclide. The dot-dashed line indicates the trajectory imposed by the potential gradient [TAS88].

The contrast between the predictions of the two models is further illustrated in Figures V.4 and V.5, where the experimental nuclide distributions obtained for the 672-MeV $^{56}Fe + ^{165}Ho$ and the 840-MeV $^{56}Fe + ^{238}U$ systems are compared to the two model calculations. In these two cases the centroids predicted by Tassan-Got's model are indicated by the dashed curve and those predicted by Randrup's model are indicated by the solid line. The gradient to the potential energy surface is indicated by the arrow. The primary distributions (diamonds) are obtained by kinematical reconstruction for the 672-MeV $^{56}Fe + ^{165}Ho$ system and by neutron evaporation corrections for the 840-MeV $^{56}Fe + ^{238}U$ [MER86]. The random-walk nature of Tassan-Got's model is evident in the way the N-Z curve wanders instead of having the continuous smoothness of the curve obtained from Randrup's model. This effect can be understood from the fact that a mean trajectory approach was used in Randrup's model [RAN82], while the trajectory of the dinuclear system was followed step by step with a Monte Carlo procedure in Tassan-Got's model [TAS88, 89, 91].

Various explanations were suggested to account for the strong negative drift in such asymmetric systems. In a study by Moretto *et al.* [MOR83], a feedback mechanism was explored. This mechanism is due to the existence of a temperature gradient between the two fragments. The lighter nucleus is hotter and therefore, by assuming that particle fluxes depend strongly on temperature, a net transfer of particles from the lighter fragment to the heavier one occurs. Thus, more mass and energy are transferred to the heavier fragment. However, it was shown by Tassan-Got that it does not account for all the discrepancy between theory and experiment [TAS88]. Model calculations were performed by Tassan-Got for the 370-MeV ^{40}Ar on ^{197}Au system with the constraint of thermal

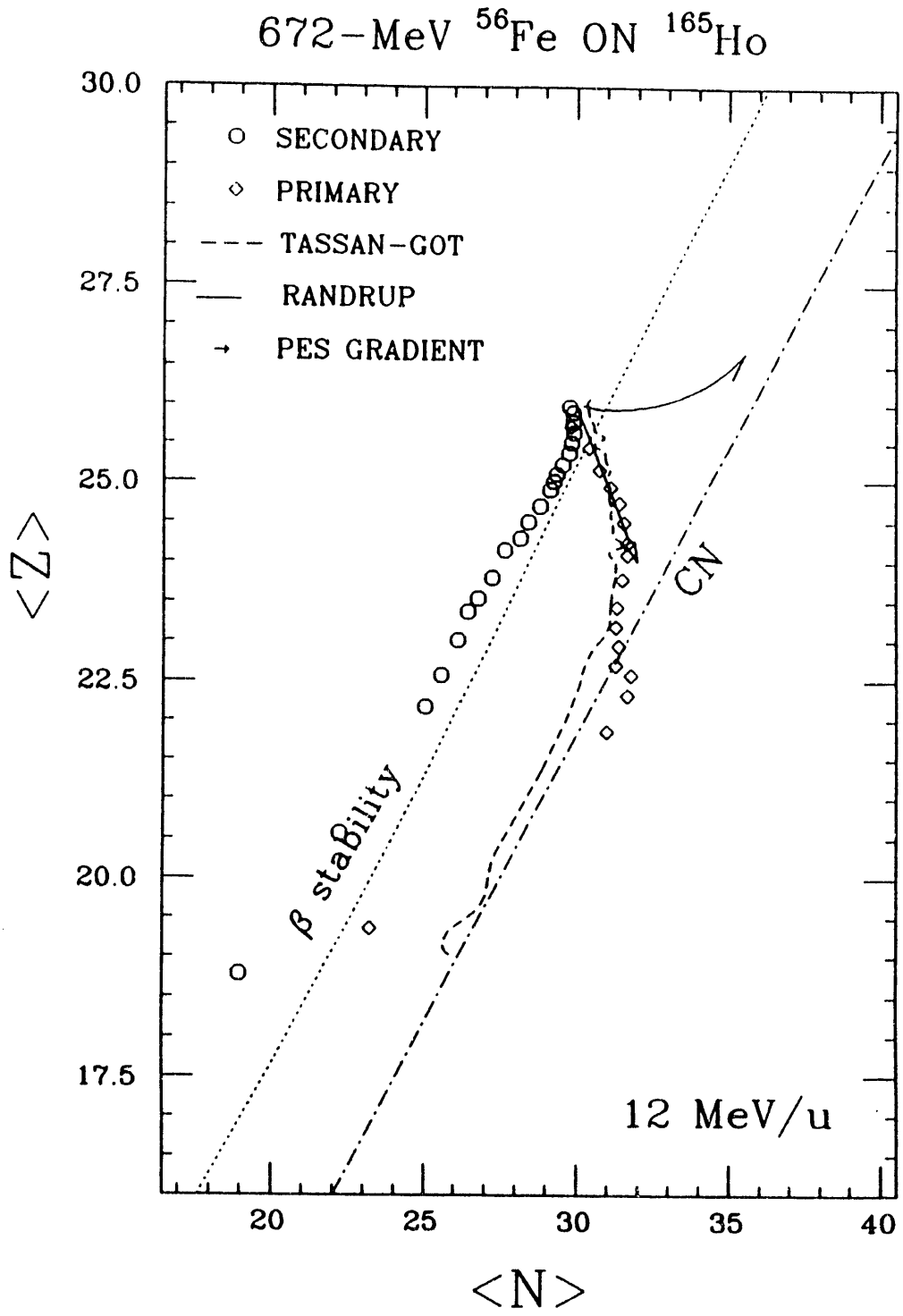

Figure V.4 Evolution of the nuclide distribution in the N-Z plane of the projectile-like fragments produced by the 672-MeV ^{56}Fe + ^{165}Ho system, as a function of energy loss. The experimental distributions are indicated by the circles for secondary fragments and diamonds for primary fragments. The primary distributions predicted by Randrup's model and Tassan-Got's model are indicated by the solid and dashed lines, respectively. The PES gradient at injection point is shown by the arrow.

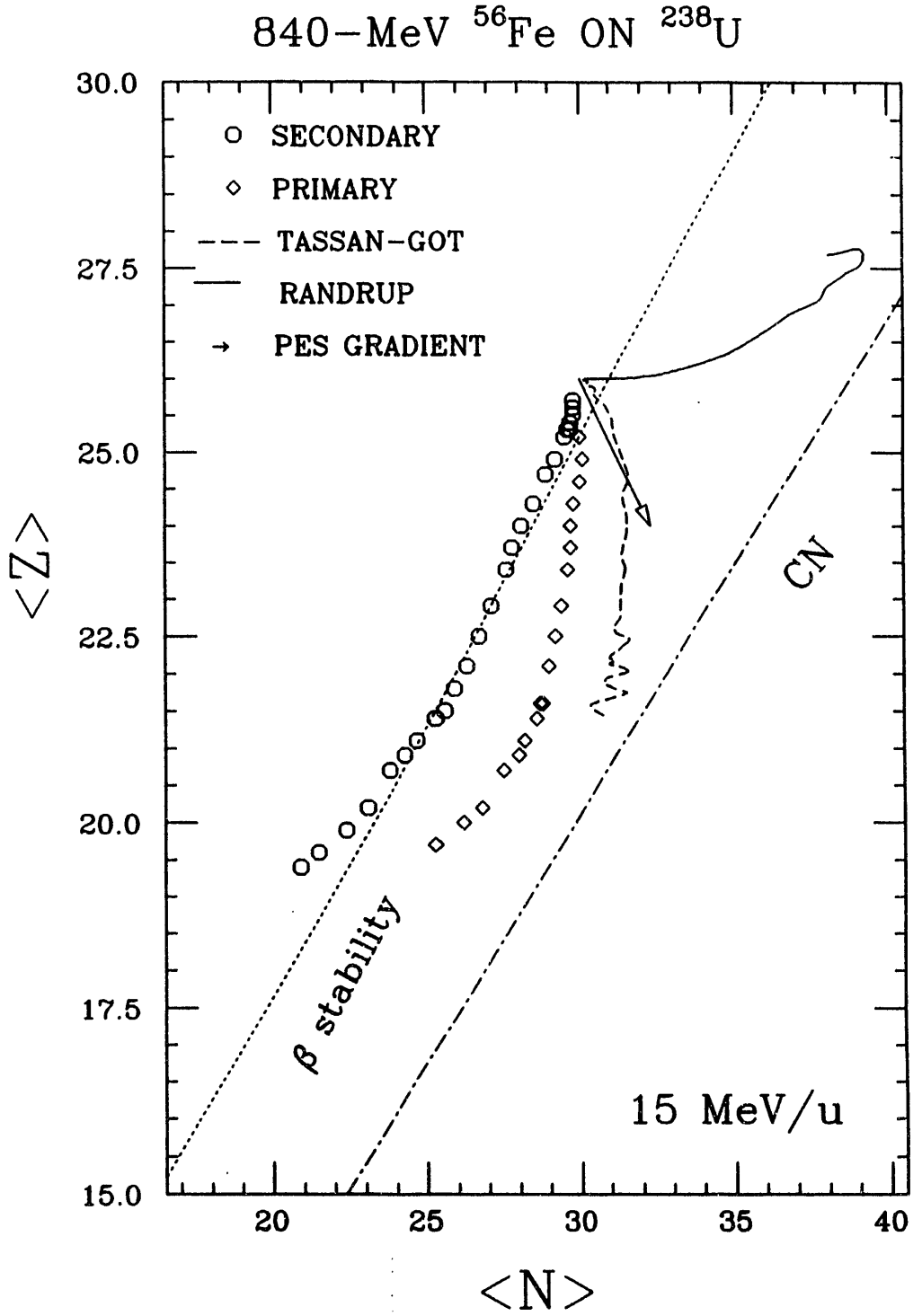

Figure V.5 Evolution of the nuclide distribution in the N-Z plane of the projectile-like fragments produced by the 840-MeV ^{56}Fe + ^{238}U system, as a function of energy loss. The experimental distributions are indicated by the circles for secondary fragments and diamonds for primary fragments. The primary distributions predicted by Randrup's model and Tassan-Got's model are indicated by the solid and dashed lines, respectively. The PES gradient, at injection point is shown by the arrow. The experimental data is from reference [MER86].

equilibrium between the two fragments. The predictions obtained for primary mass and charge distributions were compared to predictions obtained without the thermal equilibrium constraint, as shown in Figure V.6 [TAS88]. No noticeable difference is observed between the two results. Therefore, it could be concluded that a temperature gradient does not significantly affect nucleon transfer.

In another theory by Griffin *et al.*. [GRI87], a non-classical permeation current flowing between the interacting heavy ions from the deeper potential into the shallower one was calculated. This was performed by finding the exact numerical solutions to the simple one-dimensional Schrödinger Double Well model. After an extension of these calculations to three dimensions, and since the depth of the neutron potential well decreases with increasing neutron excess (N - Z), the resulting situation is a flow of neutrons from the heavy nucleus, which has a higher (N - Z) value, to the light nucleus. However, these quantal effects cannot be included in the models discussed here because of their classical treatment of the problem. The calculations from Tassan-Got's model reproduce the negative drift towards mass asymmetry even without taking into account the quantal effects described by Griffin [TAS88]. It could thus be argued that these effects could not be the source of the drift. However, since Tassan-Got's model predictions do not always reproduce experimental results [MAR91], no rigorous conclusion can be made about the influence of quantal effects.

In Tassan-Got's approach the direction of nucleon transfer is dictated by the sign of the difference between the Fermi energies of the two heavy ions [TAS88]. This difference is expressed as

$$\Delta V = e_2 - e'_1 - (e_1 - e'_2) \qquad \text{(V.2)}$$

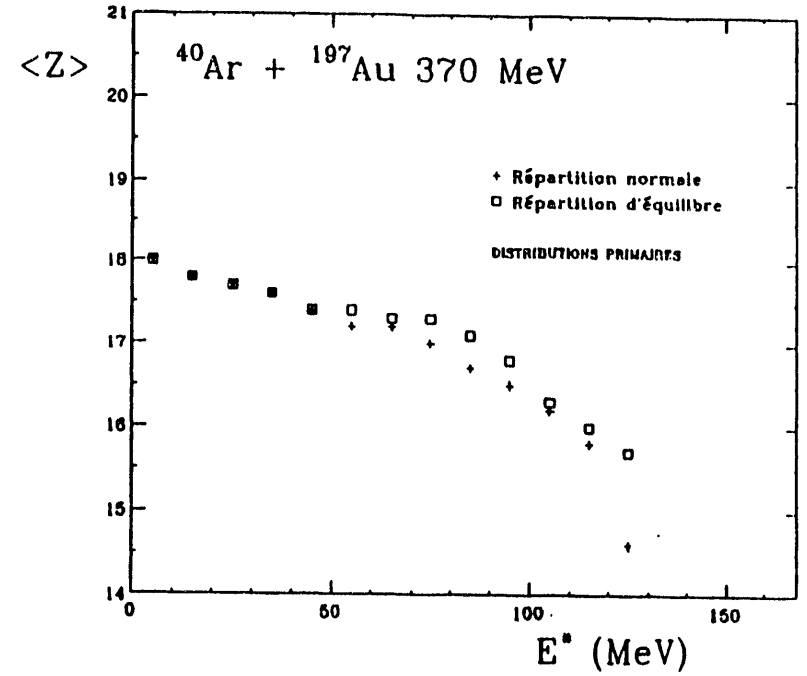

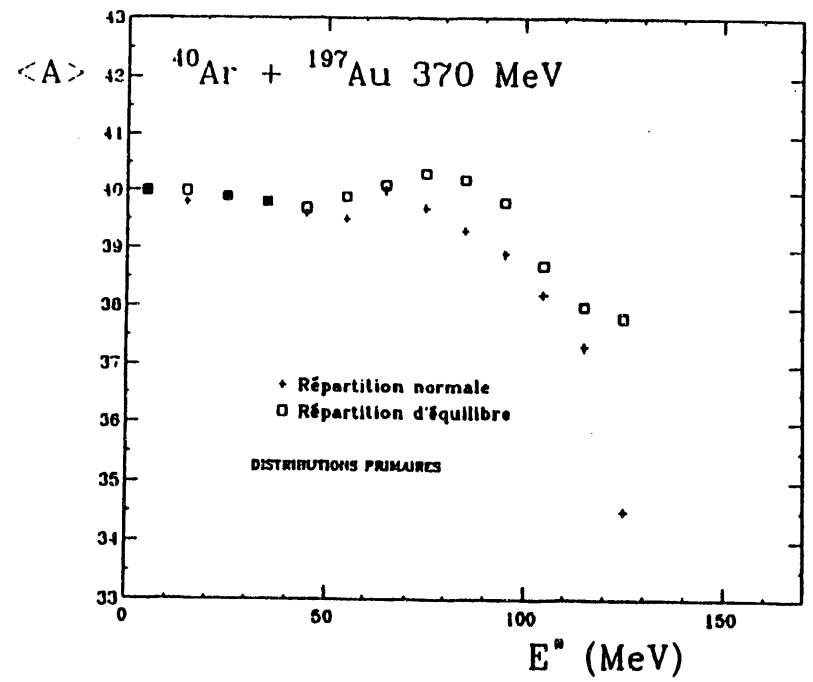

Figure V.6 The charge and mass distributions as a function of excitation energy predicted by Tassan-Got's model for the 370-MeV ^{40}Ar on ^{197}Au system. The squares indicate calculation with a the constraint of thermal equilibrium between the two fragments and the crosses refer to the calculation with no constraint [TAS88].

where e_2 and e'_2 are the Fermi energies of the heavier fragment before and after nucleon transfer occurs, respectively; similarly e_1 and e'_1 describe the lighter fragment. For positive values of ΔV, nucleons are transferred to the lighter nucleus and the opposite is true for negative values of ΔV. An important property of Tassan-Got's model, which is derived from calculations of ΔV, is that the direction of net nucleon transfer is the one that minimizes a quantity equivalent to that of equation V.1, but without the centrifugal term. [TAS88]. The effect of the centrifugal potential on the primary mass distribution is shown in Figure V.7, where the potential defined by equation V.1 is calculated as a function of the mass of one of the primary products for the reaction ^{40}Ar on ^{197}Au. Three different values of relative angular momentum are shown. For systems with an injection point around a mass number of 40 for the lighter ion, the centrifugal part of the potential favors mass symmetry for high values of relative angular momentum, while asymmetry is favored for angular momentum 0 $\hbar$. However, Tassan-Got's model predictions fail to reproduce experimental values at high energy damping [TAS88]. This is attributed by Tassan-Got to the fact that, at long interaction times, the boundaries between the two fragments become increasingly blurred, and therefore, the system can no longer be considered binary.

V.B Equilibration of the Neutron-to-Proton Ratio

Experimental evidence suggests that charge equilibration is reached faster than mass equilibration in deep-inelastic heavy-ion reactions. The N/Z equilibration is attained at very early stages of the reaction, as characterized by relatively small energy losses. Since this conclusion is deduced from the

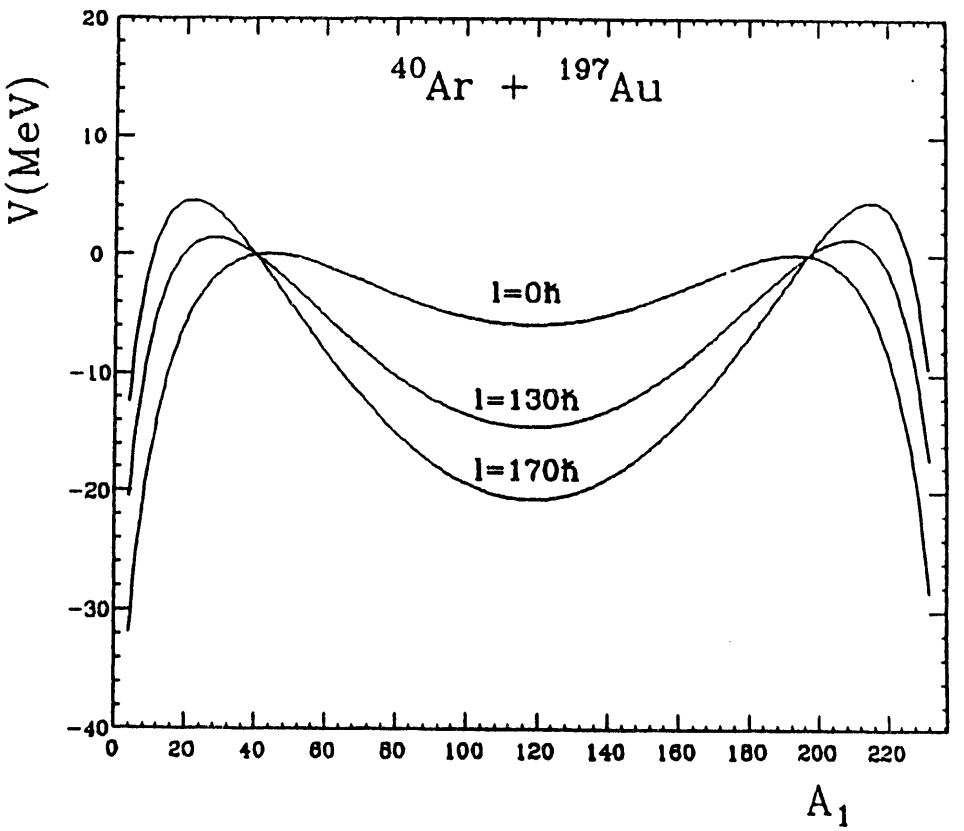

Figure V.7 The potential energy surface as a function of the mass of one fragment for the 370-MeV ^{40}Ar + ^{197}Au system, for different values of relative angular momentum [TAS88].

observation of secondary events, it is necessary to examine the effects of evaporation on the results.

The N/Z ratios of the PLF's produced in the 505-MeV and the 672-MeV ^{56}Fe on ^{165}Ho, and the 840-MeV ^{56}Fe on ^{238}U reactions are plotted as a function of TKEL in Figure V.8. The N/Z ratios of post-evaporation products (circles) remain fairly constant for most values of TKEL. A decrease in N/Z is observed for the 672-MeV ^{56}Fe on ^{165}Ho, and the 840-MeV ^{56}Fe on ^{238}U when the limit of TKEL imposed by the Coulomb barrier is reached. The N/Z ratios of the primary PLF's (solid line) were obtained by applying evaporation corrections to generate a primary ratio, with the assumption that the evaporated mass is mostly due to neutron evaporation. The increase of the primary N/Z ratio with increasing TKEL for the three systems is indicative of the formation of products rich in neutrons .

A correlation between the N/Z ratio and charge and neutron drifts was studied by DeSouza *et al.*. [SOU88]. These drifts, calculated as <Z>-Zp and <N>-Np, the differences between average secondary quantities and entrance channel values, for the systems ^{40}Ca (N/Z = 1), ^{58}Ni (N/Z = 1.07), ^{64}Ni (N/Z = 1.29), and ^{48}Ca (N/Z = 1.4) on ^{238}U at 8.5 MeV/u, are plotted as a function of energy loss in Figures V.9-a and V.9-b. The proton drifts show a strong correlation with the N/Z ratio of the projectile, as observed in Figure V.9-a. Smaller drifts are observed for systems with larger projectile N/Z ratios. The proton drifts were also found to depend on the driving force, which is expressed as the PES gradient; for a small driving force charge transfer is not significant. This effect was shown in Figure I.4, where the nuclide distributions for the 8.5 MeV/u ^{58}Ni, and ^{64}Ni on ^{238}U were displayed. A larger proton transfer is observed for the ^{58}Ni case, which is characterized by a larger gradient than for the ^{64}Ni case.

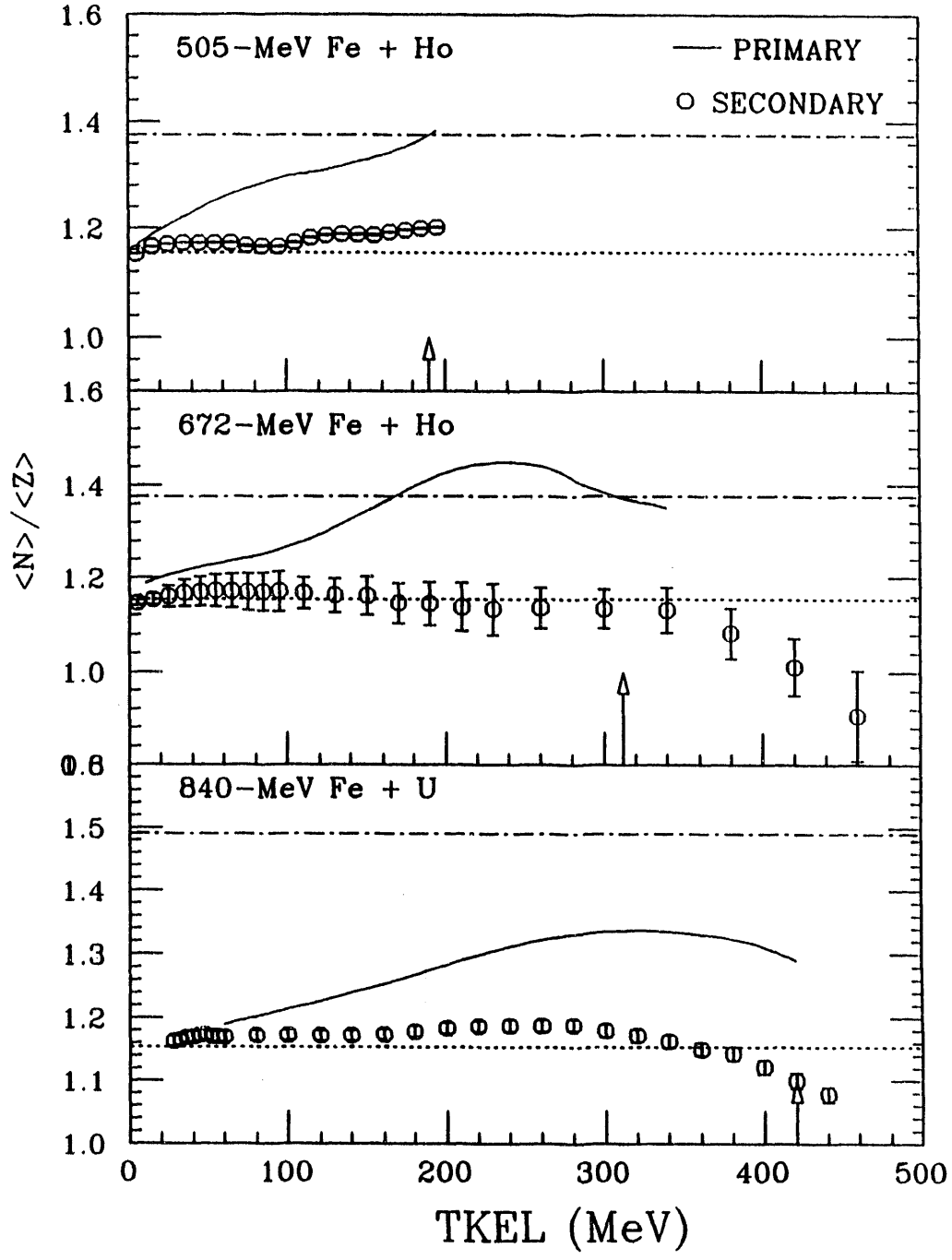

Figure V.8 Experimental values of the <N>/<Z> ratio as a function of energy loss for the reactions 505-MeV ^{56}Fe + ^{165}Ho [BEN85, 87, 88], 672-MeV ^{56}Fe + ^{165}Ho, and 840-MeV ^{56}Fe on ^{238}U [MER86]. Secondary distributions are indicated by circles and primary distributions are indicated by the solid line. The N/Z ratio of the projectile and the composite system are indicated by the dotted and dot-dashed lines, respectively.

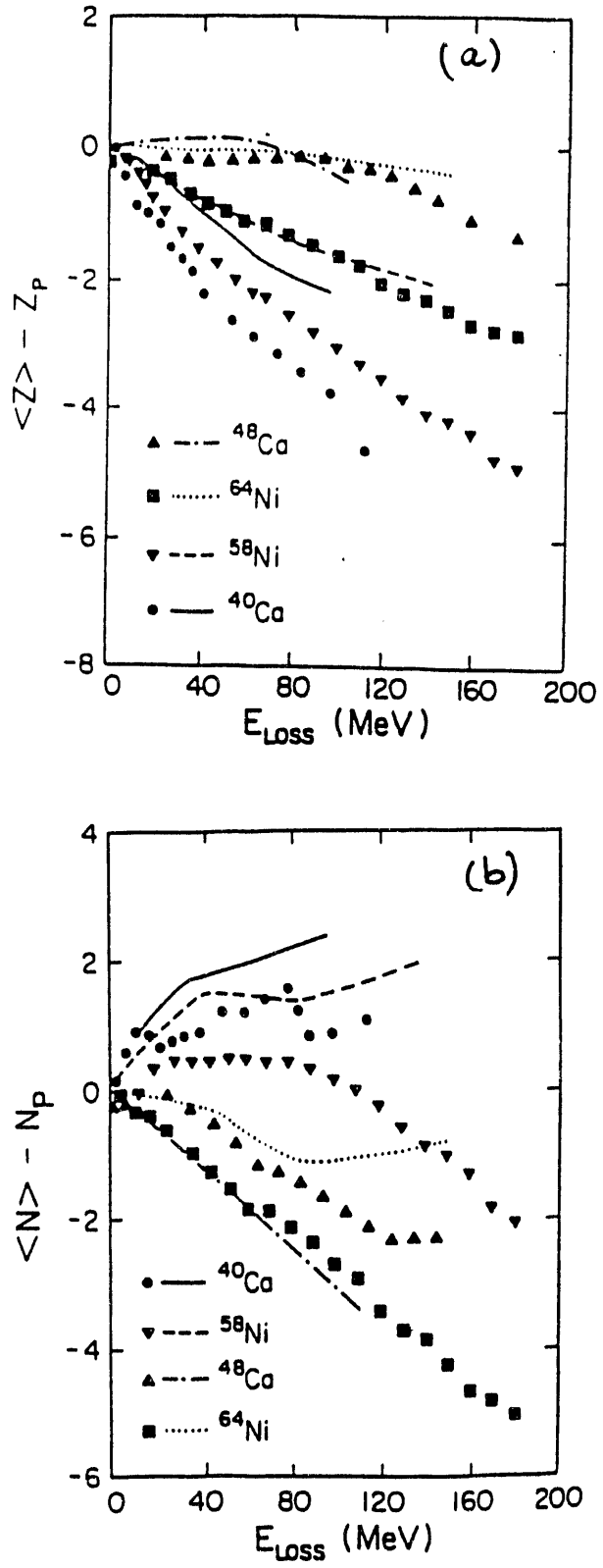

Figure V.9 Average proton (a) and neutron (b) drifts for the reactions ^{40}Ca (N/Z = 1), ^{48}Ca (N/Z = 1.4), ^{58}Ni (N/Z = 1.07), and ^{64}Ni (N/Z = 1.29) on ^{238}U (N/Z = 1.59) at E/A = 8.5 MeV, as a function of energy loss. The lines indicate Randrup's model predictions corrected for evaporation.

Figure V.9-b shows that the neutron drifts do not exhibit the same correlation with the projectile N/Z ratio as do the proton drifts. However, neutron evaporation is considerably more significant than proton evaporation and, since it is not taken into account in the calculations of the proton and neutron drifts, the correlation between the projectile N/Z ratio and the neutron drifts is not as rigorously observed as in the case of proton drifts. The results for the systems with ^{58}Ni and ^{40}Ca are consistent with the correlation observed for the proton drift, while the order is inverted for the ^{48}Ca and ^{64}Ni systems. No correlation could be found between the mass asymmetry of the entrannce channel and the magnitude of the proton and neutron drifts. It seems that these latter differences in projectile N/Z ratios have a more important impact on the drifts than do mass asymmetries.

V.C. Distribution Variances

In a deep-inelastic mechanism the variances of fragment distributions are a measure of the number of nucleons exchanged between the interacting heavy ions. This is true in the context where nucleon exchange is considered as a stochastic process and, in that case, the number of nucleons exchanged between the two partners is expressed as

$$N_{ex} = \sigma_A^2, \qquad (V.3)$$

At low energy dissipation σ_A^2 depends linearly on the square root of the relative kinetic energy above the Coulomb barrier $\sqrt{T}$, which is calculated as

$$\sqrt{T} = \sqrt{E_{cm} - V_c - TKEL}, \qquad (V.5)$$

where E_{cm} is the initial center-of-mass kinetic energy, V_c is the Coulomb energy in the spherical nuclei approximation, and TKEL is the total kinetic energy loss [SCH77]. The linear dependence of $\sqrt{T}$ on σ_A^2 is an indication of the proportionality between the number of exchanges and the energy dissipated, thus supporting the idea of using nucleon exchange as means for energy dissipation.

A plot of $\sqrt{T}$ as a function of σ_A^2 is shown in Figure V.10 for the 465-MeV (solid squares) and 672-MeV (circles) $^{56}Fe + ^{165}Ho$ systems. In both cases $\sqrt{T}$ is linearly proportional to σ_A^2 thus verifying the linear relationship between σ_A^2 and $\sqrt{T}$. The slope of the $\sqrt{T}$ vs σ_A^2 curve for the higher bombarding energy system was found to be about 1.5 times larger than that of the lower bombarding energy system. This is an expected result since the same number of exchanges would result in about the same amount of energy dissipation in both systems and thus, the higher bombarding energy system would be left with a higher $\sqrt{T}$ value. However, at large energy damping, the 465-MeV data seems to reach a plateau, while the 672-MeV data continues to decrease.

V.D. Excitation Energy Division

Knowledge of how the excitation energy of the system is divided between the two fragments of a deep-inelastic reaction is crucial to understanding the mechanisms involved in these reactions. It is particularly interesting to know if statistical equilibrium is reached at the short interaction times (10^{-20} sec) that are characteristic of these reactions. However, the excitation energy of the reaction fragments cannot be measured directly and has to be inferred from other measured observables.

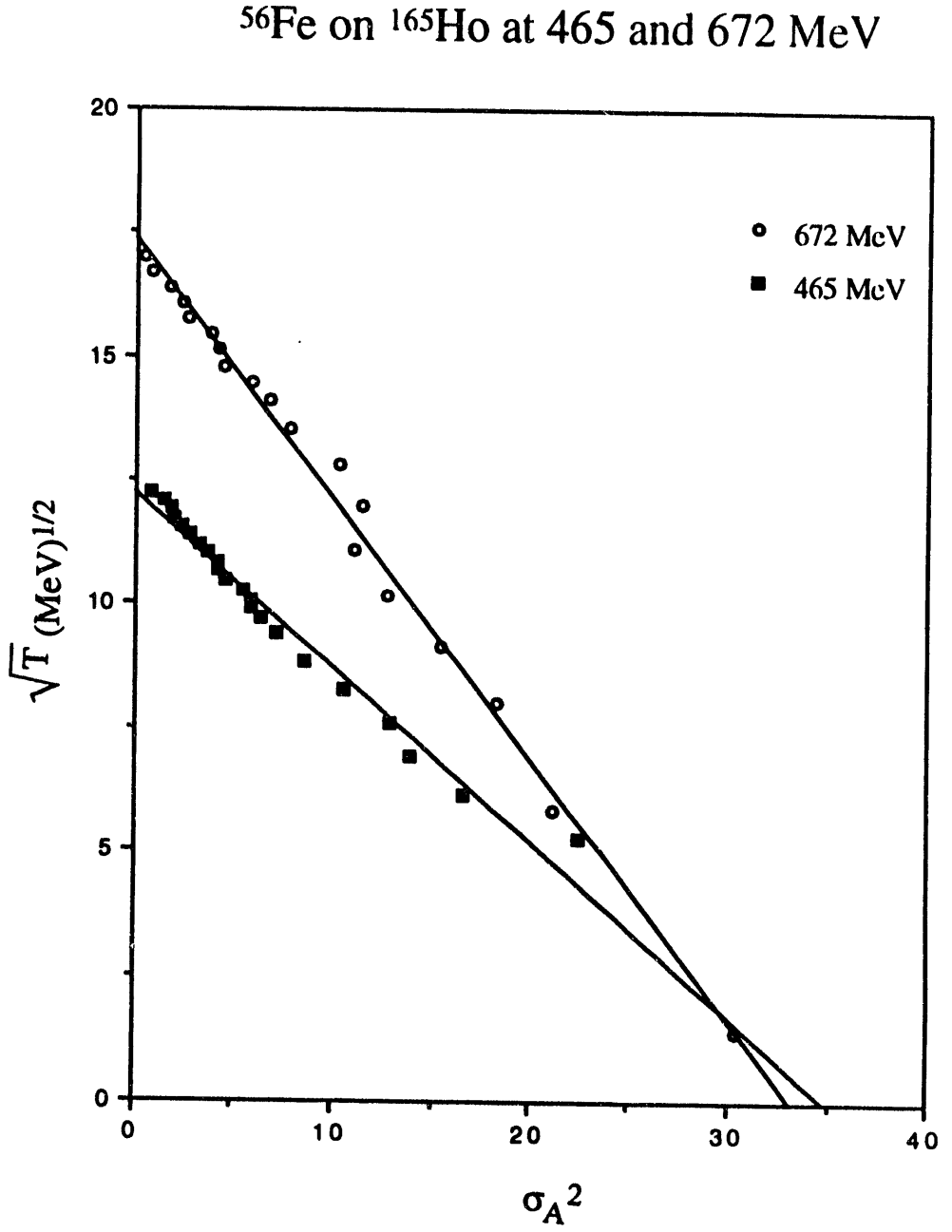

Figure V.10 The square root of the available kinetic energy above the Coulomb barrier as a function of σ_A^2 for the 465-MeV (diamonds) and 672-MeV (circles) ^{56}Fe on ^{165}Ho reactions. The 465-MeV data are from reference [BRE83a]. The equations obtained after performing linear fits are:
$\sqrt{T} = 12.235 - 0.352\ \sigma_A^2$ for the 465-MeV system.
$\sqrt{T} = 17.522 - 0.551\ \sigma_A^2$ for the 672-MeV system.

The kinematic coincidence technique was used in the study of the 505-MeV ^{56}Fe on ^{165}Ho system by Benton *et al.* [BEN85, 87, 88] and the 629-MeV ^{74}Ge on ^{165}Ho system by Planeta *et al.* [PLA90]. The results for the Fe + Ho system are illustrated in Figure V.11, where the PLF excitation energy ratio E^*_{PLF}/E^*_{TOT} is plotted as a function of TKEL. The limits of equal excitation energy division and thermal equilibrium are indicated . These results suggest that equal sharing of the energy is favored at low energy losses (<50 MeV), whereas for larger energy losses, the data show a tendency towards a division according to mass ratios. However, there is no evidence of thermal equilibrium, even at the highest energy loss values. A qualitatively similar behavior is exhibited by the data of the Ge + Ho system, as shown in Figure V.12.

The present study of the 672-MeV ^{56}Fe on ^{165}Ho system is intended to provide a wider range of energy damping than previously explored. It is especially interesting to compare its results to the ones obtained with the same reaction at a lower bombarding energy (505 MeV). The PLF's fraction of excitation energy is plotted in Figure V.13 as a function of energy loss for the two Fe + Ho systems . The same qualitative behavior is observed for both cases. A larger portion of excitation energy is stored in the PLF than the TLF at low energy damping. As the energy loss increases, the system evolves gradually towards a configuration that decreases the temperature gradient between the two fragments but does not fully equilibrate, even at the highest energy damping.

One remarkable feature in Figure V.13 is the higher PLF excitation energy ratios in the higher bombarding energy case. A possible explanation could be the higher relative velocity, or a shorter interaction time. To further explore this point, the $\langle E^*_{PLF}/E^*_{TOT}\rangle$ ratios obtained for asymmetric systems at different bombarding energies (the 476-MeV ^{56}Fe + ^{238}U, the 505-MeV and 672-MeV ^{56}Fe

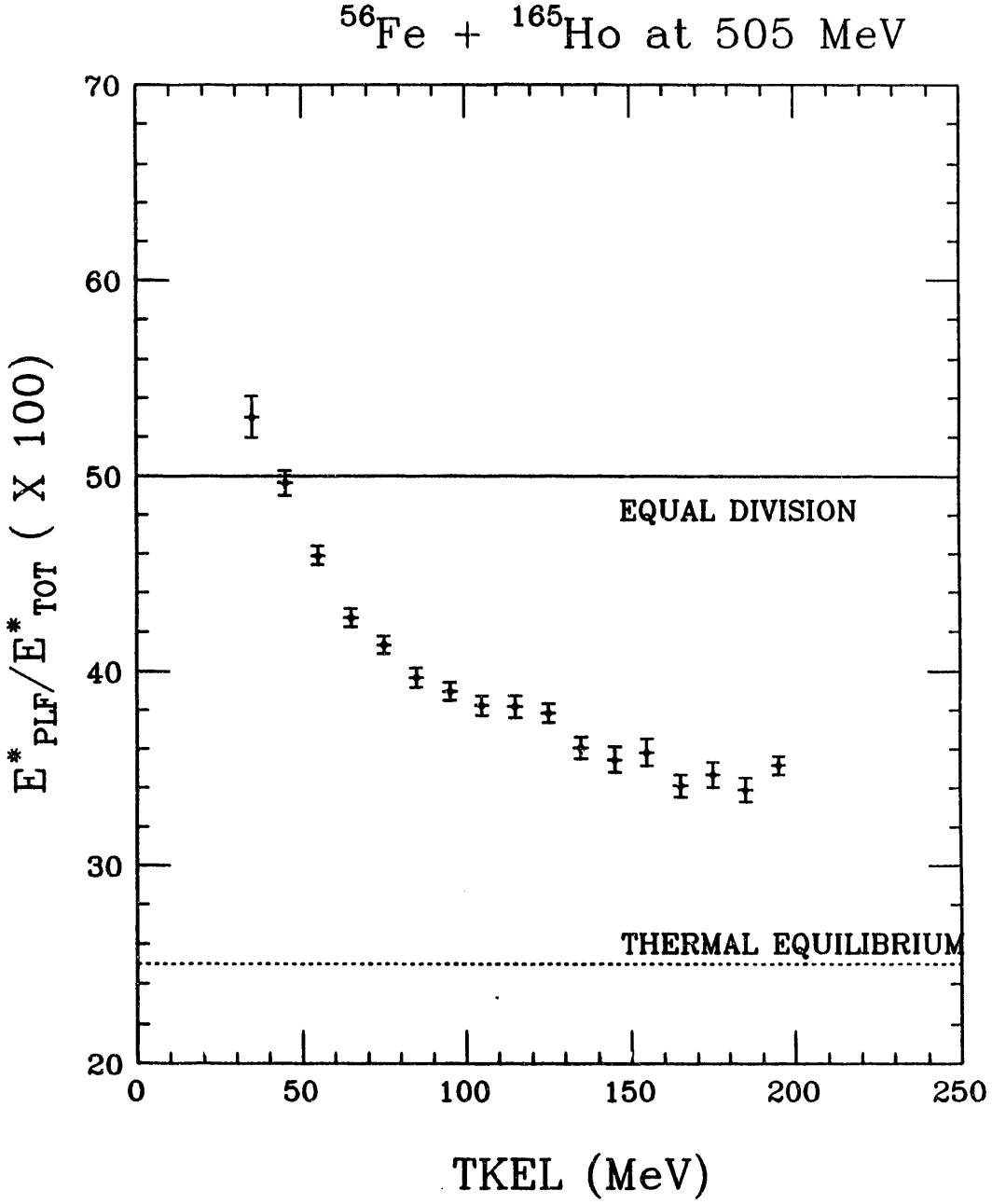

Figure V.11 The PLF excitation energy ratio as a function of energy loss for the 505-MeV ^{56}Fe on ^{165}Ho system. All isotopes are included. The limits of equal excitation energy division (solid line) and thermal equilibrium (dotted line) are indicated [BEN87].

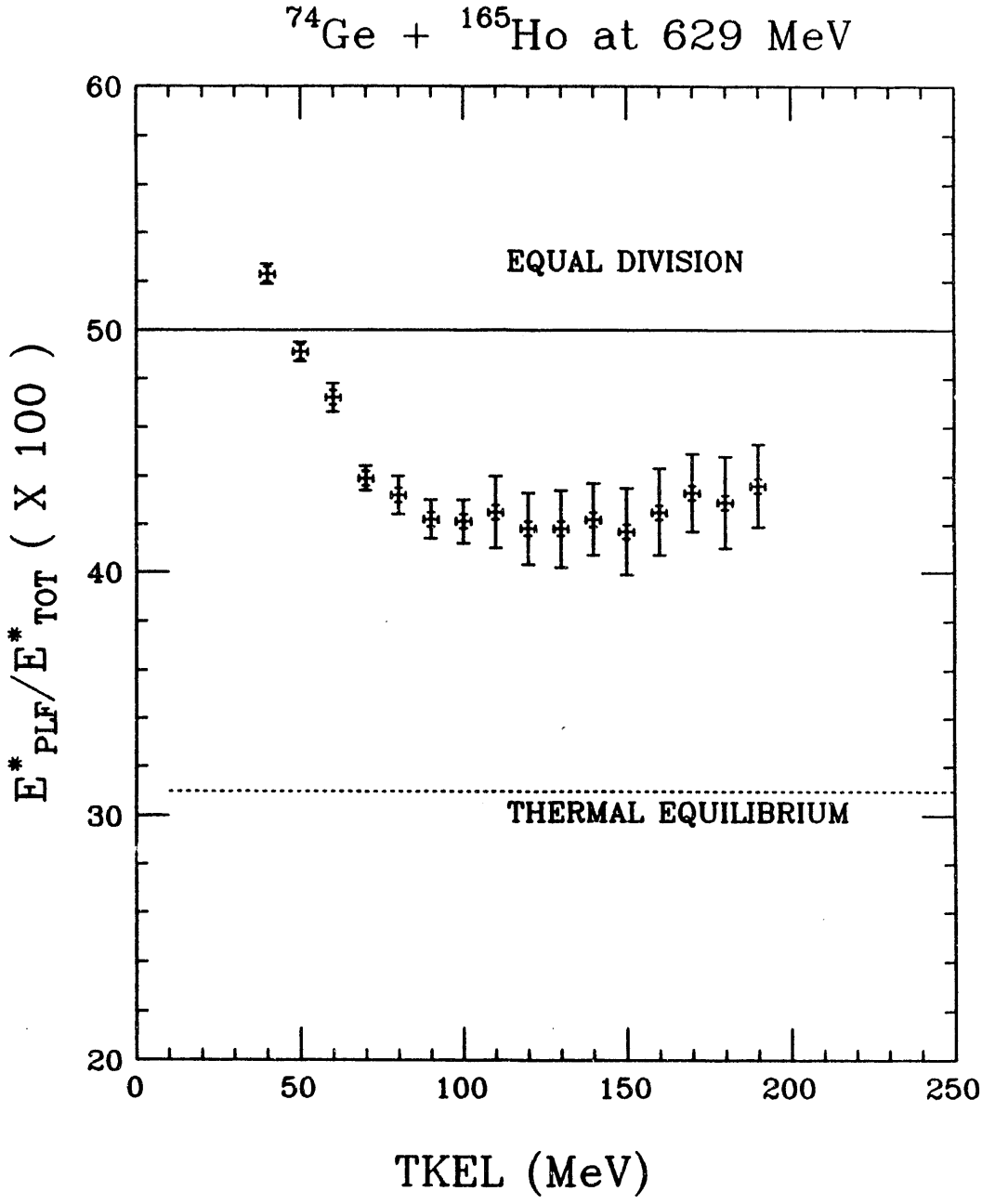

Figure V.12 The PLF excitation energy ratio as a function of energy loss for the 629-MeV ^{74}Ge on ^{165}Ho system. All isotopes are included. The limits of equal excitation energy division (solid line) and thermal equilibrium (dotted line) are indicated [KWI90].

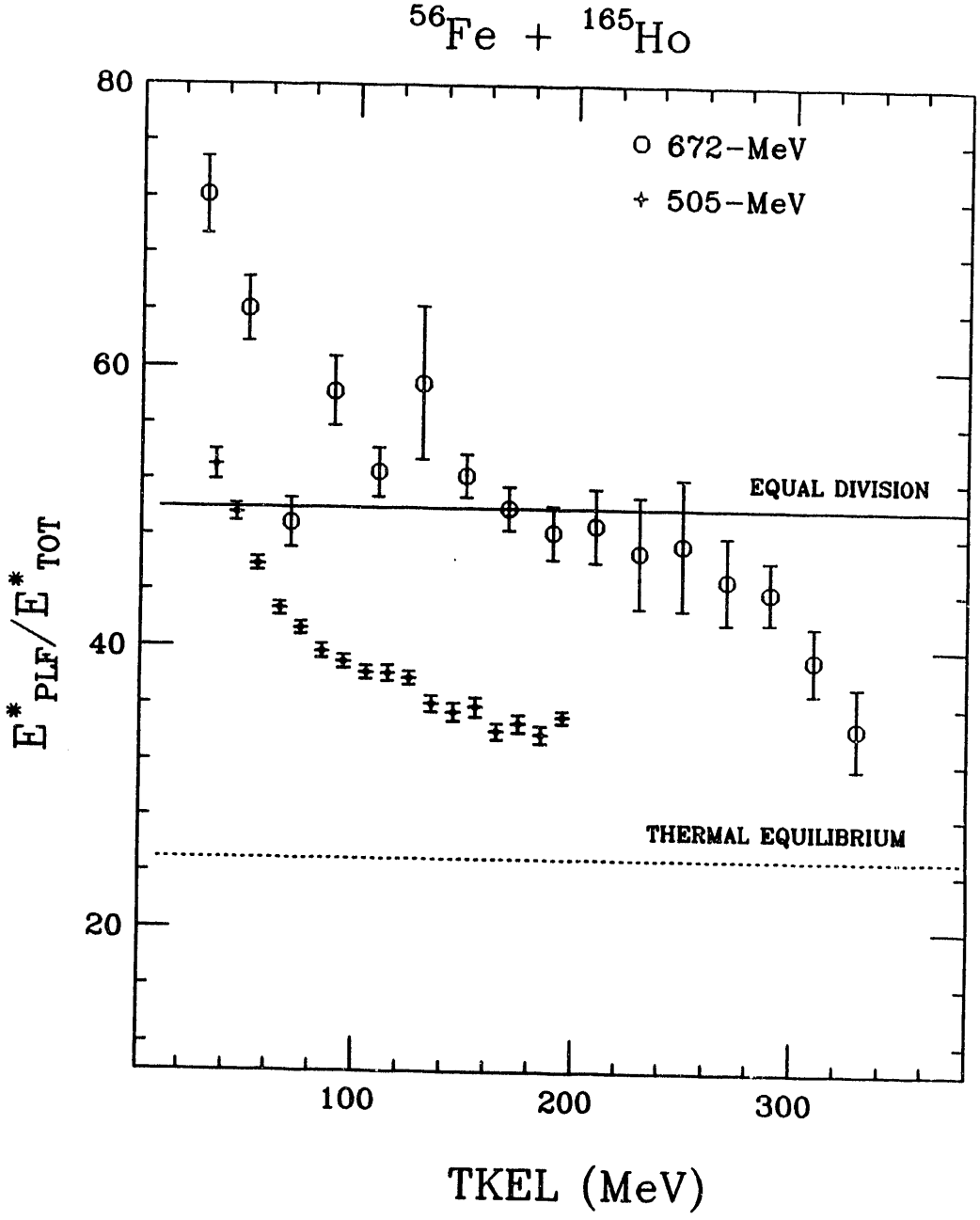

Figure V.13 The PLF excitation energy ratio as a function of energy loss for the 505-MeV (crosses) and the 672-MeV (circles) ^{56}Fe on ^{165}Ho system. The solid and dotted lines indicate the limits of equal excitation energy division and thermal equilibrium, respectiveley. All isotopes are included. The 505 MeV data is from reference [BEN87].

on ^{165}Ho, and the 629-MeV ^{74}Ge on ^{165}Ho systems) are plotted as a function of energy loss in Figure V.14. The limits of equal division and thermal equilibrium for each system are as indicated. There appears to be a direct dependence between the bombarding energy and the magnitude of the PLF excitation energy fraction: the higher the bombarding energy the larger the ratio of excitation energy stored in the PLF.

V.E. Mass Dependence of Excitation Energy Ratio

Another feature of the excitation energy division in deep-inelastic reactions is its apparent dependence on the exit channel. This correlation was observed for the 505-MeV ^{56}Fe + ^{165}Ho system by Benton *et al.* [BEN85, 87, 88] and the 629-MeV ^{74}Ge + ^{165}Ho system by Planeta *et al.* [PLA90]. Figures V.15-a and V.15-b show the PLF excitation energy ratio obtained for the 505-MeV Fe + Ho system, as a function of A'_{PLF} and A''_{PLF}, for TKEL values between 100 MeV and 150 MeV. The same type of plot is shown in Figure V.16-a and V.16-b for different TKEL bins, for the 629-MeV Ge + Ho system. Figures V.15-a and V.16-a show that in both systems the PLF is hotter than the TLF for pickup reactions (A'_{PLF}> A of projectile) at low energy damping. The opposite is true for stripping reactions (A'_{PLF}<A of projectile). The mass dependence is weaker at higher dissipation energies. The dependence of the E^*_{PLF}/E^*_{TOT} on the primary PLF mass (A'_{PLF}) is also observed for the present data of the 672-MeV Fe + Ho system, but to a lesser degree, as shown in Figures III.15, and III.17 of Chapter III. The results of the 629-MeV ^{74}Ge on ^{165}Ho system (Figure V.16-a) show that the correlation between primary fragment mass and excitation energy sharing

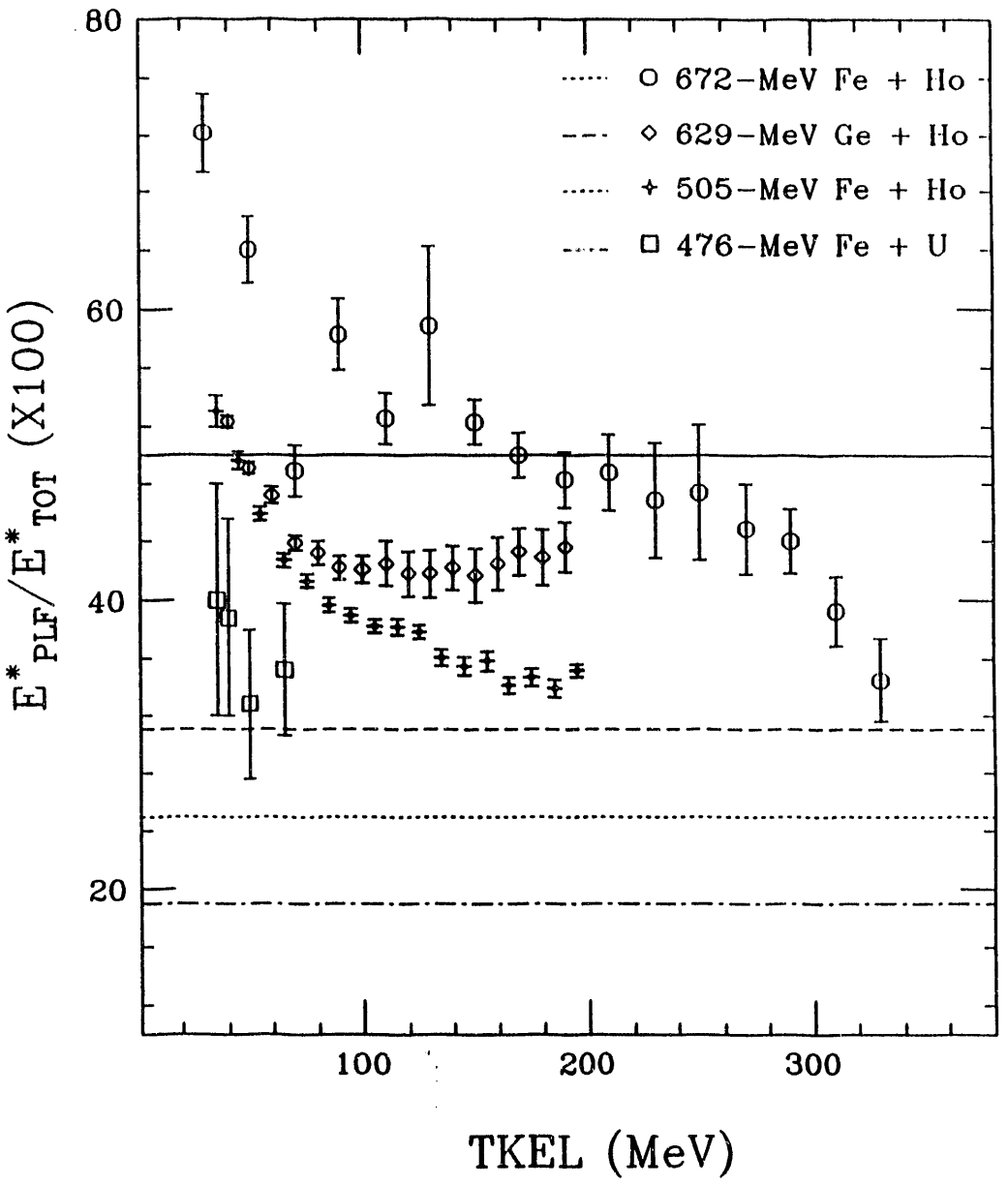

Figure V.14 The PLF excitation energy ratio as a function of energy loss for the 505-MeV (crosses) and 672-MeV (circles) ^{56}Fe on ^{165}Ho, the 476-MeV ^{56}Fe on ^{238}U (squares), and the 629-MeV ^{74}Ge on ^{165}Ho (diamonds) reactions . All isotopes are included. The 476-MeV ^{56}Fe on ^{238}U data is from reference [VAN84], the 505-MeV ^{56}Fe on ^{165}Ho data from reference [BEN87], and the 629-MeV ^{74}Ge on ^{165}Ho from reference [KWI90]. The equal excitation energy division limit is indicated by the solid line. The thermal equilibrium limit is indicated by the dashed line for Ge + Ho, the dotted line for Fe + Ho, and the dot-dashed line for Fe + U.

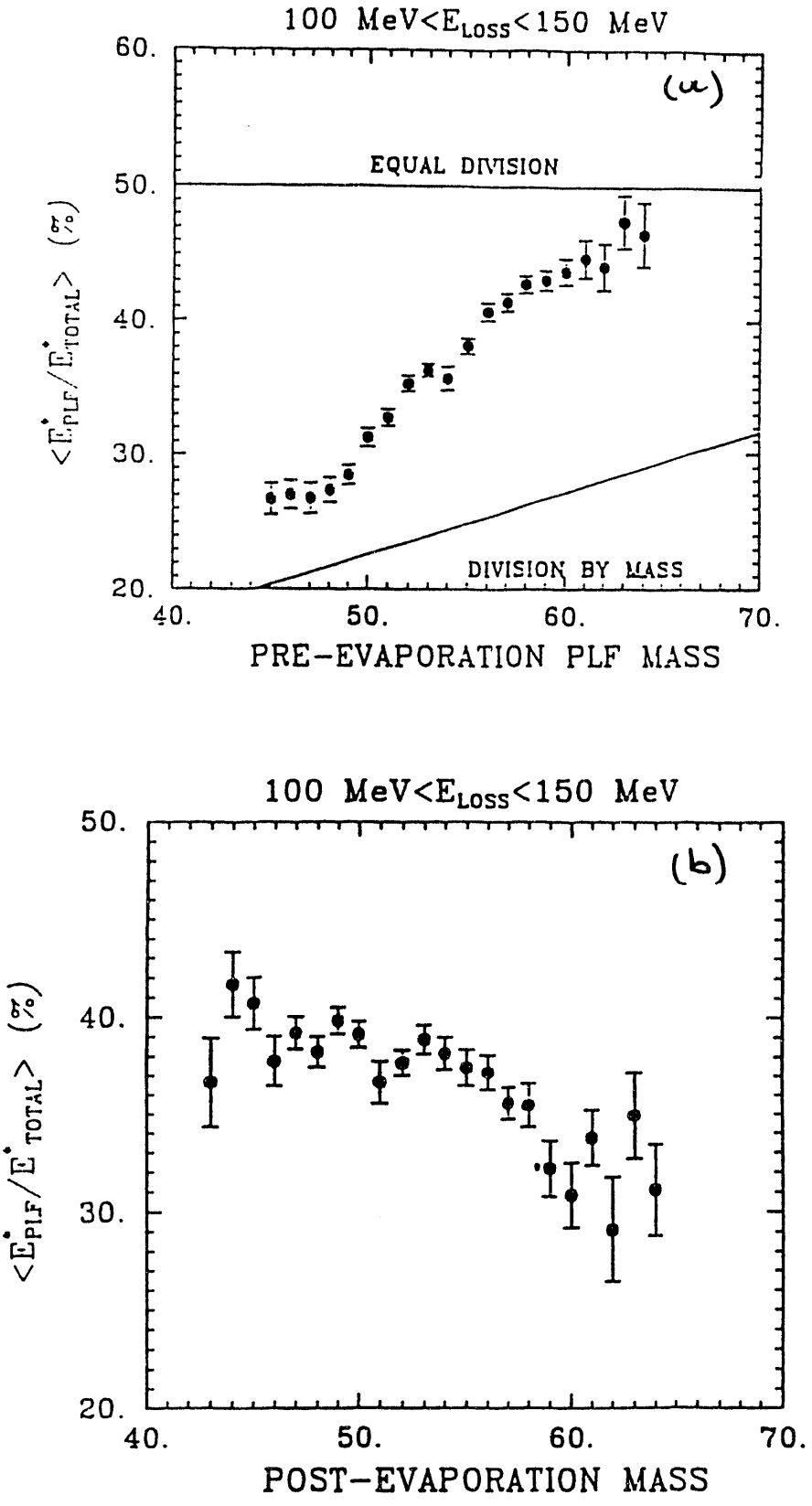

Figure V.15 The PLF excitation energy division ratio as a function of (a) pre-evaporation mass, and (b) post-evaporation mass for the 505-MeV ^{56}Fe on ^{165}Ho reaction. Only data in the 100-150 MeV energy loss range are included [BEN87].

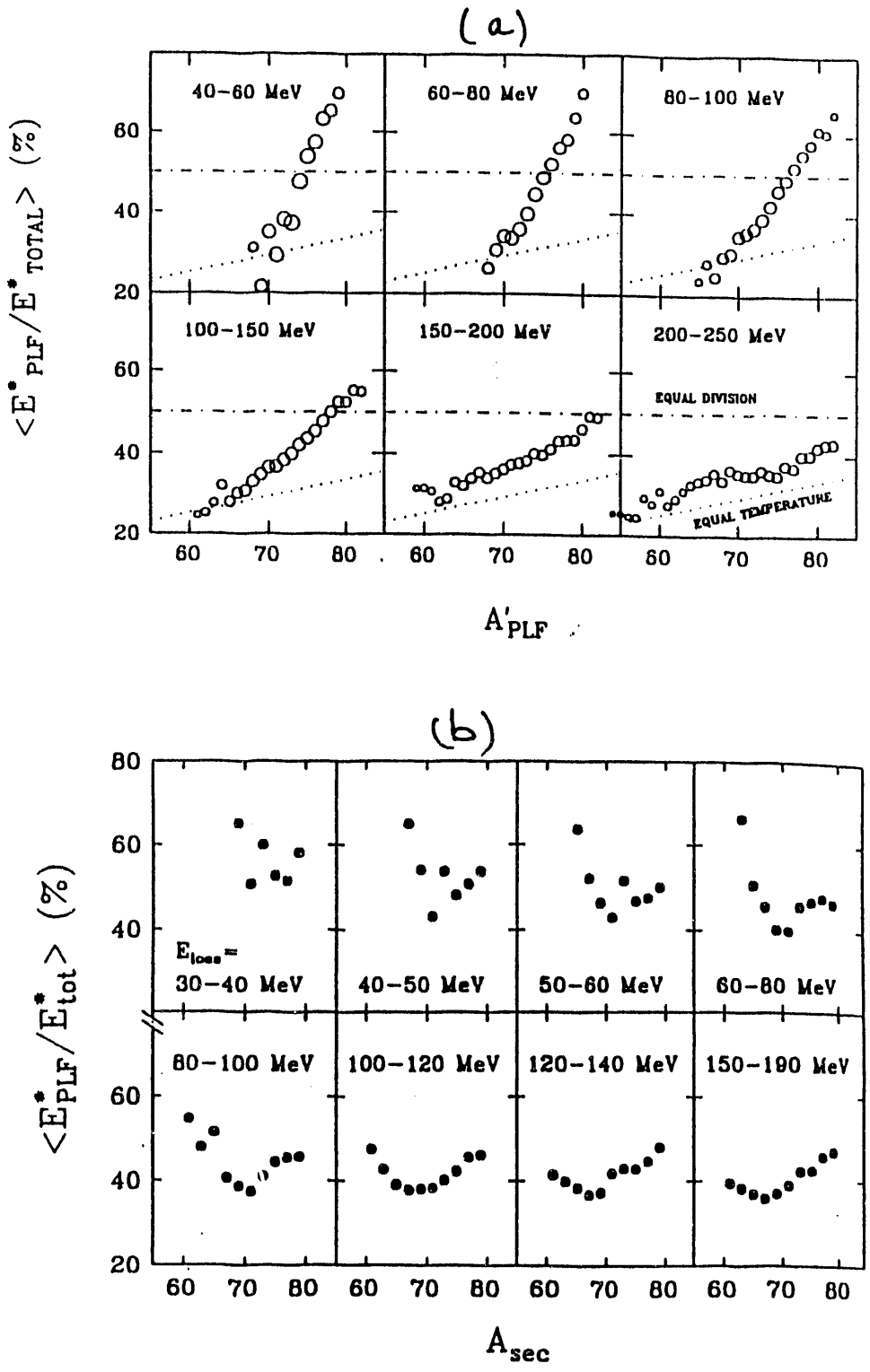

Figure V.16 The PLF excitation energy division ratio as a function of (a) pre-evaporation mass, and (b) post-evaporation mass for the 629-MeV ^{74}Ge on ^{165}Ho reaction, for several energy loss bins [KWI90,TOK91].

decreases with increasing energy loss. No such energy sharing is noticeable in the 672-MeV ^{56}Fe on ^{165}Ho system.

Figures V.15-b and V.16-b show that the correlation of the E^*_{PLF}/E^*_{TOT} ratio with the post-evaporation mass is weaker than its correlation with the pre-evaporation mass, and has a different character. In the case of the Fe + Ho system, the E^*_{PLF}/E^*_{TOT} centroids associated with larger post-evaporative masses are smaller than those associated with smaller post-evaporative masses for the 100-150 MeV TKEL bin. This can be explained by the fact that the larger secondary masses are produced by primary fragments with smaller excitation energies, and therefore, lost only a small amount of mass by evaporation.

Similarly, the smaller secondary masses are associated with larger excitation energies. Therefore, for a constant total excitation energy, E^*_{TOT}, a smaller ratio is obtained for large secondary masses, and a larger ratio is obtained for small secondary masses. However, while this reasoning is always valid for cases of primary distributions with no net drift, it has to be applied more carefuly when dealing with distributions with strong positive or negative drifts. The same behavior of the E^*_{PLF}/E^*_{TOT} ratio as a function of $A"_{PLF}$ is observed in the Ge + Ho system for TKEL values smaller than ~100 MeV. The dependence of E^*_{PLF}/E^*_{TOT} on $A"_{PLF}$ decreases considerably with increasing energy loss. This is consistent with the decrease in its dependence on A'_{PLF}. Plots of E^*_{PLF}/E^*_{TOT} as a function of $A"_{PLF}$ for inclusive events, and for events gated on TKEL, displayed in Figures III.16 and III.18, respectively, show that the same trend is followed by the products of the 672-MeV Fe + Ho reaction.

V.F Monte Carlo Simulations

The dependence of the excitation energy division on the direction of transfers seems to support the assumption of energy dissipation by nucleon exchange. However, it was suggested by Tõke *et al.* [TOK89] that such a strong correlation cannot be fully attributed to physical phenomena and that systematic errors and instrumental effects contribute to the mass dependence. To investigate the sensitivity of the E^*_{PLF}/E^*_{TOT} centroids to these effects, Monte Carlo simulations of the experiment for the 505- MeV ^{56}Fe + ^{165}Ho reaction [BEN85, 87, 88] were performed by Toke *et al.* [TOK89, 90, 91]. The results of the simulation obtained are compared to the reported experimental data [BEN85, 87, 88] in Figure V.17, where the E^*_{PLF}/E^*_{TOT} centroids are plotted as a function of the pre-evaporation mass. A very good agreement between the experimental data and the Monte Carlo results is observed. Since the Monte Carlo calculations are obtained after analysis of simulated events starting with a mass-independent division of the excitation energy, it could be implied that the kinematic coincidence technique is responsible for the correlations between fragment mass and excitation energy. This was thought to be especially due to the finite mass resolutions of the detected fragments [TOK89].

Monte Carlo simulations were also used by Kwiatkowski *et al.* [KWI90] in the study of the 629-MeV ^{74}Ge+ ^{165}Ho system. The results of this study, shown in Figure V.18, confirm the correlation between the excitation energy division and the fragment mass. They show, however, that some of the dependence is due to recoil effects from light particle evaporation and to finite TLF angle resolution.

Similar Monte Carlo simulations based on reference [KWI90] were used to model the 672-MeV ^{56}Fe + ^{165}Ho experiment that is analyzed in the present work.

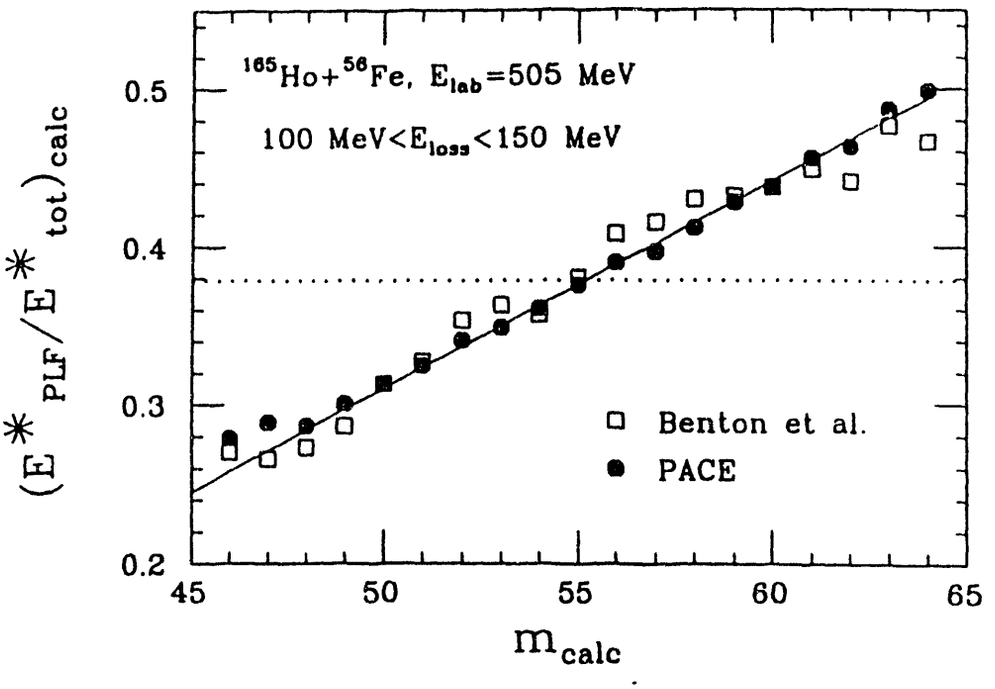

Figure V.17 Comparison of the experimentally observed correlation between the primary PLF mass and the excitation energy division (squares) for the 505-MeV ^{56}Fe on ^{165}Ho system with the results of a Monte Carlo simulation (solid circles), assuming a constant energy division (dotted line). The solid line represents results obtained with an analytical expression by Toke *et al.* [TOK89].

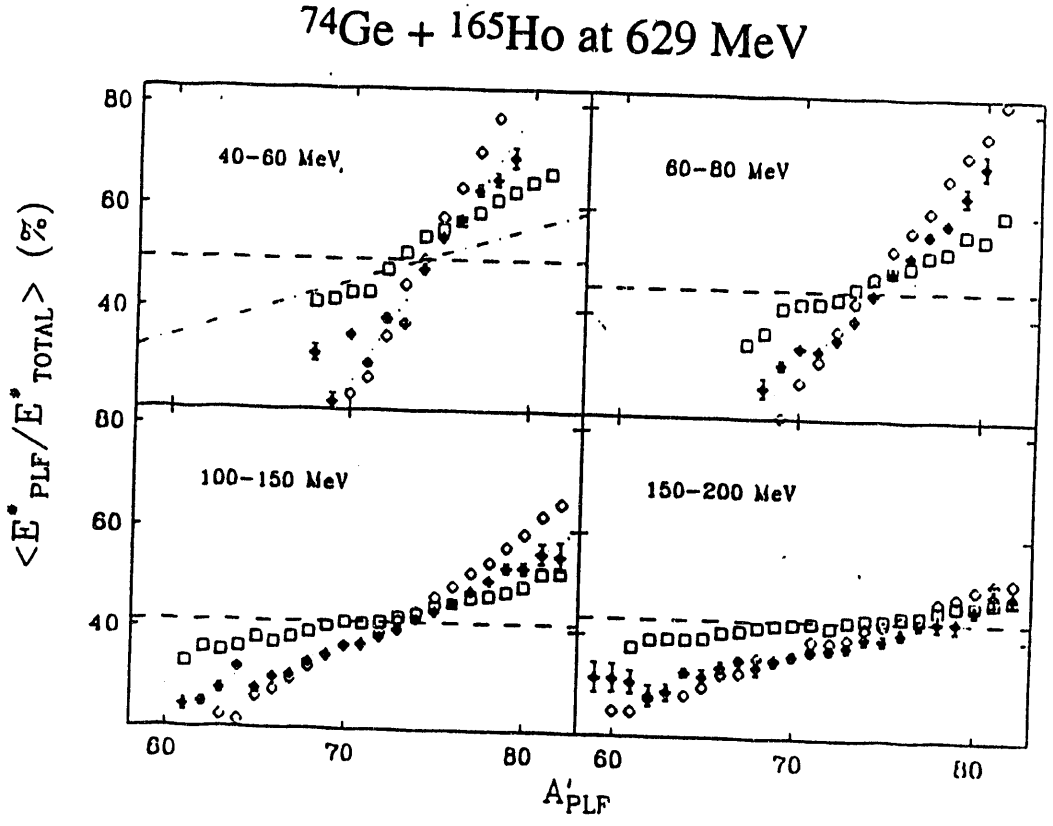

Figure V.18 Comparison of the experimentally observed correlation between the primary PLF mass and the excitation energy division for the 629-MeV ^{74}Ge on ^{165}Ho system, with the results of a Monte Carlo simulation. Solid diamonds indicate experimental data. Open diamonds are the results of the simulation assuming the average behavior of the experimental data (dotted line). Open squares are the results of the simulation assuming a mass-independent excitation energy division (dashed line). The dot-dashed line for the 40-60 MeV case is based on the analytical formula of reference [TOK89].

The parameters that define the reaction, such as mass and charge of the projectile and target, the laboratory bombarding energy, and the detector angular acceptances, were used as inputs to the Monte Carlo code. Other inputs related to the instrumentation are the experimental resolutions in PLF mass and charge, estimated to be 1.3 and 0.3, respectively, and the resolution in the TLF angle (2.5°) and PLF angle (0.5°). These are introduced in the code to reproduce as closely as possible the experimental setup.

The first step in the Monte Carlo simulation procedure is the generation of primary nuclide distributions (in the N-Z plane in this case) that would describe the primary distribution of projectile-like fragments emitted in the reaction in question. The characteristic centroids and widths of the primary PLF distributions obtained "experimentally" by the kinematic reconstruction technique were employed to generate the "simulated" primary N-Z distributions. This ensures that the measured events are reproduced by the "simulated" secondary events before the kinematic reconstruction. A further comparison of real and simulated data would otherwise be meaningless. The direction of the pre-evaporated fragments emitted in the reaction was described by a center-of-mass angular distribution

$$\frac{d\sigma}{d\Omega} \propto \frac{1}{\sin\theta_{cm}} \qquad \text{(V.6)}$$

The secondary nuclide distributions, equivalent to those measured experimentally were obtained by subjecting the primary distributions to evaporation corrections using results from PACE II. At this point, it was necessary to make assumptions about the excitation energy of the PLF, since it is required as an input to PACE II. Two different hypotheses were investigated: a sharing of the excitation energy independent of the primary PLF mass, where the average value of

the E^*_{PLF}/E^*_{TOT} ratio obtained experimentally (~ 50 %) was used, and a mass dependent division based on the experimental results.

The recoil effects due to particle evaporation from the emitted fragments were taken into account and the distribution of the recoil velocities was simulated by a Maxwellian formulation [STE88]. The mass and charge resolution of the secondary PLF, as well as the velocity vectors of the secondary PLF and TLF, were randomized to reproduce the finite mass, charge and angular resolutions that are measured experimentally.

The secondary distributions that were obtained were characterized by the same parameters as the experimental distributions: PLF mass, charge, kinetic energy and angle, and TLF angle. The simulated data were then analyzed in a way identical to the analysis of the experimental events, and the PLF excitation energy ratios that were determined from these calculations, were compared to the experimental results.

Before proceeding to a comparison of the experimental E^*_{PLF}/E^*_{TOT} ratios to the values obtained from the simulation, it is necessary to verify that the experimental nuclide distribution are reproduced by the Monte Carlo procedure. The centroids and variances of the secondary N and Z distributions obtained with the simulated data are compared to those of experimental distributions in Figures V.19 and V.20, respectively. The centroids are well reproduced by the simulation. However, the variances for the simulated events are higher than the experimental ones. A similar comparison is made between the centroids and variances of the simulated reconstructed primary and the experimental reconstructed primary in Figures V.21 and V.22. Both centroids and variances show a fairly good agreement between simulated events and real data. The differences in the

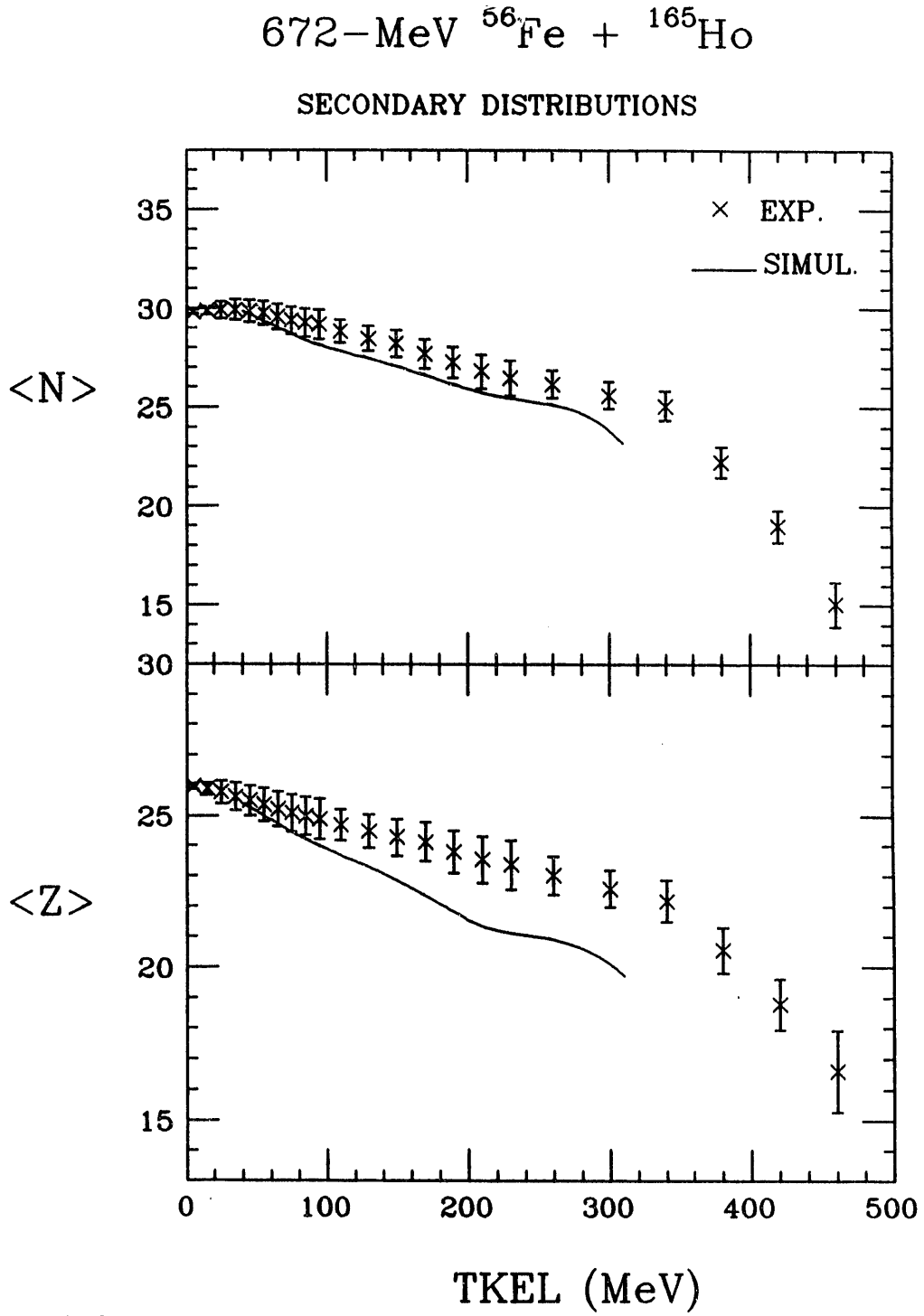

Figure V.19 The experimental <N> and <Z> values for secondary distributions, compared to the results of a Monte Carlo simulation (soild line), for the 672-MeV ^{56}Fe on ^{165}Ho system.

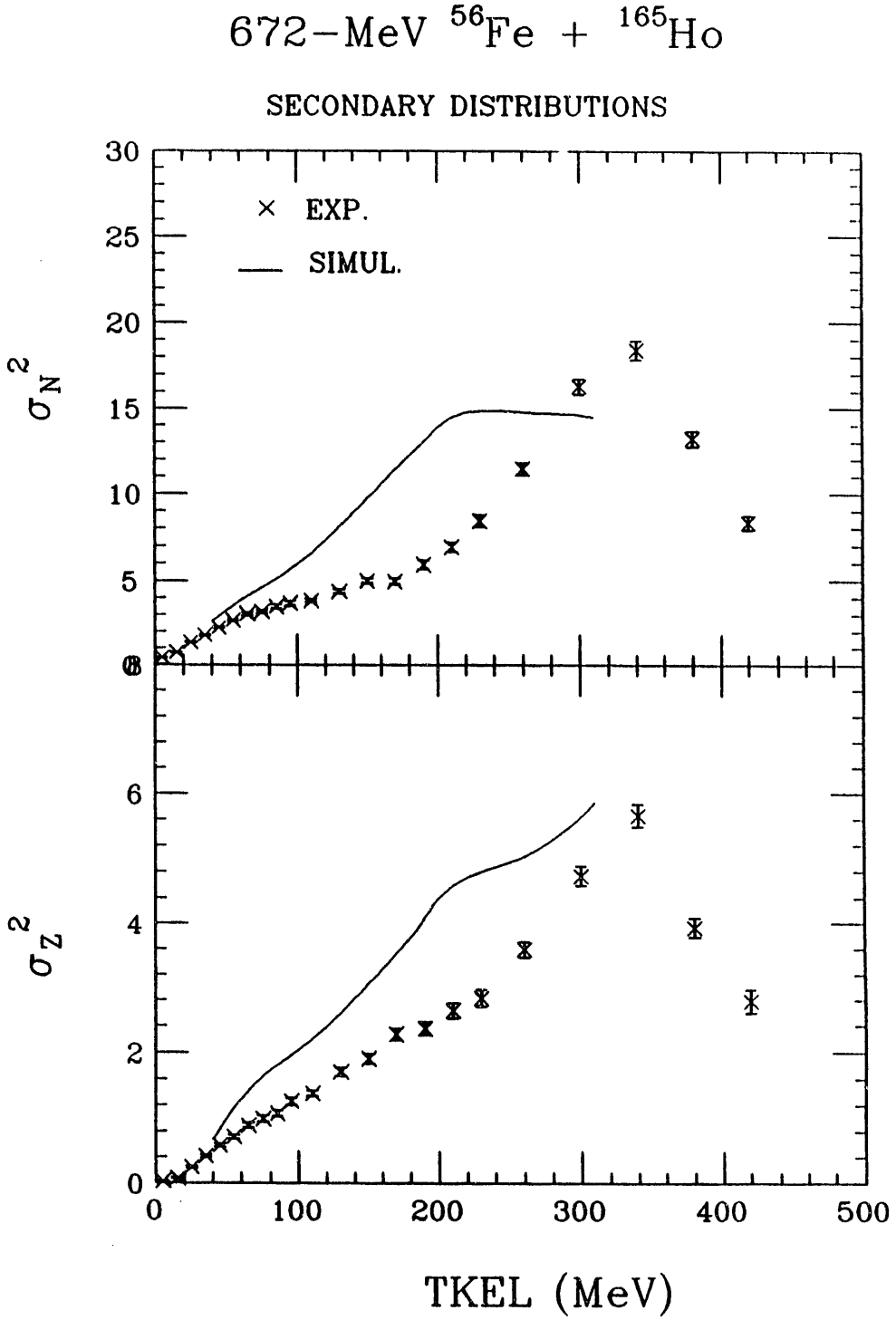

Figure V.20 The experimental σ_Z^2 and σ_N^2 values for secondary distributions, compared to the results of a Monte Carlo simulation (solid line), for the ^{56}Fe on ^{165}Ho system at 672 MeV.

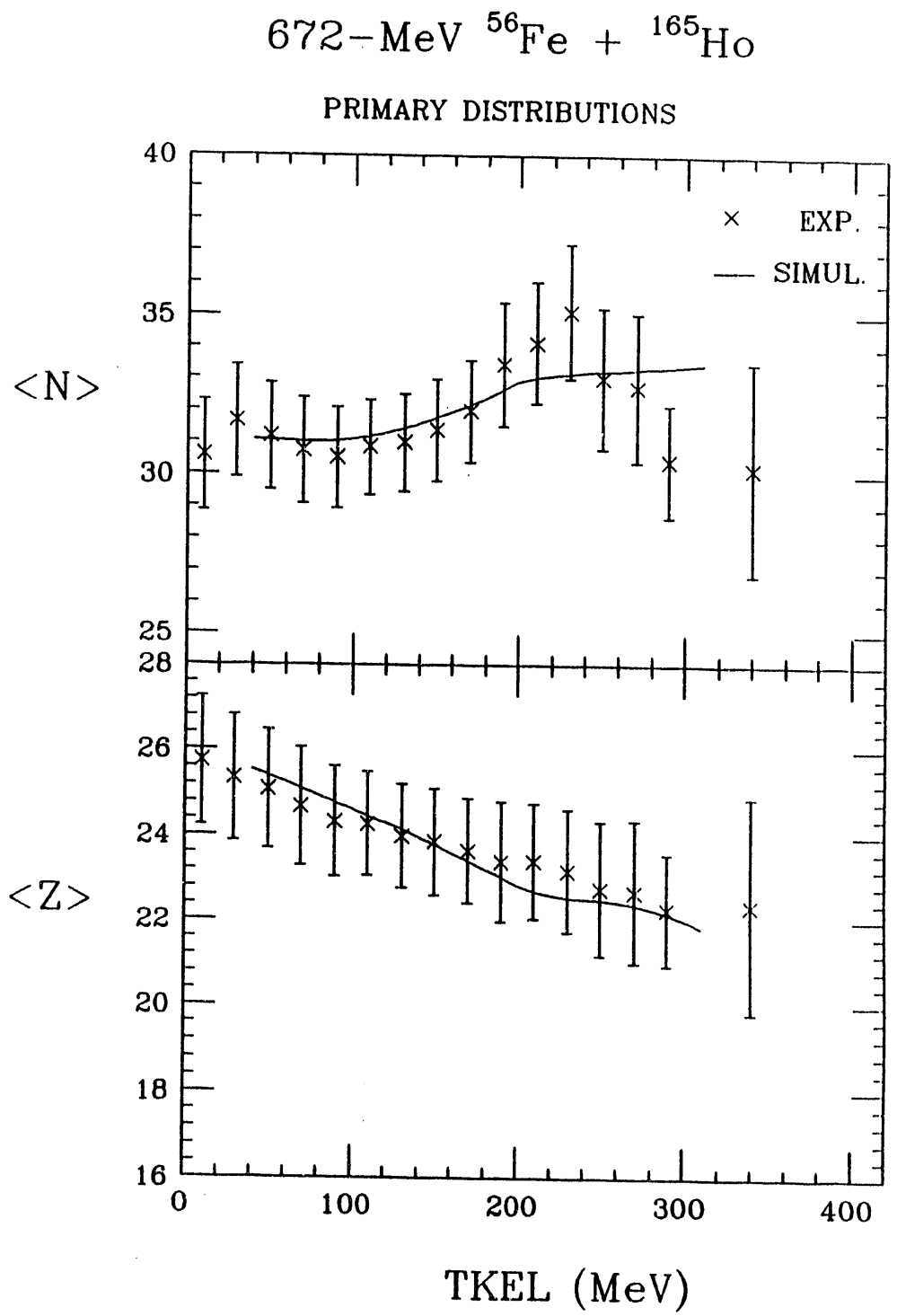

Figure V.21 The experimental <N> and <Z> values for primary distributions obtained with kinematical reconstruction, compared to the results of a Monte Carlo simulation (solid line), for the 672-MeV ^{56}Fe on ^{165}Ho system.

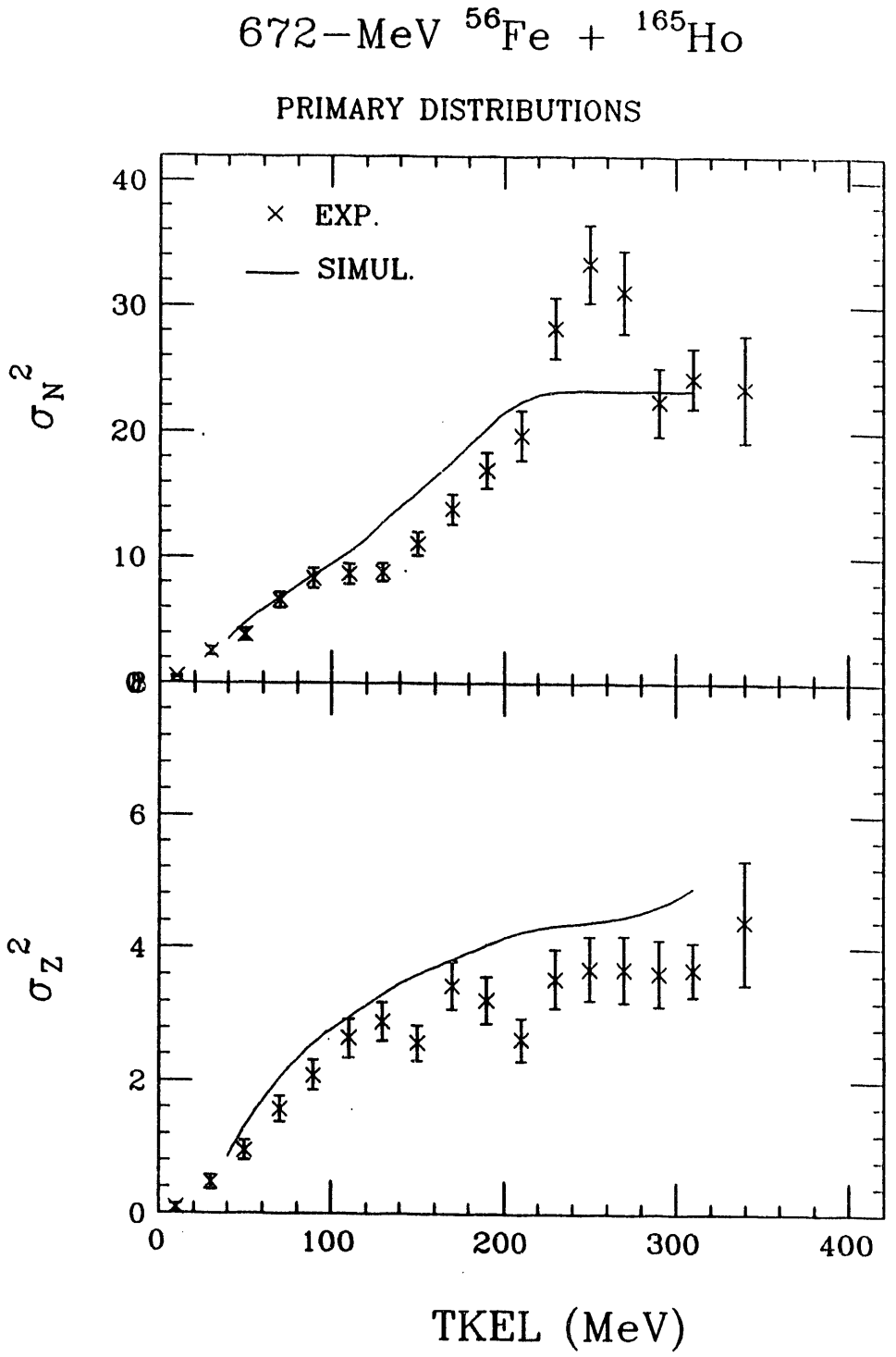

Figure V.22 The experimental σ_Z^2 and σ_N^2 values for primary distributions obtained with kinematical reconstruction, compared to the results of a Monte Carlo simulation (solid line).

secondary variances may be attributed to the random nature of the Pace II code which was used for evaporation corrections in two steps of the simulation.

The E^*_{PLF}/E^*_{TOT} centroids were determined by one-dimensional Gaussian fits and by moment analysis. Both methods yielded similar values of E^*_{PLF}/E^*_{TOT}. The PLF excitation energy ratio determined experimentally for the 672-MeV ^{56}Fe + ^{165}Ho system is compared to the results of the Monte Carlo simulation in Figure V.23, for three selective bins of TKEL. The two assumptions of the division of excitation energy are shown by the dotted line for the assumption of mass-invariant division, and by the experimental data points for the assumption of mass-dependent division. The results obtained after applying the kinematic reconstruction in the case of mass-invariant division, are shown by the solid line. The results from the case of mass-dependent division are shown by the dashed line. In the case where a mass-independent division was assumed, the deviation from the initial E^*_{PLF}/E^*_{TOT} value increases with increasing TKEL. This behavior is not observed for the case of mass-dependent division, where only a slight shift from the initial values of E^*_{PLF}/E^*_{TOT} is observed. The E^*_{PLF}/E^*_{TOT} ratios obtained with this latter case reproduce the experimental data better than do the E^*_{PLF}/E^*_{TOT} ratios obtained with the mass-independent assumption. This indicates that the correlation observed between the excitation energy sharing and the exit channel is not entirely due to instrumental effects. This is qualitatively consistent with the re-analysis of the 629-MeV ^{74}Ge + ^{165}Ho system by Toke *et al.* [TOK90], where it was confirmed that some of the correlation between excitation energy division and primary fragment mass was indeed physical. However, there are still disagreements about the magnitude of this correlation.

The effects of instrumental uncertainties on the E^*_{PLF}/E^*_{TOT} ratios were further investigated by performing the Monte Carlo simulations of the 672-MeV

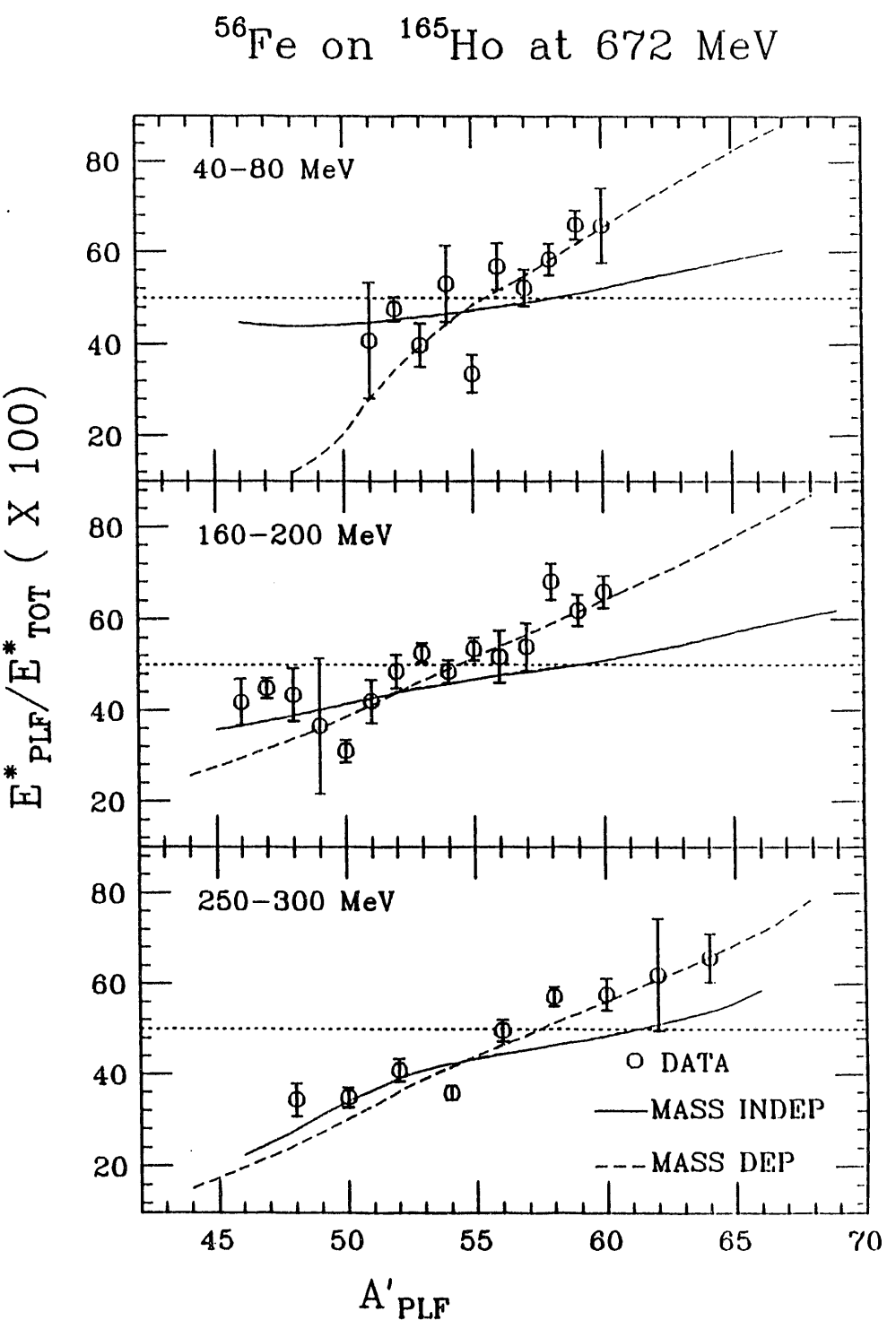

Figure V.23 The observed correlation between the PLF excitation energy ratio and the primary fragment mass (circles), compared to the results of a Monte Carlo simulation, for the reaction ^{56}Fe on ^{165}Ho at 672 MeV. The solid line indicates simulation results based on a mass-independent partition of the excitation energy (dotted line). The dashed line is the result of the simulation with a mass-dependent division of the excitation energy (average behavior of the data). The dotted line indicates the limit of excitation energy equipartion.

^{56}Fe on ^{165}Ho reaction with different values for the input parameters. The mass independent excitation energy division assumption was used since a more drastic shift was exhibited by the E^*_{PLF}/E^*_{TOT} when the simulation was ran with this assumption. The finite TLF angle resolution, which was observed in the data of two Fe + Ho systems and the Ge + Ho system, was thought to contribute significantly to the mass correlation effects on the excitation energy division. To test this hypothesis, the Monte Carlo simulation was performed with the angular resolutions $\Delta\theta_{PLF}$ and $\Delta\phi_{PLF}$ set to 0.5^o, while the remaining input parameters were left unchanged. Two other parameters that are likely to introduce uncertainties in the determination of E^*_{PLF}/E^*_{TOT} are the charge (Z) and mass (A) resolutions of the detected PLF's. Therefore, the simulation procedure was also run with both A and Z resolutions set to 0.2 units of mass and charge, keeping the remaining parameters at their experimental values.

The E^*_{PLF}/E^*_{TOT} ratios obtained with the new TLF angle resolution are compared to the values obtained with the experimental TLF angle resolution in Figure V.24, where E^*_{PLF}/E^*_{TOT} is plotted versus A'_{PLF} for three different ranges of TKEL. One noticeable change is observed for the low TKEL bin (40-80 MeV), where the E^*_{PLF}/E^*_{TOT} ratio obtained with the 0.5^o resolution (dashed line) is closer to the initial assumption than the result with the 2.5^o resolution, (dotted line), especially for $A'_{PLF} < 58$. A small shift is also observed at high TKEL (250-300 MeV bin), where the E^*_{PLF}/E^*_{TOT} ratio in the 0.5^o case is closer to 50% for high A'_{PLF} (>58). No variation of E^*_{PLF}/E^*_{TOT} is observed for the intermediate values of TKEL (160-200 Mev bin). The same type of plot is shown in Figure V. 25 for the case changing the Z and A resolutions. No sizable variation is observed at all values of TKEL. Thus, it appears that A and Z resolutions have no effect on the determination of E^*_{PLF}/E^*_{TOT}, while TLF angle

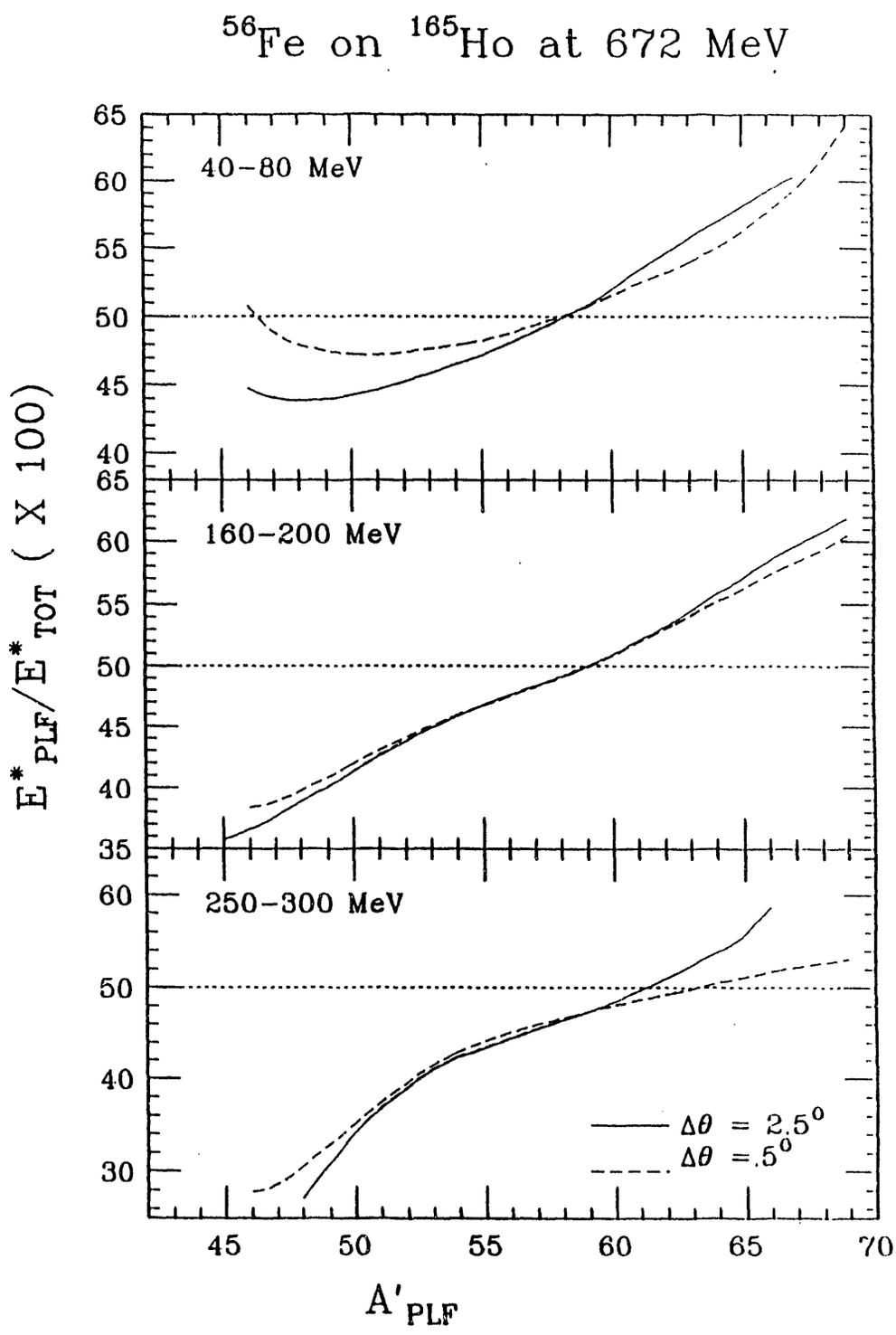

Figure V.24 The PLF excitation energy ratio predicted by a Monte Carlo simulation as a function of primary PLF mass, for the reaction ^{56}Fe on ^{165}Ho at 672 MeV. The solid line is obtained with the angular resolution set to the experimental value (2.5°), and the dashed line is based on an a more ideal value for the angular resolution (0.5°). The dotted line indicates the limit of excitation energy equipartion.

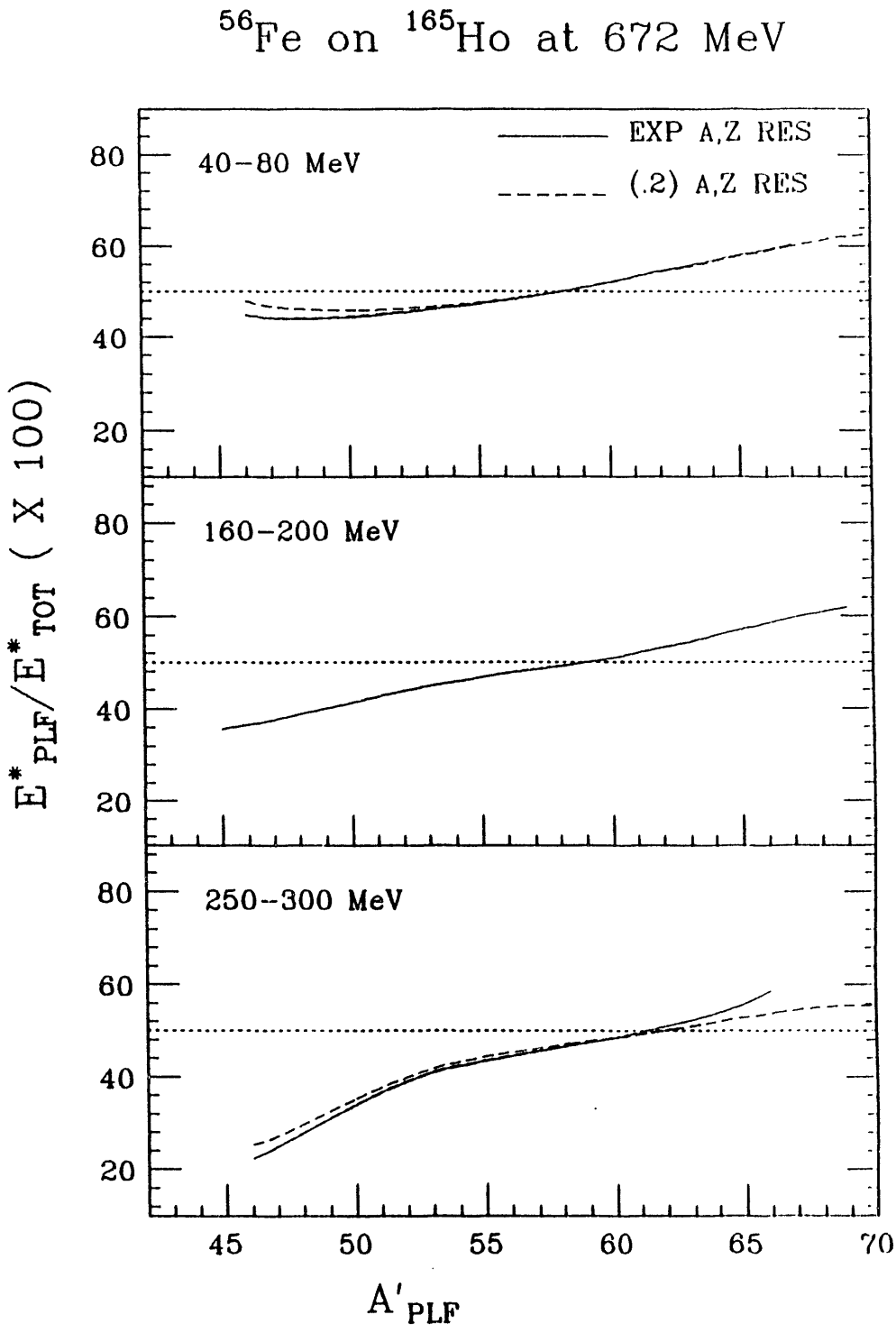

Figure V.25 The PLF excitation energy ratio predicted by a Monte Carlo simulation as a function of primary PLF mass. The solid line is obtained with the mass and charge resolution set experimental values, (1.3 mass units, and .3 units of charge), and the dashed line is based on an ideal mass and charge resolutions (0.2 units of mass and charge, respectively). The dotted line indicates the limit of excitation energy equipartion.

resolution introduces a slight correlation between E^*_{PLF}/E^*_{TOT} and A'_{PLF}. However, a problem still remains, since the mass independent excitation energy division configuration that was used in the simulation program could not be reproduced after kinematic reconstruction.

A reanalysis of the 629-MeV ^{74}Ge + ^{165}Ho data was performed by Planeta *et al* [TOK91] with a method that does not require an exact knowledge of the experimental resolutions. In this new analysis, the correlation between excitation energy division and mass transfer were studied by plotting the average evaporated mass $\langle A'_{PLF} - A''_{PLF} \rangle$ versus the measured post-evaporation mass for different bins of energy loss. The presence of a correlation between excitation energy division and primary PLF mass was confirmed. However, this study also showed that finite resolutions were responsible for the quasi parabolic dependence of the average evaporated mass on the measured post-evaporation mass of the PLF [TOK91]. A more detailed examination of the different steps of the Monte Carlo simulation, the kinematic reconstruction step in particular, should be considered.

V.G Nuclear Temperature

One of the questions addressed in the study of deep-inelastic heavy-ion reactions is whether the reaction fragments reach thermal equilibrium before they separate into a PLF and a TLF. The nuclear temperature of each fragment, as obtained by kinematical reconstruction is plotted as a function of energy loss in Figure V.26. The numerical results can also be found in Tables A.14, and A.15. Both temperatures increase with increasing TKEL and a steeper slope is observed below 100 MeV of TKEL. The temperature of the PLF exceeds that of the TLF at all values of the energy loss, indicating that thermal equilibrium has not been

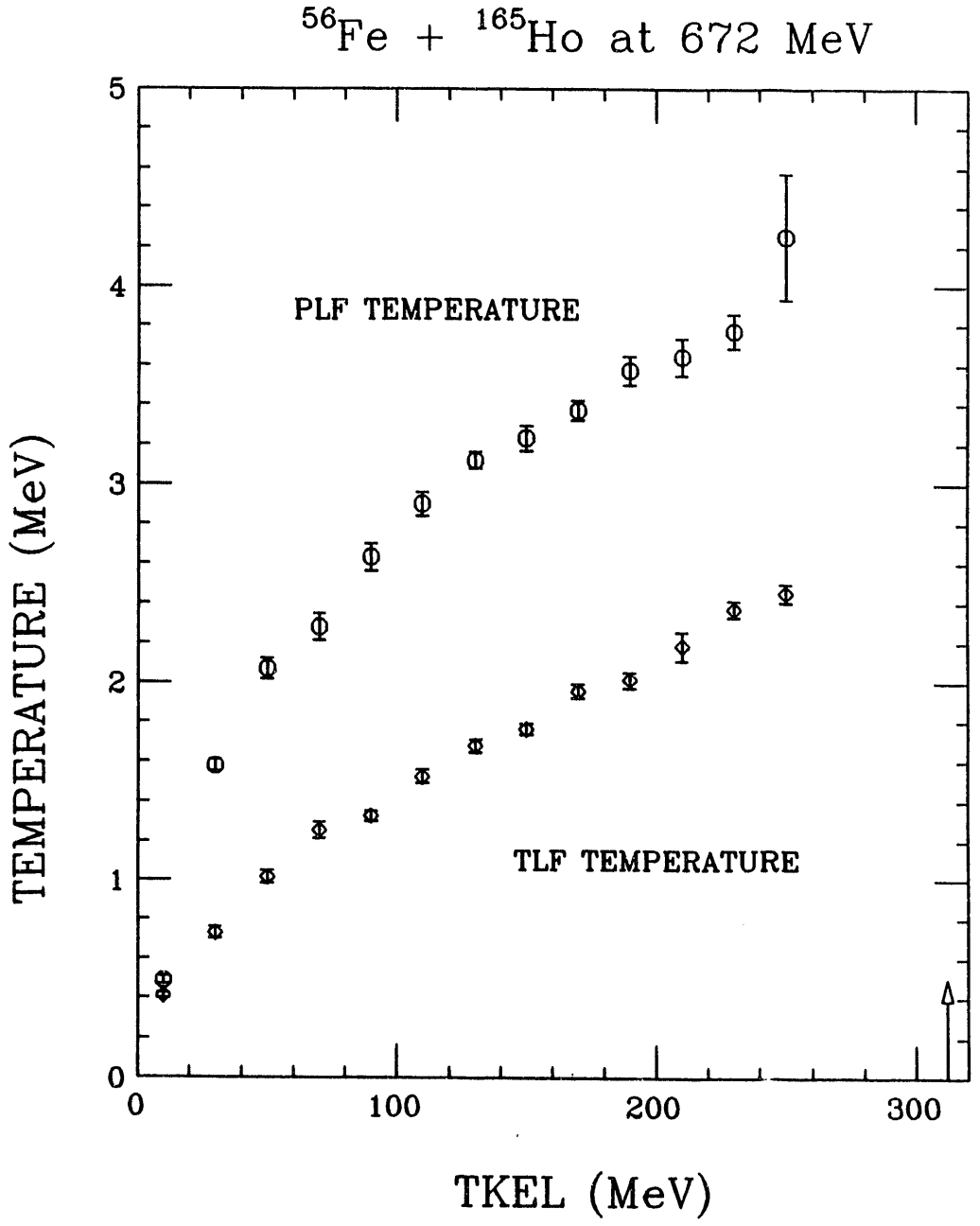

Figure V.26 Nuclear temperature of the projectile-like and target-like fragments as a function of energy loss, for the reaction ^{56}Fe on ^{165}Ho at 672 MeV. The arrow indicates the limit imposed by the spherical Coulomb barrier.

established between the two fragments. This can also be seen in Figure V.27, where the ratio, τ_{PLF}/τ_{TLF}, of the PLF temperature to the TLF temperature is displayed as a function of TKEL. Figure V.27 shows that the system evolves towards a lesser temperature gradient between the two fragments. However, it is still far from reaching equilibrium.

The study of the 505-MeV ^{56}Fe + ^{165}Ho reaction by Benton *et al.* [BEN 85, 88] showed the same qualitative behavior for the temperature ratio. However, the lower bombarding energy system was closer to the limit of equal temperature than is the present system. This could imply that the interaction time of the higher bombarding energy system, which is characterized by a higher relative velocity, is not sufficiently long to allow thermalization.

V.H Comparison Between Results with Kinematic Reconstruction and Neutron Evaporation Correction.

This section presents a correlation between the results of the two types of analysis conducted in the present work on the data of the 672-MeV ^{56}Fe on ^{165}Ho system. The primary mass and charge distributions that were obtained by using the kinematic coincidence technique are compared to the primary distributions obtained by applying neutron evaporation corrections to the measured secondary distributions. The function describing the average behavior of the experimental E^*_{PLF}/E^*_{TOT} ratio in terms of primary PLF mass was used to determine the PLF excitation energy when performing the neutron evaporation corrections.

The centroids and variances obtained with the two methods are summarized in Tables A.16 through A.19 and are displayed as a function of TKEL in Figures V. 28 and V.29. The results are represented by diamonds for the kinematic

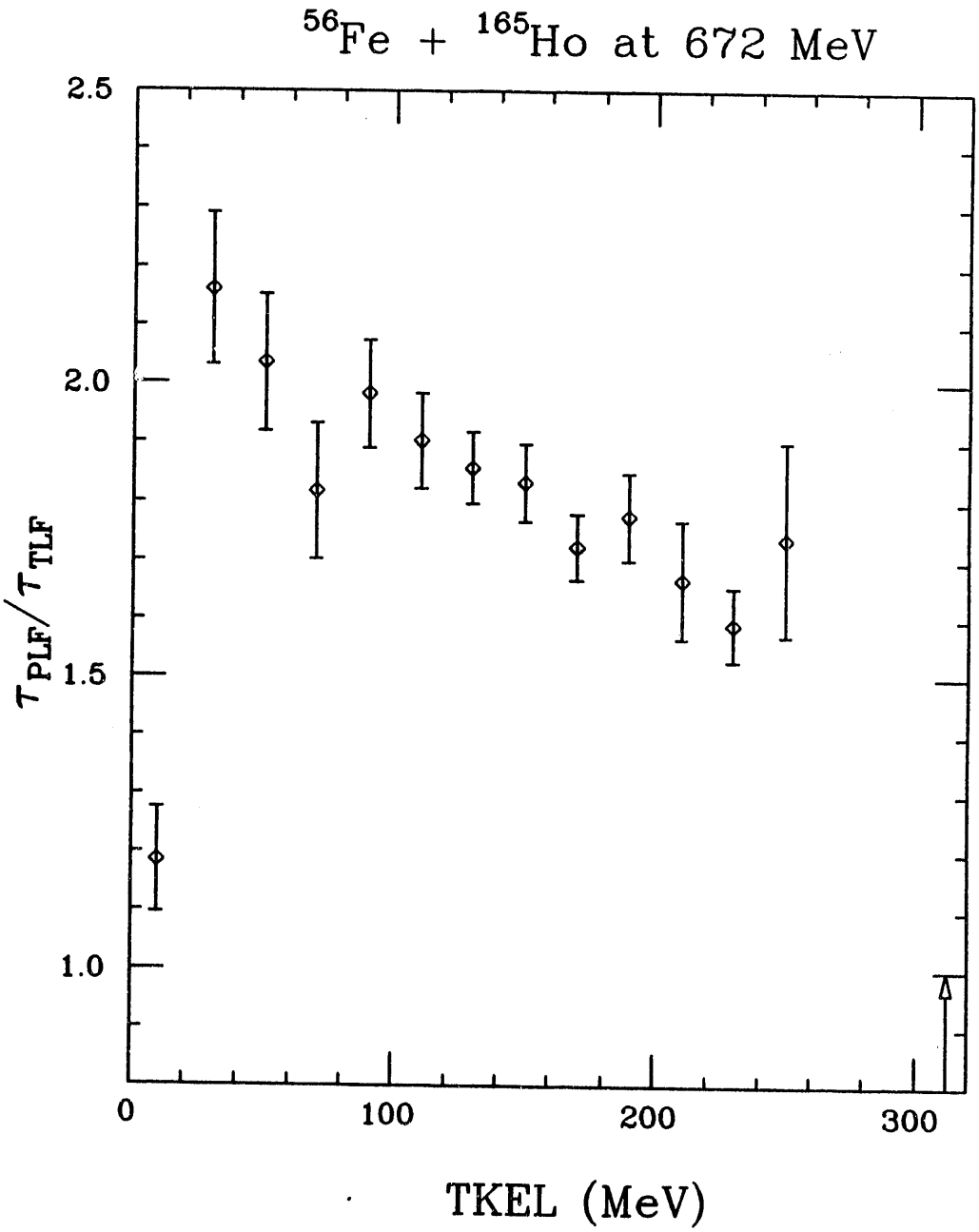

Figure V.27 Ratio of the nuclear temperature of the projectile-like and target-like fragments as a function of energy loss, for the reaction ^{56}Fe on ^{165}Ho at 672 MeV. The arrow indicates the limit imposed by the spherical Coulomb barrier.

reconstruction method, and by circles for the evaporation correction method.

The N and Z centroids and the <N>/<Z> ratio obtained with the two different procedures are in agreement as shown in Figure V.28. The agrrement in the <Z> values is consistent with the assumption that charge evaporation from the PLF is negligible for the 672-MeV ^{56}Fe + ^{165}Ho system. Such result can be expected since the N/Z ratio of the PLF's produced in this reaction vary between 1.15 and 1.38 and charge evaporation becomes less important with increasing N/Z ratio.

The variances σ_Z^2 from the two techniques are in a fairly good agreement at all values of TKEL. A difference is observed for the σ_N^2 variances, those obtained with the evaporation correction method are higher for TKEL values close to the limit of the spherical entrance channel Coulomb barrier (312 MeV). This result is not surprising, since in the evaporation correction method only neutron evaporation was taken into account. In addition, in this method the mass evaporated from the PLF was evaluated by determining the average functional dependence of ΔA on an assumed E^*_{PLF} as described in Section II.D.2, and the proton evaporation that may occur in regions of low N/Z ratios is unaccounted for. In the kinematic reconstruction method ΔA is evaluated exactly from experimental measurements, and ΔZ and the PLF excitation.were determined by the iterative procedure described in Section II.D.3. This latter method is more sensitive to the details of the distribution, such as long tails, and thus gives larger variances. The factor ρ_{NZ} obtained with the evaporation correction method suggests a tendency towards a correlation between proton and neutron exchange. However, the kinematics reconstruction method results in ρ_{NZ} values close to zero: this would mean that there is almost no dependence between proton and neutron exchange. It

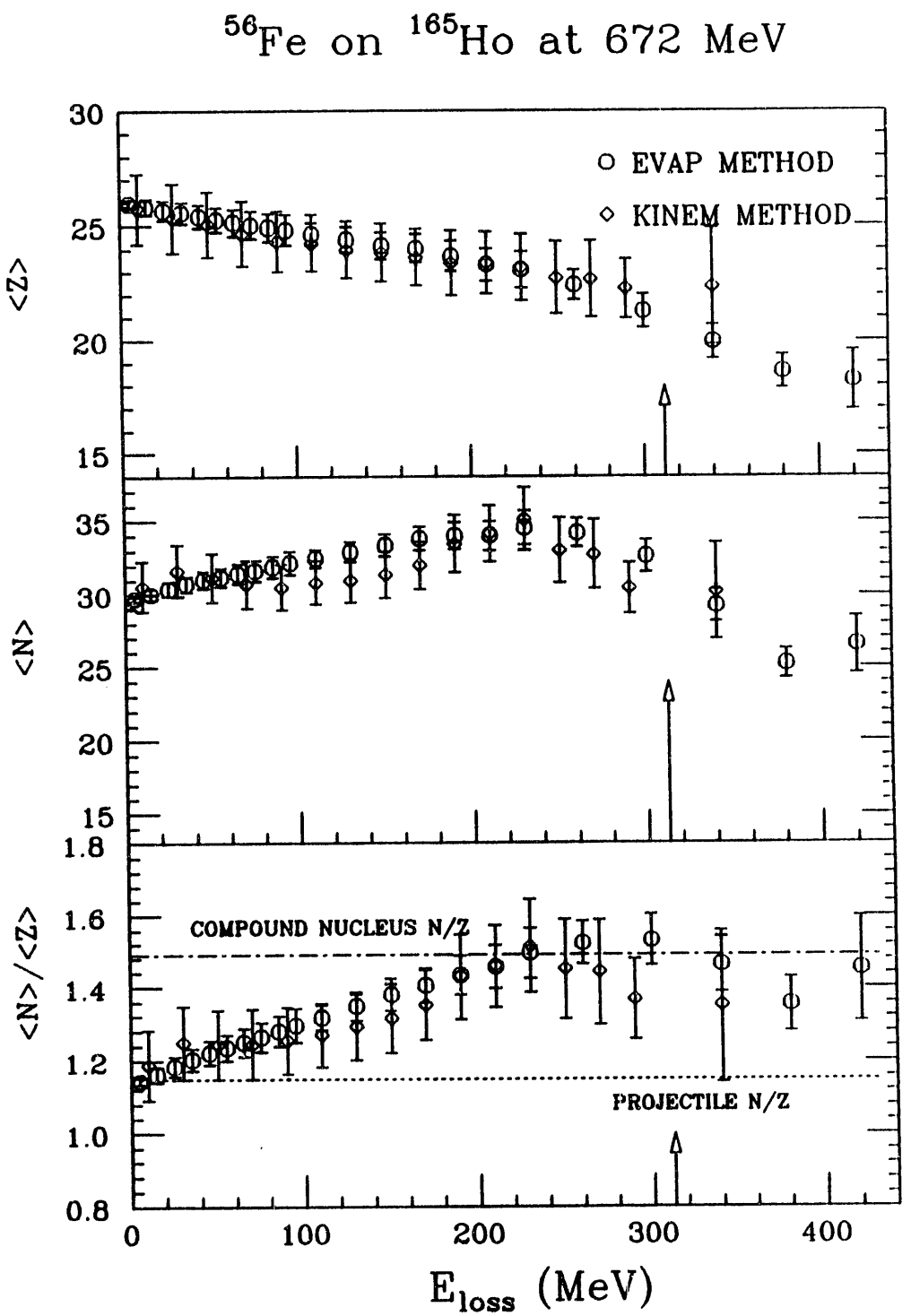

Figure V.28 The <N>, <Z>, and <N>/<Z> values for experimental primary distributions, for the reaction ^{56}Fe on ^{165}Ho at 672 MeV. The diamonds indicate results obtained with the kinematical reconstruction method. The circles indicate the results of applying neutron evaporation corrections to the secondary distributions. The N/Z ratio of the projectile (dotted line) and the composite system (dot-dashed line) are indicated. The arrow shows the limit of energy loss imposed by the spherical entrance channel Coulomb barrier.

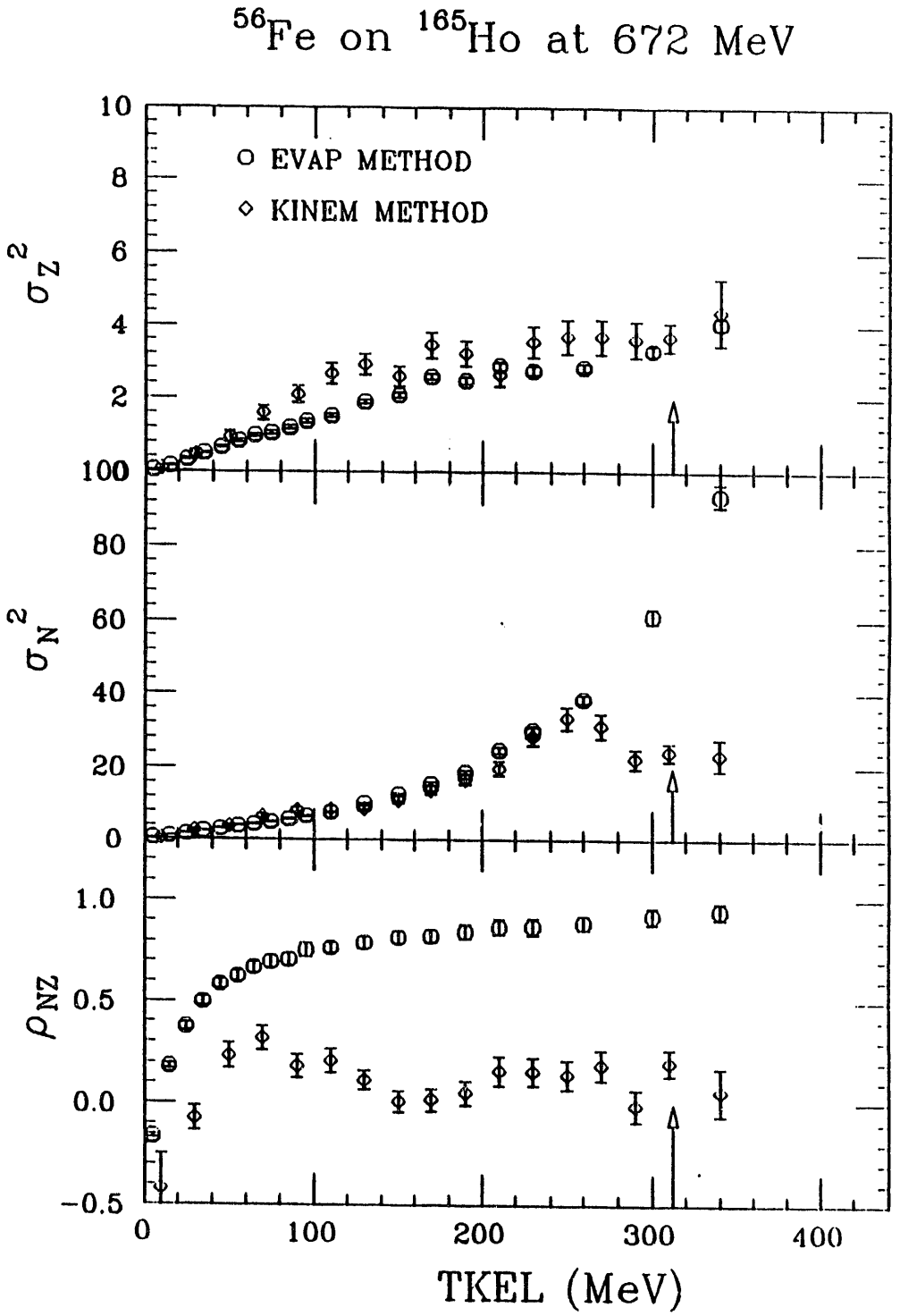

Figure V.29 The variances σ_Z^2 andσ_Z^2, and the correlation factor $\rho_{NZ}$for experimental primary distributions, for the reaction ^{56}Fe on ^{165}Ho at 672 MeV. The diamonds indicate results obtained with the kinematical reconstruction method. The circles indicate the results of applying neutron evaporation corrections to the secondary distributions.

is worthwhile to point out that the nucleon exchange models of Randrup and Tassan-Got predict a gradual increase of ρ_{NZ} with increasing energy loss.

CHAPTER VI SUMMARY AND CONCLUSIONS

Two aspects of heavy-ion reactions in the deep-inelastic region have been studied for the reaction $^{56}Fe + ^{165}Ho$ at 12 MeV/u: the evolution of the nuclide distributions of as a function of kinetic energy loss, and the division of excitation energy between the reaction fragments. A simultaneous detection of the projectile-like and target-like fragments was used to obtain information about the pre-evaporation reaction products' mass and excitation energies.

The centroids, variances and correlation factor of the mass and charge distributions of the projectile-like fragments were determined with the method of moment analysis, and their evolution as a function of total kinetic energy loss was described. A gradual decrease of the experimental N and Z centroids with increasing energy loss was observed. The determination of the primary distributions, by applying neutron evaporation corrections to the secondary distributions, showed that the drift in <N> is due to light particle evaporation, while the drift in <Z> is a consequence of the deep-inelastic mechanism. The result is the formation of neutron-rich nuclei with N/Z ratios approaching the N/Z ratio of the composite system (1.38). This behavior is indicative of charge equilibration between the two reaction fragments. Another consequence of a decrease in the primary charge along with a small increase in primary neutron number is a slight drift of the Fe + Ho system towards mass asymmetry. This negative drift is opposite to the direction that would minimize the potential energy of the system and drive it towards mass symmetry.

The predictions of two nucleon exchange models, Randrup's model and Tassan-Got' model, were compared to the experimental data of Fe-induced

reactions. Both models succeeded in reproducing the experimental N and Z centroids, and the N/Z ratio for the 672-MeV ^{56}Fe on ^{165}Ho system. Significant differences between the predictions of the two models were observed for the 505-MeV ^{56}Fe on ^{165}Ho system and the 840-MeV ^{56}Fe on ^{238}U system. Tassan-Got's model reproduced the centroids quite well while Randrup's model overpredicted both the N and Z centroids. It is interesting to point out that the N/Z ratio was equally well reproduced by both models, for all the systems studied here, despite their differences in the prediction of the individual N and Z centroids. An examination of the primary distributions obtained from the two models showed that the means to charge equilibration is by driving the system to mass symmetry in Randrup's model, and to mass asymmetry in Tassan-Got's model. This could explain why Tassan-Got's model reproduces the experimental results for systems where a greater mass asymmetry was observed, better than for systems with weaker drifts towards mass asymmetry.

The drive towards symmetry predicted by Randrup's model is attributed by Tassan-Got to the presence of a kinetic term in Randrup's formulation of the Lagrangian of the system. A similar reasoning holds for the potential energy surface which also contains a kinetic term (due to the centrifugal force). In Randrup's formulation of the Lagrangian, the two fragments are considered as one entity; this is equivalent to assuming that the two nuclei have lost their individual characteristics. However, this is true only at long interaction times. Conversely, the interacting nuclei are treated as separate entities in Tassan-Got's model, even at the long interaction times when the two fragments are no longer distinguishable. Therefore, a model which would describe the collision with Tassan-Got's theory at short interaction times, and Randrup's theory at longer interaction times would be an interesting option to consider.

An increase of the experimental charge and neutron variances (σ_Z^2 and σ_N^2) with increasing energy loss was observed for the 672-MeV ^{56}Fe + ^{165}Ho system. This, in addition to the linear dependence between the square root of the available kinetic energy above the Coulomb barrier and σ_A^2, confirms the role of nucleon exchange in energy dissipation. The variances and the correlation factor are equally well reproduced by both nucleon exchange models for the asymmetric systems studied. This seems to indicate that nucleon exchange could account for most of the energy dissipation for the Fe-induced reactions studied here. The one exception is the symmetric system 840-MeV ^{56}Fe + ^{56}Fe, where both models underpredicted σ_N^2 and σ_Z^2 values. The study of Cl-induced reactions by Marchetti *et al.* [MAR91, 92] also showed that both Tassan-Got's model and Randrup's model underpredict the charge and neutron variances, especially for the nearly symmetric systems ^{37}Cl +^{40}Ca. Therefore, another point that should be considered in developing models that describe energy dissipation in deep-inelastic mechanisms, is the role of other modes of energy dissipation, such as collective modes of excitation, and perhaps the role of fast fission at long interaction times.

The binary character of deep-inelastic collisions was used for a kinematic reconstruction of the primary reaction, and the determination of the primary mass of the PLF was then used with the statistical evaporation code for excitation energy determination. The fraction of excitation energy stored in the projectile-like fragment was found to exceed 50% at low energy loss, and to decrease with increasing energy loss, but without ever reaching thermal equilibrium. The same qualitative behavior of E^*_{PLF}/E^*_{TOT} with energy loss was featured by other systems studied with the kinematic coincidence method [BEN 85, 87, 88, KWI90]. However, much larger E^*_{PLF}/E^*_{TOT} values were obtained for the 672-MeV ^{56}Fe on ^{165}Ho system. This is reflected in the high nuclear temperatures

(up to 4 MeV) that were attained by the projectile-like fragments. The large PLF excitation energy ratios obtained for the 672-MeV ^{56}Fe on ^{165}Ho system are attributed to its higher bombarding energy.

A small correlation between the PLF excitation energy ratio, E^*_{PLF}/E^*_{TOT}, and the reaction exit channel was observed. A larger portion of excitation energy is stored in the acceptor nucleus than in the donor nucleus. A stronger dependence of the excitation energy division on the primary reaction was observed for the 505-MeV ^{56}Fe on ^{165}Ho and the 629-MeV ^{74}Ge on ^{165}Ho systems [BEN85, 88, KWI90] than for the 672-MeV ^{56}Fe on ^{165}Ho system. Monte Carlo simulations of the present experiment were performed to test the dependence of the analysis results on instrumental effects. They confirmed the existence of some correlation between the finite resolutions of the measured parameters and the calculated physical quantities. However, a further examination of the instrumental effects, by running the Monte Carlo simulation with different values for the resolution of the experimental setup, showed only a weak dependence of the simulation on the experimental parameters. A more detailed examination of the different steps of the Monte Carlo simulation, the kinematic reconstruction step in particular, should be considered.

The results of the two types of analysis performed on the data of the 672-MeV ^{56}Fe on ^{165}Ho system are qualitatively consistent with the conclusion that the stochastic exchange of nucleons is the major contributor to energy dissipation in deep-inelastic reactions. Studies of heavy-ion reactions at intermediate energies suggest that deep-inelastic processes still persist in this energy regime [BOR88, 90, TAS 88,89], and that a binary character of the reaction still dominates [LOT92]. Therefore, the study of the excitation energy division between the fragments of heavy-ion reactions at intermediate bombarding

energies could be a useful tool to explore the transition between deep-inelastic mechanisms towards other mechanisms associated with intermediate energy heavy-ion reactions, such as multifragmentation.

APPENDIX A

Table A.1 The secondary centroids <N> and <Z> for the ^{56}Fe + ^{165}Ho reaction at 672-MeV. The energy loss scale TKEL has been corrected for evaporation assuming equal excitation energy division between the reaction fragments.

TKEL (MeV)	<Z>	<N>
5	25.98 ± 0.41	29.80 ± 0.45
15	25.91 ± 0.85	29.93 ± 0.94
25	25.74 ± 1.31	29.83 ± 1.46
35	25.54 ± 1.47	29.87 ± 1.66
45	25.48 ± 1.63	29.78 ± 1.84
55	25.25 ± 1.69	29.67 ± 1.91
65	25.24 ± 1.74	29.87 ± 1.98
75	25.00 ± 1.69	29.61 ± 1.93
85	24.88 ± 1.70	29.53 ± 1.94
95	24.73 ± 1.79	29.60 ± 2.06
110	24.56 ± 1.36	29.08 ± 1.55
130	24.17 ± 1.36	28.54 ± 1.54
150	23.81 ± 1.36	27.95 ± 1.53
170	23.57 ± 1.32	27.40 ± 1.47
190	23.30 ± 1.24	27.14 ± 1.38
210	22.97 ± 1.24	26.63 ± 1.38
230	22.83 ± 1.16	26.35 ± 1.28
260	22.26 ± 0.85	25.76 ± 0.94
300	21.87 ± 0.83	25.38 ± 0.93
340	21.39 ± 0.84	24.88 ± 0.94
380	20.38 ± 0.84	23.17 ± 0.91
420	18.86 ± 0.89	20.52 ± 0.93
460	16.71 ± 1.34	16.21 ± 1.24

Table A.2 The variances σ_Z^2 and σ_N^2, and correlation factor ρ_{NZ}, for the secondary PLF distributions obtained with the reaction $^{56}Fe + ^{165}Ho$ at 672 MeV. The energy loss, TKEL, has been corrected for evaporation assuming equipartition of the excitation energy between the projectile-like and the target-like fragments.

TKEL (MeV)	σ_Z^2	σ_N^2	ρ_{NZ}
5	0.032 ± 0.017	0.387 ± 0.026	-0.325 ± 0.087
15	0.095 ± 0.041	0.748 ± 0.080	-0.074 ± 0.043
25	0.288 ± 0.083	1.316 ± 0.167	0.043 ± 0.051
35	0.504 ± 0.104	1.551 ± 0.211	0.172 ± 0.064
45	0.479 ± 0.113	1.644 ± 0.246	0.287 ± 0.081
55	0.691 ± 0.143	2.200 ± 0.323	0.376 ± 0.088
65	0.803 ± 0.154	2.436 ± 0.350	0.308 ± 0.089
75	0.938 ± 0.162	2.268 ± 0.318	0.433 ± 0.082
85	1.020 ± 0.180	2.845 ± 0.368	0.573 ± 0.105
95	1.416 ± 0.265	3.068 ± 0.442	0.534 ± 0.110
110	1.574 ± 0.196	3.608 ± 0.380	0.553 ± 0.076
130	2.021 ± 0.233	4.394 ± 0.484	0.647 ± 0.089
150	2.064 ± 0.244	5.070 ± 0.558	0.667 ± 0.091
170	2.262 ± 0.246	4.391 ± 0.466	0.692 ± 0.087
190	2.184 ± 0.235	5.449 ± 0.561	0.739 ± 0.091
210	2.529 ± 0.265	6.649 ± 0.649	0.760 ± 0.092
230	2.593 ± 0.276	8.242 ± 0.755	0.803 ± 0.096
260	2.677 ± 0.213	9.990 ± 0.664	0.825 ± 0.071
300	3.725 ± 0.287	13.90 ± 0.886	0.073 ± 0.870
340	4.408 ± 0.326	17.77 ± 0.896	0.070 ± 1.090
380	4.153 ± 0.279	15.90 ± 0.890	0.069 ± 1.040
420	2.834 ± 0.240	9.820 ± 0.782	0.818 ± 0.078
460	1.649 ± 0.258	6.293 ± 0.827	0.795 ± 0.126

Table A.3 The centroids <N> and <Z> for the reaction $^{56}Fe + ^{165}Ho$ at 672 MeV. The energy loss scale, TKEL, has been corrected for evaporation assuming thermal equilibrium between the projectile-like and the target-like fragments.

TKEL (MeV)	<Z>	<N>
5	25.97 ± 0.40	29.80 ± 0.44
15	25.91 ± 0.86	29.92 ± 0.96
25	25.68 ± 1.32	29.85 ± 1.48
35	25.51 ± 1.45	29.85 ± 1.64
45	25.43 ± 1.64	29.78 ± 1.85
55	25.26 ± 1.64	29.64 ± 1.86
65	25.17 ± 1.63	29.85 ± 1.86
75	24.89 ± 1.63	29.55 ± 1.87
85	24.74 ± 1.68	29.53 ± 1.93
95	24.68 ± 1.75	29.21 ± 1.99
110	24.30 ± 1.33	28.83 ± 1.52
130	24.03 ± 1.29	28.26 ± 1.46
150	23.65 ± 1.28	27.59 ± 1.43
170	23.32 ± 1.17	27.12 ± 1.30
190	22.96 ± 1.18	26.59 ± 1.32
210	22.82 ± 1.11	26.35 ± 1.23
230	22.37 ± 1.13	25.91 ± 1.26
260	21.91 ± 0.79	25.26 ± 0.88
300	21.52 ± 0.79	25.00 ± 0.88
340	20.66 ± 0.79	23.73 ± 0.88
380	19.03 ± 0.85	20.85 ± 0.89
420	16.57 ± 1.30	15.97 ± 1.20

Table A.4 The secondary variances σ_Z^2 and σ_N^2, and the correlation factor ρ_{NZ} for the reaction $^{56}Fe + ^{165}Ho$ at 672 MeV. The energy loss scale has been corrected for evaporation assuming thermal equilibrium between the PLF and the TLF.

TKEL (MeV)	σ_Z^2	σ_N^2	ρ_{NZ}
5	0.033 ± 0.017	0.393 ± 0.026	-0.316 ± 0.082
15	0.105 ± 0.042	0.781 ± 0.083	-0.057 ± 0.040
25	0.327 ± 0.085	1.412 ± 0.177	0.000 ± 0.048
35	0.529 ± 0.104	1.558 ± 0.206	0.251 ± 0.066
45	0.484 ± 0.113	1.700 ± 0.257	0.264 ± 0.083
55	0.688 ± 0.138	2.265 ± 0.326	0.352 ± 0.082
65	0.894 ± 0.155	2.482 ± 0.338	0.347 ± 0.082
75	1.001 ± 0.168	2.740 ± 0.330	0.552 ± 0.093
85	1.330 ± 0.240	2.993 ± 0.406	0.554 ± 0.106
95	1.339 ± 0.219	3.766 ± 0.516	0.552 ± 0.100
110	1.718 ± 0.208	3.662 ± 0.386	0.602 ± 0.082
130	2.233 ± 0.237	4.838 ± 0.507	0.648 ± 0.082
150	2.147 ± 0.230	4.813 ± 0.477	0.691 ± 0.084
170	2.176 ± 0.221	5.282 ± 0.518	0.736 ± 0.086
190	2.393 ± 0.231	6.225 ± 0.585	0.750 ± 0.084
210	2.658 ± 0.274	8.170 ± 0.714	0.791 ± 0.092
230	2.723 ± 0.294	9.908 ± 0.883	0.825 ± 0.097
260	3.291 ± 0.247	12.30 ± 0.872	0.070 ± 0.075
300	4.601 ± 0.320	18.230 ± 0.902	0.067 ± 1.052
340	4.618 ± 0.296	18.000 ± 0.904	0.067 ± 1.119
380	3.242 ± 0.251	11.186 ± 0.840	0.075 ± 0.833
420	1.924 ± 0.283	7.890 ± 0.953	0.824 ± 0.122

Table A. 5 The <N> centroids of the primary distributions with the assumptions of even excitation energy partition and thermal equilibrium between the reaction fragments, for the reaction $^{56}Fe + ^{165}Ho$ at 672 MeV.

	Even E* Division	Thermal equilibrium
TKEL (MeV)	<N>	<N>
5	29.69 ± 0.17	29.69 ± 0.17
15	30.02 ± 0.37	30.07 ± 0.37
25	30.42 ± 0.49	30.26 ± 0.48
35	30.77 ± 0.53	30.41 ± 0.52
45	31.05 ± 0.56	30.48 ± 0.56
55	31.19 ± 0.62	30.44 ± 0.60
65	31.43 ± 0.67	30.44 ± 0.64
75	31.58 ± 0.70	30.45 ± 0.66
85	31.87 ± 0.72	30.51 ± 0.69
95	32.05 ± 0.78	30.48 ± 0.73
110	32.35 ± 0.60	30.40 ± 0.55
130	32.67 ± 0.66	30.32 ± 0.62
150	33.16 ± 0.73	30.27 ± 0.65
170	33.28 ± 0.79	29.98 ± 0.71
190	33.58 ± 0.86	29.78 ± 0.78
210	33.98 ± 0.95	29.64 ± 0.82
230	34.27 ± 1.10	29.19 ± 0.88
260	35.00 ± 0.87	29.11 ± 0.72
300	36.16 ± 0.98	29.09 ± 0.83
340	36.88 ± 1.15	27.25 ± 0.86
380	35.06 ± 1.30	23.30 ± 0.90
420	32.69 ± 1.55	18.41 ± 1.36

Table A.6 The excitation energy of the projectile-like fragment as a function of energy loss for inclusive isotopes, for the reaction ^{56}Fe on ^{165}Ho at 672 MeV.

TKEL (MeV)	E^*_{PLF} (MeV)
30	14.15 ± 0.59
50	27.34 ± 1.06
70	34.12 ± 1.41
90	44.78 ± 1.39
110	52.80 ± 1.65
130	62.70 ± 2.12
150	64.91 ± 2.07
170	76.16 ± 2.60
190	76.83 ± 3.83
210	91.19 ± 4.28
230	92.99 ± 5.05
260	93.06 ± 15.79
300	80.43 ± 5.63
340	67.85 ± 6.17

Table A.7 The ratio of excitation energy stored in the projectile-like fragment as a function of energy loss for inclusive isotopes, for the reaction ^{56}Fe on ^{165}Ho at 672 MeV.

TKEL (MeV)	E^*_{PLF}/E^*_{TOT}
70	73.00 ± 3.10
90	72.70 ± 2.45
110	62.90 ± 2.04
130	62.50 ± 1.10
150	58.40 ± 1.50
170	55.70 ± 1.71
190	52.10 ± 2.21
210	51.30 ± 3.58
230	53.60 ± 2.69
250	52.40 ± 2.31
290	40.80 ± 3.57

Table A.8 The average amount of mass evaporated from the projectile-like fragment as a function of energy loss, for the reaction ^{56}Fe on ^{165}Ho at 672 MeV.

TKEL (MeV)	ΔA
50	2.09 ± 0.06
70	2.87 ± 0.13
90	3.87 ± 0.14
110	4.56 ± 0.06
130	5.47 ± 0.11
150	6.34 ± 0.15
170	7.07 ± 0.17
190	8.30 ± 0.29
210	9.46 ± 0.26
230	10.28 ± 0.28
250	11.66 ± 0.48
270	9.94 ± 0.62
290	9.47 ± 0.65
310	9.84 ± 0.30
330	7.71 ± 0.73

Table A.9 The ratio of excitation energy stored in the projectile-like fragment as a function of energy loss for four gates on the primary PLF mass, for the reaction ^{56}Fe on ^{165}Ho at 672 MeV.

TKEL(MeV)	$48<A'_{PLF}<52$ E^*_{PLF}/E^*_{TOT}	$53<A'_{PLF}<55$ E^*_{PLF}/E^*_{TOT}	$57<A'_{PLF}<59$ E^*_{PLF}/E^*_{TOT}	$60<A'_{PLF}<64$ E^*_{PLF}/E^*_{TOT}
30		76.90 ± 9.87	77.66 ± 2.89	
50		58.79 ± 5.89	58.97 ± 2.68	63.52 ± 3.10
70		51.87 ± 4.12	47.05 ± 5.40	57.68 ± 3.80
90	61.95 ± 3.10	54.72 ± 4.73	54.66 ± 2.07	58.81 ± 3.22
110	50.37 ± 2.79	52.92 ± 2.10	52.10 ± 2.99	60.98 ± 3.06
130	50.15 ± 2.40	57.82 ± 2.42	54.90 ± 1.77	51.10 ± 3.63
150	51.23 ± 2.25	48.67 ± 1.80	59.94 ± 2.89	54.35 ± 4.00
170	44.72 ± 2.74	50.66 ± 3.56	58.50 ± 3.19	75.96 ± 8.15
190	34.81 ± 3.11	45.14 ± 2.27	49.33 ± 2.63	62.18 ± 4.23
210	39.08 ± 3.35	37.61 ± 3.30	65.03 ± 1.15	62.47 ± 5.09
230	41.30 ± 3.16	32.71 ± 1.77	48.50 ± 8.30	60.21 ± 4.17
250	39.93 ± 8.07	35.90 ± 2.00	50.71 ± 8.26	59.64 ± 1.88
270	30.90 ± 2.32	44.08 ± 3.56	56.91 ± 4.48	63.36 ± 2.63
290	32.14 ± 3.87	49.34 ± 2.11		54.70 ± 4.54
310	41.95 ± 10.40	57.72 ± 4.78		
330	32.93 ± 5.23			

Table A.10 The excitation energy stored in the projectile-like fragment as a function of the primary mass of the PLF for inclusive energy loss, for the reaction ^{56}Fe on ^{165}Ho at 672 MeV.

TKEL (MeV)	E^*_{PLF}/E^*_{TOT}
42	14.41 ± 4.07
44	17.63 ± 2.80
46	25.73 ± 2.67
48	33.56 ± 2.55
50	39.95 ± 2.05
52	47.61 ± 1.99
54	51.24 ± 1.72
56	53.86 ± 1.55
58	60.62 ± 2.17
60	61.07 ± 2.74
62	61.18 ± 3.91
64	67.42 ± 5.33
66	68.32 ± 6.75
68	72.76 ± 8.72

Table A.11 The ratio of excitation energy in the projectile-like fragment as a function of its secondary mass (A''_{PLF}) for inclusive energy loss, for the reaction ^{56}Fe on ^{165}Ho at 672 MeV.

A''_{PLF}	E^*_{PLF}/E^*_{TOT}
42	53.55 ± 3.32
44	55.94 ± 2.90
46	58.87 ± 2.61
48	57.11 ± 2.25
50	52.11 ± 2.10
52	52.29 ± 2.29
54	53.49 ± 2.08
56	50.86 ± 1.88
58	45.93 ± 3.39
60	38.57 ± 5.03
62	35.00 ± 9.25
64	32.27 ± 11.27

Table A.12 The ratio of excitation energy stored in the projectile-like fragment as a function of its primary mass for three selective bins of energy loss, for the reaction ^{56}Fe on ^{165}Ho at 672 MeV.

A'_{PLF}	E^*_{PLF}/E^*_{TOT} 40 -80 MeV	E^*_{PLF}/E^*_{TOT} 160 -200 MeV	E^*_{PLF}/E^*_{TOT} 200-350 MeV
46		41.88 ± 5.11	
47		44.89. ± 2.33	
48		43.43 ± 5.88	34.38 ± 3.57
49		36.57 ± 14.90	
50		30.98 ± 2.42	34.88 ± 2.23
51	40.69 ± 12.50	42.02 ± 4.82	
52	47.55 ± 2.75	48.57 ± 3.70	40.91 ± 2.49
53	39.67 ± 4.64	52.66 ± 2.13	
54	53.02 ± 8.26	48.51 ± 2.58	35.94 ± 1.57
55	33.52 ± 4.13	53.49 ± 2.45	
56	56.70 ± 5.05	51.71 ± 5.79	49.67 ± 2.45
57	52.09 ± 3.96	53.95 ± 5.12	
58	58.28 ± 3.45	67.98 ± 3.96	57.13 ± 2.19
59	65.78 ± 3.27	61.80 ± 3.39	
60	65.72 ± 8.35	65.78 ± 3.53	57.68 ± 3.55
62			62.04 ± 12.4
64			65.77 ± 5.36

Table A.13 The ratio of excitation energy stored in the projectile-like fragment as a function of its secondary mass for three selective bins of energy loss, for the reaction ^{56}Fe on ^{165}Ho at 672 MeV.

A''_{PLF}	E^*_{PLF}/E^*_{TOT} 40 -80 MeV	E^*_{PLF}/E^*_{TOT} 160 -200 MeV	E^*_{PLF}/E^*_{TOT} 250-350 MeV
40			38.04 ± 3.74
41			57.62 ± 8.41
42			
43		50.09 ± 5.61	44.60 ± 10.41
44		51.83 ± 5.18	52.73 ± 5.23
45		61.25 ± 8.12	
46		60.93 ± 3.97	50.48 ± 7.78
47		54.96 ± 3.4	44.55 ± 4.04
48		60.63 ± 3.43	49.87 ± 4.99
49		55.61 ± 3.73	58.26 ± 4.44
50		45.00 ± 5.69	44.58 ± 1.26
51		45.67 ± 1.97	
52	52.59 ± 3.53	42.56 ± 2.72	
53	97.42 ± 14.85	41.80 ± 1.82	
54	69.50 ± 5.71		
55	68.44 ± 3.22		
56	49.72 ± 2.43		
57	51.09 ± 2.30		
58	46.87 ± 3.25		
59	41.57 ± 2.76		

Table A.14 The nuclear temperature of the projectile-like fragment as a function of energy loss for inclusive isotopes, for the ^{56}Fe on ^{165}Ho reaction at 672 MeV.

A'_{PLF}	τ_{PLF} (MeV)
10	0.490 ± 0.020
30	1.580 ± 0.031
50	2.070 ± 0.052
70	2.280 ± 0.067
90	2.630 ± 0.071
110	2.900 ± 0.060
130	3.120 ± 0.042
150	3.230 ± 0.064
170	3.370 ± 0.049
190	3.570 ± 0.076
210	3.640 ± 0.094
230	3.770 ± 0.086
250	4.250 ± 0.320

Table A.15 The nuclear temperature of the target-like fragment as a function of energy loss for inclusive isotopes, for the ^{56}Fe on ^{165}Ho reaction at 672 MeV.

TKEL (MeV)	τ_{TLF} (MeV)
10	0.41 ± 0.01
30	0.73 ± 0.03
50	1.02 ± 0.03
70	1.25 ± 0.04
90	1.33 ± 0.03
110	1.53 ± 0.03
130	1.68 ± 0.03
150	1.76 ± 0.03
170	1.96 ± 0.04
190	2.01 ± 0.04
210	2.18 ± 0.07
230	2.37 ± 0.04
250	2.49 ± 0.05

Table A.16 The primary centroids <N> and <Z>. obtained with neutron evaporation corrections assuming a mass-dependent division of the excitation energy as described by the average behavior of the data, for the $^{56}Fe + ^{165}Ho$ reaction at 672-MeV.

TKEL (MeV)	<Z>	<N>
5	25.96 ± 0.16	29.70 ± 0.17
15	25.81 ± 0.40	30.03 ± 0.38
25	25.66 ± 0.43	30.40 ± 0.49
35	25.55 ± 0.47	30.76 ± 0.54
45	25.41 ± 0.50	31.05 ± 0.58
55	25.26 ± 0.53	31.19 ± 0.63
65	25.14 ± 0.56	31.43 ± 0.68
75	25.03 ± 0.58	31.65 ± 0.71
85	24.92 ± 0.60	31.90 ± 0.74
95	24.82 ± 0.64	32.16 ± 0.80
110	24.64 ± 0.48	32.44 ± 0.61
130	24.41 ± 0.53	32.90 ± 0.68
150	24.15 ± 0.57	33.33 ± 0.76
170	24.04 ± 0.59	33.79 ± 0.81
190	23.70 ± 0.66	33.98 ± 0.91
210	23.32 ± 0.71	33.99 ± 1.00
230	23.10 ± 0.80	34.54 ± 1.16
260	23.43 ± 0.66	34.19 ± 0.97
300	21.28 ± 0.73	32.62 ± 1.09
340	19.93 ± 0.75	29.21 ± 1.10
380	18.61 ± 0.74	25.20 ± 1.01
420	18.24 ± 1.31	26.50 ± 1.96

Table A.17 The variances σ_Z^2 and σ_N^2, and correlation factor ρ_{NZ}, for the primary PLF distributions obtained with the reaction $^{56}Fe + ^{165}Ho$ at 672 MeV. Neutron evaporation corrections were performed with a mass-dependent excitation energy division as described by the average behavior of the experimental data

TKEL (MeV)	σ_Z^2	σ_N^2	ρ_{NZ}
5	0.040 ± 0.004	0.531 ± 0.007	-0.161 ± 0.008
15	0.153 ± 0.011	1.052 ± 0.024	0.180 ± 0.012
25	0.332 ± 0.019	1.701 ± 0.046	0.374 ± 0.018
35	0.500 ± 0.024	2.374 ± 0.067	0.498 ± 0.021
45	0.667 ± 0.030	3.076 ± 0.087	0.586 ± 0.024
55	0.826 ± 0.036	3.908 ± 0.114	0.628 ± 0.026
65	0.969 ± 0.042	4.360 ± 0.131	0.668 ± 0.027
75	1.046 ± 0.046	5.020 ± 0.156	0.696 ± 0.029
85	1.186 ± 0.051	5.767 ± 0.184	0.708 ± 0.030
95	1.349 ± 0.061	6.728 ± 0.227	0.754 ± 0.034
110	1.502 ± 0.048	7.762 ± 0.197	0.767 ± 0.025
130	1.879 ± 0.062	10.115 ± 0.277	0.792 ± 0.027
150	2.066 ± 0.073	12.782± 0.372	0.818 ± 0.030
170	2.567 ± 0.086	15.500 ± 0.476	0.824 ± 0.031
190	2.477 ± 0.094	18.741 ± 0.632	0.847 ± 0.036
210	2.874 ± 0.116	24.656 ± 0.866	0.870 ± 0.038
230	2.749 ± 0.121	30.075 ± 1.083	0.871 ± 0.041
260	2.830 ± 0.101	38.520 ± 1.087	0.890 ± 0.033
300	3.301 ± 0.138	61.337 ± 2.041	0.926 ± 0.040
340	4.061 ± 0.162	93.683± 3.048	0.950 ± 0.040

Table A.18 The primary centroids <N> and <Z> obtained by the kinematical reconstruction method, for the ^{56}Fe + ^{165}Ho reaction at 672-MeV.

TKEL (MeV)	<Z>	<N>
10	25.74 ± 1.51	30.58 ± 1.72
30	25.34 ± 1.47	31.65 ± 1.76
50	25.08 ± 1.39	31.18 ± 1.67
70	24.67 ± 1.38	30.72 ± 1.66
90	24.32 ± 1.30	30.50 ± 1.57
110	24.27 ± 1.21	30.82 ± 1.48
130	23.98 ± 1.22	30.97 ± 1.51
150	23.85 ± 1.25	31.36 ± 1.59
170	23.64 ± 1.23	31.97 ± 1.61
190	23.38 ± 1.42	33.44 ± 1.95
210	23.39 ± 1.36	34.12 ± 1.91
230	23.17 ± 1.45	35.11 ± 2.13
250	22.74 ± 1.59	33.00 ± 2.23
270	22.68 ± 1.68	32.72 ± 2.34
290	22.26 ± 1.32	30.42 ± 1.74
340	22.35 ± 2.54	30.18 ± 3.32

Table A.19 The variances σ_Z^2 and σ_N^2, and correlation factor ρ_{NZ}, for the primary PLF distributions obtained by kinematical reconstruction in the reaction $^{56}Fe + {}^{165}Ho$ at 672 MeV.

TKEL (MeV)	σ_Z^2	σ_N^2	ρ_{NZ}
10	0.087 ± 0.062	0.468 ± 0.095	-0.418 ± 0.172
30	0.471 ± 0.109	2.561 ± 0.325	-0.074 ± 0.060
50	0.949 ± 0.150	3.845 ± 0.459	0.234 ± 0.062
70	1.574 ± 0.195	6.594 ± 0.598	0.317 ± 0.058
90	2.085 ± 0.229	8.277 ± 0.763	0.180 ± 0.057
110	2.647 ± 0.290	8.652 ± 0.810	0.208 ± 0.058
130	2.898 ± 0.288	8.790 ± 0.705	0.114 ± 0.047
150	2.579 ± 0.270	11.080 ± 0.943	0.010 ± 0.052
170	3.440 ± 0.358	13.886 ± 1.204	0.016 ± 0.054
190	3.218 ± 0.354	16.979 ± 1.413	0.051 ± 0.058
210	2.631 ± 0.324	19.697 ± 1.930	0.159 ± 0.071
230	3.538 ± 0.436	28.240 ± 2.382	0.154 ± 0.070
250	3.692 ± 0.473	33.379 ± 3.093	0.141 ± 0.071
270	3.687 ± 0.493	31.130 ± 3.275	0.186 ± 0.074
290	3.620 ± 0.491	22.383 ± 2.707	0.012 ± 0.077
310	3.678 ± 0.399	24.241 ± 2.394	0.199 ± 0.064
340	4.386 ± 0.925	23.420 ± 4.244	0.058 ± 0.116

REFERENCES

AWE84 T. C. Awes, R. L. Ferguson, R. Novotny, F. E. Obenshain, F. Plasil, S. Pontoppidan, V. Rauch, G.R. Young, and H. Sann, *Phys. Rev. Lett.* **52**, 251 (1984).

BAB78 R. Babinet, B. Cauvin, J. Girard, H. Nifenecker, B. Gatty, D. Guerreau, M. Lefort, and X. Tarrago, *Nucl. Phys.* **A296**, 160 (1978).

BEC73 R. Beck and D. H. E. Gross, *Phys. Lett.* **47B**, 143 (1973).

BEN85 D. R. Benton, Ph. D. Thesis PP # 86-030; University of Maryland (1985).

BEN87 D. R. Benton, H. Breuer, F. Khazaie, K. Kwiatkowski, V. Viola, S. Bradley, A. C. Mignerey, and A. P. Weston Dawkes, *Phys. Lett.* **B185**, 326 (1987).

BEN88 D. R. Benton, H. Breuer, F. Khazaie, K. Kwiatkowski, V. Viola, S. Bradley, A. C. Mignerey, and A. P. Weston Dawkes, *Phy. Rev.* **C38**, 1207 (1988).

BLO78 J. Blocki, Y. Boneh, J. R. Nix, J. Randrup, M. Robel, A. J. Sierk, and W. J. Swiatecki, *Ann. of Phys. (NY)* **113**, 330 (1978).

BOR88 B. Borderie, M. Montoya, M. F. Rivet, D. Jouan, C. Cabot, H. Fuchs, D. Gardes, H. Gauvin, D. Jacquet, and F. Monnet, *Phys. Lett.* **B205**, 26 (1988).

BOR90 B. Borderie, M. F. Rivet, and L. Tassan-Got, Internal Report INPO-DRE-90-06; Orsay, France, 1990.

BRE83a H. Breuer, A. C. Mignerey, V. E. Viola, K. L. Wolf, J. R. Birkelund, D. Hilsher, J. R. Huizenga, W. U. Schröeder, and W. W. Wilcke, *Phys. Rev.* **C28**, 1080 (1983).

BRE83b H. Breuer, N. R. Yoder, A. C. Mignerey, K. Kwiatkowski, and K. L. Wolf, *Nucl. Instrum. and Methods* **204**, 419 (1983).

BRE89 H. Breuer *et.al.*, Lisa Collaboration, Department of Physics and Astronomy, University of Maryland, 1989.

BRO74 R. A. Broglia, C. H. Dasso, and A. Winther, *Phys. Lett.* **53B**, 301 (1974).

BRO76 R. A. Broglia, C. H. Dasso, and A. Winther, *Phys. Lett.* **61B**, 113 (1976).

BRO78a R. A. Broglia, O. Civitarese, C. H. Dasso, and A. Winther, *Phys. Lett.* **73B**, 405 (1978).

BRO78b R. A. Broglia, C. H. Dasso, G. Pollarolo, and A. Winther, *Phys. Rev. Lett.* **41**, 25 (1978).

BRO80 R. A. Broglia, C. H. Dasso, and A. Winther, Nordita 80/16

CAR83 J. Carter et al, *Zeit. Phys.* **A313**, 57 (1983).

CAU78 B. Cauvin, R. C. Jared, P. Russo, R. P. Schmitt, R. Babinet, and L. G. Moretto, *Nucl. Phys.* **A301**, 511 (1978).

DE82 J. N. De, *Phys. Lett.* **113B**, 455 (1982).

EYA78 Y. Eyal, A. Gavron, I. Tsenurja, A. Fraenkel, Y. Eisen, S. Wald, R. Bass, C. R. Gould, G. Keyling, R. Renfordt, K. Stelzer, R. Zitmann, A. Gobbi, U. Lynem, H. Stelzer, I. Rode, and R. Bah, *Phys. Rev. Lett.* **41**, 625 (1978).

FEL84 H. Feldmeir, *Nucl. Phys.* **A428**, 223c (1984).

FIN74 H. J. Fink, J. Maruhn, W. Scheid, and W. Greiner, *Z. Physik*, **A268**, 321 (1974).

FRA80 N. Frascaria, P. Colombani, A. Gamp, M. Riou, J. P. Garron, J. C. Roynette, C. Stéphan, A. Ameaume, C. Bizard, J. L. Laville and M. Louvel, Z. *Physik.* **A294**, 167-172 (1980).

FRE84 H. Freiesleben and J. V. Kratz, *Phys. Rev.* **106**, 1 (1984).

GAV80 A. Gavron, *Phys. Rev.* **C2**, 230 (1980).

GOB80 A. Gobbi and W. Nörenberg, *Heavy Ion Collisions*, Vol. 2, Ed. R. Bock (North-Holland, Amsterdam, 1980), p. 127.

GOU78 C. R. Gould, R. Bass, J. V. Czarnecki, V. Hartmann, K. Stetzer, R. Zitzmann, and Y. Eyal, Z. *Phys.* **A284**, 353 (1978).

GRI81 J. J. Griffin, Y. Boneh, M. Dworzecka, and K. K. Kan, *Nucl. Phys.* **A360**, 181 (1981).

GRI82 J. J. Griffin et al, *Nucl. Phys.* **A382**, 159 (1982).

GRI87 J. J. Griffin, J. A. Lukasiak, M. Dworzecka, *Zeit. Phys.* **A326**, 51 (1987).

GRO74 D. A. E. Gross and H. Kalinowski, *Phys. Lett.* **48B**, 302 (1974).

GRO75 D. H. E. Gross, *Nucl. Phys.* **A240**, 472 (1975).

GRO77 D. H. E. Gross, *Phys. Lett.* **68B**, 412 (1977).

HEN79 D. C. Hensley, *IEEE Trans. Nucl. Sci. NS-26*, **No 24**, 4454-58 (1979).

HIL79 D. Hilscher, J. R. Birkelumd, A. D. Hoover, W. U. Schröeder, W. W. Wilker, J. R. Huizerga, A. C. Mignerey, K. L. Wolf, H. F. Breuer, and V. E. Viola, Jr., *Phys. Rev.* **C20**, 576 (1979).

HOF76 H. Hofmann and P. J. Siemens, *Nucl. Phys.* **A257**, 165 (1976).

KWI90 K. Kwiatkowski, R. Planeta, S. H. Zhou, V. E. Viola, H. Breuer, M. A. McMahan, A. C. Mignerey, *Phys. Rev.* **C41**, 958 (1990).

LEF78 M. Lefort and C. H. Ngô, *Ann. Phys.* **V. 3**, # 1 (1978).

LOC82 D. -K. Lock, R. Vandenbosch, and A. Lazzarini, *Nucl. Phys.* **A384**, 241 (1982).

LOC85 D. -K. Lock, R. Vandenbosch, and J. Randrup, *Phys. Rev.* **C31**, 1268 (1985).

LOT92 B. Lott, S. P. Baldwin, B. M. Szabo, B. M. Quednau, W. U.. Schröder, J. Tõke, L. G. Sobotka, J. Barreto, R. J. Charity, L. Gallamore, D. G. Sarantites, D. W. Stracener, and R. T. de Souza, *Phys. Rev. Lett.* **68**, 3141 (1992).

MAR91 A. A. Marchetti, Ph. D. Thesis. # ER-4021-8, University of Maryland (1991).

MAR92 A. A. Marchetti, A.C. Mignerey, H. Madani A. Gökmen, W.L. Kehoe, B. Libby, K. Morley, H. Breuer, K. Wolf, and F. Obenshain, submitted to Physical Review C (1992).

MAR93 A. A. Marchetti and A. C. Mignerey, *Nucl. Instrum. and Methods* **A324**, 288 (1993).

MER86 C. Merouane, Ph. D. Thesis. # ORO-5172-0026 University of Maryland (1986).

MIG81 A. C. Mignerey, Annual Progress Report, ORO-5172-0019, (1981).

MOR79 L. G. Moretto, Conference on Large Scale Collective Excitation, Hungary, June 11 - 15, 1979.

MOR83 L. G. Moretto, *Zeit. Phys.* **A310**, 61 (1983).

NOR74 W. Nörenberg, *Phys. Lett.* **53B**, 289 (1974).

NOR75 W. Nörenberg, Z. *Phys.* **A274**, 241 91975).

OAK87 Computer Handbook of the Holi field Heavy-Ion Research Facility; Oak Ridge National Laboratory, Oak Ridge, Tennessee, 1987.

PEN90 V. Penumetcha, G. A. Petitt, T. C. Awes, J. R. Beene, R. L. Ferguson, F. E. Obenshain, F. Plasil, G. R. Young, S. P. Soresen, *Phys. Rev.* **C42**, 1489 (1990).

PLA78 F. Plasil, R. L. Ferguson, H. C. Britt, R. H. Stokes, B. H. Enkkila, P. D. Goldstone, M. Blann, and H. H. Gutbrod, *Phys. Rev. Lett.* **40**, 1164 (1978).

PLA90 R. Planeta, K. Kwiatkowski, S. W. Zhou, V. E. Viola, H. Breuer, M. A. McMahan, W. Kehoe, and A. C. Mignerey, *Phys. Rev.* **C41**, 3942 (1990).

RAN78a J. Randrup, *Ann. Phys. (NY)* **112**, 356 (1978).

RAN78b J. Randrup, *Nucl. Phys.* **A307**, 319 (1978).

RAN79 J. Randrup, *Nucl. Phys.* **A327**, 490 (1979).

RAN82 J. Randrup, *Nucl. Phys.* **A383**, 468 (1982).

SAM85 S. K. Samaddar, J. N. De, and K. Krishan, *Phys. Rev.* **C31**, 1053 (1985).

SCH77 W. U. Schröeder and J. R. Huizerga, *Ann. Rev. Nucl. Sci.* **27**, 465 (1977).

SCH84 W. U. Schröeder and J. R. Huizenga, in *Treatise on Heavy-Ion Science*, Vol. 2, Ed. by D. A. Bromley, Plenum, New York, 1984; Chapter 3.

SIW76 K. Siwek-Wilczyn´ska, and J. Wilczyn´sk, *Nucl. Phys.* **A264** 115 (1976).

SOB86 L. G. Sobotka, G. J. Wozniak, R. J. McDonald, M. A. McMahon, R. J. Charity, L. G. Moretto, Z. H. Liu, F. S. Stephens, R. M. Diamond, and M. A. Delphanque, *Phys. Lett.* **B175**, 27 (1986).

SOH85 H. Sohlbach, H. Freiesleben, P. Braun-Munzinger, W. F. W. Schneider, D. Schül, B. Kohlmeyer, M. Marinescu, and Pühlhofer, *Phys. Lett.* **153B**, 385 (1985).

SOH87a H. Sohlbach, H. Freiesleben, W. F. W. Schneider, D. Schül, P. Braun-Munzinger, B. Kohlmeyer, M. Marinescu, and F. Pühlhofer, *Nucl. Phys.* **A467**, 349 (1987).

SOH87b H. Sohlbach, H. Freiesleben, W. F. W. Schneider, D. Schül, B. Kohlmeyer, M. Marinescu, and F. Pühlhofer, *Z. Phys.* **A328**, 205 (1978).

SOU88 R. T. deSouza, W. U. Schröeder, J. R. Huizenga, R. PLaneta, K. Kwiatkwoski, V. E. Viola, and H. Breuer, *Phys. Rev.* **C37**, 1783 (1988).

STE88 H. Stege, H. -J. Keim, H. A. Bösser, B. Kohlmeyer, F. Pühlhofer, and W. F. W. Schneider, *Nucl. Phys.* **A489**, 146 (1988).

TAM79 Tamain, R. Chechik, H. Fuchs, F. Hanappe, M. Morjean, C. Ngô, J. Peter, M. Dakowski, B. Lucas, C. Mazur, M. Ribrag and C. Signarbieux, *Nucl. Phys.* **A330**, 253 (1979).

TAS88 L. Tassan-Got, Ph.D. Thesis, INPO- T-89-02; Orsay, France, 1988.

TAS89 L. Tassan-Got and C. Stephan, Internal Report INPO-DRE-89-46, 1989.

TAS91 L. Tassan-Got and C. Stéphan, *Nucl. Phys.* **A524** , 121 (1991).

TOK89 J. Tõke, W. U. Shröeder, and J. R. Huizenga, *Phys. Rev.* **C40**, R1577 (1989).

TOK90 J. Tõke, W. U. Shröeder, and J. R. Huizenga, *Nucl. Instrum. and Methods* **A288**, 406 (1990).

TOK91 J. Tõke, R. Planeta, W. U. Shröeder, and J. R. Huizenga, *Phys. Rev.* **C44**, 390 (1991).

VAN84a R. Vandenbosch, A. Lazzarini, D. Leach, D. -K. Lock, A. Ray, and A. Seamster, *Phys. Rev. Lett.* **52** 1964, (1984).

VAN84b R. Vandenbosch, A. Lazzarini, D. Leach, D. -K. Lock, A. Ray, and A. Seamster, Workshop on Nuclear Dynamics III, Copper Mountain, Co, p.67 (1984).

WEI80 H. A. Weidenmüller, Progress in *Nuclear and Particle Physics* **3**, 49 (1980).

WIL73 W. W. Wilczn´ski, *Phys. Lett.* **B47**, 484, (1973).

WIL80 W. W. Wilcke, J. R. Birkeland, H. J. Wollershe, A. D. Houra, J. R. Huizenga, W. U. Shröeder, and L. E. Tubbs, *Atomic data and Nuclear data Tables* **25**, 529 (1980).

WIL87 J. L. Wile, W. U. Schröeder, J. R. Huizenga, and D. Hilscher, *Phys. Rev.* **C35**, 1608 (1987).

END

DATE FILMED

6/21/93